AD-A060 353 BATTELLE COLUMBUS LABS OHIO F/G 11/6

AMORPHOUS GLASSY METAL AND MICROCRYSTALLINE ALLOYS FOR AEROSPAC--ETC(U)

JUN 78 E W COLLINGS, R E MARINGER, C E MOBLEY F33615-74-C-5179

UNCLASSIFIED AFML-TR-78-70 NL

1 OF 3

AD
A060353

LEVEL II

4

AFML-TR-78-70

AD A060353

AMORPHOUS GLASSY METAL AND MICROCRYSTALLINE ALLOYS FOR AEROSPACE APPLICATIONS

E. W. COLLINGS
R. E. MARINGER
C. E. MOBLEY
BATTELLE, COLUMBUS LABORATORIES
COLUMBUS, OHIO 43201

JUNE 1978

TECHNICAL REPORT AFML-TR-78-70
Final Report January 1975 – August 1977

Approved for public release; distribution unlimited.

AIR FORCE MATERIALS LABORATORY
AIR FORCE WRIGHT AERONAUTICAL LABORATORIES
AIR FORCE SYSTEM COMMAND
WRIGHT-PATTERSON AIR FORCE BASE, OHIO 45433

NOTICES

When Government drawings, specifications, or other data are used for any purpose other than in connection with a definitely related Government procurement operation, the United States Government thereby incurs no responsibility for any obligation whatsoever; and the fact that the Government may have formulated, furnished, or in any way supplied the said drawings, specifications, or other data, is not to be regarded by implication or otherwise as in any manner licensing the holder or any other person or corporation, or conveying any rights or permission to manufacture, use or sell any patented invention that may in any way be related thereto.

This report has been reviewed by the Information Office (IO) and is releasable to the National Technical Information Service (NTIS). At NTIS, it will be available to the general public, including fireign nations.

This technical report has been reviewed and is approved for publication.

Harold L. Gegel
HAROLD L. GEGEL
Project Scientist

FOR THE COMMANDER

Henry C. Graham
HENRY C. GRAHAM
Actg Chief, Processing and High
Temperature Materials Branch
Metals and Ceramics Division
Air Force Materials Laboratory

Copies of this report should not be returned unless return is required by security considerations, contractual obligations, or notice on a specific document.

AIR FORCE/56780/2 October 1978 — 300

UNCLASSIFIED

SECURITY CLASSIFICATION OF THIS PAGE (When Data Entered)

REPORT DOCUMENTATION PAGE

READ INSTRUCTIONS BEFORE COMPLETING FORM

1. REPORT NUMBER
AFML-TR-78-70

2. GOVT ACCESSION NO.

3. RECIPIENT'S CATALOG NUMBER

4. TITLE (and Subtitle)
AMORPHOUS GLASSY METAL AND MICROCRYSTALLINE ALLOYS FOR AEROSPACE APPLICATIONS.

5. TYPE OF REPORT & PERIOD COVERED
Final rept.
Jan 1975 - Aug 1977

6. PERFORMING ORG. REPORT NUMBER

7. AUTHOR(s)
E. W. Collings, R. E. Maringer, and C. E. Mobley

8. CONTRACT OR GRANT NUMBER(s)
F33615-74-C-5179

9. PERFORMING ORGANIZATION NAME AND ADDRESS
Battelle, Columbus Laboratories
505 King Avenue
Columbus, OH 43201

10. PROGRAM ELEMENT, PROJECT, TASK AREA & WORK UNIT NUMBERS
73510819 62102F

11. CONTROLLING OFFICE NAME AND ADDRESS
Air Force Materials Laboratory (LLM)
Wright-Patterson AFB, OH 45433

12. REPORT DATE
June 1978

13. NUMBER OF PAGES
234

14. MONITORING AGENCY NAME & ADDRESS (if different from Controlling Office)
257 p.

15. SECURITY CLASS. (of this report)
Unclassified

15a. DECLASSIFICATION/DOWNGRADING SCHEDULE

16. DISTRIBUTION STATEMENT (of this Report)

Approved for public realeas; distribution unlimited.

17. DISTRIBUTION STATEMENT (of the abstract entered in Block 20, if different from Report)

18. SUPPLEMENTARY NOTES

19. KEY WORDS (Continue on reverse side if necessary and identify by block number)

amorphous alloys
microcrystalline alloys
titanium alloys
strength
hardness
elastic modulus
PTO
iron phosphorus carbon alloys
iron phosphorus carbon alloys with boron
iron phosphorus carbon alloys with silicon
iron phosphorus carbon alloys with silicon and boron
(Continued.....)

20. ABSTRACT (Continue on reverse side if necessary and identify by block number)

This report discusses the results of a program, initiated in January, 1975, for the preparation and examination of the mechanical characteristics of amorphous and rapidly-quenched polycrystalline alloys with properties relevant to aerospace applications. In it are described (a) the preparation and properties of a rapidly quenched Ti-6Al-4V alloy powder substitute, and its successful consolidation by vacuum-hot-pressing and hot-isostatic-pressing into test shapes from which were machined tensile bars and compression-test specimens. Composition was found to be retained, and the properties of the wrought starting (Con't.)

DD FORM 1 JAN 73 1473 EDITION OF 1 NOV 65 IS OBSOLETE

Unclassified

SECURITY CLASSIFICATION OF THIS PAGE (When Data Entered)

407080 78 10 19 048 LB

19. Key Words (Continued)

sputtering	vacuum hot pressing -- titanium alloy powders	titanium aluminum alloy
splat quenching	hot isostatic pressing -- titanium alloy powders	titanium aluminum alloy powder
melt spinning		
melt extraction		

20. Abstract (Continued)

Cont material were essentially recovered; (b) the preparation by sputtering, splat quenching, melt spinning and melt extraction of 30 metallic glass candidate alloys, and the measurement of several of their properties. The performance of "solution strengthening" studies on a well-categorized metallic glass basic alloy, $Fe_{80}P_{13}C_7$, and the preparation and examination of the properties of an advanced high-specific-strength Ti-base Be-free metallic-glass alloy; (c) the examination of melt-extracted rapidly-quenched-polycrystalline solution- and precipitate-strengthened Ti-base fibers, and the preparation and properties of a ductile polycrystalline Ti-base fiber with specific strength comparable to that of the best metallic glass ribbon fiber presently available.

LEVEL II

FOREWORD

The research discussed herein was supported by the Air Force Materials Laboratory, Wright-Patterson Air Force Base under Contract Number F33615-74-C-5179 entitled "Amorphous Glassy Metal and Microcrystalline Alloys for Aerospace Applications", and monitored by Dr. H. L. Gegel. This report was prepared by E. W. Collings, Battelle Program Manager, with contributions from R. E. Maringer and C. E. Mobley. Principal participants in the program were E. W. Collings, R. E. Maringer and C. E. Mobley; and important technical contributions to the various stages of it were made by H. L. Gegel (AFML, elastic, microstructural and tensile properties), J. J. Mueller (Battelle, hot isostatic pressing), R. K. Malik (Battelle, vacuum hot pressing), C. W. Marschall (Battelle, mechanical properties of fibers), S. D. Dahlgren (Battelle Northwest, high-rate sputtering), R. Wang (Battelle Northwest, x-ray diffraction), D. Shechtman (AFML and Technion, electron microscopy and diffraction), K. Teegarden (University of Rochester, sputtering and related studies under sub-contract), Professor D. Turnbull (Harvard, consultant), P. R. Held, R. D. Smith, O. M. Stewart (Battelle, technical assistance), and the personnel of several Battelle service groups.

TABLE OF CONTENTS

TABLE OF CONTENTS (cont'd)

TABLE OF CONTENTS (cont'd)

TABLE OF CONTENTS (cont'd)

TABLE OF CONTENTS (cont'd)

LIST OF ILLUSTRATIONS

LIST OF ILLUSTRATIONS (cont'd)

LIST OF ILLUSTRATIONS (cont'd)

LIST OF ILLUSTRATIONS (cont'd)

LIST OF ILLUSTRATIONS (cont'd)

LIST OF ILLUSTRATIONS (cont'd)

LIST OF ILLUSTRATIONS (cont'd)

LIST OF TABLES

LIST OF TABLES (cont'd)

LIST OF TABLES (cont'd)

LIST OF TABLES (cont'd)

LIST OF TABLES (cont'd)

SECTION I

INTRODUCTION

According to our proposal, one of the aims of the program was "to develop techniques for producing and handling an alloy powder-substitute. The powder substitute will consist of small diameter, low aspect-ratio (L/D), particulates made by the melt extraction process.* These particulates, herein referred to as L/D powder, should be amenable to being processed using conventional powder-metallurgical methods." We also stated that an accompanying aim of the program "is to investigate and develop improved metallic fibers for use in fiber-reinforced composite materials." Fibers are sought which will be superior to those currently available with regard to strength, ductility, density, and cost. They will be either <u>microcrystalline</u> in structure or <u>amorphous</u> (metallic glass). The latter title represents an entirely new class of material within which we expect to find a wide range of property variations. Preliminary evidence suggests that some metallic glasses possess unusual strength and plasticity properties. During the course of the research, it is intended to study the mechanical properties of representatives of numerous metallic glass systems and to make 'diagnostic' physical-property investigations of structural and thermal stability."

What follows is a complete report, showing within the space of nine detailed sections, how the essential program goals were fully accomplished.

---

*Patents covering the proprietary process known as "melt extraction" are owned by Battelle Development Corporation.

1.1 Preparation and Properties of Compacted Melt Extracted Staple Fiber

This "program within a program" was spurred by the aerospace industry's growing interest in powder metallurgical processing, the use of which is already leading to improvements in metallurgical quality, and savings in energy, materials, and cost. In our proposal, we noted that "because of the potential cost savings in the manufacture of aircraft and aerospace structural components, the application of powder metallurgy technology to the fabrication of titanium alloy structures is of prime interest to the Air Force. The present high cost of titanium alloy structural components stems from the large volume of material input in the form of forgings and extrusions for structural components and the associated cost of machining away the excess material. Powder metallurgy is a technology which can directly impact the area of effective material utilization while at the same time minimizing metal removal costs.

Although significant strides are being made in the areas of manufacturing techniques for making near-net shapes from powder, the cost of input powder is one of the retarding forces to rapid advancement and application of this technology in production. These powder-making processes which yield powder of quality suitable for structural applications, i.e., rotating electrode (REP) and hydride-dehydride, are presently quite costly with some associated problems of contamination still to be solved. On the other hand, there are other processes which yield potentially cheaper powder, but they offer products of lower quality or are not as nearly developed". The first phase of the program offered a solution to this problem along the following lines.

For some materials, particularly reactive ones such as titanium alloys, the usual methods of powder production are hampered by difficulties in the control of chemical homogeneity and purity. The reactivity of titanium and its alloys dictates the use of a containerless melting procedure. Accordingly vacuum-protected pendant drop melt extraction was identified as a promising method for the production of Ti-6Al-4V, the alloy of interest in this section of the program, in the form of staple fiber (the so-called L/D powder).

The preparation of continuous filament was the first problem to be investigated. Techniques of L/D powder preparation were then explored using stainless steel (air melted) as a working substance. And the information acquired in these two preliminary studies was coupled in order to produce the first batches of Ti-6Al-4V L/D powder. Test quantities of Ti-6Al-4V L/D powders having two different L/D ratios were produced, consolidated by vacuum hot pressing (VHP) and hot isostatic pressing (HIP), and the resulting compactions were evaluated in terms of composition, mechanical properties, and microstructures. As an interesting corollary we note, that by performing tests on the continuous filament prior to installing the notched staple-fiber wheel, the mechanical properties of the starting powder could, in effect, be examined prior to subsequent thermomechanical processing. The L/D powder process is thus the only one that exists in which the properties of the powder product can be so fully documented.

In the powder sub-program we considered the preparation of

- Continuous filament
- L/D powders
- Vacuum-hot-pressed (VHP) compactions
- Hot isostatically pressed (HIP) compactions.

and studied mechanical properties and microstructures after various heat treatments.

The program was eminently successful in that after a complete processing sequence, beginning with wrought Ti-6Al-4V rod as an experimental starting alloy, and ending with a VHP-ed or HIP-ed heat-treated compaction, we were able to recover the essential properties of the starting material, which also served as a reference.

1.2 Metallic Glass Studies

At the inception of this program, metallic glass fibers had been identified as potentially important reinforcing materials in fiber-reinforced composites. This is still true today, although progress in the fabrication and evaluation of test sheets of metallic-glass-fiber-reinforced materials has been disappointingly slow. But in addition, further applications of metallic glass fibers, particularly in woven form, are today being found.

Fiber-reinforced composites are of interest to both the air-frame and engine designer. In an air-frame, the region in the vicinity of a fastener is often of considerable importance from a structural integrity standpoint, but at the same time the existence of component overlap makes inspection difficult in most cases, and impossible in others. Since crack detection is difficult, prevention becomes crucially important. Accordingly some degree of plasticity of the material in the vicinity of the fastener hole is a desirable attribute. In order to be able to take advantage of the fiber-composite materials in air-frame construction, a reinforcing filament must be found that is capable of plastically deforming around the hole and so minimize the possibility of crack initiation. The requisite combination of strength and plasticity is not an attribute of either boron or graphite filaments. Neither are they attractive from a cost standpoint.

In engine manufacture the technology exists for manufacturing epoxy-graphite or epoxy-boron gas-turbine compressor blades. Unfortunately, blades made from these materials are unable to satisfactorily withstand the impact of foreign objects ingested by the engine. Again the limitations are in the properties of presently available fiber-reinforcements.

It is considered that metallic glass fibers will be favorable ingredients of air-frame and engine components from the standpoints of strength, ductility, <u>and</u> cost. For example, tensile strengths of about 3.3 to 5.3 x 10^5 psi have been reported for certain iron-base metallic glasses, and a specific strength (i.e., strength/density) as high as 22 x 10^5 in. has been measured in a Ti-base metallic glass.

In addition, metallic glass alloys generally show an unusual amount of bend ductility, a property which is inherent in the metallic glass atomic structure.

Accordingly a program was designed for the preparation by several rapid-quench processes, and a subsequent property evaluation, of numerous metallic glass candidates. During the course of this program, 30 metallic glass alloys were prepared by sputtering (both normal and high-rate), splat quenching (by the gun and rotating disk techniques), melt spinning, and pendant drop melt extraction. "Solution strengthening" studies were carried out on a well-categorized metallic glass base alloy $Fe_{80}P_{13}C_7$ to which B, Si, and B + Si had been added, in such a way as to keep the Fe/metalloid ratio fixed at 80:20. Properties measured and discussed included Young's modulus, hardness, and direct measurements of tensile strength. In addition an advanced high-specific strength, Be-free metallic glass alloy was prepared and examined.

1.3 High-Specific Strength Polycrystalline Fibers

Microcrystalline but not amorphous materials can also be produced by rapid melt-quench techniques. Because of favorable mechanical and physical properties, these too are of interest to the Air Force as strengthening fibers. For example, it has long been known that considerable increases in strength and modulus in aluminum alloys can accrue as a result of rapid quenching from the melt. The mechanism of strengthening in these materials is due to one or several of the following effects: fine grain size; second phase dispersion; high concentration of solution strengthener retained as a result of the rapid quench. Fibers made from these sorts of alloys may prove to be just as important technically as metallic glass fibers in strengthening applications, either in conventional or woven form.

To accomplish this phase of the program, we took Ti-6Al-4V as a base and explored the effect of alloying into it small amounts of other elements that would produce strengthening either through the precipitate dispersion method or through solution strengthening. The rapid quenching associated with pendant drop melt extraction would of course take care of the grain refinement. In an initial series of studies some 25 alloys were prepared using an in-situ melting procedure, and quickly screened for desirable mechanical properties. As a result of this work, alloy compositions were selected and pre-alloyed starting rods were prepared, again from Ti, Al and V, strengthened with elements such as Be, B, Si, Cu, and Fe. Melt-extracted fibers prepared from these alloys were examined in detail. The results were extremely promising. Not only did some of the alloys have excellent bend ductility, but their specific strengths were comparable to those of the best metallic glass fibers yet discovered.

SECTION II

EXPERIMENTAL DETAILS

In order to prepare microcrystalline or amorphous materials, numerous rapid-quenching techniques are available. Amorphous materials themselves are prepared by rapidly "by-passing" the thermodynamic freezing point during solidification from either the vapor phase or the melt. The usual techniques of vapor quenching, during which equivalent solidification rates as high as 10^{15} K s^{-1} are possible, consist of vacuum deposition, flash evaporation, sputtering, and plasma spraying. In liquid quenching, or quenching from the melt, through techniques such as melt extraction*, melt spinning, and splat quenching, cooling rates in the range 10^4 - 10^8 K s^{-1} are claimed.

2.1 Sputtering

In this technique, positive ions generated in an independently maintained gas-discharge plasma are accelerated towards a target (a cathode) consisting of the material to be deposited. Target material dislodged by the bombardment is transported towards the anode, or substrate where it deposits as a rapidly-quenched layer. The usual laboratory scale equipment is slow. But apparatus, such as that located at Battelle's Pacific Northwest Laboratories can deposit layers at a rate of typically 1μm min^{-1} [1]. In this study, a few samples were prepared by both conventional and high-rate sputtering.

Using conventional equipment, the University of Rochester, under subcontract, prepared the following sputtered materials: $Fe_{75.2}Cr_{19.6}B_{5.2}$ $Fe_{73}Cr_{2.5}B_{24.5}$, $Fe_{11.3}Cr_{7.4}B_{81.3}$, $Ti_{93}B_7$, $Ti_{34}B_{66}$, and $Fe_{84}B_{16}$, where the subscripts refer to compositions in atomic percent. And through the courtesy of Dr. S. D. Dahlgren of Battelle's Pacific Northwest Laboratory, high-rate sputtering onto room-temperature, and liquid-nitrogen-cooled copper substrates was used to prepare massive samples (3.8 cm diam x ~ 0.25 mm in thickness) of $Fe_{80}P_{13}C_7$.

*Patents covering the proprietary process known as "melt extraction" are owned by the Battelle Development Corporation.

2.2 Techniques of Splat Quenching

In splat quenching, a liquid droplet is rapidly frozen against a cooled surface which itself may be either stationary or in motion. Figure 1 shows a representative set of liquid-quench procedures, all closely related, which are commonly used in laboratory preparation of metastable alloys. Figure 1a exemplifies a method initially employed by Duwez, a pioneer in the field. A droplet of liquid alloy is explosively projected onto a copper ramp, upon which it smears itself out into a thin rapidly chilled flake.[2] In Figure 1b, a liquid droplet is flicked out of a curved furnace tube onto a chilled block. This method, which has been named by Toda and Maddin[3] "the torsion catapult method", has achieved cooling rates of 10^5 to 10^6 deg/sec. Similar cooling rates are obtained using a piston-and-anvil method, or the "impacted droplet" technique described by Beghi, Matera, and Piatti,[4] Figure 10. Methods which involve a rapidly moving substrate are the "rotating drum" of Pond and Maddin[5]*, Figure 1d, the "double-roller" method, Figure 1e, employed by Chen and Wang (1971)[6], and Chen, Leamy and Barmatz[7], and the levitated-droplet rotating-disc method, Figure 1f. In Figure 1g we draw attention to a method which is reminiscent of conventional liquid bath quenching. Pampillo[8] has successfully prepared amorphous specimens of a Pd-based alloy by the quenching of liquid alloys sealed up in quartz tubes. This method yields rod-like samples eminently suitable for mechanical testing. Interesting laboratory results have also been obtained using the so-called "self-substrate" technique. In this, as the name suggests, surface layers melted by some impulsive energy source, are rapidly resolidified by thermal diffusion.

The techniques referred to above, and others; and the quenching rates obtainable by some of them, are discussed in numerous review articles, two of the more recent ones being those of Chen[9] and Takayama[10]. Table 1, taken from the latter article, lists the quench rates expected from some of the standard splat quenching techniques referred to above.

---

*This method yielded a filament rather than a "splat".

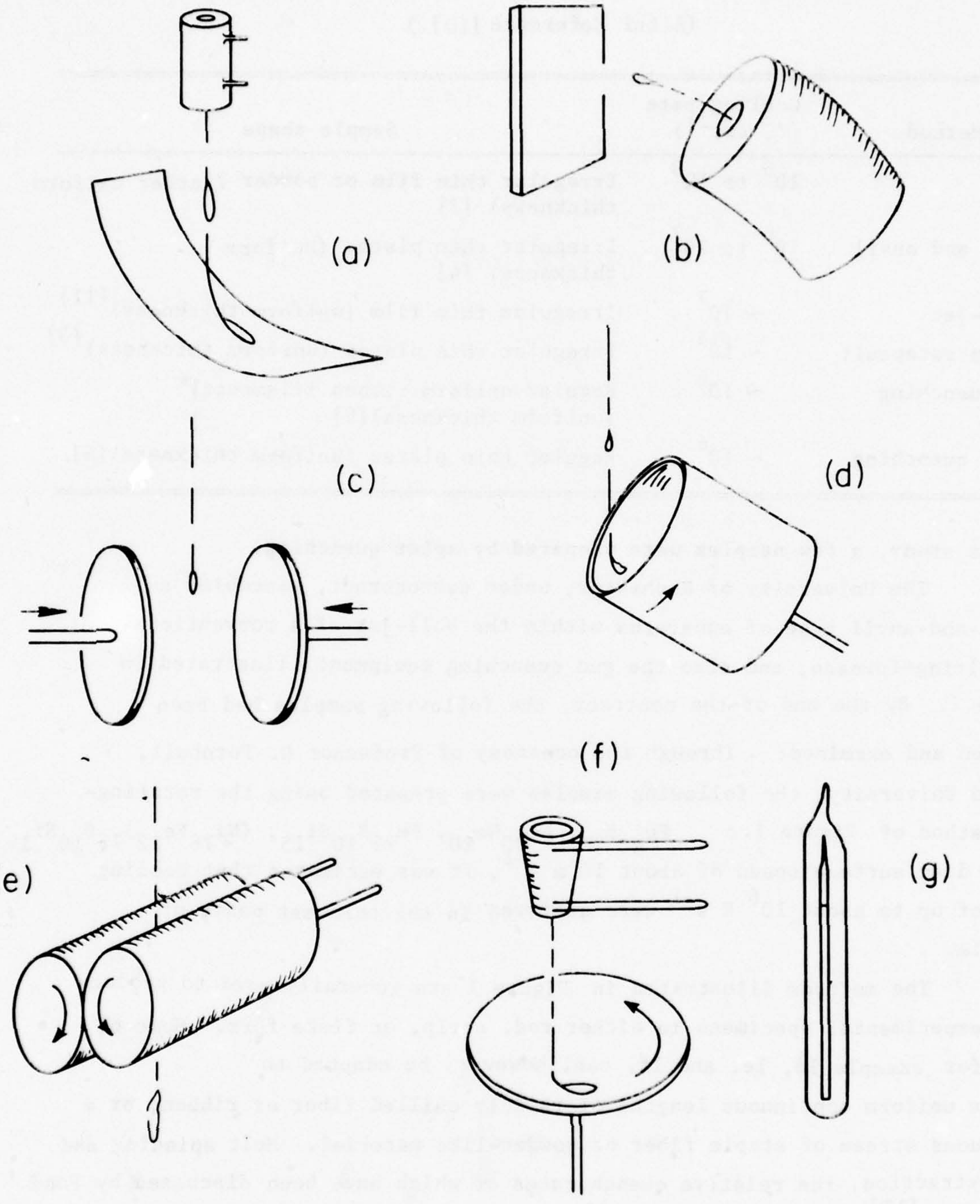

FIGURE 1. REPRESENTATIVE SPLAT QUENCH TECHNIQUES

TABLE 1. QUENCH RATES AND SAMPLE SHAPES IN SPLAT QUENCHING (After Reference [10].)

Method	Cooling rate (°C sec^{-1})	Sample shape
Gun	10^6 to 10^8	Irregular thin film or powder (rather uniform thickness) [2]
Piston and anvil	10^6 to 10^7	Irregular thin plates (uniform thickness) [4]
Plasma-jet	$\sim 10^7$	Irregular thin film (uniform thickness) [11]
Torsion catapault	$\sim 10^6$	Irregular thin plates (uniform thickness) [3]
[Drum quenching	$\sim 10^6$	Regular uniform ribbon filaments (uniform thickness) [5]]*
Roller quenching	$\sim 10^6$	Regular thin plates (uniform thickness) [6]

In this study, a few samples were prepared by splat quenching.

The University of Rochester, under subcontract, assembled a piston-and-anvil type of apparatus within the bell-jar of a conventional arc-melting furnace, and also the gun quenching equipment illustrated in Figure 2. By the end of the contract, the following samples had been prepared and examined: Through the courtesy of Professor D. Turnbull, Harvard University, the following samples were prepared using the rotating-disc method of Figure 1.: $Fe_{80}B_{20}$, $Fe_{80}Ge_{20}$, $Fe_{75}B_{10}Si_{15}$, $(Ni_{78}Fe_{22})_{75}B_{10}Si_{15}$. With a disc surface speed of about 10 m s^{-1}, it was estimated that cooling rates of up to about 10^6 K s^{-1} were achieved in the thinnest parts of the film.

The methods illustrated in Figure 1 are generally used to produce short experimental specimens in either rod, strip, or flake form. Some of them, for example 1d, 1e, and 1f, can, however, be adapted to produce uniform continuous lengths of rapidly chilled fiber or ribbon, or a continuous stream of staple fiber or powder-like material. Melt spinning and melt extraction, the relative quench rates of which have been discussed by Pond and Winter [12], are two such modifications of particular relevance to this program to be discussed in detail below.

---

*Ribbon rather than true "splat".

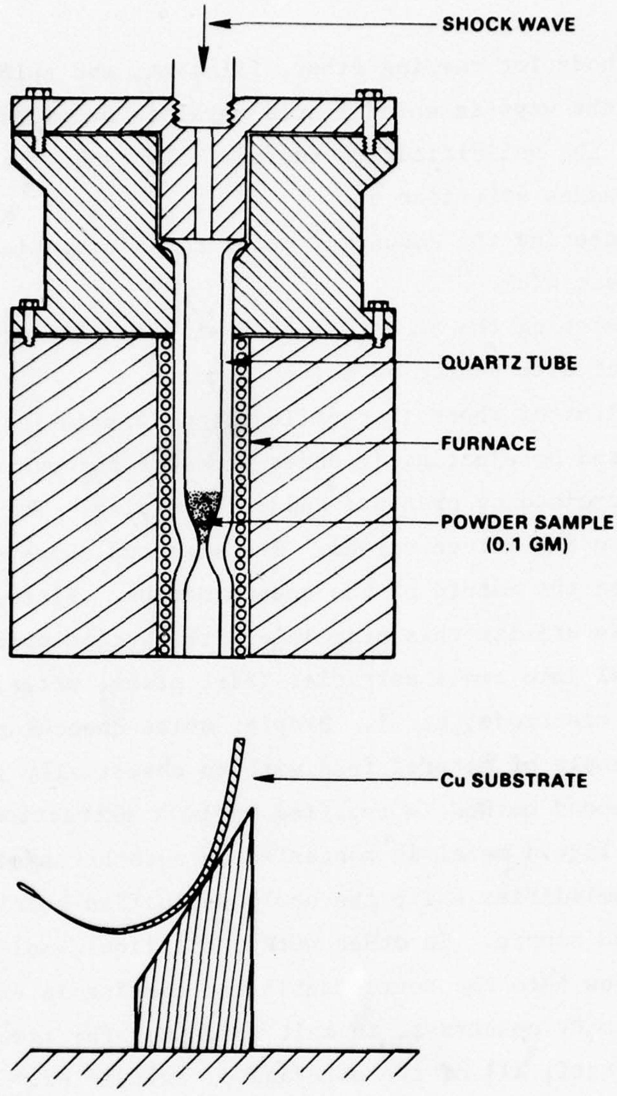

FIGURE 2. GUN QUENCHING APPARATUS ASSEMBLED BY THE UNIVERSITY OF ROCHESTER

2.3 Fiber Processing Techniques

Methods for casting fiber, filament, and splats may be classified according to the ways in which liquid metal is supplied to, and heat removed from, the solidification surface. Two subdivisions may be arrived at if one focusses attention on

(a) Metering the amount of metal to an essentially infinite heat sink

(b) Metering the amount of heat sink in contact with an essentially infinite source of molten metal.

The first of these is typified by melt spinning, where the molten metal is metered by ejecting it under pressure through an orifice. Metering control is exercised by pressure and orifice size. The heat sink is large with respect to the molten stream. The size and shape of the product depend, of course, upon the nature of the quench medium. Virtually all of the powder casting methods utilize this principle with various means being used to break up molten metal into small particles (air, steam, water, inert gas, spinning cup, rotating electrode, etc.). Droplet splat quenching, using a Duwez gun, is another example of metered feed with an essentially infinite heat sink.

The second method is typified by melt extraction, where a relatively large body of liquid metal is contacted by a rather small mold area. The liquid metal solidifies while the newly solidified metal is still in contact with the molten source. In other words, the liquid-solid interface can continue to grow into the source until the casting is extracted from contact with the melt. By constrast, in melt spinning, the liquid-solid interface can grow only until all of the material is solidified.

It is expected that there is little difference in the cooling rates at the actual mold-metal interface in melt extraction or melt spinning. But a difference can arise between the average quench rates experienced by the melt spun and melt extracted filaments produced at the same disk velocity, as a result of the principles outlined above. The limited metal feed in melt spinning generally produces a thinner produce and hence a higher <u>average</u> quench rate product. A considerably higher

disk velocity is required in melt extraction (relative to melt spinning) to produce the same thickness of filament under the conditions normally used. For example, using an orifice of 0.5 mm diam. an ejection pressure of about 10 psi, and a disk velocity of 26 ms^{-1}, melt spun ribbon 20 to 30 μm thick is produced. At 26 ms^{-1}, melt extraction would produce a filament about 60 μm thick. It would be necessary to melt extract at disk velocities in excess of 100 ms^{-1} (or to drastically reduce the disk-bath contact time) to produce ribbon fiber of less than 30 μm in thickness (assuming, of course, use of the same alloy, equivalent superheat, and identical disk parameters). By sharpening the disk periphery, this relationship can be changed, thus it is possible to produce thinner melt extracted filaments. Making amorphous materials by melt extraction is basically a matter of providing greater disk velocities and/or reduced thickness filaments.

2.4 Melt Spinning

Battelle's initial fiber-casting program, which began some ten years ago, centered around two techniques known respectively as free-flight melt spinning and chill block melt spinning, which had been developed and patented by R. B. Pond[13,14]. In both methods, a stable liquid jet of the material being cast is formed by ejecting the liquid through an appropriate orifice, after which the jet is either solidified while in free flight to produce circular cross-section (i.e., wire) fibers or impacted against and solidified on a moving heat sink to produce rectangular cross-section (i.e., ribbon) fiber. In free flight melt spinning, wires of many lower melting point metals and alloys and also ferrous base alloys in the diameter range of 25 μm through 750 μm were successfully cast.

The average quench rate associated with the free flight method ranged from 10^1 to 10^3 K s^{-1}, with the greater quench rate occurring in the smaller diameter fiber. Typically, chill block melt spun ribbon fibers possess width to thickness ratios of 10 or greater, and thickness dimensions of about 2 μm to about 250 μm. Quench rates for the chill block melt spinning process range from 10^4 K s^{-1} for the thick fibers through 10^6 K s^{-1} for the thin fibers. The quench rate statements are based on direct measurements (i.e., calorimetry)

and inferred via measurements of the fiber's secondary dendrite arm spacing. The high quench rate associated with the chill block melt spinning method makes this process particularly attractive for the production of nonequilibrium microcrystalline and amorphous materials. For example, extended solid solubility has been documented in chill block melt spun aluminum-chromium and aluminum-zirconium alloys. Also, improved mechanical properties and superplasticity have been noted for consolidated chill block melt spun ribbon of 7075 aluminum alloy.[15]

The particular form of the chill-block melt spinning approach adopted for the present study is illustrated schematically in Figure 3. The assembly shown is contained in a 3.2 m diameter chamber which permits operation in vacuum, or in an inert atmosphere. The melt (normally a 30 g charge) is held in a closed mullite or alumina tube crucible (38 cm long by 3 cm I.D.) at the end of which has been drilled a 0.5 mm orifice. The tube crucible rests inside a graphite susceptor. Heating is accomplished using a 15 kW induction unit; while temperature is measured using a chromel-alumel thermocouple inside the susceptor and in contact with the outer surface of the crucible. The chill block is a 5 cm thick, 20 cm diameter water cooled copper drum capable of rotating at 100 - 2500 rpm. The crucible is mounted directly above the surface of the drum, the distance between the orifice and the drum surface being about 2 cm. The molten metal is ejected by argon pressure (usually about 10 psi) and directed to strike the drum surface at an angle of about 85 - 90 degrees in a plane perpendicular to the drum axis. In normal operation, the chamber is evacuated, then backfilled with argon to one or two psi below atmospheric pressure. Runs were usually made in the argon environment. Typically the melt was ejected from the tube with a superheat of about 100°C.

Operating parameters were established using $Fe_{80}P_{13}C_7$ as a working substance, after which an extensive program of materials preparation was carried out, the results of which are the subject of another section of this report. Disk surface speeds of 27 ms^{-1} were employed to produce ribbons about 0.9 mm wide and about 0.02 - 0.03 mm thick.

A list of the alloys prepared by this process is given in Table 2.

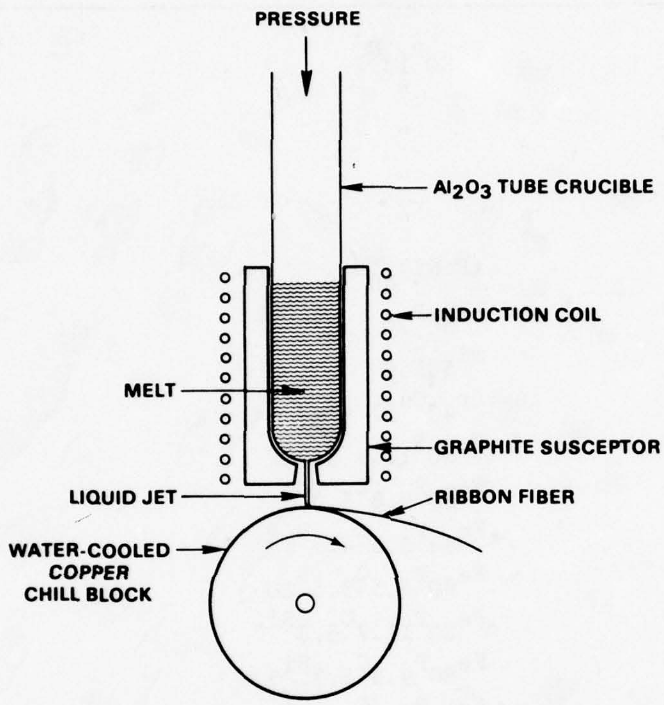

FIGURE 3. SCHEMATIC ILLUSTRATION OF CHILL-BLOCK MELT SPINNING SYSTEM

TABLE 2. LIST OF ALLOYS PREPARED IN THIS PROGRAM BY CHILL-BLOCK MELT SPINNING

Run Number	Alloy
MS-7	$Fe_{80}P_{13}C_7$
MS-9	"
MS-10	"
MS-11	"
MS-12	"
MS-13	$(FeNi)_{80}B_{20}$
MS-15	$Fe_{80}B_{20}$
MS-16	$Ni_{50}B_{50}$
MS-17	$Zr_{43}Cu_{57}$
MS-19	$Fe_{80}P_{11.7}C_{6.3}B_2$
MS-20	$Fe_{80}P_{9.8}C_{5.3}B_5$
MS-21	$Fe_{80}P_{8.5}C_{4.5}B_7$
MS-22	$Fe_{80}P_{6.5}C_{3.5}B_{10}$
MS-23	$Fe_{80}P_{11.7}C_{6.3}Si_2$
MS-24	$Fe_{80}P_{9.8}C_{5.3}Si_5$
MS-25	$Fe_{80}P_{8.5}C_{4.5}Si_7$
MS-26	$Fe_{80}P_{6.5}C_{3.5}Si_{10}$
MS-27	$Fe_{80}P_{11.7}C_{6.3}Si_1B_1$
MS-28	$Fe_{80}P_{9.8}C_{5.3}Si_{2.5}B_{2.5}$
MS-29	$Fe_{80}P_{8.5}C_{4.5}Si_{3.5}B_{3.5}$
MS-30	$Fe_{80}P_{6.5}C_{3.5}Si_5B_5$

While the melt spinning methods are particularly suited for producing wire and ribbon fibers of many nonreactive and low melting point alloys, the requirements for a stable crucible/orifice and jet severely limit the process utilization. For example, titanium filaments have not been melt spun since a stable crucible material is unavailable. Also, operating difficulties with the orifice and jet have been encountered in previous attempts to melt spin such materials as boron and beryllium, and other reactive alloys. Realizing the process limitations imposed by the orifice, Battelle's Columbus Laboratories, some years ago began a research program to develop a new fiber casting method. This lead to the conception and implementation of the pendant drop melt extraction* process for continuously casting metallic fiber.

2.5 Pendant Drop Melt Extraction

In pendant drop melt extraction the melt is a droplet supported by its own surface tension on the end of a rod, generally of the same material. The pendant drop melt extraction method for continuous casting metallic fiber and filament is totally crucible and orifice free. As such, it is particularly attractive for the fiberizing of very reactive metals, such as titanium niobium, zirconium, and hafnium. Due to the relative simplicity of the concept, a wide variety of energy sources for droplet melting may be combined with a variety of melt-extraction disk designs. Appropriate energy sources include flames (such as oxy-acetylene flames), plasma torches, focused radiant energy, laser beams, and electron beams. The feed stock is generally in the form of a rod, and the only requirements of the melting-bar feed system are that a stable (i.e., pendant) droplet, formed on the tip of the feed material, be accessible for contact with the melt extracting disk. The feed stock need not be fully dense. We have demonstrated that fibers can be successfully cast from green-powder-compact bars. The use of powder-

---

*Patents covering the proprietary process known as "pendant drop melt extraction" are owned by the Battelle Development Corporation.

compacted feed stock introduces a significant versatility to the process, as it allows production of materials commercially unavailable in dense bar or rod form. We have also found that a mixture of powders can be blended and pressed to produce feed stock, with in-situ alloying occurring on the melting and casting of the desired composition fibers (see Table 3).

The pendant drop method has been used to produce fiber from a variety of materials, including solder, tin, zinc, aluminum, copper, various steels (including stainless), some superalloys, and chromium. Product dimensions are usually about 25 μm to 125 μm effective diameter.* The relatively fine sizes are due to the great ease with which the melt can be brought into limited contact with the extracting disk. Pendant drop melt extraction is particularly suited for producing fine (i.e., small diameter) fibers and is thereby a high quench rate system. Secondary dendrite arm spacings for pendant drop melt extracted 310 stainless steel fiber (~25 microns diameter) are submicron, indicating an effective quench rate of the order of 10^6 K s^{-1}.

Since the fibers solidify on the disk, with the solidification front advancing radially outward from the surface of the disk toward the molten bath, fiber cross-sectional shape and dimensions are controlled by the shape of the contact surface, and by those other parameters such as disk material, disk cross section, melt superheat, thermal conductivity of the hot metal, linear velocity of the disk periphery, etc., which control the rate and direction of the extraction of heat from the metal being cast. Fibers of heavier cross section require a greater amount of heat removal per unit length than fine fiber. Melt viscosity and surface tension, as well as the chemistry of the bath surface (especially the presence of slags or oxide films), also play a role in the process and affect the product since they strongly influence the dynamics of the liquid flow at the melt-disk interface.

The pendant drop melt extraction method is readily adaptable to vacuum operation. One Battelle experimental unit utilizes a 1 kva power supply and tungsten filament electron beam system as the heating source, and a variable speed (200-1200 rpm) air or water cooled melt extracting disk system for solidifying the fibers, Figure 4. The entire assembly (i.e.,

---

*Diameter of the equivalent circle.

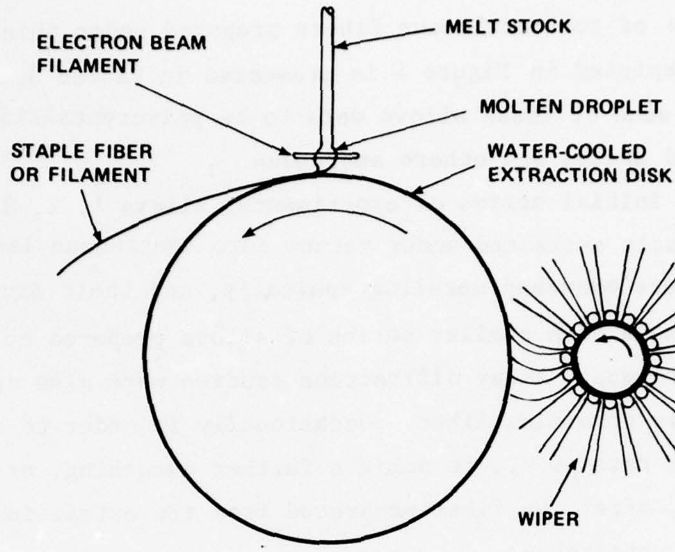

FIGURE 4. SCHEMATIC OF THE PENDANT DROP MELT EXTRACTION EQUIPMENT USED IN THIS PROGRAM FOR THE PREPARATION OF RAPIDLY-QUENCHED AMORPHOUS OR POLYCRYSTALLINE FILAMENT (i.e., CONTINUOUS FIBER) OR STAPLE FIBER

feed bar, filament, and melt extraction disk) is contained in an 18-inch diameter bell jar equipped with a roughing and diffusion pump. This equipment has been used to extract fibers of stainless steels, nickel, titanium, and titanium alloys, hafnium, niobium, and zirconium. Successful operation in vacuum provides confirming evidence that there is no metallurgical reaction (such as welding) between the disk periphery and the solidifying fiber. Multiple edge disks may be used to cast fibers from a single pendant drop. For example, it has been demonstrated that three or four edges can be operated simultaneously at spacings as close as 0.5 mm.

2.5.1 Pendant Drop Melt Extraction -- Continuous Fiber

A list of the continuous fibers prepared under this program by the apparatus depicted in Figure 4 is presented in Tables 3, 4, and 5. By design, some of these alloys were to be polycrystalline in the rapidly-quenched state, and others amorphous.

In an initial series of experiments, Alloys 1, 2, 3 and 4 (Table 5) were melt extracted under vacuum into continuous lengths of fiber. These were examined metallographically, and their microstructures compared with those of a similar series of alloys prepared by a conventional splat cooling process. X-ray diffraction studies were also carried out on a particularly promising fiber. Occasionally in order to increase the secondary quench rate (i.e., to achieve further quenching, or to inhibit further heating, after the fiber separated from the extraction disk) the following steps were taken:

(a) The casting edge of the wheel was notched, so as to yield a discontinuous product. The purpose of this modification was to interrupt an otherwise continuous heat path between the pendant droplet and the fiber leaving the wheel.

(b) In one or two trial cases the melt extraction process was carried out in air in order to take advantage of ambient-temperature gas quenching. An inert atmosphere would, of course, be generally preferable.

(c) The melt-extracted fiber was deposited into a bath of water (apparatus operated in air) or oil (vacuum apparatus).

Runs ME-3 through ME-16 were carried out in vacuum using a 20 cm diameter, 1.27 cm thick copper disk with a "pointed" (90 degree) unnotched periphery. This produced, in runs ME-11, ME-12, ME-13, ME-15 and ME-16, continuous fibers of amorphous material (as judged by bend ductility). Runs ME-17 through ME-20 utilized a 20 cm diameter, 1.27 cm thick copper disk with a flat periphery.

TABLE 3. LIST OF CONTINUOUS-FIBER Ti-6Al-4V-BASE IN-SITU-MELTED ALLOYS PREPARED BY PENDANT DROP MELT EXTRACTION AS PART OF A SCREENING STUDY

Sample Designation	Alloying Addition to Ti-6Al-4V Base
T64-1	1018 Steel
2	Fe
3	Fe + Cu
4	Fe + Cu
5	Fe + Cu
6	430F SS
7	430F SS + Cu
8	Fe + Cu
9	Cu
10	Ti-Mo (25 at.%)
11	Elgiloy
12	Elgiloy + Cu
13	Graphite
14	TiB_2 + Cu
15	TiB_2
16	$TiSi_2$ + Cu
17	TiB_2 + Fe + Cu
18	TiC
19	TiC + Fe + Cu
20	308 SS
21	308 SS
22	308 SS
23	TiB_2 + TiC
24	Elgiloy + Cu + W
25	Fe

TABLE 4. POLYCRYSTALLINE ALLOY CANDIDATES PREPARED FROM PRE-CAST ALLOY RODS BY PENDANT DROP MELT EXTRACTION

Run Name or Alloy Code	Polycrystalline Alloy Candidate	Disk Speed ($m\ min^{-1}$)
ME-3	80Ti-5.4Al-3.6V-8Fe-3Cu	255-765
ME-4	"	190-255
ME-5	80Ti-5.4Al-3.6V-6Fe-5Cu	255-380
ME-6	"	215-765
ME-7	90.5Ti-1.5Al-1V-6.5Si	255-380
ME-8	"	125-830
ME-9	86.4Ti-5.8Al-3.8V-4B	255-1275
ME-10	92.5Ti-1.5Al-1V-3Be-2B	255-510

TABLE 5. METALLIC GLASS ALLOY CANDIDATES PREPARED FROM PRE-CAST ALLOY RODS BY PENDANT DROP MELT EXTRACTION

Sample Code	Run Code	Metallic Glass Candidates: Composition	Metallic Glass Candidates: Alloy Class*	Disk Speed ($m\ min^{-1}$)
1		$Fe_{80}B_{20}$	LTM/Mtld.	--
2		$Fe_{80}Ge_{20}$	LTM/Mtld.	--
3		$Fe_{75}B_{10}Si_{15}$	LTM/Mtld.	--
4		$(Ni_{78}Fe_{22})_{75}B_{10}Si_{15}$	LTM/Mtld.	--
5		$Fe_{75}Ge_{10}Si_{15}$	LTM/Mtld.	--
6		$Zr_{43}Cu_{57}$	ETM/Nbl.M.	--
7		$Ti_{30}Cu_{70}$	ETM/Nbl.M.	--
8		$Nb_{50}Ni_{50}$	ETM/LTM	--
7	ME-11**	$Ti_{30}Cu_{70}$	ETM/Nbl.M.	2630
8	ME-12	$Nb_{50}Ni_{50}$	ETM/LTM	2630
9	ME-13	$Ti_{60}Ni_{30}Si_{10}$	ETM/LTM	2630
10	ME-14	$Ti_{55}Ni_{30}Si_{15}$	"	2630
9	ME-15	$Ti_{60}Ni_{30}Si_{10}$	"	2630
1	ME-16 ***	$Fe_{80}B_{20}$	LTM/Mtld.	2630
1	ME-17 ***	"	"	1330
1	ME-18 ***	"	"	625
1	ME-19 ***	"	"	270
1	ME-20 ***	"	"	2630

* ETM = Early Transition Metal
LTM = Late Transition Metal
Nbl.M. = Nobel Metal
Mtld. = Metalloid

** Alloys 1 - 8 were prepared and studied in 1976, the "ME-" series in 1977. Two compositions were thus repeated.

*** Extraction-parameter investigation.

2.5.2 Melt Extraction -- A Thickness/Velocity Relationship

Using $Fe_{80}B_{20}$ as a working substance the relationship between disc speed and filament thickness was investigated. A flat-edged water-cooled disc was sued, and the casting was performed in vacuum. Disk speed was varied between 270 and 2630 m min^{-1} (runs ME-17 through ME-20, Table 5) and the filament thicknesses obtained were plotted as in Figure 5. The data were found to fit an equation of the form:

$$\delta = K\,(v)^{-1/2} \tag{1}$$

where δ = filament thickness, μm

v = disk surface velocity, ms^{-1}

and K = constant = $315 \times 10^{-6}\ m^{3/2}\ s^{-1/2}$ for Figure 2-5 data.

The proportionality constant, K, in Equation (1) depends on a number of process variables, including disk temperature, melt superheat, disk surface finish, etc. Assuming that the contact distance (i.e., the arc length over which the melt is in contact with the extraction disk) remains essentially constant with increasing disk surface velocity, allows the thickness-velocity relation (Equation (1) to be converted into an appropriate thickness-versus-time relation. As the contact distance was about one centimeter in the $Fe_{80}B_{20}$ melt extraction experiments, Equation (1) leads to the relation:

$$\delta = 3150\,\sqrt{t} \tag{2}$$

where t = bath-disk contact time, s.

Equation (2-2) is consistent and comparable to the Carslaw and Jaeger [16] thickness-time relation associated with solidification on water-cooled chills.

The Carslaw and Jaeger solution is:

$$\delta = 2\gamma\,\sqrt{\alpha_s t} \tag{3}$$

where γ is determined from

$$\gamma e^{\gamma^2}\,\mathrm{erf}\gamma = (T_m - T_o)\,\frac{C_s}{L\sqrt{\pi}} \tag{4}$$

where α_s = thermal diffusivity of the solid = $\frac{K_s}{C_s \rho}$

T_m = melting temperature of the material

T_o = disk temperature

C_s = specific heat of the solid

and L = heat of fusion.

Substituting the following values of the thermal variables, consistent with iron, into Equations (3) and (4),

T_m = 1160°C (Eutectic temperature of $Fe_{80}B_{20}$)

T_o = 60°C

C_s = 0.16 cal/gm-C

$L \approx$ 65 cal/gm

K_s = thermal conductivity of the solid = 0.07 cal/cm-C-s

and ρ = density of the solid $\approx$ 7.0 gm/cm^3

leads to an estimated thickness-time relation of

$$\delta = 4310 \sqrt{t} \quad (5)$$

which is considered a reasonable correlation between theory and experiment, considering the lack of precise values for (1) the contact distance used in obtaining Equation (2), and (2) the appropriate thermal properties for the $Fe_{80}B_{20}$ alloy.

It is interesting to note that the experimentally determined thickness-time relation (Equation (2)) for the melt extracted $Fe_{80}B_{20}$ is quite similar to the thickness-time relation obtained by Taylor[17] for the skin solidification of steel on water-cooled copper chills.

Consistent with the observed thickness-time relation, the quench rate is expected to depend on the inverse square of the product thickness. For the 50- and 150-micron thickness of $Fe_{80}B_{20}$ ribbons, calculated quench rates are 1.3×10^5 and 1.5×10^4 C per second, respectively. As anticipated, for these quench rates, none of the filaments comprising the data

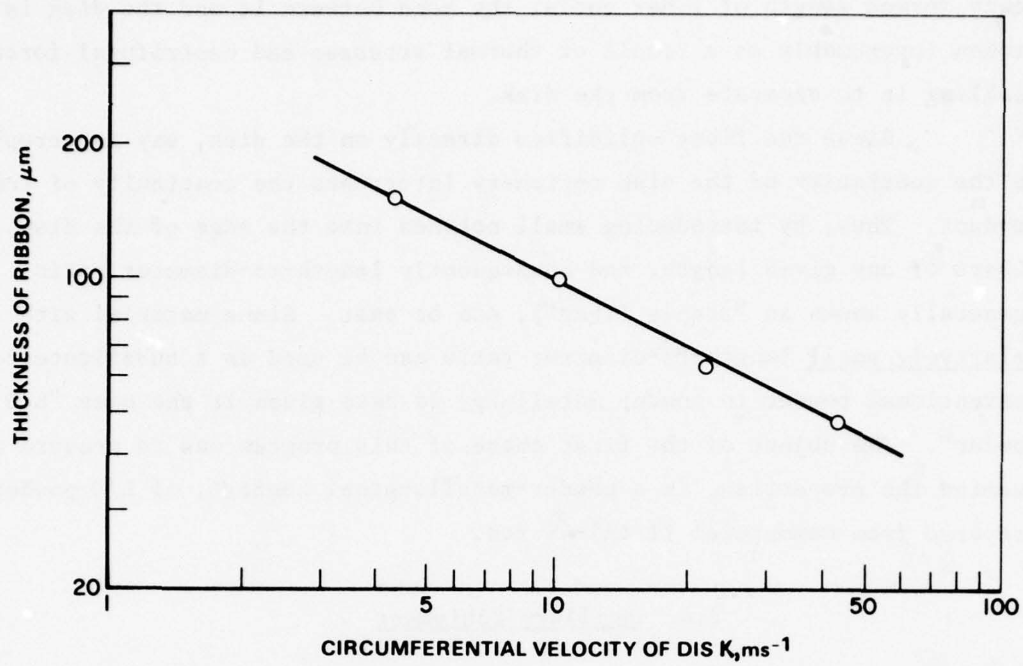

FIGURE 5. RELATIONSHIP BETWEEN FILAMENT THICKNESS AND DISK SPEED IN THE PENDANT DROP MELT EXTRACTION OF $Fe_{80}B_{20}$. Vacuum environment, copper disc, estimated superheat = 20°C.

in Figure 5 were amorphous. However, extension of the data in Figure 5 clearly shows that increased disk speeds (or equivalently, decreased contact times) will produce thinner products with higher quench rates and, in turn, will yield amorphous products.

2.5.3 Pendant Drop Melt Extraction -- Staple Fiber

In pendant-drop melt extraction, the edge of a rotating heat-extracting disk is passed through the surface of a droplet of molten metal. On emerging from the droplet, the periphery of the disk carries a layer of solidified metal with it, and so extracts it from the melt. As the

newly formed length of fiber cools, the bond between it and the disk is broken (presumably as a result of thermal stresses and centrifugal force) enabling it to separate from the disk.

Since the fiber solidifies directly on the disk, any interruption in the continuity of the disk periphery interrupts the continuity of the product. Thus, by introducing small notches into the edge of the disk, fibers of any given length, and consequently length-to-diameter ratio (generally known as "staple fiber"), can be cast. Since material with relatively small length-to-diameter ratio can be used as a substitute for conventional powder in powder metallurgy we have given it the name "L/D powder". The object of the first phase of this program was to prepare and examine the properties, in a powder-metallurgical context, of L/D powder prepared from commercial Ti-6Al-4V rod.

2.6 Ancillary Equipment

Numerous additional items of equipment were necessary for consolidating L/D powder, and examining the properties of the resulting compactions, and of the products of the various fiber-preparation operations. The facilities used (and which cannot be described here) consisted of:

(a) Hot Isostatic Pressing Facility
  - Powder processing facility
  - Autoclave facility

(b) Vacuum Hot Pressing Facility
  - Numerous vacuum hot presses

(d) Mechanical testing laboratory

(e) Metallographic Laboratory
  - Optical metallographs
  - Electron microscopes
  - Scanning electron microscope

(f) Metal Physics Laboratory

SECTION III

PREPARATION AND PROPERTIES OF COMPACTED Ti-6Al-4V MELT EXTRACTED STAPLE FIBER

Spurred by potential savings in energy, materials, and consequently cost, the interest of the aerospace industries in powder metallurgical processing is growing. For some materials, particularly reactive ones such as titanium alloys, current methods of powder production are hampered by difficulties in the control of chemical homogeneity and purity. The reactivity of titanium and its alloys dictates the use of a containerless melting procedure. Accordingly, vacuum-protected pendant drop melt extraction was identified as a promising method for the production of Ti-6Al-4V, the alloy of interest in this section of the program, in the form of staple fiber (the so-called L/D powder).

The preparation of continuous filament was the first problem to be investigated. Techniques of L/D powder preparation were then explored using stainless steel (air melted) as a working substance. And the information acquired in these two preliminary studies was coupled in order to produce the first batches of Ti-6Al-4V L/D powder. Test quantities of Ti-6Al-4V L/D powders having two different L/D ratios were produced, consolidated by vacuum hot pressing (VHP) and hot isostatic pressing (HIP), and the resulting compacts were evaluated in terms of composition, mechanical properties, and microstructures. It is interesting to note, that by performing tests on the continuous filament prior to installing the notched staple-fiber wheel, the mechanical properties of the starting powder can be, in effect, examined prior to subsequent thermomechanical processing. The L/D powder process is thus the only one that exists in which the properties of the powder product can be so fully documented.

In this section we discuss in turn the preparation and properties of

- continuous filament
- L/D powders
- vacuum-hot-pressed (VHP) compactions
- hot isostatically pressed (HIP) compactions

Various batches of filament received standard "mill anneal" and "recrystallization" heat treatments, the latter being related to the heat treatment associated with VHP and HIP. These conditions are defined in

Table 6, from which it can be seen that the produce of the VHP and HIP processes can be expected to be, from a phase equilibrium and microstructural standpoint, in the "recrystallized" condition.

TABLE 6. DEFINITION OF HEAT TREATMENT AND THERMOMECHANICAL PROCESSING PARAMETERS

Mill anneal (MA)	1350°F/2 hr/air cool
Recrystallization anneal	1700°F/4 hr/furnace cool (100 deg/h) to 1400°F/furnace cool (650 deg/h) to 900°F/air cool
Hot isostatic press (HIP)	1750°F/10 ksi/3 hr/furnace cool
Vacuum hot press (VHP)	1750°F/8 ksi/1 hr/furnace cool

3.1 Preparation and Properties of Continuous Fiber Produced by Pendant Drop Melt Extraction

In setting up preparation parameters, continuous lengths of Ti-6Al-4V were melt extracted under vacuum and coiled in a rotating collector installed within the bell jar. Melt extraction discs were of either copper or brass and had been cut, a dozen or more at a time, from 0.040-inch thick sheet. They were either 7 or 8 inches in diameter, and water cooled out to a radius of 3 inches. The edge of the 7-inch-diameter disk was thus about 1/2 inch away from the cooling water, while that of the 8-inch-diameter disk was about 1 inch away. In experiments with Ti-6Al-4V, brass disks of either 7- or 8-inch diameter appeared to operate more smoothly than a 7-inch-diameter copper disk, but were roughly equivalent to 8-inch-diameter copper disks. In all cases, the edges of the disks had been beveled at an angle of 45° on both sides. Finishing the

surface with 600-grit paper and polishing with 6 μm diamond paste gave the best results. Extraction was generally found to proceed most smoothly when the disk temperature was somewhat higher than ambient. One of several coils of fiber produced is depicted in Figure 6.

In these initial experiments we were particularly concerned about possible loss of Al, and possible oxygen and nitrogen pickup, and the influence of this on the mechanical properties. Extensive chemical investigations, the results of which are given in Table 7, showed only slight Al loss, and indicated an oxygen content not significantly higher than that of the starting material, wrought 3/8-inch-diameter bar stock.

A scanning-electron-micrograph of the as-cast fiber is given in Figure 7; and optical and electron micrographs of the filaments in the "as-cast", "mill annealed" and "recrystallized" conditions are given in Figures 8 and 9. Mill annealing does little to modify the as-cast martensitic structure -- Figures 8a and 8b, and Figures 9a and 9b. The recrystallization heat treatment, however, results in a characteristic α-platelet plus intergranular-β structure seen in Figure 8c (500X) and Figure 9c (3,750X and 15,000X)/

TABLE 7. CHEMICAL COMPOSITION OF PDME-PRODUCED CONTINUOUS FIBER COMPARED TO THAT OF THE STARTING MATERIAL (COMMERCIAL WROUGHT TI-6A1-4V ROD STOCK)

Specimen	Data Source	Composition in Weight Percent				
		Al	V	C	N	O
Melt Stock	Manufacturer	6.7	4.2	0.02	0.015	0.198
"	Leco, Inc.			0.029		0.237
Cast Filament	Battelle	6.2	4.2	0.263		0.238
"	"	6.2	4.1			
"	"	6.4	4.1			
"	"	6.4	4.1			
"	"	6.2	4.1			
"	Leco, Inc.			0.0362		
"	"			0.0362		
"	"			0.0485		
"	"			0.0465		
"	AFML/Sherry Labs			0.1	0.031	0.258

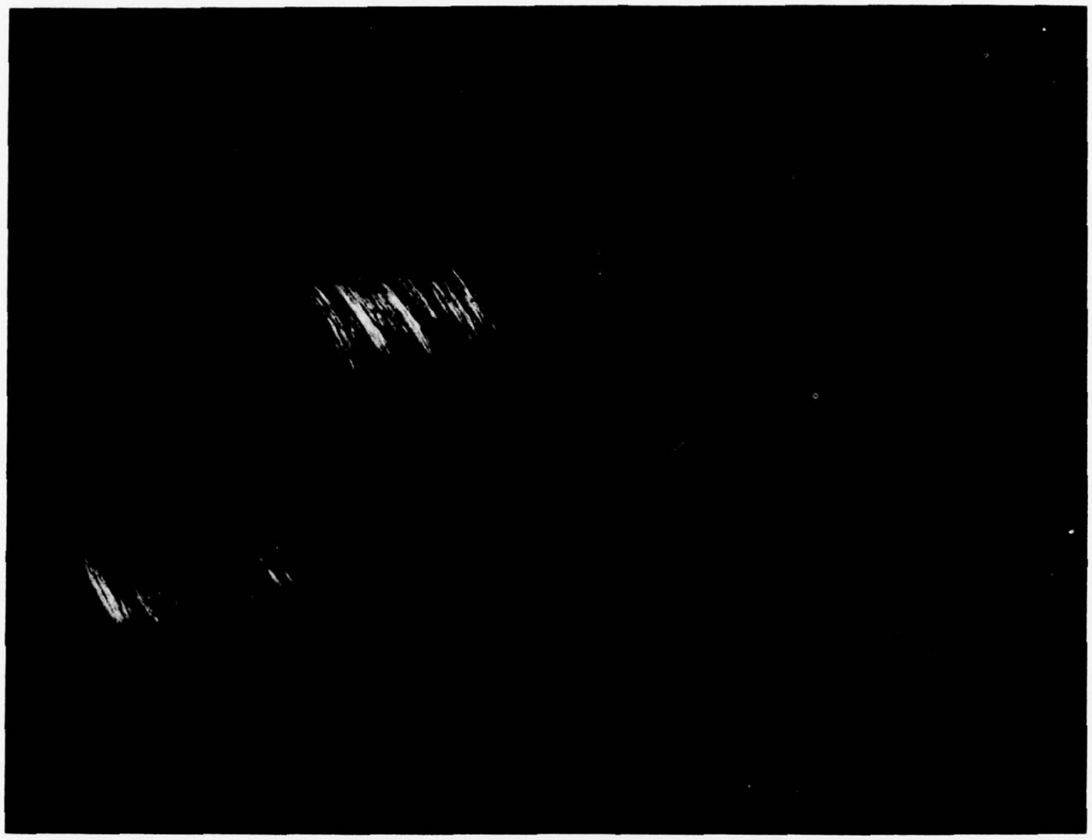

FIGURE 6. ONE OF SEVERAL COILS (ABOUT 14 cm DIAM) OF Ti-6Al-4V FIBER PRODUCED DURING THE PRELIMINARY PHASE OF THE L/D-POWDER PROGRAM

FIGURE 7. SCANNING ELECTRON MICROGRAPH OF PENDANT DROP MELT EXTRACTED Ti-6Al-4V FIBER. The "wheel surfaces" and "free surfaces" are clearly distinguishable. Fiber width, ~ 35 μm

(a)

As-Cast
(α')

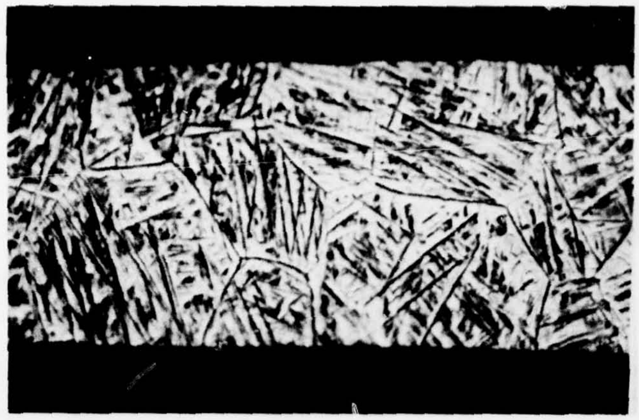

(b)

Mill Annealed
(reverted α')

(c)

Recrystallized
($\alpha+\beta$)

FIGURE 8. OPTICAL MICROGRAPHS OF SECTIONS OF Ti-6Al-4V PENDANT DROP MELT EXTRACTED CONTINUOUS FIBER, 500X. Mill annealing merely "reverts" the martensitic as-cast structure; but recrystallization yields the α-platelet plus intergranular-β structure characteristic of the 1700°F anneal.

(a)
As-Cast
(α')

(b)
Mill Annealed
(reverted α')

(c)
Recrystallized
(α+β)

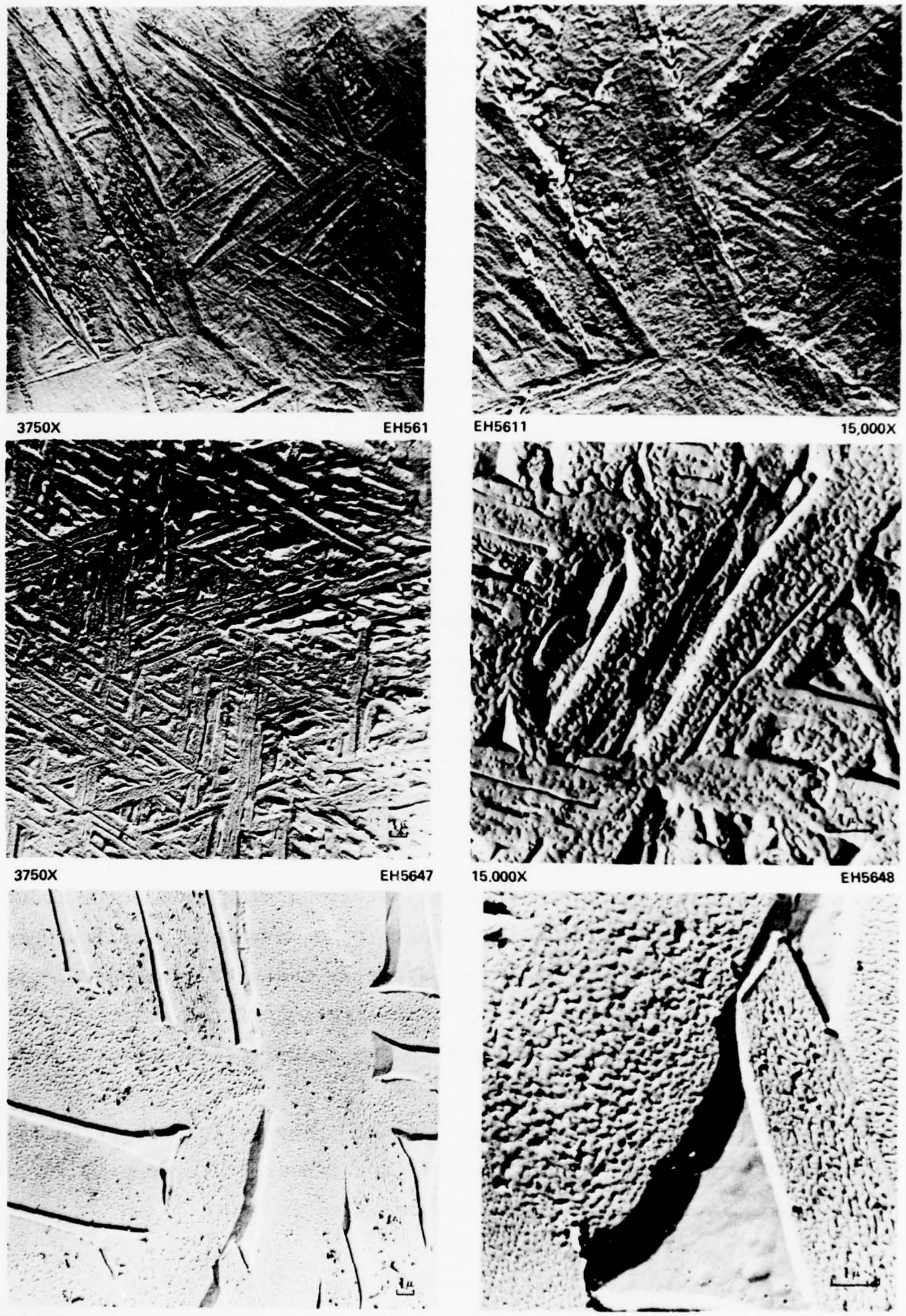

FIGURE 9. ELECTRON MICROGRAPHS (REPLICA) OF PDME CONTINUOUS FIBERS - TWO MAGNIFICATIONS, 3750X AND 15,000X, AND THREE HEAT TREATMENT CONDITIONS. (Printing reduction factor, ~0.7).

3.1.1 Mechanical Properties of Melt-Extracted Fibers

Bundles of fibers were heat treated under carefully controlled conditions to avoid contamination. They were wrapped in Ta foil and enclosed in quartz tubes along with getter-packages of Ti chips; and sealed off under argon at a pressure which was adjusted so as to be atmospheric at the annealing temperatures.

In investigating the mechanical properties, the following steps were taken:

- Fiber densities were measured by the water-immersion method
- Young's modulus of several specimens from each heat treatment were measured using an acoustic (sound velocity) technique, through the courtesy of Dr. H. L. Gegel of the Air Force Materials Laboratory (WPAFB). This information was useful in its own right; but association with the results of the elastic portion of the subsequent tensile test, enabled an effective cross-sectional area to be calculated. In other words the tensile test modulus was normalized to the acoustic modulus.
- Using a conventional tensile-testing machine elastic modulus and ultimate tensile strength were measured. Results were computed on the basis of directly measured cross-sectional areas, and also through normalization of the statically measured elastic modulus to the acoustically measured value.

The results of the mechanical property investigation of as-cast, mill-annealed, and recrystallized fibers are presented in Tables 8, 9, and 10, respectively; and summarized in Table 11.

TABLE 8. TENSILE TESTS Ti-6Al-4V FIBERS

Condition: As-spun $E = 13.44 \times 10^6$ psi*

Spec. No.	C/S Area (10^{-6} in^2) A_1 (a)	C/S Area (10^{-6} in^2) A_2 (b)	0.2% Offset Yield Strength Y (ksi) based on A_1	0.2% Offset Yield Strength Y (ksi) based on A_2	Tensile Strength (ksi) based on A_1	Tensile Strength (ksi) based on A_2	Elongation (%)
1	7.3	~			106.3	~	0.15
2	7.3	~			117.6	~	0.1
3	8.3	4.97			76.8	127.5	0.1
4	8.3	5.26			92.0	144.5	<0.1
5	6.9	3.17			63.1	136.9	<0.1
6	8.5	6.41	(c)	(c)	79.9	105.8	0.1
7	8.3	5.28			95.5	149.3	0.15
8	6.9	4.91			94.4	132.3	0.1
9	7.6	7.75	112.3	109.7	112.3	109.7	0.2
10	6.9	6.32			86.2	94.1	<0.1
11	7.4	~	(c)	(c)	55.1	~	<0.1

*Acoustic measurement

(a) $A_1 = W/\rho L$

(b) $A_2 = (P/\zeta)\cdot(L/E)$

(c) Failed at <0.2% strain

TABLE 9. TENSILE TESTS Ti-6Al-4V FIBERS

Condition: Mill-Annealed* E = 15.73 x 10^6 psi**

Spec. No.	C/S Area (10^{-6} in^2) A_1[(a)]	C/S Area (10^{-6} in^2) A_2[(b)]	0.2% Offset Yield Strength Y (ksi) based on A_1	0.2% Offset Yield Strength Y (ksi) based on A_2	Tensile Strength (ksi) based on A_1	Tensile Strength (ksi) based on A_2	Elongation (%)
1	24.3	13.27	(c)	(c)	78.0	142.8	0.1
2	22.5	13.80	102.8	167.6	116.5	190.0	0.45
3	19.1	13.9_7	108.4	148.2	122.2	167.1	0.5
4	23.7	17.8_4	(c)	(c)	80.9	107.3	0.15
5	23.7	20.4_5	99.4	116.3	115.2	133.5	0.35
6	18.2	9.9_6	(c)	(c)	68.4	124.9	0.1

* 1350°F/2 hr/air cool

** Acoustic measurement

(a) $A_1 = W/\rho L$

(b) $A_2 = (\rho/\zeta)\cdot(L/E)$

(c) Failed at < 0.2% strain

TABLE 10. TENSILE TESTS Ti-6Al-4V FIBERS

Condition: Recrystallized* E = 15.59 x 10^6 psi**

Spec. No.	C/S Area (10^{-6} in^2) A_1 (a)	A_2 (b)	0.2% Offset Yield Strength (ksi) based on A_1	A_2	Tensile Strength (ksi) based on A_1	A_2	Elongation (%)
1	13.1	7.0_0	(c)	(c)	84.6	158.1	0.1
2	8.9	6.6_2	(c)	(c)	61.9	83.2	0.0
3	13.1	8.6_4	88.3	133.9	88.3	133.9	0.2
4	11.0	8.2_8	(c)	75.7	75.7	100.5	<0.1
5	8.5	6.3_5	(c)	75.4	75.4	100.9	<0.1
6	13.1	8.6_4	168.8	115.3	115.3	174.9	0.35
7	13.6	9.5_2	108.5	155.1	108.5	155.1	0.3
8	8.9	5.5_5	78.2	125.4	78.2	125.4	0.1
9	13.3	9.6_5	111.0	153.0	111.0	153.0	0.2
10	9.2	6.4_1	79.5	114.1	79.5	114.1	0.1

* 1700°F/4 hr/furnace cool to
1400°F (100 deg./hr - no faster)
furnace cool to
900°F (650 deg./hr - no slower)
air cool

** Acoustic measurement

(a) $A_1 = W/\rho L$

(b) $A_2 = (P/\zeta)\cdot(L/E)$

(c) Failed at < 0.2% strain

TABLE 11. SUMMARY OF TENSILE PROPERTIES OF Ti-6Al-4V FIBERS

Condition	Microstructure	Modulus,[a] E (10^6psi)	Average Tensile Strength (ksi) based on: A_1[b]	A_2[c]
As-spun	Martensitic α'	13.44	89.0	125.0
Mill-annealed[d]	Reverted α'	15.73	96.9	144.3
Recrystallized[e]	$\alpha + \beta$	15.59	87.8	129.9

(a) From sound velocity measurement

(b) $A_1 = W/\rho L$

(c) $A_2 = (P/\zeta)\cdot(L/E)$

(d) Mill anneal (MA): 1350°F/2 hr/air cool

(e) Recrystallization anneal: 1700°F/4 hr/furnace cool to 1400°F (100 deg./hr - no faster) furnace cool to 900°F (650 deg./hr - no slower) air cool

3.2 Preparation and Properties of L/D Powder

3.2.1 Preparation

In preparation for the melt extraction of L/D powders of Ti-6Al-4V, several preliminary experiments were performed in air using 304 stainless steel. These experiments involved pendant drop melt extraction from a one-quarter-inch round rod using an oxy-acetylene torch as the heat source. The extraction disk was of 0.040-inch-thick copper, 7 inches in diameter, with the edge tapered to a point (included angle $\simeq 90°$). The bulk of the PDME was done at about 600 rpm ($\sim$11 linear feet per second edge velocity). Operating in this mode, with a continuous edge, the stainless steel could be readily cast into a semicontinuous product of approximately 0.002-inch effective diameter.

In order to prepare L/D powders, the edge of the disk must be notched at appropriate intervals. Initial notches were made by simply denting the edge of the disk with the small, rounded end of a chisel at one-quarter-inch intervals. This produced fibers averaging just under one-quarter inch in length (Run #1, see Figure 3-5). Next, notches were introduced half way between each of the previous notches. This configuration produced, on the average, fibers just under one-eighth inch long (Run #2). Since the notches were introduced by hand, there was considerable variation in individual fiber length. By replacing the chisel with a steel screw thread (10 threads per inch), it was possible to introduce very regularly spaced notches into a second disk of otherwise similar design. This spacing produced fibers of slightly less than 0.08 inch (Run #3). Notches were then introduced using a screw with 20 threads per inch, and this produced fibers of slightly less than 0.04 inch in length (Run #4).

About 100 to 200 grams of each L/D stainless steel powder were produced. These were poured loosely into a graduate to obtain a loose-packed density. Then they were poured into a vibrating graduate to obtain a greater density. The results are shown in Table 12.

1 mm

FIGURE 10. STAINLESS STEEL STAPLE FIBER PRODUCED, IN AIR, AS A PRELIM NARY STEP IN THE DEVELOPMENT OF EXPERIMENTAL PROCEDURES FOI THE PRODUCTION OF L/D POWDER.

TABLE 12. 304 STAINLESS STEEL L/D POWDER

Particle Length, in.	Length-to-diameter Ratio	Loose Pour Density, g/cc	Density After Vibration, g/cc
0.23	115	0.69	1.28
0.11	55	0.83	1.54
0.08	40	0.85	1.49
0.04	20	2.15	3.14

Analysis of the Results. The theoretical density of a cubic close packing of spheres is 74 percent of that of the material of which the spheres are composed. A random close packing possesses 86 percent of the density of cubic close packing, so that overall the relative density of a random close packing of spherical objects is 65 percent. Applying this result to the 304 stainless steel of density 7.7 g/cc, we obtain a theoretical density for spherical powder of 5.0 g/cc. This value is applied to the data of Table 12 in order to compute the percentage theoretical density (spherical-powder base) of our L/D powder. The results are presented in Table 13. and summarized in Figure 11, which illustrates the distinct difference in handling and packing which occurs as the L/D ratio decreases toward (and presumably below) 20. The L/D powder becomes visibly more powder-like in its behavior, with "bird-nesting" or clumping of fibers virtually disappearing at an aspect ratio of about 20. The figure clearly reflects the pronounced change in character of the L/D powder mass below the L/D $\cong$ 20 to 30 range. Also indicated is a rapid increase of packing density expected as L/D decreases in the range below L/D $\cong$ 20.

TABLE 13. PACKING DENSITY OF STAINLESS STEEL L/D POWDER (BASED ON THE PACKING DENSITY OF IDEAL SPHERICAL POWDER)

Particle Length, in.	Length-to-diameter Ratio	Loose Pour Density, g/cc	Density After Vibration, g/cc	Percent Theoretical Density
0.23	115	0.69	1.28	26
0.11	55	0.83	1.54	31
0.08	40	0.85	1.49	30
0.04	20	2.15	3.14	63
	[1]	-	-	[100]

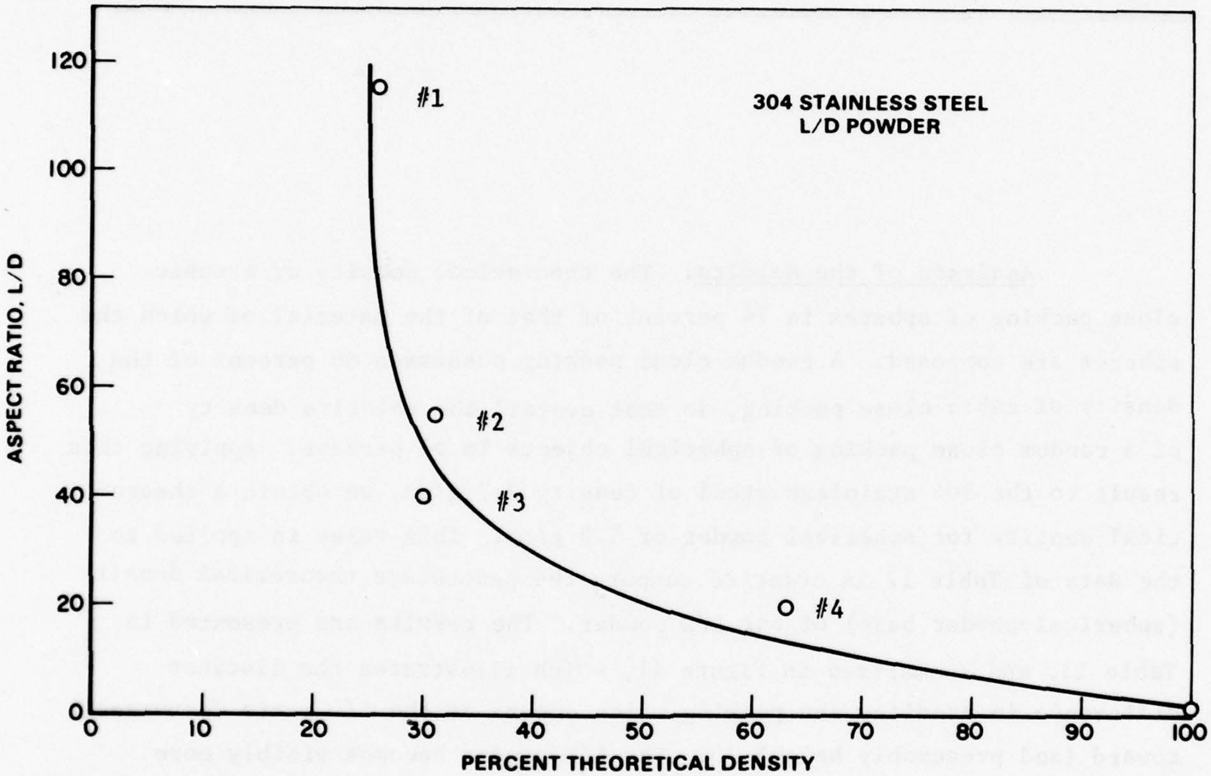

FIGURE 11. PACKING DENSITY AS A FUNCTION OF ASPECT RATIO, 304-SS POWDER (referred to 100% for random spherical powder)

The results of the stainless steel L/D-powder casting experiments were transferred to the vacuum equipment, and studies were commenced using wrought Ti-6Al-4V 1/4-inch diam. and 3/8-inch diam. rod as feed stock. Initial

experiments did, in fact, model the titanium results in vacuum reasonably well. The initial difficulties observed in the titanium experiments related almost entirely to vapor deposition from the molten drop onto the surface of the extracting disk. If one maintains the cleanest surface on the disk, and the best vacuum in the system, the conditions are ideal for adherence of the deposit to the disk, with the result that most wiper systems are incapable of removing the deposit to provide a clean, uniform extraction surface. However, if the vacuum is kept at about 5 x 10^{-4} mm, and if the wiper is treated with a very small amount of silicone oil, the vapor deposits will not adhere to the extracting disk surface. These precautions permit the extraction to proceed in a more or less continuous fashion without degradation of the process or the product.

The results (L/D-1) of the first successful powder-production run are portrayed in Figure 12. When a sufficient quantity of this material had been collected, work immediately commenced on the powder handling and compaction investigation. While this was going on a successful attempt was made to improve the general handling and compaction characteristics of the powder. By carefully shaping a new extraction disk, Figure 13, which included among other things the reduction of the notch spacing, a very satisfactory improved powder (L/D-2, Figure 14 was produced. This was also subjected to handleability tests, and compaction process evaluation.

3.2.2 Properties of the L/D-1 and L/D-2 Powder Substitutes

In the preparation of powder we were particularly concerned about possible contamination by oxygen and nitrogen. Accordingly, four batches of powder we subjected to independent chemical analysis. The results of this work, presented in Table 14, show that the oxygen level in the powder was no higher than in the starting material. A significant increase in the nitrogen level was noted, however, the final nitrogen content was no greater than 650 wt. ppm. The observed increase in carbon level, attributed to the lack of a cold trap on the vacuum pumping system, is avoidable.

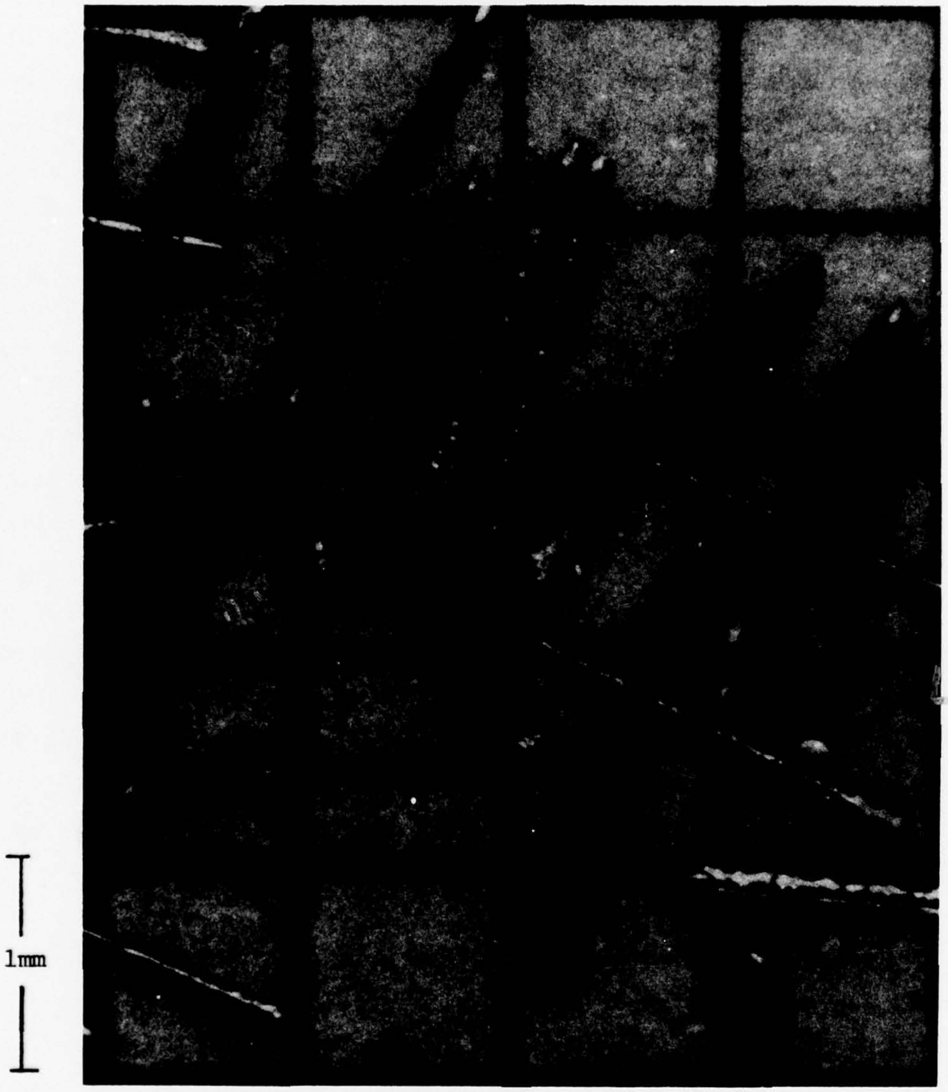

FIGURE 12. RESULTS OF THE FIRST SUCCESSFUL TRIAL IN THE PRODUCTION OF Ti-6Al-4V POWDER-SUBSTITUTE -- DESIGNATED L/D-1.

FIGURE 13. BEVELLED AND NOTCHED EXTRACTION DISK USED IN THE PRODUCTION OF THE L/D-2 TYPE Ti-6Al-4V POWDER.

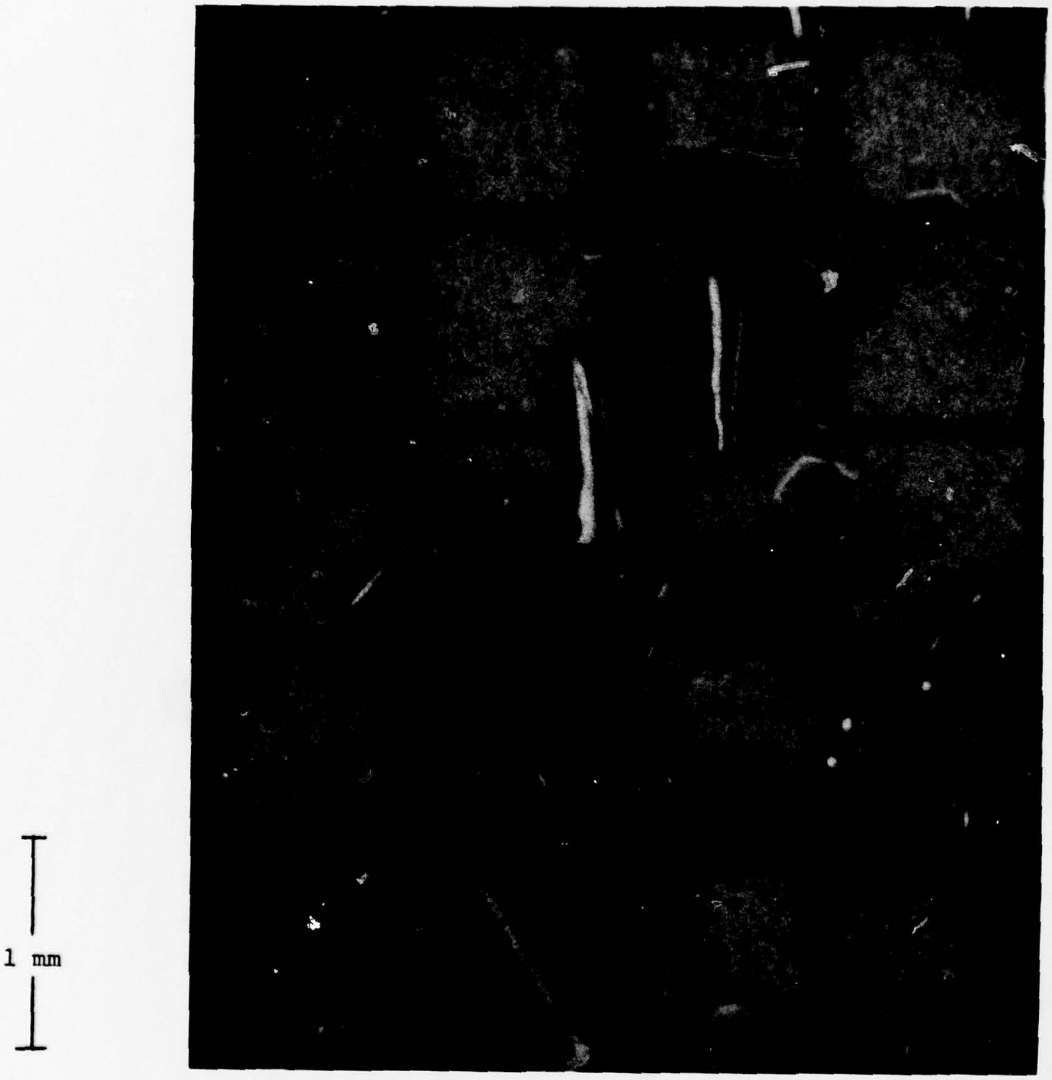

FIGURE 14. FINAL FORM OF THE Ti-6Al-4V POWDER -- DESIGNATED L/D-2.

TABLE 14. CHEMICAL COMPOSITION OF PDME-PRODUCED Ti-6Al-4V L/D-POWDER SUBSTITUTE COMPARED TO THAT OF THE STARTING MATERIAL

Specimen	Data Source	Composition in Weight Percent				
		Al	V	C	N	O
Melt Stock	Manufacturer	6.7	4.2	0.02	0.015	0.198
	Leco, Inc.			0.029		0.237
L/D Powder	Leco, Inc.			0.0315	0.0641	0.205
"	"			0.0323	0.0623	0.206
"	"			0.0339	0.0638	0.217
"	"			0.0331	0.0650	0.207

The packing density of each grade of powder was determined by vibrating and tap-settling in a one-inch diameter glass measuring cylinder. Nominal packing densities of 30 and 77 percent of theoretical* were obtained for the L/D-1 and L/D-2 powders, respectively. When packed into a 3/8-inch diameter mold, the less flowable L/D-1 powder packed to only 20 percent of theoretical whereas a density of 74 percent was obtained with the L/D-2 powder. Dimensions and handling characteristics are summarized in Table 15.

*referred to 100% for random spherical packing.

TABLE 15. DIMENSIONS AND HANDLING CHARACTERISTICS OF L/D-1 AND L/D-2 POWDER

Characteristic	L/D-1	L/D-2
Shape	long and thin with needle-like ends	short ingot-shaped particles
Size	approximately 0.002 in. (0.05 mm) diameter by < 0.1 in. (2.5 mm) long	approximately 0.012 in. (0.2 mm) wide by 0.003 in. (0.076 mm) thick by approximately 0.05 in. (1.27 mm) long
L/D Ratio	50	9
Flowability	flows only with superimposed vibration	flows relatively freely like a coarse powder
Packing density (% theo)		
loose, 1-inch cylinder	30	77
3/8-inch mold	20	74

Cold die pressing experiments performed in a 3/8-inch diameter die showed that the L/D-1 powder was capable of being pressed into solid pellets of nominal 54 percent density at 50 ksi. Firm pellets were obtained, but they delaminated easily upon being stressed transversely. A considerable amount of spring back of the punch occurred upon release of the force on the die punch. Cold die pressing of the L/D-2 powder yielded a pellet which crumbled easily with handling.

3.3 Vacuum Hot Pressing Consolidation Program

This section discusses the vacuum hot pressing of a test billet which was subsequently cut up into tensile specimens, compression specimens, metallographically examined, and chemically analyzed. Vacuum hot pressing

(VHP) has been shown to be a viable, low-cost technique for fabricating titanium structural components such as complex aircraft fittings and engine disks from powders [18]. Using the process, many different kinds of powder or starting materials including wire pieces (0.020-inch diameter by 0.025-inch long) have been consolidated into 99.5 to 99.9% dense test plates or billets or shapes. Fully dense parts have been obtained irrespective of the density of the green compact or of loose powders or vibration-packed powders.

The hot-pressing process offers a number of advantages over other powder consolidation processes. These are

(1) Low capital requirements

(2) Dynamic vacuum assures complete outgassing and therefore high-purity parts which, in turn, yields exceptional mechanical properties

(3) A high degree of dimensional control and good surface finish are obtained with hot-pressed parts because of the use of dies. The process results in "net" parts for many applications.

(4) No gas storage or gas containment facilities and equipment are required with hot pressing, which employs more easily contained and maintained hydraulic systems.

(5) There are several other process-related advantages that could be listed. Some of these are reduced floor space requirements and ease of press and furnace maintenance in hot-pressing systems.

The various prealloyed powders or starting materials that have been vacuum hot pressed to full density include the following:

- Ti-6Al-4V hydride/dehydride powder
- Nuclear Metals' spherical Ti-alloy powder
- Ti-6Al-4V hydride powder.

We were, therefore, full confident that Ti-6Al-4V L/D powders could be compacted to bulk density by VHP.

3.3.1 Consolidation of L/D-1 Powder

Application of the VHP process was confined to the L/D-1 powder. About 100g of it were pressed into a disk, 5.1 cm in diameter and 1.1 cm thick. This disk and the starting powder are depicted in Figure 15.

Equipment used consisted of Battelle's 15-ton vacuum hot press in association with the following tooling:

The Die

OD = 6.0 inches (15.25 cm)
ID = 2.5 inches (6.35 cm)
Height = 6.0 inches (15.25 cm)
Material = Type 304 stainless steel

The Top and Bottom Punches

Diameter = 2.0 inches (5.08 cm)
Height = 3.0 inches (7.62 cm)
Material = Type 304 stainless steel

The ATJ Graphite Sleeve

OD = 2.52 inches (6.4 cm)
ID = 2.0 inches (5.08 cm)
Height = 6.0 inches (15.25 cm)

The stainless steel die was preheated in air to about 650°C enabling it to expand and accept the insertion of the graphite sleeve. The two punches were placed in the dies and the assembled tools were outgassed empty at 815°C in a vacuum of 4×10^{-5} torr in Battelle's 15-ton hydraulic press. The tool assembly was allowed to cool overnight, loaded with about 100 grams of the L/D-1 powder, replaced in the press, and evacuated to about 4×10^{-5} Torr. The assembly was induction heated to 955°C in dynamic vacuum, during which no significant outgassing occurred, hopefully because of the prior 815°C vacuum heating cycle. The powder was vacuum hot pressed at 955°C and 800 psi (0.56 kg/mm^2) for 1 hour. The assembly was again allowed to cool overnight in dynamic vacuum, after which the pressed Ti-6Al-4V disk was removed from the die assembly and lightly machined to improve its appearance as an exhibit, Figure 15.

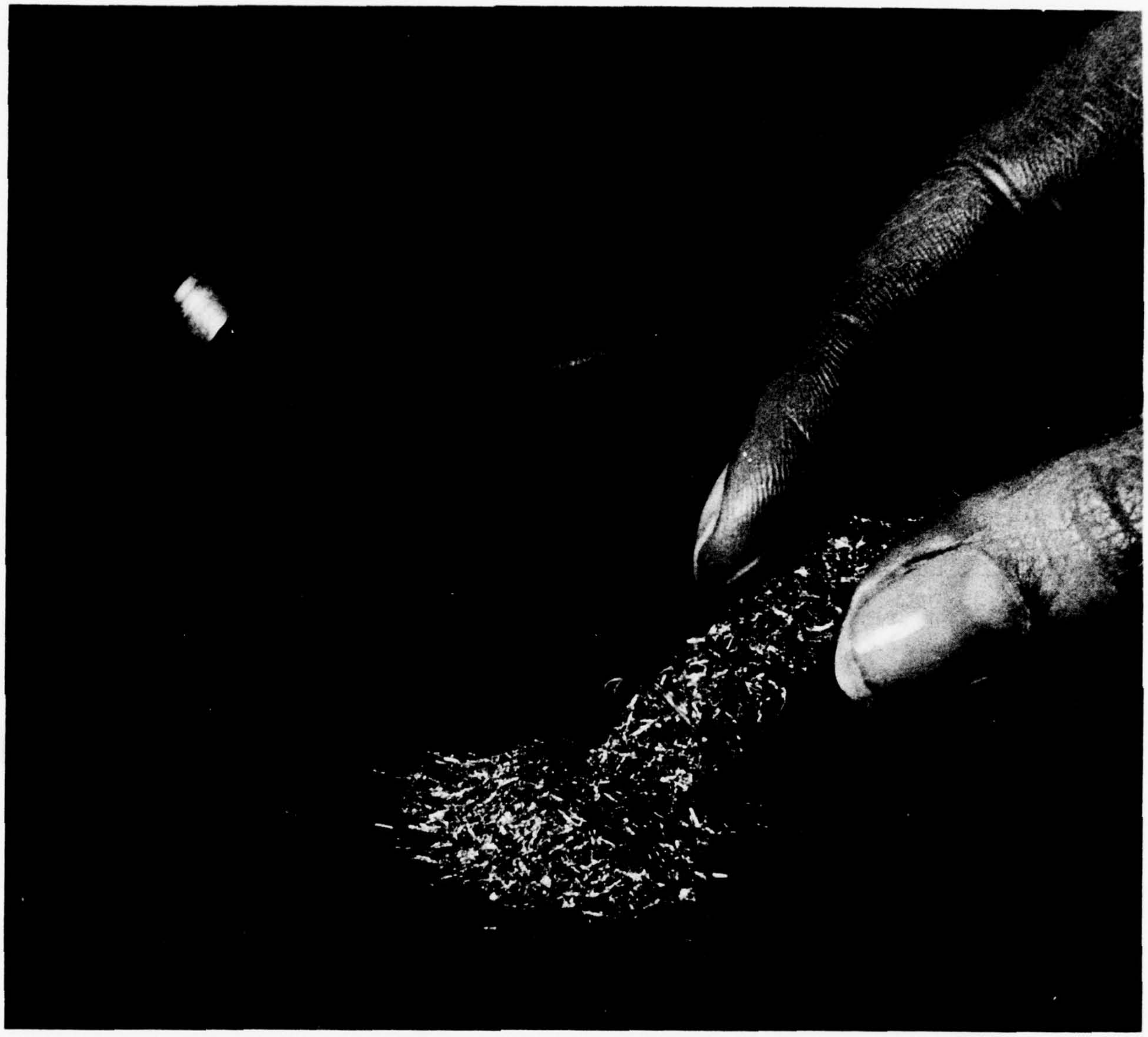

FIGURE 15. VACUUM HOT PRESSED DISK (5.1 cm x 1.1 cm) AND AN EXAMPLE OF THE L/D-1 POWDER FROM WHICH IT WAS FABRICATED.

3.3.2 Properties of the Vacuum Hot Pressed L/D-1 Powder Compaction

(a) Chemical Analysis. In a powder consolidation process one is always concerned with the removal of entrained air. This is particularly important with a reactive material such as titanium, and one whose properties are so strongly affected by the presence of dissolved oxygen and nitrogen. The results of several sets of independent chemical analyses carried out on samples cut from the VHP disk are presented in Table 16, from which it is seen that although the nitrogen level has not increased significantly above that of the starting powder, a 20% increase in the oxygen level took place, and a slight increase in the carbon level, took place.

TABLE 16. CHEMICAL ANALYSIS OF THE VHP DISK COMPARED WITH THAT OF THE L/D POWDER STARTING MATERIAL

Specimen	Data Source	Composition in Weight Percent				
		Al	V	C	N	O
L/D Powder	Leco, Inc.			0.0315	0.0641	0.205
"	"			0.0323	0.0623	0.206
"	"			0.0339	0.0638	0.217
"	"			0.0331	0.0650	0.207
VHP Sample	Leco, Inc.			0.0469	0.0561	0.239
					0.0571	0.238
"	AFML/Sherry Labs			0.073	0.024	0.265
"	"					0.273
"	Battelle	7.0	4.6			

(b) Density. Further sectioning of the as-recieved VHP disk yielded samples for density measurement and for the machining of tensile bars. The results of two density determinations, carried by the water-immersion method, are given in Table 17 where a comparison is made with the measured density of the wrought starting material. The reason for the significantly greater density of the VHP material is not known.

TABLE 17. DENSITY OF THE AS-RECEIVED (i.e., UN-HEAT-TREATED) VHP L/D-1. THE ESTIMATED EXPERIMENTAL UNCERTAINTY IS ± 0.003 g/cc

Sample	Density	
	g/cc	lb/in^3
Wrought (reference material)	4.417	0.159_6
VHP (two determinations)	4.437	0.160_3

(c) Microstructures. Microstructures of the as-pressed VHP product were examined by optical metallography and electron microscopy. The purpose of the optical metallography was to compare the structure of the VHP consolidation with that of the wrought as-received and wrought mill-annealed starting material; and also to ascertain that the consolidate retained no "memory" of the physical form of the L/D-1 particles. The results of the optical work are shown in Figure 16.

The replica electron micrographs are shown in Figure 17. It can be seen by comparing Figure 17 with Figure 9c, that the VHP sample is essentially in the "recrystallized" condition. This is to be expected since the recrystallization anneal is:

1700°F/4 hr/furnace cool (100 deg/h) to
1400°F/furnace cool (650 deg/h) to
900°F/air cool

while the VHP process is defined by:

1700°F/8 ksi/1 hr/furnace cool

(d) Compressive Strengths of VHP Specimens. Small compression test samples were machined from the VHP disk and tested in the as-VHP and mill-annealed* conditions. The results of these studies are given in Table 18...

*redundant following VHP.

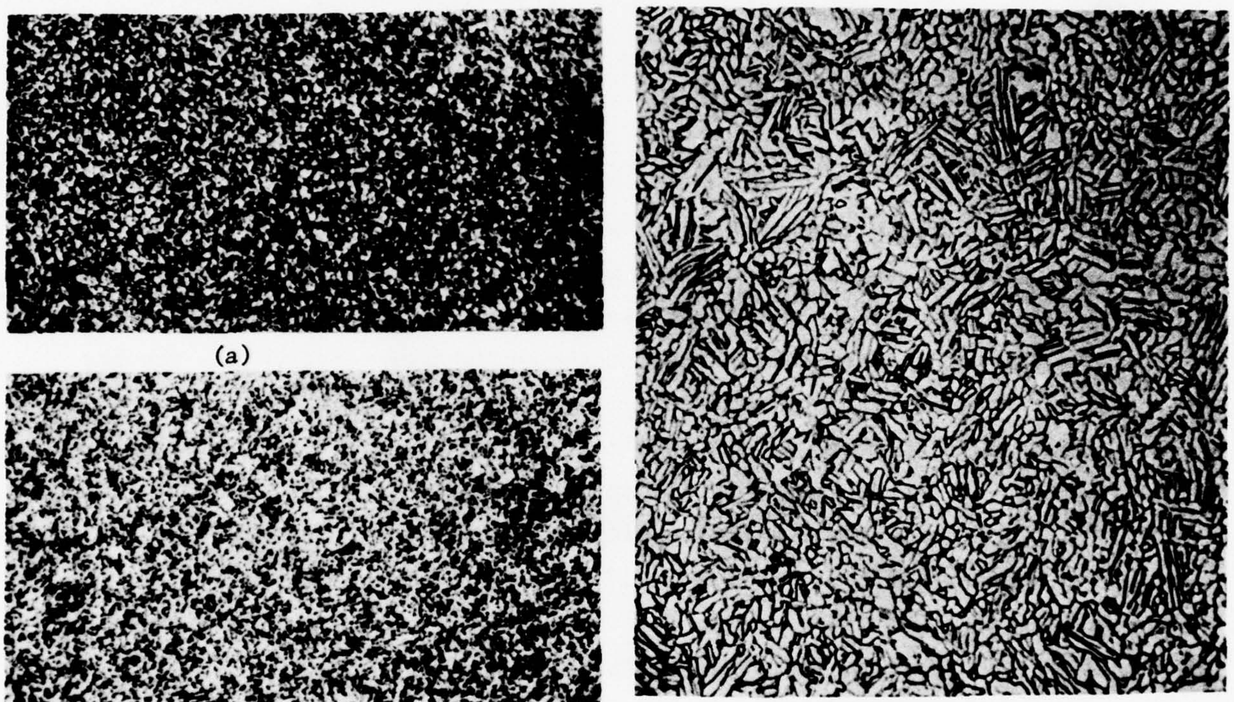

(a) (b) (c)

WROUGHT 250X VHP

FIGURE 16. OPTICAL METALLOGRAPHS OF (a) WROUGHT (AS REC.), (b) WROUGHT (MILL-ANN), AND (c) VHP (AS-PRESSED POWDER) Ti-6Al-4V, IN WHICH NO PRIOR PARTICLE BOUNDARIES (1.3 CM IN WIDTH, ON THIS SCALE) ARE DETECTABLE.

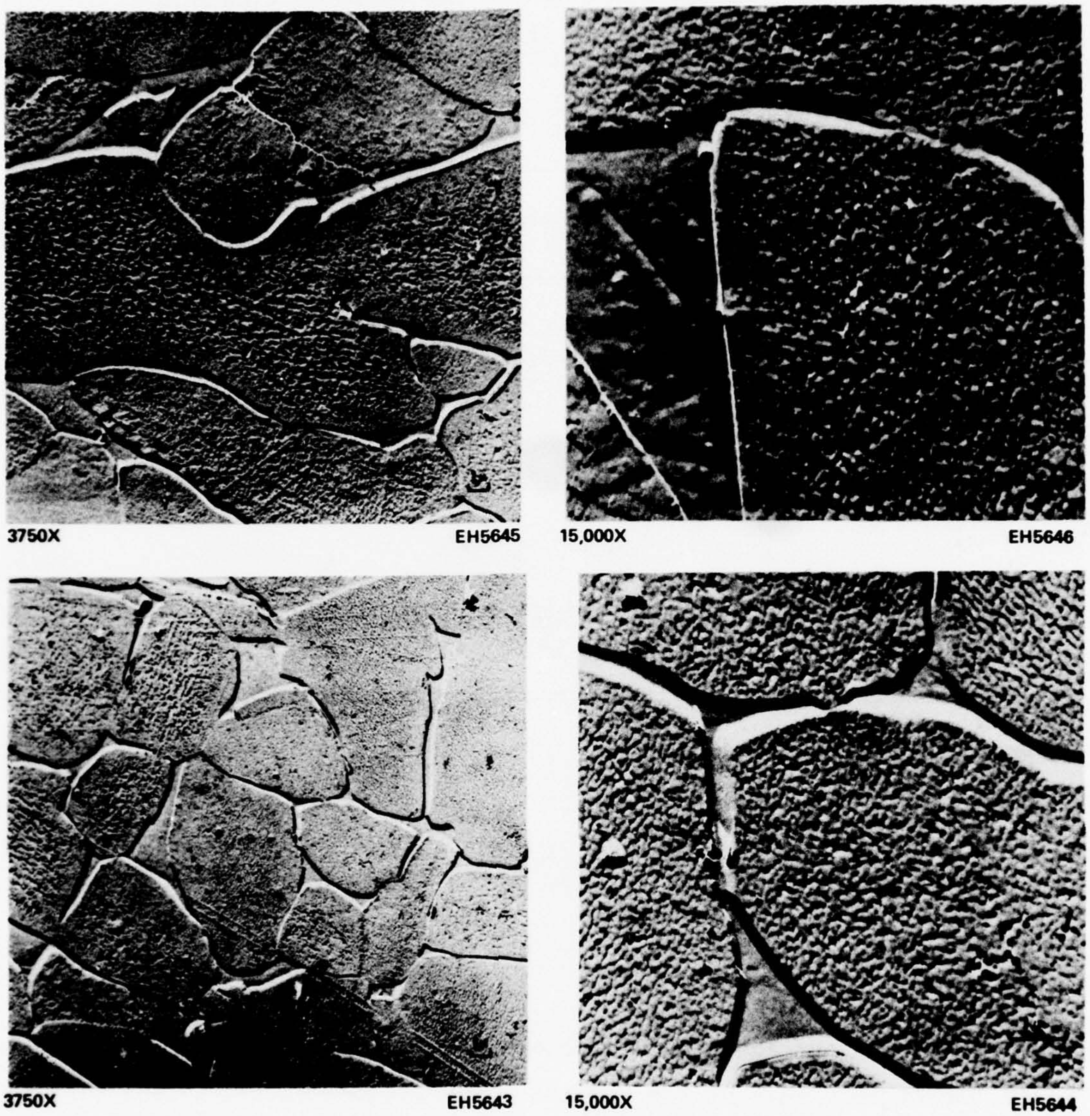

FIGURE 17. REPLICA ELECTRON MICROGRAPHS OF VACUUM HOT PRESSED (VHP) Ti-6Al-4V L/D-1 POWDER. AS EXPECTED THE STRUCTURE IS α PLUS INTERGRANULAR β, AND COMPARABLE TO THE 1700°F RECRYSTALLIZED STRUCTURE OF FIGURE 3-4(c). (Printing reduction factor, ~0.7)

TABLE 18. RESULTS OF COMPRESSION TESTS ON VACUUM HOT PRESSED (VHP) L/D-1 POWDER COMPARED WITH THOSE FOR THE WROUGHT (W) COMMERCIAL STARTING MATERIAL.

Sample Code	Modulus, E (10^6 psi)	0.2% Offset Yield Strength, Y (ksi)
VHP-LD1-AR-1	18.5	143.9
AR-2	17.1	144.6
VHP-LD1-MA-1	17.1	147.6
MA-2	16.9	149.4
W-AR-1	15.7	131.3
AR-2	15.8	130.5
W-MA-1	15.9	144.7
MA-2	15.8	143.2

AR = as received
MA = mill-annealed

The average compressive elastic modulus of the VHP material is 10% higher than that of the wrought alloy presumably due to the influence of the slightly higher interstitial content. Similarly, the compressive yield strength is 7% higher, although no quantitative information on ductility is available.

(e) Tensile Strengths of VHP Test Bars. Test bars machined from the VHP disc were tensile tested in the as-VHP and mill-annealed conditions. For comparison, test bars of wrought commercial Ti-6Al-4V (the starting material) were machined to exactly the same dimensions and also tested in the as-received and mill-annealed conditions. The results of this work are given in Table 19.

TABLE 19. RESULTS OF TENSILE TESTS ON VACUUM HOT PRESSED (VHP) L/D-1 POWDER COMPARED WITH THOSE FOR THE WROUGHT (W) COMMERCIAL STARTING MATERIAL

Sample Code*	Modulus, E (10^6psi)	0.2% Offset Yield Strength, Y (ksi)	Ultimate Tensile Strength, U.T.S. (ksi)	Elongation (%)	Area Reduction, RA (%)
VHP-LD1-AR-1	16.4	140.1	151.2	9.4	12.4
AR-2	16.9	140.9	150.8	6.5	10.5
VHP-LD1-MA-1	15.6	138.6	147.5	8.1	18.3
MA-2	16.0	138.5	148.3	14.3	
W-AR-1	15.2	134.9	157.3	14.0	47.1
AR-2	14.3	137.3	159.1	14.2	38.5
W-MA-1	14.7	140.9	154.9	14.5	42.6
MA-2	14.7	141.7	155.8	14.6	

* AR = as-received
MA = mill-annealed

The average tensile elastic modulus of the VHP material is 10% higher than that of the wrought alloy. As before, this is due, presumably, to the influence of the interstitial content. It is reassuring, when considering the reproducibility of experimental data, however, to note that the modulus of the VHP sample (16.2 x 10^6 psi) is practically equal to that of the fiber from which it was processed (15.7 x 10^6 psi, Table 11).

The tensile offset yield strengths of the VHP and wrought samples are comparable (139.5 compared to 138.7 ksi, resp.); but the VHP samples all exhibit reduced ductility, presumably again due to the influence of the higher interstitial content. The test bars and their fracture surfaces are depicted in Figure 18.

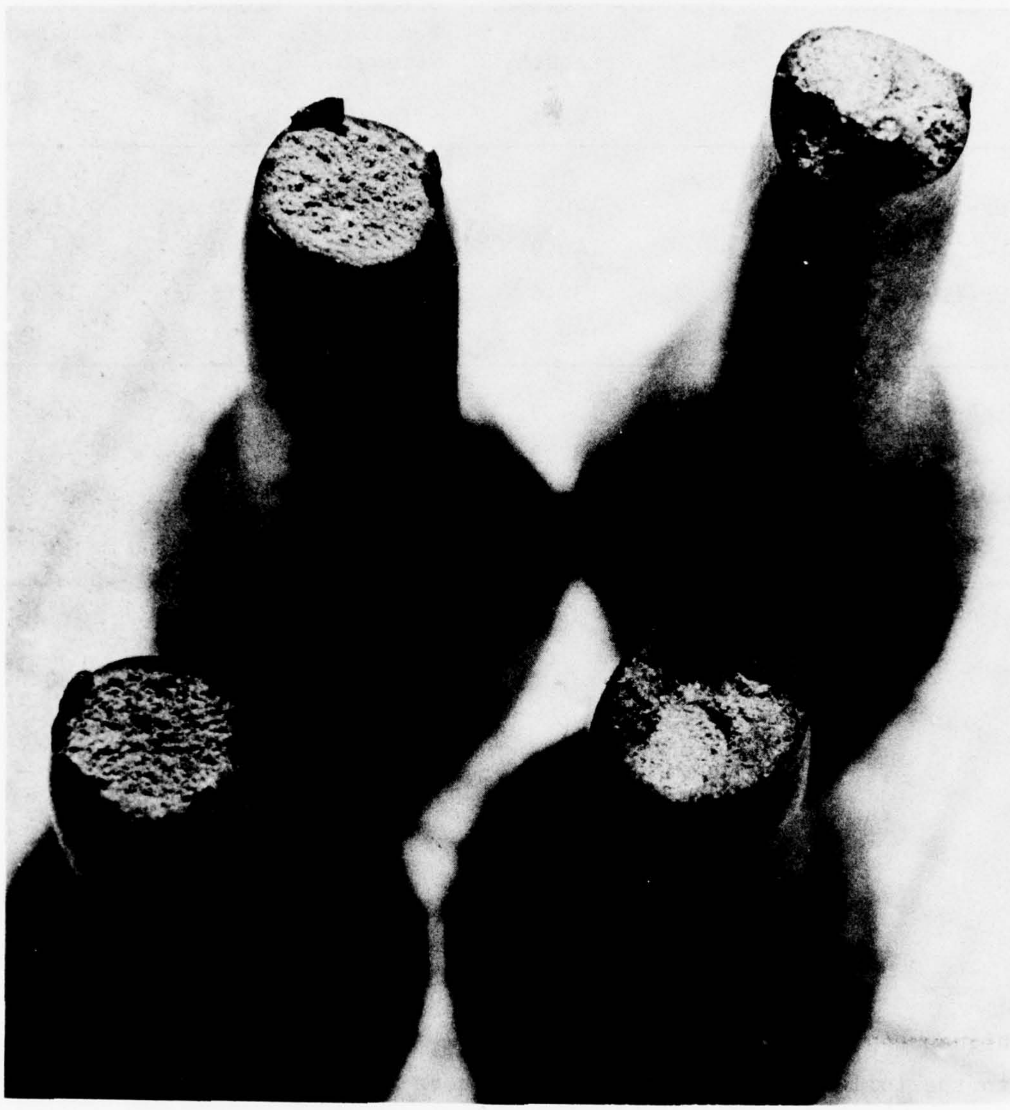

VHP WROUGHT

FIGURE 18. FRACTURED TENSILE BARS OF VHP L/D-1 (LEFT) AND WROUGHT (RIGHT) Ti-6Al-4V. THE LOWER DUCTILITY OF THE VHP MATERIAL IS EVIDENT. BACKGROUND, 1 mm-SQUARE PAPER.

3.4 Hot Isostatic Pressing Program

Hot isostatic pressing was performed on each of the two grades of L/D powder to provide ten small-diameter pellets for compression testing and several other 1-in. diameter billets to be retained as exhibits, Figure 19, after which various examination and testing procedures were carried out.

FIGURE 19. FULLY DENSE CYLINDERS LIGHTLY MACHINED FROM HIP-ed CYLINDERS OF L/D-1 (LEFT) AND L/D-2 (RIGHT) Ti-6Al-4V POWDER-SUBSTITUTE.

3.4.1 HIP-Consolidation of L/D-1 and L/D-2 Powders

Eleven 3/8-in. diameter cylinders were cold pressed from L/D-1 powder at a pressure of 50 ksi. Higher pressures, which resulted in significant die damage, were not used.

One pellet was submitted for "green" compression testing. The other 10 pellets were canned for HIP. The L/D-2 powder did not need to be pre-cold pressed, but was loaded directly into the HIP container. The larger HIP cans for producing 1-in.-diameter billets were also loaded with L/D-2 powder without a prepressing operation, and were then tap-packed to maximum density. The L/D-1 powder was pressed directly into the larger HIP containers to maximize the powder charge size by eliminating the need for assembly clearance for a prepressed pellet.

The HIP containers were made from seamless steel tubing and fitted with plugs at each end. The container tubes with their lower end-plugs welded in place were first given an outgassing treatment of 15 hr at 1600°F in vacuum. They were then loaded with prepressed pellets or loose powder as described above, following which the top end-plugs with their attached evacuation stems were welded on. The filled cans were evacuated and heated overnight at 600°F to remove sorbed gases. At the conclusion of this treatment no pressure build-up was detected after isolation from the vacuum pump. The evacuation stems were then pinched off and sealed by welding. The parameters of the hot isostatic pressing operation were 1750°F/10,000 psi/1 hour.

The small pellets were consolidated in the first of two HIP cycles. The larger billets were consolidated in the second cycle. Because of the non-uniform deformation of the HIP containers experienced in the first HIP cycle, the second cycle involved the following modifications.

- Instead of the commonly used procedure of simultaneously heating and pressurizing to the maximum conditions, a low pressure of 500 psi was applied and heating to the maximum temperature was done without further pumping. The pressure was then increased to the maximum value.

- The HIP container was encased in a heavy-walled steel sleeve.

After pressing, both the small (1/2-in. high, 1/4-in. diam.) and large cylinders were machined, the former to be used for compression testing. Figure 20 shows a group of the consolidated compression-test samples, together with one of the green-compacted starting pellets.

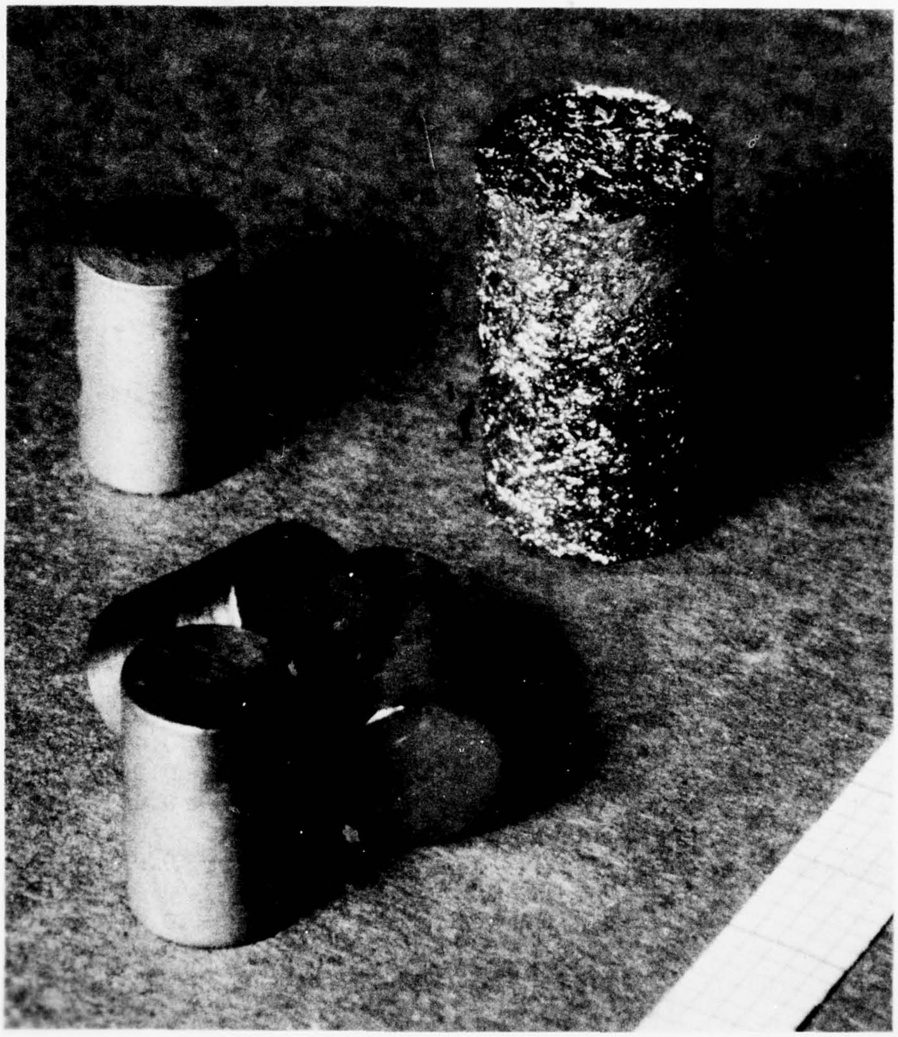

FIGURE 20. HIP-COMPACTED AND MACHINED COMPRESSION TEST SPECIMENS, AND A "GREEN"-COMPACTED STARTING PELLET.

3.4.2 Properties of the Hot Isostatic Pressed L/D Powder Compactions

(a) Chemical Analysis

The results of chemical analysis carried out on material removed during the machining, after HIP-ing, of the compression test specimens are given in Table 20, where a comparison can be made with the composition of the starting L/D powder.

No explanation can be offered for the surprising decrease in the nitrogen content. On the other hand, presumably due to a more sophisticated handling procedure than was used in the vacuum hot pressing, the oxygen content of the HIP-ed material is only 10% higher than that of the starting powder.

TABLE 20. CHEMICAL ANALYSIS OF HIP-PROCESSED L/D POWDER COMPARED WITH THAT OF THE AS-EXTRACTED POWDER

Specimen	Data Source	Composition in Weight Percent				
		Al	V	C	N	O
L/D Powder	Leco, Inc.			0.0315	0.0641	0.205
"	"			0.0323	0.0623	0.206
"	"			0.0339	0.0638	0.217
"	"			0.0331	0.0650	0.207
HIP Sample	AFML/Sherry Labs			0.05	0.036	0.255
"	"			0.05	0.031	0.269
"	"			0.04	0.013	0.215
"	"			0.06	0.020	0.215
"	Battelle	6.8	4.1			
"	Leco, Inc.			0.0536	0.0142	0.215
					0.0139	0.215

(b) Density

Density determinations were made on HIP-ed samples prepared from both L/D-1 and L/D-2 powder using the water-immersion method. The results of this work, presented in Table 21 are in excellent agreement with the measured density of the wrought commercial Ti-6Al-4V.

TABLE 21. DENSITY OF AS-HIP-ED SAMPLES PREPARED FROM L/D-1 AND L/D-2 POWDER

Sample	Density (g/cc)	Density (lb/in.^{3})
Wrought	4.417	0.159_6
HIP-LD1	4.421	0.159_7
	4.425	0.159_9
HIP-LD2	4.418	0.159_6
	4.417	0.159_6

(c) Microstructures

Microstructures of the as-HIP-ed material were examined by optical metallography (250X), and compared with that of the wrought alloy, in order to evaluate grain size and to ascertain that whether the shapes of the L/D-1 and L/D-2 powders had been completely obliterated by diffusion and recrystallization during pressurized heat treatment. The results of optical metallography are given in Figure 21.

Replica electron micrographs (3750X and 15000X) of HIP-processed samples prepared from the two kinds of powder are given in Figure 22. As was the case after vacuum hot processing, the HIP-ed material is in essentially the standard "recrystallized"condition (c.f., Subsection 3.3.2(c)).

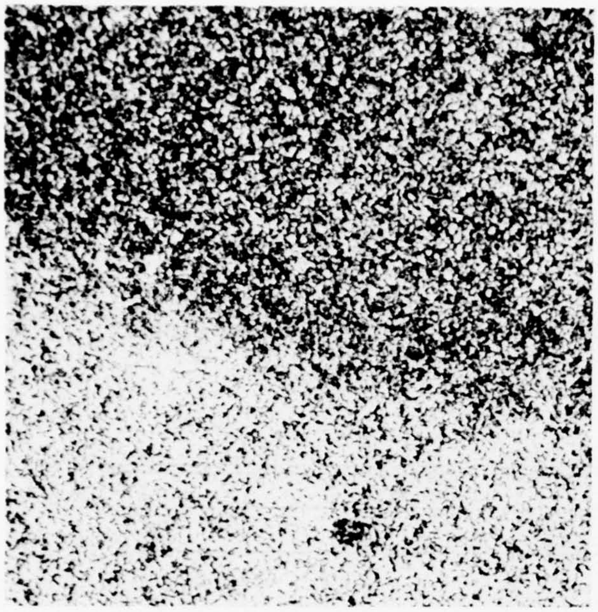

(a) Wrought As-received

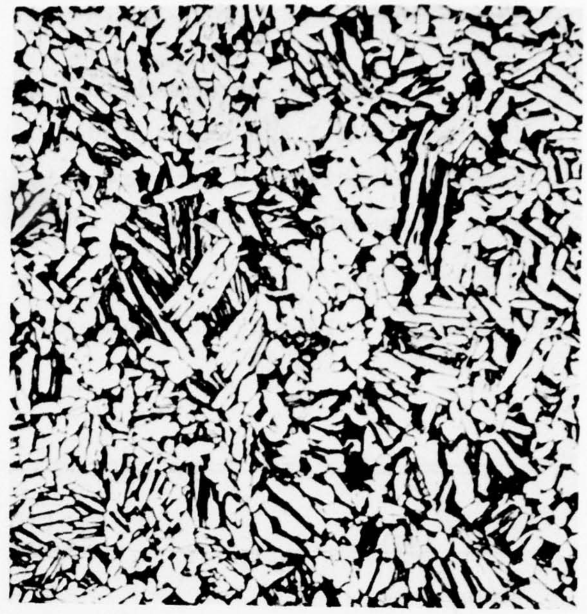

LD-1 (c) 250X

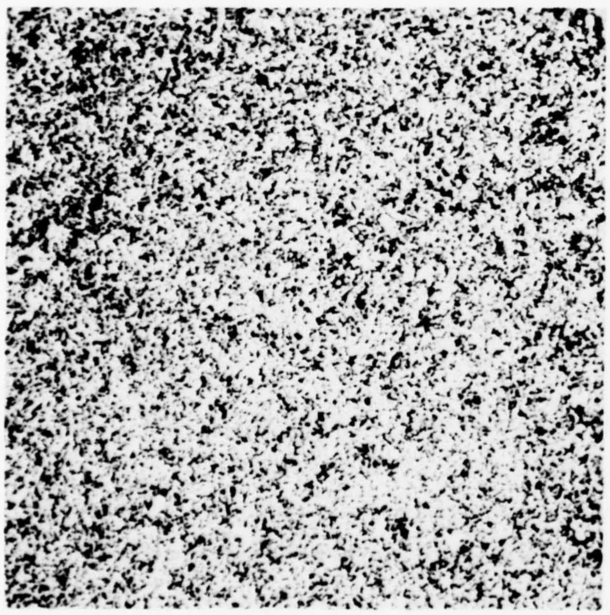

(b) Wrought Mill-annealed

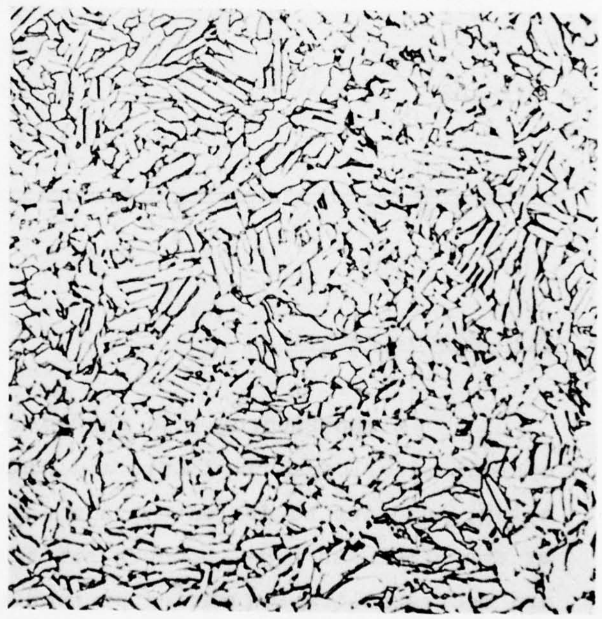

LD-2 (d) 250X

FIGURE 21. OPTICAL MICROGRAPHS OF (a) WROUGHT (AS-RECEIVED), (b) WROUGHT (MILL-ANNEALED) Ti-6Al-4V ALLOY, COMPARED WITH THE RESULTS OF APPLYING HOT ISOSTATIC PRESSING TO (c) L/D-1 POWDER AND (d) L/D-2 POWDER. No prior particle boundaries are detectable (particle cross-sections on this scale: L/D-1, 1.3 cm diam; L/D-2, 5 cm x 2 cm).

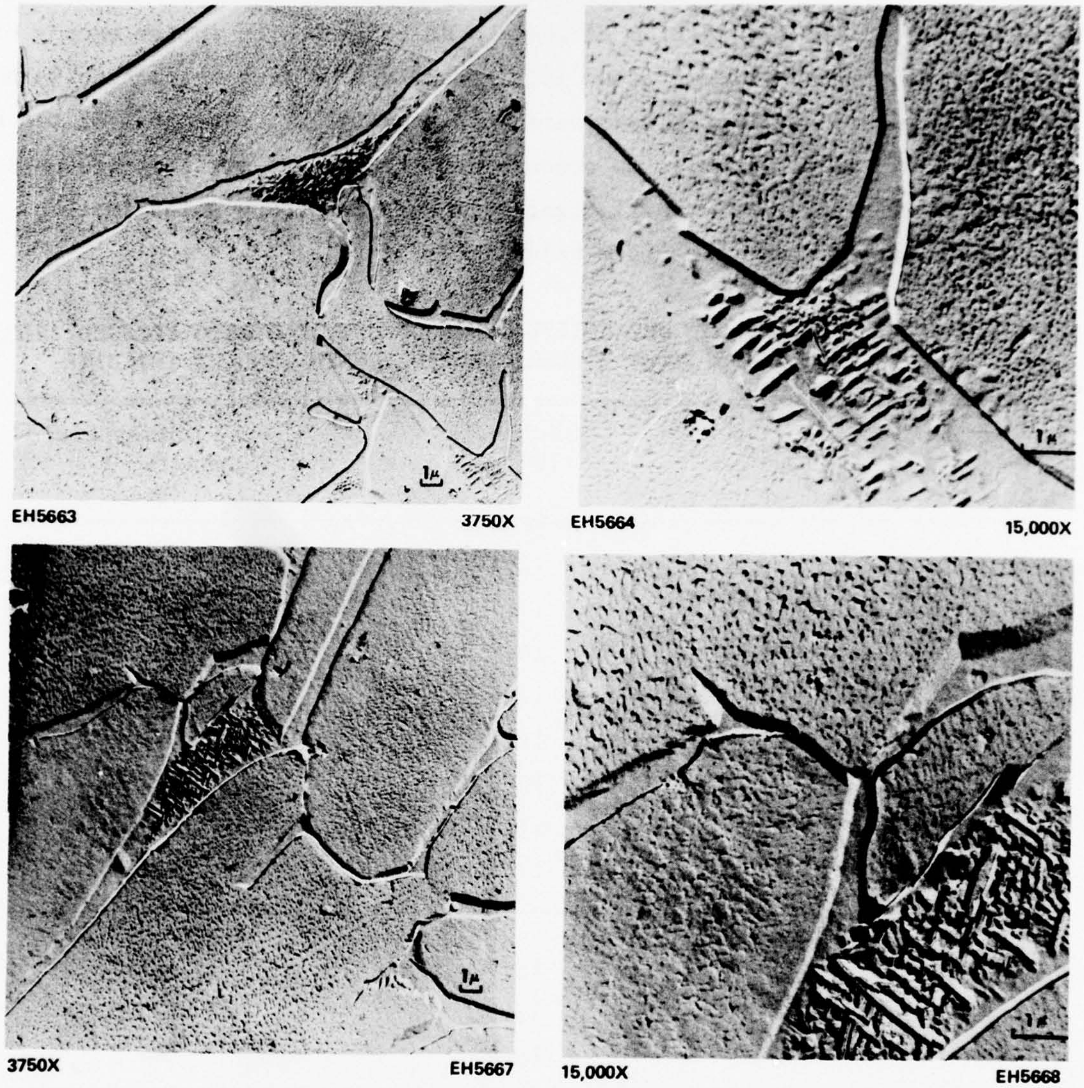

FIGURE 22. REPLICA ELECTRON MICROGRAPHS OF HOT ISOSTATIC PRESSED (HIP) Ti-6Al-4V POWDER.

(a) L/D-1 powder; (b) L/D-2 powder.

The as-HIP-ed structure is essentially in the standard "recrystallized" condition. The micrographs indicate no differences in micro structure between the L/D-1 and L/D-2 constituted specimens. (Printing reduction factor, ~0.7)

(d) Compressive Strengths of HIP Ti-6Al-4V L/D Powder

In the VHP section of the powder program, the entire supply of available powder was compressed into a single disc from which tensile bars and compression-test cylinders were subsequently cut. The goal of the HIP section of the program was to produce net shapes, and for this reason it was decided to prepare only small right cylinders for compression testing. The results of the tests are given below in Table 22.

TABLE 22. RESULTS OF COMPRESSIVE TESTS ON HOT ISOSTATIC PRESSED (HIP) L/D-1 AND L/D-2 POWDER, COMPARED WITH WROUGHT (W) DATA

Sample Code*	Modulus, E (10^6 psi)	0.2% Offset Yield Strength, Y (ksi)
HIP-LD1-AR-1	17.4	151.1
AR-2	17.7	145.3
HIP-LD1-MA-1	16.7	150.3
MA-2	17.5	151.1
HIP-LD2-AR-1	17.1	144.9
AR-2	16.8	146.4
HIP-LD2-MA-1	17.5	145.3
MA-2	17.4	144.9
W-AR-1	15.7	131.3
AR-2	15.8	130.5
W-MA-1	15.9	144.7
MA-2	15.8	143.2

* AR = as-received
MA = mill-annealed

The average compressive elastic modulus of the HIP material is 9% higher than that of the wrought alloy, while the 0.2% offset yield strength is 7% higher. This increase in strength and modulus under compression is attributed to the slightly higher interstitial content of the HIP-ed material.

3.5 Summary of Chemical and Mechanical Property Data

A complete set of chemical analysis data is compiled for comparison in Table 23; while a complete set of mechanical property data, for both compression and tension, is given in Table 24. In that table it is interesting to note that the compressive and tensile yield strengths of mill-annealed wrought Ti-6Al-4V are higher than the as-received values and more nearly equal to those of the VHP- and HIP-processed materials. This suggests on one hand, that such alloys are difficult to heat treat without contamination even when elaborate precautions are taken; and on the other, that the deterioration of properties which occur under VHP or HIP are hardly more severe than under mill-annealing of wrought stock.

3.6 Conclusion

The research results presented in this section have demonstrated that melt extraction is a viable process for producing controlled purity samples of Ti-6Al-4V L/D-type powders. These powders can be handled conveniently and can be consolidated by VHP or HIP techniques to produce sound billets with acceptable mechanical properties.

TABLE 23. CHEMICAL COMPOSITIONS OF WROUGHT Ti-6Al-4V BAR, AND THOSE OF THE FILAMENT, POWDER, VHP SAMPLE, AND HIP SPECIMENS PREPARED IN THE "L/D-POWDER" PHASE OF THIS PROGRAM

Specimen	Data Source	Composition in Weight Percent				
		Al	V	C	N	O
Melt Stock	Manufacturer	6.7	4.2	0.02	0.015	0.198
"	Leco, Inc.			0.029		0.237
Cast Filament	Battelle	6.2	4.2	0.263		0.238
"	"	6.2	4.1			
"	"	6.4	4.1			
"	"	6.4	4.1			
"	"	6.2	4.1			
"	Leco, Inc.			0.0362		
"	"			0.0362		
"	"			0.0485		
"	"			0.0465		
"	AFML/Sherry Labs			0.1	0.031	0.258
L/D Powder	Leco, Inc.			0.0315	0.0641	0.205
"	"			0.0323	0.0623	0.206
"	"			0.0339	0.0638	0.217
"	"			0.0331	0.0650	0.207
VHP Sample	Leco, Inc.			0.0469	0.0561	0.239
					0.0571	0.238
"	AFML/Sherry Labs			0.073	0.024	0.265
"	"					0.273
"	Battelle	7.0	4.6			
HIP Sample	AFML/Sherry Labs			0.05	0.036	0.255
"	"			0.05	0.031	0.269
"	"			0.04	0.013	0.215
"	"			0.06	0.020	0.215
"	Battelle	6.8	4.1			
"	Leco, Inc.			0.0536	0.0142	0.215
					0.0139	0.215

TABLE 24. SUMMARY OF MECHANICAL PROPERTY DATA (COMPRESSIVE AND TENSILE) FOR WROUGHT, VHP, AND HIP-PROCESSED Ti-6Al-4V ALLOYS

Sample	Density (g/cm^3)	Modulus, E (10^6 psi)		0.2% Offset Yield Strength, Y (ksi)		Ultimate Tensile Strength, UTS (ksi)
		Compressive	Tensile	Compressive	Tensile	
W-AR/MA	4.417	15.8 ± 0.1	14.7 ± 0.4	130.9 ± 0.6[a] 144.0 ± 1.0[b]	136.1 ± 1.7[a] 141.3 ± 0.6[b]	156.8 ± 1.8
VHP-LDL-AR/MA	4.437	17.4 ± 0.7	16.2 ± 0.6	146.4 ± 2.6	139.5 ± 1.2	149.5 ± 1.8
HIP-LD1-AR/MA	4.423	17.3 ± 0.4	-	149.5 ± 2.8	-	-
HIP-LD2-AR/MA	4.418	17.2 ± 0.3	-	145.4 ± 0.7	-	-

(a) = AR
(b) = MA

SECTION IV

PREPARATION AND PROPERTIES OF POLYCRYSTALLINE RAPIDLY QUENCHED MELT-EXTRACTED FIBER

Microcrystalline alloys can be produced by rapid quenching methods. Many of the alloys which have been investigated have been shown to have some unusual mechanical properties. For example, a considerable increase in the strength of certain aluminum-base alloys quenched with solidification rates of some 10^4 degrees C/second has been noted. An increase in the modulus of elasticity has even been observed for some of these materials as a result of the presence of a very stable dispersed phase. The mechanism of strengthening in rapidly quenched systems was thought to be associated with (a) the fine grain size, (b) a fine dispersion of second phase, and (c) the anomalously high concentration of the solution strengthener permitted by the rapid-quench technique. Such alloys may prove to be as important, technologically, as metallic glasses provided that sufficiently high quench rates can be maintained in production facilities.

Rapid quenching from the melt may lead to the achievement of a very fine grain size (if not complete amorphousness). In a pure substance, the fine-grain structure is extremely unstable. But in two-phase material some degree of elevated temperature stability is obtainable, especially if the equilibrium phases differ considerably in chemical composition, since under this condition, reversion to equilibrium is inhibited by the necessity for a massive flux of atoms over considerable distances. Such a stable, refined-grain structure is conducive to superplasticity. Although most readily obtainable in a two-phase eutectic or eutectoidal system (in which spinodal decomposition is very effective), a fine (1-5 μm), stable, equiaxed grain structure can sometimes be stabilized by the presence of grain-boundary-pinning precipitate particles. An excellent example of this is to be found in the boron-containing Ti-6Al-4V alloy considered in one of the following sections.

Rapid solidification techniques have been used both to harden and to increase the modulus of Al alloys. It seems that maximal strength consistent with adequate ductility can be achieved by arranging for arrays of dislocation pinning sites separated by about 50 lattice spacings, and

that such an arrangement is possible as a result of rapid melt quenching. Dispersion hardening, by the presence of both stable and metastable phases produced as a result of rapid quenching, has frequently been demonstrated. In addition, enhanced solid-solution strengthening through splat-cool-induced extended solid solubility can be expected.

As a result of melt quenching considerable improvements in the strengths and moduli of polycrystalline metals can be anticipated. This is particularly true of aluminum alloys, which have been the subjects of many investigations over a number of years.

For example, considerable increases in the strengths of the alloys

Al - 5Cr, Al - 2.5Cr - 4Si, and Al - 5Cr - 8Si

were obtained by Esslinger[19] in an investigation in which solidification rates of some 10^4 deg/sec were employed. Dispersion hardening was the mechanism, the rapid solidification being conducive to the production of a fine-grain precipitate. Esslinger noted that a stable dispersed phase yielded a strengthened material with relatively high thermal stability, whereas the converse was true if the dispersant happened to be a metastable phase.

The influence of melt-quenching (by the gun technique c.f., Figure 1a and Figure 2 on the structure and hardness of alloys of aluminum with iron and other first-series transition elements has been studied by Jones[20]. Alloys studied were Al-Fe (0.7-39.2%Fe), binary alloys of Al with the transition elements Ti, V, Cr, Mn, Co, and Ni (8% solute), and Al-Ni (11 and 24%). The purpose of the investigation, in which microhardness measurements were coupled with the results of optical metallography, was to optimize the microstructure so as to obtain, through dislocation pinning, an increased strength consistent with adequate ductility. These specimens were not of course amorphous, as is generally found to be the case for splat-cooled aluminum alloys.

Mechanical properties and microstructures of melt-quenched Al alloys have also been the subject of study by Toda and Maddin[3]. The Al-Au (0.25, 0.5, 1.0, 2.5, and 5.0 w/o) Alloys were prepared using a so-called "torsion catapault" apparatus (Figure 1b) by means of which quench-rates of about 10^5 to 10^6 deg/sec were obtained. Mechanical properties of the bulk materials were compared after

subjecting them both to heat treatments of ten hours at 200°C and 300°C in air. The melt quenching was found to result in significant increases in strength.

To summarize, as a result of a combination of grain refinement, dispersion effects and solid solution strengthening, all induced by melt quenching, improvements in both the strengths and moduli of experimental aluminum-base alloys have been obtained. This suggested that in an investigation of metallic fibers produced by spinning from the melt, the properties of polycrystalline (hopefully, microcrystalline) rapidly quenched materials should be considered as well as those of metallic glass candidates.

Prior to the initiation of this program, no such melt-quenching investigations had been carried out on alloys of titanium. In view of its importance as an aerospace alloy, and its potentiality as a lightweight high-strength fiber for composite applications, a program was planned in which the principles of melt-quench strengthening, as outlined above, were to be applied to titanium. The commercial alloy Ti-6Al-4V was taken as base. Small amounts of other elements were added to it, either singly or in combination, melt extraction was carried out, and the properties of the resultant fiber were examined.

In the polycrystalline studies to be described, the starting material was handled in each of two different ways. In one method, alloying ingredients were physically attached in some way to the base Ti-6Al-4V specimen rod, and blending took place in the molten droplet itself. In the other method, pre-alloyed rods were employed. The former variant -- "in-situ alloying -- is discussed first.

4.1 Elastic Moduli and Tensile Strengths of in-situ-Melted Solution and Precipitate-Strengthened Polycrystalline Melt Extracted Fibers

4.1.1 Iron-Base Alloys

In preliminary experiments involving the casting of Fe-P-C alloys, tubes of mild steel were filled with weighed amounts of C and FeP. The intention was to melt a droplet on the end of the tube, allowing alloying to take place in the droplet, and to melt extract the desired alloy ($Fe_{80}P_{13}C_7$). While it was in principle possible to obtain fiber by this method, the process was only barely controllable. The droplet bubbled violently and extraction proceeded in an erratic fashion. It was assumed that the effervescence was either by gases trapped in the powder, or by a chemical reaction within the melt. Attempts to improve the stability of the droplet by prior baking of the melt stock and by the addition of aluminum to it were only moderately successful.

Accordingly, work on Fe-base alloys was suspended, and attention was directed towards a study of the preparation and properties of Ti-6Al-4V-base material.

4.1.2 Multiple-Solute Ti-6Al-4V-Base Alloys

The starting stock was Ti-6Al-4V in the form of 3/8-inch or 1/4-inch diameter rods. In one series of investigations, alloying materials, in the form of wires or rods of various metals (Table 25), were fastened longitudinally to the Ti-6Al-4V stock. For the most part, once melting of the principal rod began, the attached wires would melt and alloy smoothly into the pendant drop.

Alloys were also prepared by adding materials in powdered form (Table 25). Slots (roughly 1-mm wide by 1-mm deep) were cut parallel to the lengths of the titanium alloy rods. Intermetallic compound powders were mixed with alcohol, and the resultant thick slurry was smeared into the slots and allowed to dry. The dried

cement had enough cohesion and strength to bond to the slots during the mounting and extracting procedures; and, as a result, alloyed very smoothly into the basic stock.

TABLE 25. LIST OF ALLOYING ADDITIONS TO Ti-6Al-4V USED IN "in-situ ALLOYED" PENDANT DROP MELT EXTRACTION

(a) Wires and Rods
Fe (soft iron wire)
1018 steel (0.2 C, 0.9 Mn, bal Fe)
Cu (electrical wire)
430F stainless steel (16 Cr, bal Fe)
Elgiloy (40 Co, 20 Cr, 15 Ni, 7 Mo, 0.15 C, bal Fe)
Graphite (pencil lead)
308 stainless steel (20 Cr, 11 Ni, 2 Mn, bal Fe)
W (electron-beam filament wire)
(b) Powders
TiB_2
$TiSi_2$
TiC

AD-A060 353 BATTELLE COLUMBUS LABS OHIO F/G 11/6
AMORPHOUS GLASSY METAL AND MICROCRYSTALLINE ALLOYS FOR AEROSPAC--ETC(U)
JUN 78 E W COLLINGS, R E MARINGER, C E MOBLEY F33615-74-C-5179

UNCLASSIFIED AFML-TR-78-70 NL

2 OF 3

AD
A060353

4.1.3 Description of Multicomponent Alloys

The numerous alloys prepared by the two procedures described above are listed in Table 26, along with a subjective indication of their as-cast properties.

TABLE 26. LIST OF Ti-6Al-4V-BASE ALLOYS PREPARED *in situ* BY PDME

Alloying Addition	Character - Subjective (See Below*)
1018 Steel	Dead Brittle
Fe	Ductile, Strong
Fe + Cu	Very Ductile and Tough
Fe + Cu	Ductile, Strong
Fe + Cu	Ductile, Strong
430F SS	Dead Brittle, Weak
430F SS + Cu	Dead Brittle
Fe + Cu	Ductile, Strong
Cu	Ductile, Strong
Ti-Mo (25 at.%)	Ductile, Strong
Elgiloy	Very Ductile and Tough
Elgiloy + Cu	Ductile, Strong
Graphite	Brittle, Strong
TiB_2 + Cu	Ductile, Strong
TiB_2	Slight Ductility
$TiSi_2$ + Cu	Brittle, Weak
TiB_2 + Fe + Cu	Slight Ductility, Strong
TiC	Slight Ductility, Strong
TiC + Fe + Cu	Ductile, Strong
308 SS	Very Ductile and Tough
308 SS	Very Ductile and Tough
308 SS	Very Ductile and Tough
TiB_2 + TiC	Ductile - Cast Very Poorly
Elgiloy + Cu + W	Ductile, Strong
Fe	Ductile, Strong

* Dead Brittle -- breaks when stressed between fingernail and finger
Slight Ductility -- shows some bending before breaking
Ductile -- bends over sharp radius
Very Ductile and Tough -- survives "e" test
Weak -- breaks readily between fingers in tension
Strong -- difficult to hold in fingers and break in tension.

4.1.4 Properties of Selected Multicomponent Alloys

Several materials, selected on the basis of favorable performance in the subjective tests, were exposed to detailed evaluation. This consisted of density measurement, elastic modulus (*via* sound velocity) measurement, and tensile testing.

(a) Elastic Modulus and Density

Elastic modulus was determined from the results of acoustic wave velocity (v) measurement, carried out at the Air Force Materials Laboratory through the courtesy of Dr. H. L. Gegel, Program Monitor. The relationship between modulus (E) and sound velocity is,

$$E = \rho v^2 , \tag{6}$$

where ρ, the density, was measured using the aqueous buoyancy method. Alloys selected for strength and modulus testing are listed in Table 27.

TABLE 27. ALLOYS SELECTED FOR STRENGTH AND MODULUS TESTING

Alloy	Symbol
Ti-6Al-4V plus (Fe, Ni, Cr; i.e., 308 SS)	A
Ti-6Al-4V plus (8Fe - 3Cu)	B
Ti-6Al-4V plus (40Co - 20Cr - 10Fe)	C
Ti-6Al-4V plus (TiB_2)	D

The results of the sound velocity, density, and modulus determinations are presented in Table 28.

TABLE 28. SOUND VELOCITY, DENSITY, AND MODULUS FOR SEVERAL STRENGTHENED Ti-6Al-4V-BASE ALLOYS

Alloy Symbol (Table 4-3)	Sound Velocity, v (km/s)	Density, ρ (g/cc)	Elastic Modulus, E (10^6 psi)
A	4.242	4.597	
	4.091	4.608	
	4.201	4.604	
		4.664	
	4.178 ± 0.06	4.618 ± 0.03	11.45 ± 0.02
B	3.975	4.625	
	3.904		
	3.940 ± 0.04		10.20 ± 0.01
C	4.191	4.724	
	4.179	4.690	
	4.207		
	4.142		
	4.180 ± 0.02	4.707 ± 0.02	11.68 ± 0.01
D	5.145	4.497	
	5.019	4.511	
	4.951	4.493	
	5.039 ± 0.08	4.500 ± 0.01	16.22 ± 0.02

(b) Tensile Testing

Using grips specially designed for the holding of wire specimens, tensile tests were carried out on samples A, B, C, and D defined above. Prior to the tests, the compliance of the machine was calibrated using

steel wires of known moduli. In lieu of measuring filament cross-sectional area, an effective area was assigned, which normalized the tensile-test modulus value to that obtained acoustically; a method which had previously been successfully applied to the melt-extracted "un-alloyed" Ti-6Al-4V fibers -- Tables 8, 9 and 10.

The results of the tensile tests are listed in Tables 29, 30, 31, and 32 and summarized in Figure 23 and Table 33.

TABLE 29. RESULTS OF TENSILE TESTS ON MELT EXTRACTED FIBERS Ti-6Al-4V PLUS (Fe, Ni, Cr, i.e., 308 SS) - ALLOY A

Specimen Identification	E,(a) 10^6 psi	P/δ, lb/in	Area, $10^{-6}in^2$ $= \frac{P}{\delta} \cdot \frac{L}{E}$	Prop. Limit Load, g	Yield Load			Breaking Load g	Prop. Limit, ksi	Yield Strength			Ult. Tensile Str., ksi	Elong. in 1", %
					Upper Y.P., g	Lower Y.P., g	0.2% Off. Set g			Upper Y.P., ksi	Lower Y.P., ksi	0.2% Off. Set, ksi		
1	11.45	75.4	6.59	455	455	455	580	685	152	152	152	194	229	0.4
2	11.45	117.8	10.29	515	515	505	630	815	110	110	108	135	174	0.45
3	11.45	113.0	9.87	480	480	480	690	810	107	107	107	154	181	0.4
4	11.45	91.0	7.95	420	605	605	680	710	116	168	168	188	197	0.3
5	11.45	104.4	9.12	420	475	465	650	770	101	115	112	157	186	0.45
6	11.45	119.7	10.45	560	600	565	710	885	118	126	119	150	187	0.65
7	11.45	104.4	9.12	465	465	445	650	685	112	112	107	157	165	0.3

(a) E is calculated from measured sound velocity, v, and mass density, ρ: $E = v^2\rho$

TABLE 30. RESULTS OF TENSILE TESTS ON MELT EXTRACTED FIBER Ti-6Al-4V PLUS (8Fe-3Cu) - ALLOY B

Specimen Identification	E,[(a)] 10^6 psi	P/δ, lb/in	Area, 10^{-6}in^2 $= \frac{P}{\delta} \cdot \frac{L}{E}$	Prop. Limit Load, g	Yield Load			Breaking Load g	Prop. Limit, ksi	Yield Strength			Ult. Tensile Str., ksi	Elong. in 1", %
					Upper Y.P., g	Lower Y.P., g	0.2% Off. Set g			Upper Y.P., ksi	Lower Y.P., ksi	0.2% Off. Set, ksi		
1	10.20	87.8	8.61	450	590	540	540	690	115	151	138	138	177	0.35
2	10.20	93.3	9.15	550	-	-	-	750	132	-	-	-	181	0.1
3	10.20	97.9	9.60	470			750	750	108	-	-	172	172	0.2
4	10.20	143.0	14.02	630	630	610	960	2165	99	99	96	151	340*	0.6
5	10.20	86.7	8.50	360	410	400	-	500	93	106	104	-	130	0.15
6	10.20	88.8	8.71	415	415	415	-	600	105	105	105	-	152	0.15

(a) E is calculated from measured sound velocity, v, and mass density, ρ: $E = v^2\rho$

*eliminated from average, Table 33.

TABLE 31. RESULTS OF TENSILE TESTS ON MELT EXTRACTED FIBERS Ti-6Al-4V PLUS (40Co-20Cr-10Fe) - ALLOY C

Specimen Identification	E,[(a)] 10^6 psi	P/δ, lb/in	Area, $10^{-6}in^2$ $= \frac{P}{\delta} \cdot \frac{L}{E}$	Prop. Limit Load, g	Yield Load Upper Y.P., g	Yield Load Lower Y.P., g	Yield Load 0.2% Off. Set g	Breaking Load g	Prop. Limit, ksi	Yield Strength Upper Y.P., ksi	Yield Strength Lower Y.P., ksi	Yield Strength 0.2% Off. Set, ksi	Ult. Tensile Str., ksi	Elong. in 1", %
1	11.68	154.0	13.18	1000	-	-	1270	1270	167	-	-	212	212	0.2
2	11.68	164.4	14.08	600	600	588	1020	1470	94	94	92	160	230	0.55
3	11.68	114.7	9.82	800	960	920	1020	1130	179	215	206	229	253	0.55
4	11.68	638.4	54.66	1050	-	-	-	1590	42	-	-	-	64*	<0.1
No Ident.	11.68	91.6	7.84	360	-	-	-	500	101	-	-	-	140	~0.1
5	11.68	61.2	5.24	-	-	-	-	255	-	-	-	-	107	<0.1
6	11.68	64.2	5.50	300	-	-	-	440	120	-	-	-	176	0.15
No Ident.	11.68	76.0	6.51	360	455	445	-	466	122	154	151	-	158	0.1

(a) E is calculated from measured sound velocity, v, and mass density, ρ: $E = v^2\rho$

*eliminated from average, Table 33.

TABLE 32. RESULTS OF TENSILE TESTS ON MELT EXTRACTED FIBERS Ti-6Al-4V PLUS TiB_2 - ALLOY D

Specimen Identification	E,(a) 10^6 psi	P/δ, lb/in	Area, $10^{-6}in^2$ $= \frac{P}{\delta} \cdot \frac{L}{E}$	Prop. Limit Load, g	Yield Load			Breaking Load g	Prop. Limit, ksi	Yield Strength			Ult. Tensile Str., ksi	Elong. in 1", %
					Upper Y.P., g	Lower Y.P., g	0.2% Off. Set g			Upper Y.P., ksi	Lower Y.P., ksi	0.2% Off. Set, ksi		
1	16.22	312.5	19.27	3.2 lb	-	-	-	4.47 lb	166	-	-	-	232	0.15
2	16.22	303.0	18.68	1.95 lb	-	-	-	3.88 lb	104	-	-	-	208	0.2
3	16.22	261.8	16.14	2.75 lb	-	-	4.05 lb	4.10 lb	170	-	-	251	254	0.4
4	16.22	289.0	17.82	2.80 lb	-	-	5.2 lb	5.52 lb	157	-	-	292	310	0.55
5	16.22	221.2	13.64	2.50 lb	-	-	3.63 lb	3.68 lb	183	-	-	266	270	0.3

(a) E is calculated from measured sound velocity, v, and mass density, ρ: $E = v^2\rho$

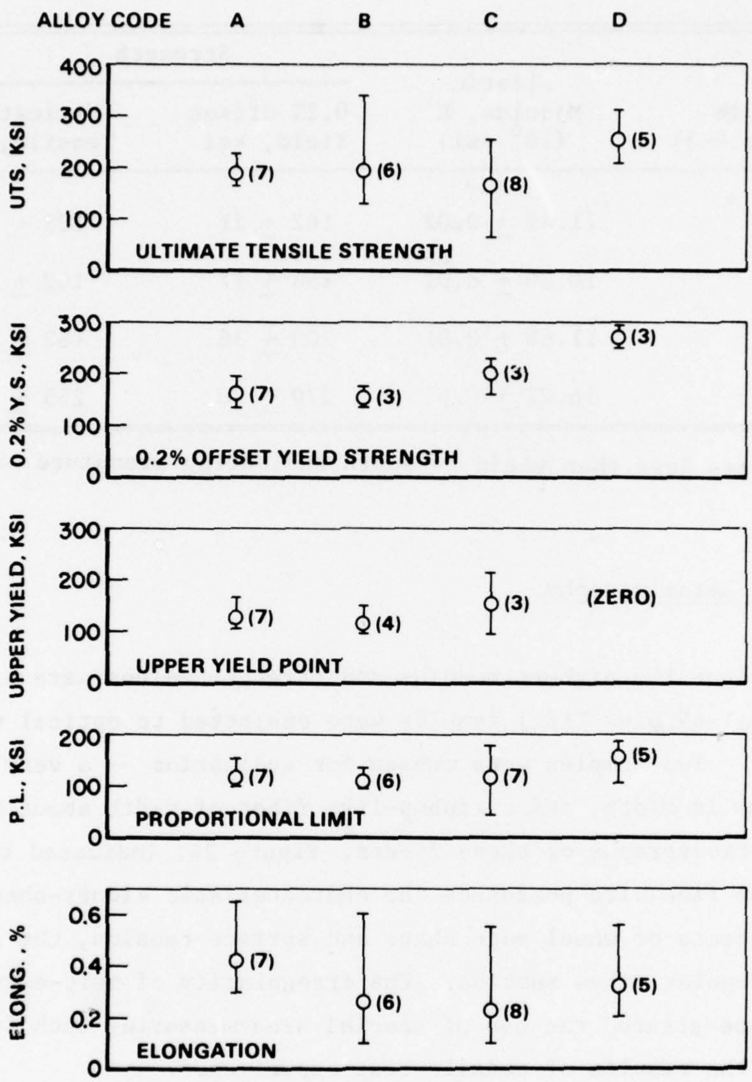

FIGURE 23. TENSILE PROPERTIES OF FOUR "in-situ-MELTED" Ti-6Al-4V-BASE FIBERS. EACH DATUM POINT IS THE AVERAGE OF (n) DETERMINATIONS, AND THE ERRORS ARE INDICATED BY THE BARS.

TABLE 33. SUMMARY OF THE MECHANICAL PROPERTIES OF FOUR "in-situ-MELTED" ALLOYS

Alloy Name (See Table 4-3)	Elastic Modulus, E (10^6 psi)	Strength 0.2% Offset Yield, ksi	Ultimate Tensile, ksi*
A	11.45 $\pm$ 0.02	162 $\pm$ 21	188 $\pm$ 21
B	10.20 $\pm$ 0.01	154 $\pm$ 17	162 $\pm$ 21
C	11.68 $\pm$ 0.01	200 $\pm$ 36	182 $\pm$ 52
D	16.22 $\pm$ 0.02	270 $\pm$ 20	255 $\pm$ 39

*In some cases less than yield strength, indicating premature brittle failure.

(c) Optical Metallography

Since the highest modulus and strength values were exhibited by Alloy (Ti-6Al-4V plus TiB_2) samples were subjected to optical metallographic examination. Two samples were chosen for evaluation -- a very fine wire, about 0.1 mm in width, and a ribbon-like fiber of width about 0.7 mm.

Shadowgraphs of these fibers, Figure 24, indicated that although the fine wire possesses the characteristic kidney-shape resulting from the effects of wheel edge shape and surface tension, the ribbon is of very irregular cross section. The irregularity of melt-extracted profiles necessitated the use of special area-measuring techniques in evaluating the results of tensile-test experiments.

The results of the optical metallography are given in Figures 25 and 26, respectively. The micron-sized precipitate-defined grain structure presumably contributes to the good strength values obtained. The exact nature of the precipitate decorating the grain boundaries has not been determined. In both Figures 25 and 26, however, a significant variation in microstructure is evident along the lengths of the fibers, which reflects a temporal variation in the melt-extraction conditions.

(a)

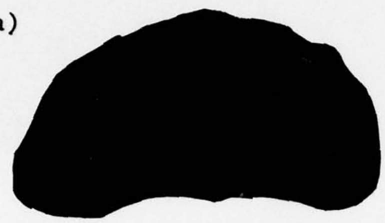

500X

(b)

150X

FIGURE 24. PROFILES OF TWO SAMPLES OF PENDANT DROP MELT-EXTRACTED FIBER -- ALLOY D (Ti-6Al-4V plus TiB_2), (a) WIDTH, 0.1 mm; AREA, 4.9 X 10^{-5} cm^2, (b) WIDTH, 0.7 mm; AREA, 6.8 X 10^{-4} cm^2.

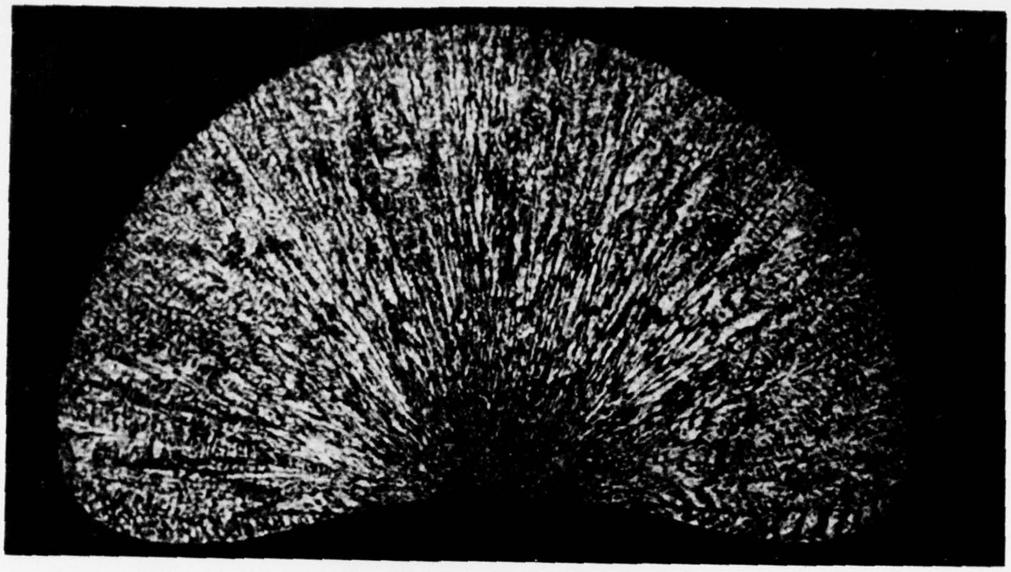

(a) 1000X

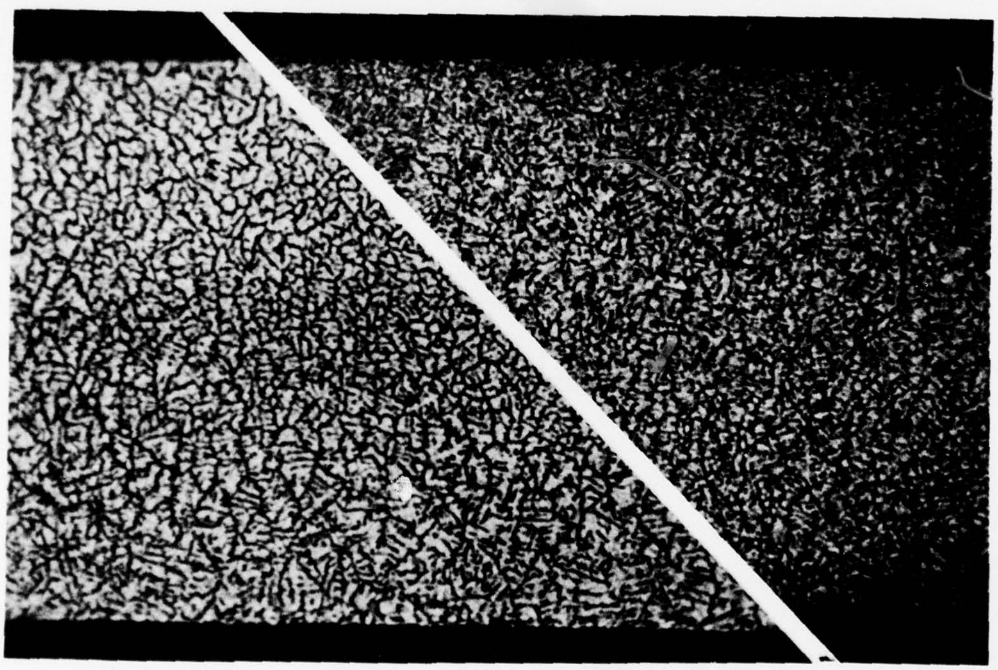

(b) (c)

FIGURE 25. OPTICAL MICROGRAPHS (1000X) OF ALLOY D "FINE WIRE". (a) CROSS SECTION; (b) AND (c) LONGITUDINAL SECTIONS AT TWO POSITIONS ALONG THE LENGTH OF THE FIBER. IN (b) THE CELL DIAMETER IS ABOUT 3 μm

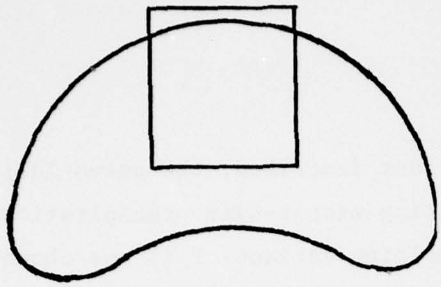

FIGURE 26. OPTICAL MICROGRAPHS (1000X) OF ALLOY D "RIBBON". (a) CROSS SECTION; (b) and (c) LONGITUDINAL SECTIONS AT TWO POSITIONS ALONG LENGTH.

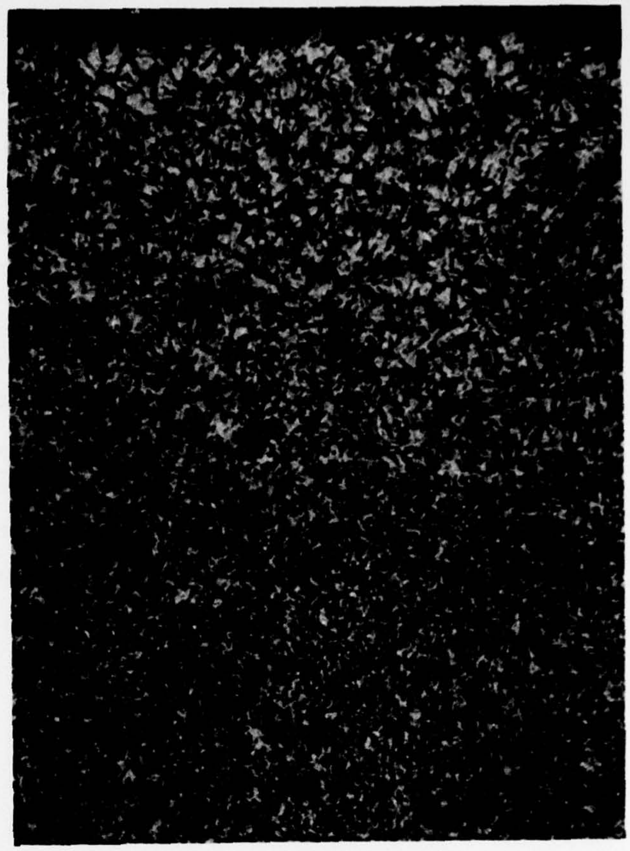

(a) 1000X

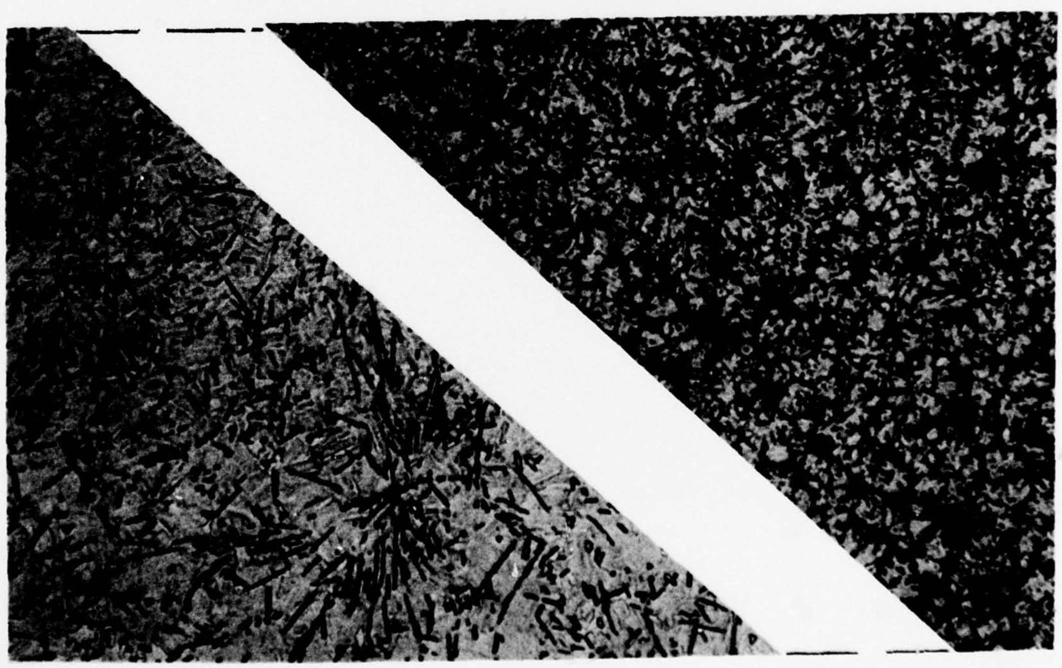

(b) (c)

4.1.5 Conclusion

As a result of the experiments just described, the potentiality of the melt-extraction process for generating micron-size precipitation networks was demonstrated. The in-situ melting variant of it was shown to be a successful screening activity during which several promising additions to the titanium-alloy base, notably Fe, Cu, and B were identified. Accordingly it was decided, as a next step in the polycrystalline program, to use carefully pre-alloyed starting materials whose compositions were based on the earlier findings, and to prepare a final series of strengthened Ti-base alloys for evaluation.

4.2 Diamond Pyramid Hardness Studies of Pre-Melted Solution- and Precipitate-Strengthened Polycrystalline Melt-Extracted Titanium-Base-Alloy Fibers

Fibers of polycrystalline Ti-base alloys were prepared by pendant drop melt extraction, and their mechanical properties examined by microhardness measurement and tensile testing.

4.2.1 Materials Preparation

Five alloys, whose compositions were chosen largely on the basis of the results of the foregoing investigation, were arc melted and drop-cast into rods about 1 cm diameter and 7 cm in length, suitable for installation in the (vacuum) pendant-drop melt extraction equipment. Alloy compositions (weight percent) and melt-extraction-disk rim speeds are given in Table 34.

TABLE 34. LIST OF POLYCRYSTALLINE Ti-BASE ALLOYS PREPARED BY PENDANT-DROP MELT EXTRACTION

Alloy Identification Number	Composition (weight %)	Disk Speed (m/min)
ME-3	80Ti-5.4Al-3.6V-8Fe-3Cu	255-765
ME-4	"	190-255
ME-5	80Ti-5.4Al-3.6V-6Fe-5Cu	255-380
ME-6	"	215-765
ME-7	90.5Ti-1.5Al-1V-6.Si	255-380
ME-8	"	125-830
ME-9	86.4Ti-5.8Al-3.8V-4B	255-1275
ME-10	92.5Ti-1.5Al-1V-3Be-2B	255-510

Of the eight samples of fiber prepared the best three were selected for detailed hardness and tensile testing.

4.2.2 Microhardness Studies

(a) Calibration

In preliminary experiments the influence of load on the measured hardness value was explored -- loads were varied between 25 g and 2.5 kg in a search for reliable and consistent results. Finally it was determined that excellent data could be obtained by using a 25 g load. As indicated in Table 35, measured Vickers Hardness Numbers (VHN's) agreed within experimental precision, with reported values for a standard steel hardness disc.

TABLE 35. ACCURACY OF HARDNESS DATA BY COMPARISON WITH STANDARD HARDNESS DISK

	Load (g)	Number of Impressions	Vicker Hardness No. (kg/mm^2)
Reported	100	--	576
Reported	15	--	597
Measured	25	31	617 ± 30
		27	613 ± 22

(b) Fiber Measurements

Clusters of fibers were mounted vertically in rapidly setting dental resin so that hardness impressions could be made across the transverse sections. On each alloy, some thirty impressions were made using a Leitz "Miniload" hardness tester. Under the load/hardness conditions encountered in the experiments, the diagonal dimensions

of the square-shaped impressions were in the range 6-9 μm. Fiber profiles were as in Figure 24a, with a larger dimension of about 0.2 mm. Since an inter-impression spacing equal to about five impression diameters was selected, some three or four fibers were needed to carry the entire set of thirty impressions. This procedure also gave a little extra significance to the average hardness values which were calculated from the usual expression,

$$H = \frac{1.8544L}{\langle d \rangle^2} \tag{7}$$

where $\langle d \rangle$ is the average of the two indentation diagonals, d1 and d2 (mm)

and L is the load in kg.

The results of a typical hardness measurement are presented in Table 36; and a summary of the results for the three samples selected for investigation, ME-4, ME-6 and ME-10, is given in Table 37. Subsequently in this chapter, the relationship between hardness and tensile strength will be considered.

TABLE 36. HARDNESS DATA, AND VHN's (25 g), FOR MELT EXTRACTED POLYCRYSTALLINE Ti-BASE ALLOY FIBER, ME-4

Diagonal Length (μm)			VHN (kg/mm^2)
d1	d2	<d>	
9.5	8.7	9.1	560
9.3	8.5	8.9	585
9.1	8.3	8.7	612
10.1	8.6	9.35	530*
8.8	8.7	8.75	606
8.6	8.7	8.65	620
8.8	8.7	8.75	606
8.8	8.3	8.55	634
9.0	8.5	8.75	606
9.5	8.7	9.1	560
9.7	8.6	9.15	554
9.2	8.8	9.0	572
9.1	8.8	8.95	579
9.7	9.0	9.35	530*
9.5	8.6	9.05	566
9.5	8.8	9.15	554
9.2	9.3	9.25	542
9.2	8.2	8.7	612
8.7	7.2	7.95	734*
9.1	8.2	8.65	620
9.6	8.8	9.2	548
8.5	7.4	7.95	734*
9.6	8.2	8.9	585
9.4	8.5	8.95	579
9.6	9.2	9.4	525*
9.4	7.6	8.5	642
9.2	8.9	9.05	566
8.7	9.0	8.85	592
9.1	8.3	8.7	612
9.1	8.4	8.75	606
9.2	8.8	9.0	572
Average of 31 values			592 ± 49
Average of 26 (un-starred) values			588 ± 28

TABLE 37. SUMMARY OF HARDNESS VALUES (VHN, kg/mm^2 AT 25 g LOADS) FOR THREE POLYCRYSTALLINE MELT EXTRACTED Ti-BASE ALLOYS

Alloy Name	Number of Hardness Values Accepted	VHN (kg/mm^2) Mean and Standard Error
ME-4	31	592 ± 49
	26	588 ± 28
ME-6	31	546 ± 46
	24	542 ± 30
ME-10	31	680 ± 63
	24	673 ± 43

4.3 Theoretical Relationship Between Hardness and Strength

4.3.1 Theories

In connection with a study of the hardness/strength ratio in metallic glasses, Davis[21] has presented a useful review of the theories of Hill [22] and Marsh [23,24].

The theory of Hill justifies the commonly observed relationship $H \sim 3Y$ between the hardness number, H, and the yield strength, Y. This theory assumed an elastically rigid yet plastic body and thus required the material displaced by the indentor to squeeze up into a rim around the edges of the imprint. The theory of Marsh on the other hand pictures a cavity being pushed into an elastic body, and results in the formula

$$H/Y = C + KB \ln Z \qquad (8)$$

$$\text{and} \quad B = 3/(3 - \lambda)$$

$$Z = 3/(\lambda + 3\mu - \lambda\mu),$$

where

$$\lambda = (1 - 2\nu)\, Y/E$$

$$\mu = (1 + \nu)\, Y/E$$

$$\nu = \text{Poisson's ratio.}$$

$$E = \text{Young's modulus}$$

These two models represent extreme limits of the juxtaposition of E, the elastic modulus, and Y, the yield strength. If E/Y is "large" we have the inelastic/plastic situation of Hill. While if E/Y is not "large" have what might be termed an elastic/nonplastic model. According to Marsh, the cross-over value of the ratio E/Y is 133.

$$\text{Thus if} \quad E/Y > 133 \quad H/Y = 3 \tag{9}$$

$$\text{and if} \quad E/Y < 133 \quad H/Y = C + KB \ln Z$$

$$\text{with} \quad C = 0.28$$

$$\text{and} \quad K = 0.60.$$

Marsh's equation can be simplified considerably by introducing some physically realistic numerical approximations to the quantities referred to.

(i) For many polycrystalline pure metals and alloys $\nu \simeq 0.3$.

(ii) $Y/E \sim 10^{-2}$, for example, for wrought Ti-6Al-4V (Table 3-19)

$Y = 136 \times 10^3$ psi (tensile)

and $E = 14.7 \times 10^6$ psi (tensile)

thus $Y/E = 0.93 \times 10^{-2}$.

(iii) $\lambda = (1-2\nu)\, Y/E \sim 0.4 \times 10^{-2}$

thus $B \simeq 1$.

(iv) $\mu = (1+\nu)\, Y/E \sim 1.3 \times 10^{-2}$

Now $Z = 3/(\lambda + 3\mu - \lambda\mu)$

but $\lambda \sim 0.4 \times 10^{-2}$

$3\mu \sim 4 \times 10^{-2}$

$\lambda\mu \sim 10^{-4}$

Thus $\lambda\mu$ is negligible compared to $\lambda + 3\mu$

hence $Z \sim 3/(\lambda + 3\mu)$

$= 1/\ 1.43\ Y/E$.

(v) $KB \ln Z \sim - K \ln (1.43\ Y/E)$

$= -K \ln 1.43 - K \ln (Y/E)$

$= -0.21 - 0.6 \ln (Y/E)$

Equation (2) thus reduces

to $H/Y = 0.07 + 0.6 \ln (E/Y)$ (10)

If $E/Y = 133$, Equation (10) gives $H/Y = 3.00$ as expected.

4.3.2 Tensile Strengths of Irregular Fibers

The direct measurement of the tensile strengths of fibers of irregular cross-sections is fraught with obvious difficulty. The measurement of cross-sectional area is tedious when the cross-section is of an irregular shape (as for example, in Figure 24). Additional problems can arise if the cross-sectional area varies along the length of the specimen as shown in the accompanying fracture cross-sections taken from the ME-6 fiber, Figure 27. It is much easier if the strength can be derived without recourse to a tensile measurement, and this is the advantage of the hardness procedure in association with equations such as (9) and (10).

Of course, if a tensile measurement is not to be made, we are forced to assume a value for the poisson ratio, ν. It is quite safe to assume $\nu \sim 0.3$. The Young's modulus, E can be determined from a sound velocity measurement at either sonic or ultrasonic frequencies (c.f., Sub-section 3.1.1). Finally, are we to use Hill's or Marsh's formula? The criterion based on E/Y cannot be applied, since Y is the quantity to be determined. Obviously, the Marsh formula must be applied first to obtain a value of Y. If then, $E/Y > 133$, we ignore the result and return to the Hill equation, $Y = H/3$.

Of course in determining Y from experimental values of E and H, Equation (10) must be solved transcendentally, since Y does not occur explicitly. This can be done using the Newton-Raphson method, as indicated below.

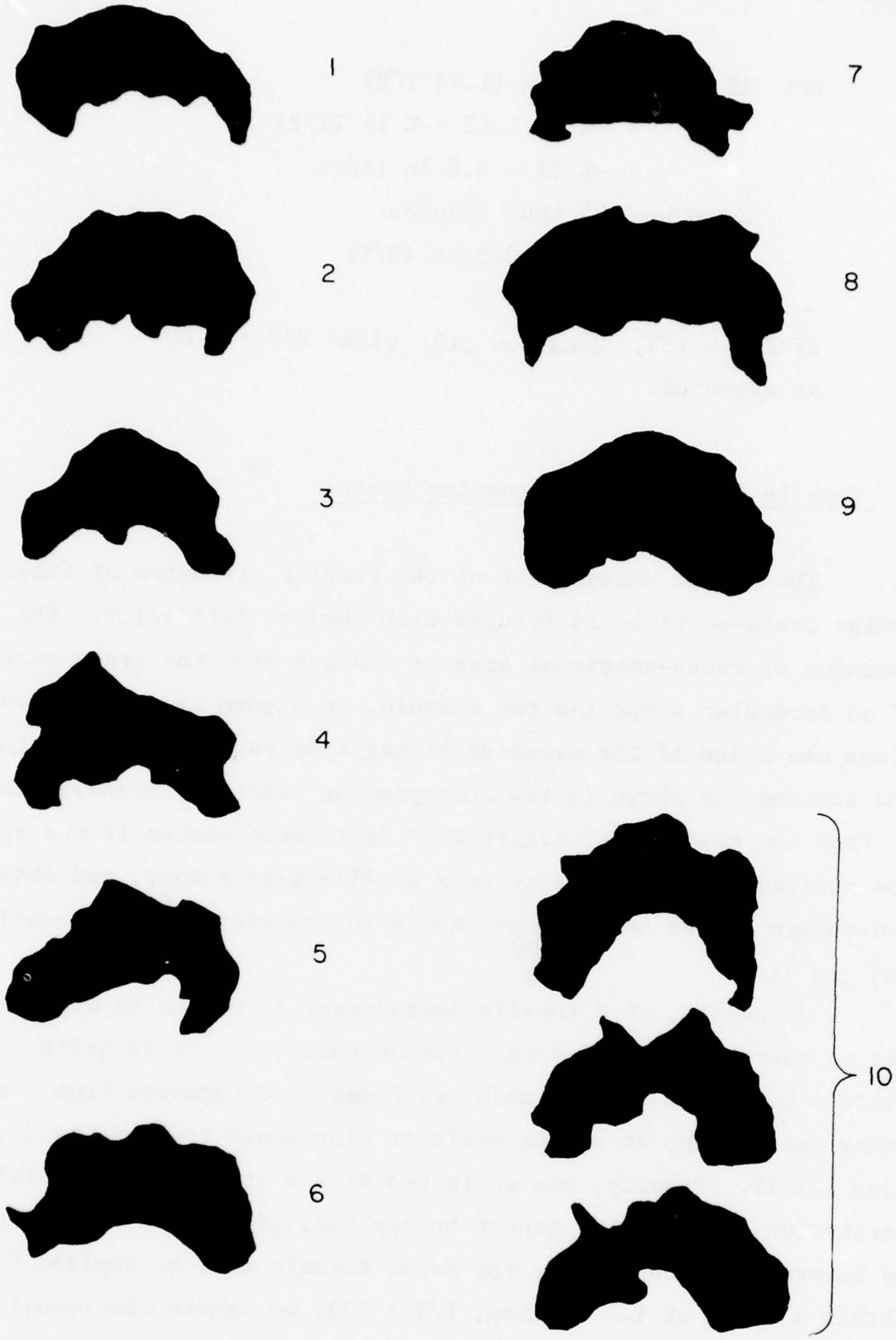

FIGURE 27. SHADOWGRAPHS OF THE FRACTURE CROSS-SECTIONS OF SAMPLE ME-6 (348X).

The tenth sample fractured in two places and both fracture cross-sections are given. The lower pair of figures in '10' represent two determinations of area - which differ by 2-1/2%. The entire set of shadowgraphs gives an indication of the manner in which the sample cross section varies along the length of the fiber. The variation between the upper pair of shadowgraphs in '10' takes place within about 2 cm.

Newton-Raphson Solution of Equation (10)

If X_i approximately satisfies $F(X_i) = 0$, then a better root is X_{i+1} where

$$X_{i+1} = X_i - \frac{F(X_i)}{F^1(X_i)} \quad . \tag{11}$$

By iterating Equation (11) a few times excellent solutions can be obtained.

In the present case we require the root, Y, of the function F(Y) viz. $0.07 - \frac{H}{Y} + 0.6 \ln \frac{E}{Y}$, after inserting values for H and E. Thus by substituting $y = 1/Y$, we iterate

$$y_{i+1} = y_i - \frac{0.07 - Hy + 0.6 \ln Ey}{-H + 0.6/y} \tag{12}$$

4.3.3 Densities of ME-4, 6 and 10

Densities were measured by the immersion method on pieces of the bulk starting ingot. A typical density determination, in this case for ME-4, is given in Table 38, which also includes the results for the other two alloys.

TABLE 38. DENSITIES OF ME-4, 6 and 10

Weight of specimen in air	14.95773 g
Weight of spec.+ suspension in water	11.79545 g
Weight of suspension in water	0.02053 g
Weight of specimen in water	11.77492 g
Loss of weight	3.18281 g
Density of water (20.5°C)	0.9981 g/cc
Volume of specimen	3.18887 cc
DENSITY OF ME-4, Detm.1	4.691 g/cc
Detm.2	4.695 g/cc
Detm.3	4.696 g/cc
DENSITY OF ME-6, Detm.1	4.686 g/cc
Detm.2	4.686 g/cc
DENSITY OF ME-10	4.326 g/cc

4.3.4 Elastic Moduli of ME-4, 6 and 10

Longitudinal acoustic wave velocities were measured at the Air Force Materials Laboratory (AFML) through the courtesy of Dr. H. L. Gegel, Air Force Program Monitor, and converted into Young's modulus numbers, E, through the usual formula $v = \sqrt{E/\rho}$, where ρ is the density. The results of this work are summarized in Table 39.

4.3.5 Estimated Yield Strengths of ME-4, 6 and 10

The results of applying the measured hardness and modulus values to Marsh's formula, viz.;

$$H/Y = 0.07 + 0.6 \ln (E/Y), \qquad (10)$$

in order to obtain an estimated yield strength are given in Table 40.

TABLE 39. SOUND VELOCITIES AND YOUNG'S MODULI FOR ME-4, 6 AND 10

Quantity	ME-4	ME-6	ME-10
Sound Velocities, v (km/s)	4.172	3.636	5.365
	3.988	3.633	5.364
	4.016	3.639	5.345
	4.135	3.971	
	4.039	3.964	
	4.049	3.779	
		3.751	
Average v (km/s)	4.067	3.768	5.358
Densities (g/cc)	4.694	4.686	4.326
Young's Modulus, E (10^3kg/mm^2)	7.76	6.65	12.42
E (ksi)	11.04	9.46	17.66

TABLE 40. ESTIMATED YIELD STRENGTHS OF ME-4, 6 and 10 USING MARSH'S FORMULA, EQUATION 4-3

Alloy Name	VHN, H (kg/mm^2)	Modulus, E ($10^3 kg/mm^2$)	Estimated Yield Strength, Y		$\frac{E}{Y}$	$\frac{H}{Y}$	$\frac{E}{H}$
			kg/mm^2	ksi			
ME-4	588 $\pm$ 28	7.76	287 $\pm$ 20	408 $\pm$ 28	27	2.1	13.2
ME-6	542 $\pm$ 30	6.65	273 $\pm$ 22	388 $\pm$ 31	24	2.0	12.3
ME-10	673 $\pm$ 43	12.42	289 $\pm$ 25	411 $\pm$ 36	43	2.3	18.5

We make note of the following points:

(a) ME-10 is harder, and possesses a considerably higher modulus than ME-4 and 6. This is presumably related to the as-quenched microstructure, which although it has not been examined as yet is assumed on the basis of composition (Table 34) to be alpha + transformed beta (martensite) in ME-4 and 6, but only alpha (i.e., free of martensite) in ME-10.

(b) The quotients E/Y, H/Y and E/H again reflect the presumed microstructural differences between ME-4 and 6 as an alloy class, and ME-10.

(c) H/Y which has the value $\sim$2.0 for the ME-4, 6 pair and 2.3 for ME-10 is considerably less than the usually expected value of 3 or more. It will be interesting, as a test of Marsh's formula, to determine whether this is a reflection of an unrealistically high value of Y or whether $Y_{exp.}$ will agree with the estimated value. Experimental measurements of the tensile strengths are considered in the next section.

4.4 Tensile Test Measurements on Pre-Melted, Strengthened, Polycrystalline Melt-Extracted Titanium-Base-Alloy Fibers

4.4.1 Experimental Procedures

In preliminary tests in which untreated as-spun fibers were mounted in conventional wire-holding grips, fracture at the grips generally occurred. In order to optimize the ratio of successful to unsuccessful tests some thought was given to improving the techniques of grip mounting and sample surface conditioning. As far as the latter is concerned, we felt that the same amount of care should be applied to preparing a wire sample for test as is usually given a test bar or plate. In other words, a gauge length free of crack-initiating surface imperfections should be prepared.

Our solution to the grip problem, although unsophisticated, was adequate for the determination of ultimate tensile stress. Wire samples were epoxyed into the shanks of "eye-ended" solder lugs -- ribbon samples into the flattened shanks of the same kind of lug. To facilitate handling right up to the time that the tensile test actually began, the lugs themselves were attached to a C-shaped cardboard yoke, as shown in Figure 28 in the case of a ribbon sample.

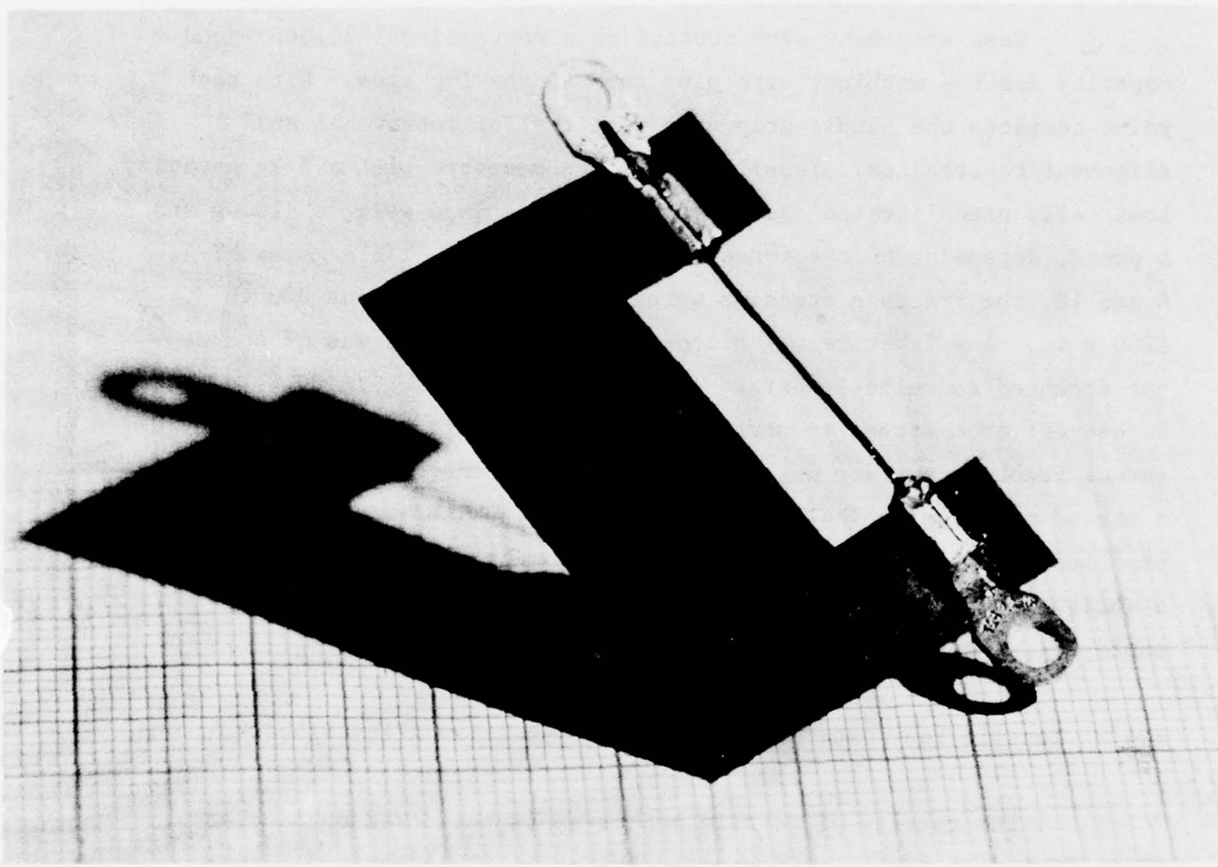

FIGURE 28. RIBBON SAMPLE MOUNTED IN PREPARATION FOR TENSILE TEST. PHOTOGRAPHED AGAINST mm-SQUARE PAPER.

In order to clean the samples and remove roughness they were treated along their entire lengths with dilute HCl. After mounting, a gauge length was produced by swabbing the center portion of the 2.5cm long specimen with full-strength Kroll's reagent (ASTM #187*). This procedure was also used to adjust the cross-sectional area, in cases where the tensile stress exceeded the capacities of either the load cell or the epoxy in the grips.

Test specimens were mounted in a conventional 20,000 pound capacity Instron machine, with pins through the lug eyes. With such point contacts the sample grip ends were free of rotational and alignment constraints. Tensile stress was measured with a 2 kg capacity load cell, precalibrated against a pair of standard weights (100 g and 1 pound, depending on the force range of interest). In samples ME-4, 6 and 10, the fracture stresses were in the range of about 800 to 1200 g wt. Any fracture which took place at the grips was of course not accepted as reliable data. A head rate of 0.002 in/min was used. To convert from stress to strength, the cross-sectional area of the actual fracture surface was measured <u>via</u> measurement of the area of a traced metallographically obtained profile. With irregularly profiled fibers, such as those obtained by melt extraction, no other technique is possible, especially when a thinned gauge length is employed. A set of fiber profiles was given in Figure 27.

4.4.2 Tensile Test Data for Three Polycrystalline Alloy Fibers

The results of tensile measurements performed on samples ME-4, ME-6, and ME-10 are presented in Tables 41, 42 and 43 and summarized in Table 44.

---

* Kroll's reagent: 10 ml HF, 30 ml HNO_3, 50 ml H_2O, applied with Q-tip to center portion of sample.

We have already shown (Figure 28) that the fiber samples exhibit considerable nonuniformity of cross-section. Quantitatively (Table 44) this amounts to some 17 percent cross-sectional area variation in ME-4 and 6; and 34 percent in ME-10, on account of two excessively thick portions.

Referring again to Table 44, we note the high strengths of ME-4 and 6, whereas that of ME-10 is some 30 percent lower. The reason for this has to do with differences in ductility. ME-4 and 6 can be bent through acute angles without breakage, while ME-10 is brittle and possesses little bend ductility. We believe that ME-10 always fractured prematurely and thus failed to fully realize its potential strength as estimated from hardness studies.

TABLE 41. RESULTS OF TENSILE TESTS ON MELT EXTRACTED TITANIUM-BASE ALLOY FIBER - I

SAMPLE : ME-4

STRAIN RATE: 0.002 in/min

Specimen Number	Area of Fracture Surface		Fracture Load (kg)	Strength	
	10^{-6} in^2	10^{-3} mm^2		kg/mm^2	ksi
1	7.4341	4.796	1.135	236.7	336.6
2	10.5861	6.830	1.418	207.6	295.3
3	10.0055	6.455	1.140	176.6	251.2
4	7.9321	5.117	1.098	214.6	305.2
5	8.0745	5.209	0.998	191.6	272.5
6	8.2956	5.352	1.250	233.6	332.2
7	8.4001	5.419	1.210	223.3	317.6
8	7.6283	4.921	1.340	272.3	387.3
9	7.3356	4.733	1.246	263.3	374.5
10	6.4452	4.158	1.105	265.8	378.0
11	6.0748	3.919	1.020	260.3	370.2
12	6.7380	4.347	1.230	283.0	402.5
13	6.9830	4.505	1.230	273.0	388.3

Average Area $5.06 \pm 0.84 \times 10^{-3}$ mm^2

Average Strength 239 ± 34 kg/mm^2

340 ± 48 ksi

TABLE 42. RESULTS OF TENSILE TESTS ON MELT EXTRACTED TITANIUM-BASE ALLOY FIBER - II

SAMPLE : ME-6

STRAIN RATE: 0.002 in/min

Specimen Number	Area of Fracture Surface		Fracture Load (kg)	Strength	
	10^{-6} in^2	10^{-3} mm^2		kg/mm^2	ksi
1	6.3437	4.093	1.205	294.4	418.7
2	8.0426	5.189	1.080	208.1	296.0
3	5.8607	3.781	1.005	265.8	378.1
4	6.8187	4.399	1.310	297.8	423.6
5	6.6066	4.262	1.045	245.2	348.7
6	7.4750	4.823	1.218	252.5	359.1
7	5.9274	3.824	0.860	224.9	319.9
8	9.7446	6.287	1.258	200.1	284.6
9	9.6679	6.237	1.318	211.3	300.5
10	7.9291	5.116	1.175	229.7	326.7
10	7.3206	4.723	"	248.8	353.9
10	7.5138	4.848	"	242.4	344.8

<u>Average Area</u> $4.80 \pm 0.82 \times 10^{-3}$ mm^2

<u>Average Strength</u> 243 ± 31 kg/mm^2

346 ± 45 ksi

TABLE 43. RESULTS OF TENSILE TESTS ON MELT EXTRACTED TITANIUM-BASE ALLOY FIBER - III

SAMPLE : ME-10

STRAIN RATE: 0.002 in/min

Specimen Number	Area of Fracture Surface		Fracture Load (kg)	Strength	
	10^{-6} in^2	10^{-3} mm^2		kg/mm^2	ksi
1	12.4742	8.048	0.730	90.7	129.0
2	5.4185	3.496	0.700	200.2	284.7
3	6.4811	4.181	0.752	179.9	255.9
4	11.1089	7.167	0.885	123.5	175.7
5	6.0021	3.872	0.702	181.3	257.9
6	7.5885	4.896	0.894	182.6	259.7
7	7.6204	4.916	0.890	181.0	257.4
8	5.5769	3.598	0.694	192.9	274.4
9	5.4335	3.505	0.704	200.9	285.7

Average Area 4.85 ± 1.67 mm^2

Average Strength 170 ± 38 kg/mm^2

242 ± 54 ksi

TABLE 44. SUMMARY OF TENSILE DATA FOR SAMPLE ME-4, 6 and 10

Sample Name	Average Area of Fracture Surface	Average Strength	
	10^{-3} mm^2	kg/mm^2	ksi
ME-4	5.06 ± 17%	239	340 ± 14%
ME-6	4.80 ± 17%	243	346 ± 13%
ME-10	4.85 ± 34%	170	242 ± 22%

4.4.3 Experimental Relationship Between Hardness and Strength for the ME-4, 6 and 10 Fibers

Table 45 compares the measured ultimate tensile strength with a yield strength computed from the measured hardness number. For ME-4 and ME-6 we note agreement to within slightly more than one standard error; while, as indicated above, ME-10 fails to achieve its expected strength potential due to premature brittle failure. The results shown in the table confirm the validity of hardness results, in association with the modified Marsh formula for estimating yield strengths in "difficult" materials.

TABLE 45. COMPARISON OF MEASURED TENSILE STRENGTH COMPARED WITH YIELD STRENGTH CALCULATED FROM HARDNESS NUMBER BY THE METHOD OF SUBSECTION 4.3.2

Alloy Name	Hardness kg/mm^2	Computed Yield Strength, kg/mm^2	Measured Ultimate Strength, kg/mm^2
ME-4	588 ± 28	287 ± 20	239 ± 34
ME-6	542 ± 30	273 ± 22	243 ± 31
ME-10	673 ± 43	289 ± 25	170 ± 38

4.5 Specific Strengths of ME-4, 6 and 10

In Table 46, the specific strengths of the three alloys under discussion are compared with data due to Tanner and Ray[25] for some commercial metallic glass fibers. We note that the specific strengths of ME-4 and 6 are greater than that of the strongest known metallic glass ribbon fiber, and close to that of Ti-Be-Zr, the metallic glass with the highest known specific strength.

TABLE 46. SPECIFIC STRENGTH (STRENGTH/DENSITY) OF POLYCRYSTALLINE FIBERS COMPARED WITH THOSE OF SOME COMMERCIAL METALLIC GLASS FIBERS[25]

Sample Name†	Hardness (kg/mm^2)	Strength (kg/mm^2)	Density (g/cm^3)	Specific Strength (10^5 cm)
ME-4	588	239	4.694	50.9
ME-6	542	243	4.686	51.9
ME-10	673	170	4.326	39.3
2615	835	249	7.30	34.1
2826A	880	278	7.46	36.9
2605	1100	370	7.40	50.0
2204	740	231*	4.13	56.0

* Calculated from hardness/3.2.

† Compositions

ME-4, ME-6, ME-10 } see Table 34, p. 89.

Metglas 2615 $Fe_{80} P_{16} C_3 B_1$

Metglas 2826A $Ni_{36} Fe_{32} Cr_{14} P_{12} B_6$

Metglas 2605 $Fe_{80} B_{20}$

Metglas 2204 $Ti_{50} Be_{40} Zr_{10}$

4.6 Tensile Strength versus Area Correlations in ME-4, 6 and 10

Close examination of the data of Tables 41, 42, and 43 suggested that a correlation existed between tensile strength and fracture surface area. Plots of the data showed clearly that strength decreased monotonically with increasing fiber diameter, while a least-squares analysis of strength *versus* reciprocal area led to the results summarized in Table 47.

TABLE 47. STRENGTH-AREA CORRELATIONS

Alloy	Strength-Area Relation*	Correlation Coefficient
ME-4	$\sigma(\text{ksi}) = 1.899 \times 10^{-3} \left(\frac{1}{A}\right) + 91.3$	0.76
ME-6	$\sigma(\text{ksi}) = 1.775 \times 10^{-3} \left(\frac{1}{A}\right) + 108.8$	0.81
ME-10	$\sigma(\text{ksi}) = 1.2495 \times 10^{-3} \left(\frac{1}{A}\right) + 61.5$	0.92

*Units of area, A, in^2.

The observed strength/thickness relationship is probably traceable to the expected variation of quench rate with thickness. As noted in Subsection 2.5.2 the quench rate varies with the inverse thickness squared. Factors which tend to enhance the strengths of rapidly-quenched fibers deteriorate as the quench rate is lowered in samples of greater thickness.

SECTION V

METALLIC GLASS COMPOSITION SELECTION AND STRUCTURE

In selecting alloying components for processing into metallic glass candidates we were guided by the results of numerous published studies. Several heuristic theories exist for the selection of alloys which have a high probability of metastable existence, at room temperature, in an amorphous state. Some models are geometrical, some chemical, while others rely on thermodynamic principles. No serious attempt at systematization has been made, and the question of amorphous versus glassy has not yet been specifically addressed, although electronic bonding is obviously an important parameter. The two classes of bond which exist in electronically conducting solids are (a) metallic and (b) covalent. The first is relatively isotropic compared to the highly directional covalent bond found in semiconductors, ceramics, and organic solids. Metallic bonding with covalent character is to be found in intermetallic compounds formed between metals of widely differing electronegativity (c.f., Nbl.Mtl.-Mtld. glasses). The highly directional metallic bond exists in metallic glasses; however, the atoms have arranged themselves in such a way that the solid does not support a complete network of covalent-like bonds; but rather a characteristic mixture of metallic and directional-metallic bonds.

In describing the structures of metallic glasses three important models have been considered. They are: the microcrystalline model; the random shell model; and the modified Bernal dense random packing model. It is through a consideration of these models that an essential difference between "amorphous" and "glassy" may develop.

In this program we produced some conventional as well as some "advanced" metallic glasses. But in addition we sought to proceed beyond the matter of glass stability as such in order to develop some high specific strength fibers.

Desirable mechanical properties generally consist of a combination of high modulus, strength, and fracture toughness. In designing the elastic modulus, the properties of equilibrium phases can be of some assistance. For guidance we can look for systems

possessing a strong A-B bond (or large heat of solution or compound formation); and which when crystalline are associated with intermetallic compounds characterized by high elastic moduli or Debye temperatures. On the other hand, the deformation properties of metallic glasses[26] are more elusive. As is the case with crystalline alloys the composition dependences of strength and fracture toughness tend to be masked by pronounced microstructural effects.

The principles of strengthening in crystalline alloys have been considered briefly in an earlier section. An important procedure is 'solution strengthening' with suitable dissolved foreign atoms. We attempted to explore the metallic glass equivalent of this by studying the effect of various alloying additions, such as B and Si, both separately and in combination, on the hardness of a well-established metallic glass base, for which role $Fe_{80}P_{13}C_7$ was selected.

5.1 Systematics of Metallic Glass Stability (Existence Theorems)

5.1.1 Geometrical Considerations

Nowick and Mader[27] seem to have been the first to discuss amorphous stabilization through atomic size difference between the constituents of a binary alloy. It is well known that space filling by a close-packed assembly of spheres is improved if size difference is permitted. This result is expected to carry over to the random-close-packing configuration. Size difference should also inhibit atomic interdiffusion, and thus should contribute to the stabilization of an amorphous structure once it has been formed. This situation is parallel to one which occurs when chemical A-B bonding (or electronegativity) rather than size difference is the dominant parameter, since an energy barrier must again be overcome in proceeding to the crystalline from the as-quenched amorphous state. In this connection it is also interesting to note, following Bennett[28], that the operation of short-range pair potentials favors the formation of groupings of regular tetrahedra. As these are not crystal-building units the short-range nearest-neighbor-type interactions are conducive to

glass formation[29]. Of course, if such a material should crystallize, the same interactions confer extreme brittleness on the resulting, generally two-phase, intermetallic-compound-containing crystalline structure.

Interactions between atoms tend to be more important than 'size effect' itself. However, it has been pointed out in a recent review paper by Takajama[10] that selecting constituents with about 10-20 percent atomic size difference remarkably extended the composition range of otherwise favorable combinations of atomic types. Large atomic size difference also, apparently, significantly increases the ease of formation and stability of amorphous alloys.

In an early discussion on amorphous structures, Cohen and Turnbull proposed that the ideal <u>monatomic</u> glass structure could be described by a Bernal dense random packing model. In support of this Finney[30], in a now-famous experiment using wax-coated ball bearings, was able to obtain an 'experimental' pair distribution function which agreed reasonably well with a function subsequently computed by Cargill[31]. Next, Polk[32] suggested that for metal-metalloid glasses the metalloid atoms simply filled the larger holes belonging to the Bernal DRP. A subsequent calculation led to a most satisfactory and significant result -- if metalloid atoms are inserted into all the larger holes in the DRP, they would amount to some 21 at.%, which is close to the eutectic composition for some alloys!

5.1.2 Considerations of Alloy Chemistry -- Atomic Interactions

The presence of a deep eutectic in the phase diagram is generally considered to be an indicator of conditions (constitutional and compositional) favorable to metallic glass existence. In the vicinity of the eutectic metallic glass tends to be retained during quenching, since crystallization is confined to a temperature regime within which the kinetics of diffusion are relatively slow.

This situation has been discussed recently by Marcus and Turnbull[33] according to whom the glass-forming tendency generally increases with ΔT, the temperature difference between the actual

liquidus and the ideal-solution liquidus. Thus "abnormally deep" eutectics should be better glass formers than "normal" eutectics.

In a review of splat cooling Jones[34] has constructed a diagram which displays the many binary alloys which have been prepared by that technique during the period 1958-1972. Of course, not all of those studied were in the amorphous state. By now it is possible to identify certain groups of elements which, when rapidly quenched from the vapor or melt, may retain the amorphous structure. Figure 29 is one attempt att systematization. Suitable metallic-glass combinations may be derived by selecting nearest-neighbor pairs of atoms from the cyclically arranged sequence.

As indicated in Figure 29, the following classes of atom may, in binary combination, yield conditions favorable to metallic glass stability:

(a)	RE	-	LTM	e.g., Gd-Co
(b)	ETM	-	LTM	e.g., Zr-Co
(c)	LTM	-	Mtld.	e.g., Co-P
(d)	Mtld.	-	Nbl.M	e.g., Si-Au
(e)	Nbl.M	-	ETM	e.g., Cu-Zr

where:

RE	=	rare earth metal
LTM	=	late transition metal (Group VIII of periodic table)
ETM	=	early transition metal (Groups III through IV)
Mtld.	=	metalloid
Nbl.M	=	noble metal

The interactions thought to be responsible for metallic-glass stability in some of these combinations are discussed below.

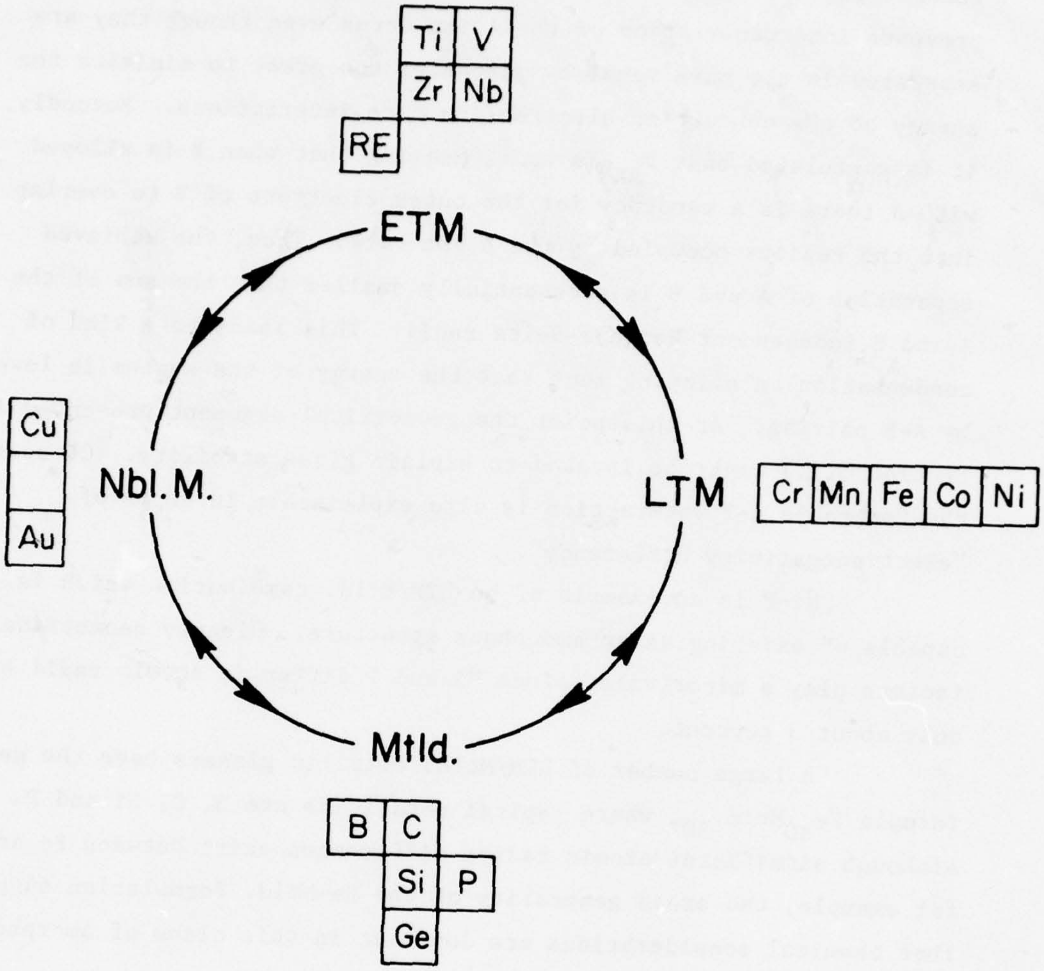

FIGURE 29. CYCLIC DIAGRAM FOR THE SELECTION OF METALLIC GLASS CANDIDATE ALLOY CONSTITUENTS

(a) Noble Metal/-, or Late Transition Metal/Metalloid Combinations

Turnbull[35] has discussed the metallic glass-forming propensity of noble-metal (or late transition metal) (A)/metalloid (B) combinations in terms of interatomic pair potentials. Firstly, as is generally

recognized, V_{AA} is characterized by a hard repulsive component, which prevents interpenetration of the A ion cores even though they are separated in the pure metal by distances too great to minimize the energy of the conduction-electron/ion core interactions. Secondly, it is postulated that V_{AB} is soft, meaning that when B is alloyed with A there is a tendency for the outer electrons of B to overlap into the regions occupied by the A ion core. Thus, the achieved separation of A and B is substantially smaller than the sum of the A and B independent Weigner-Seitz radii. This leads to a kind of condensation on alloying such that the energy of the system is lowered by A-B pairing. At this point the geometrical argument presented in Section 5.1.1 might be invoked to explain glass stability. Of course, the favorable A-B interaction is also explainable in terms of "electronegativity difference".

Ni-P is an example of an LTM/Mtld. combination which is capable of existing as an amorphous structure. Clearly geometrical factors play a minor role, since Ni and P differ in atomic radii by only about 3 percent.

A large number of LTM/Mtld. metallic glasses have the general formula $Fe_{80}Mtld._{20}$, where typical metalloids are B, C, Si and P. Although significant atomic radius differences exist between Fe and B, for example, the broad generality of the Fe-Mtld. formulation suggests that chemical considerations are dominant in this class of amorphous alloy.

The soft-interaction argument suggests that in looking for glass-forming additions to a given element one should seek alloying elements which, when in solid solution, lower rather than raise, the lattice parameter. Si, for example, decreases the lattice parameter of Ni. For Ti the lattice parameter is reduced by the addition of any of the late transition elements V, Cr, Mn and Fe. Since Ti-V, Cr, Fe are clustering systems[36] it is tentatively concluded that a competition between A-B condensation and the tendency to cluster inhibits crystallization. Al also reduces the lattice parameter of Ti, but Ti-Al is a short-range ordering system and there is no question of its being considered as a metallic-glass candidate.

(b) Inter-Transition-Metal Combinations

Experience has shown that combinations of early transition metals and late transition metals yield amorphous alloys. Since considerable size differences as well as electronic differences exist, the dominant glass-stabilization mechanism is as yet unknown for this class of alloy. We do know, however[27], that either the smaller or the larger element may play the role of "host". Examples of glass-forming binary transition-metal combinations are $Nb_{0.66}Ni_{0.34}$ to $Nb_{0.23}Ni_{0.77}$.

Giesson and Wagner[37] have pointed out that amorphous phase formation is promoted if the competing equilibrium phases have complex structures with high coordination numbers and widely differing atomic arrangements; such as the highly electron/atom ratio sensitive σ-phase and related phases. Thus, inter-transition metal combinations with average electron/atom ratios in the vicinity of 6 to 7 should yield σ-phase-based transition-metal-binary metallic glasses.

(c) Transition-Metal/Noble-Metal Combinations

Here we consider an amorphous A-B alloy in which A is an ETM and B is a noble metal. Although there are alternative ways of describing the systematics of this combination, it does follow naturally from the ETM/LTM situation discussed above, by replacing the late transition element with a noble metal.

Examples of this are Ti-Cu and Zr-Cu. The Ti-Cu alloys embody many of the characteristics and properties of metallic-glass stability discussed above. Firstly, the phase diagram exhibits numerous intermetallic compounds (favorable A-B interaction) and the system is eutectoidal. Thus, in spite of the presence of some line compounds which exist up to the liquidus, compositional ranges exist over which the liquid phase (and hence, perhaps, the amorphous phase) is relatively stable. Secondly, according to structural studies[38], the atomic volumes of the intermediate phases, from Cu_3Ti throught $CuTi_3$, are from 8-13 percent less than the stoichiometric

average of the atomic volumes of the constituents in their pure crystalline states. Thus, Ti-Cu, like the TM/Mtld. glass formers is a "volume condensation system".

5.2 Alloy Selection

In selecting components we were frequently guided by the LTM/Mtld. formulation, and also a desire to prepare experimental glasses based on ETM/Nb1.M and ETM/LTM combinations. In selecting compositions we were in some cases guided by reports of alloys which had already been successfully prepared in metallic glass form. The components and compositions of particular alloys prepared for fiber production by melt extraction and melt spinning, and for splat quenching and sputtering, are listed in Table 48.

5.2.1 Recent Special Alloys

In a recent paper, Tanner and Ray[25] have discussed compositions and properties of a family of Ti-Zr-Be metallic glasses recently prepared by liquid quenching at rates $>10^5$ deg/sec, at the Allied Chemical Corporation's Materials Research Center. As indicated in Figure 30, the formation zone of amorphous Ti-Zr-Be is a band of maximal width equivalent to about 30 at.% Be located between the binary eutectics $Ti_{62.5}Be_{37.5}$ and $Zr_{65}Be_{35}$. The results of density and hardness measurements have been reported, the latter being found to increase from 480 to 780 kg/mm^2 with increasing Be content. Since the Be-rich alloys have low densities, this system has given rise to the highest specific strength yet discovered in metallic glasses. The optimal composition, considered from the standpoints of properties and ease of production, $Ti_{50}Be_{40}Zr_{10}$ (METGLAS 2204), was characterized[25] by:

hardness	740 kg/mm^2
yield strength	240 kg/mm^2
Young's modulus	10.7×10^3 kg/mm^2
density	4.1 g/cm^3.

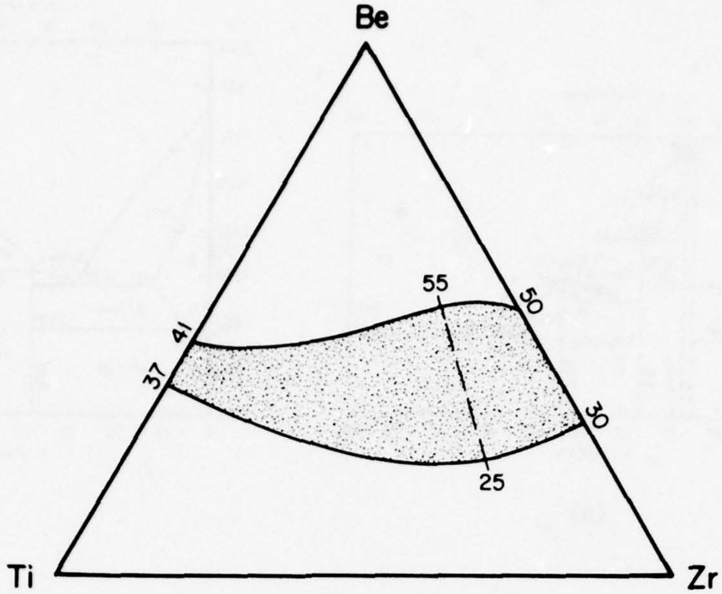

FIGURE 30. SKETCH REPRESENTING THE COMPOSITIONAL REGIME WITHIN WHICH Ti-Be-Zr METALLIC GLASSES MAY BE PRODUCED BY RAPID QUENCHING. NUMBERS REFER TO ATOMIC PERCENT Be - AFTER TANNER AND RAY[25]

A possible disadvantage of this family of alloys is the high Be content, with possible toxic hazards attendant upon its production and application. More recently, Giessen and his colleagues and students at Northeastern University have reported some of the results of an extensive investigation of Ti-rich amorphous alloys whose compositions include elements such as Ni, Fe, Cu, Al and Zr, the purpose of which was again to develop alloys of high specific strength[39]. A particularly interesting family is Ti-Ni-Si.

As indicated in Figure 31, Ti-Ni and Ti-Si possess eutectics at 995°C, 25 at %Ni and 1330°C, 14 at.%Si. These give rise to a eutectic trough in the ternary phase diagram, (indicated crudely in Figure 32) and an accompanying zone of metallic-glass stability defined approximately by

$$Ti_{80-40}Si_{10}Ni_{10-50}$$

$$Ti_{80-70}Si_{15}Ni_{5-15}$$

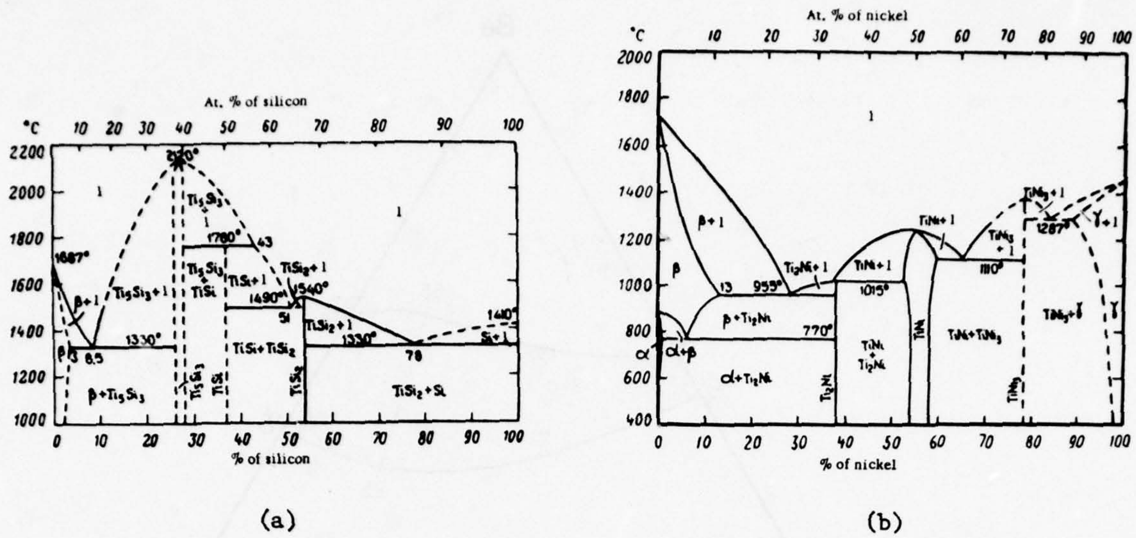

FIGURE 31. PHASE DIAGRAMS FOR (a) Ti-Ni, AND (b) Ti-Si SHOWING THE EXISTENCES OF TWO RATHER DEEP EUTECTICS

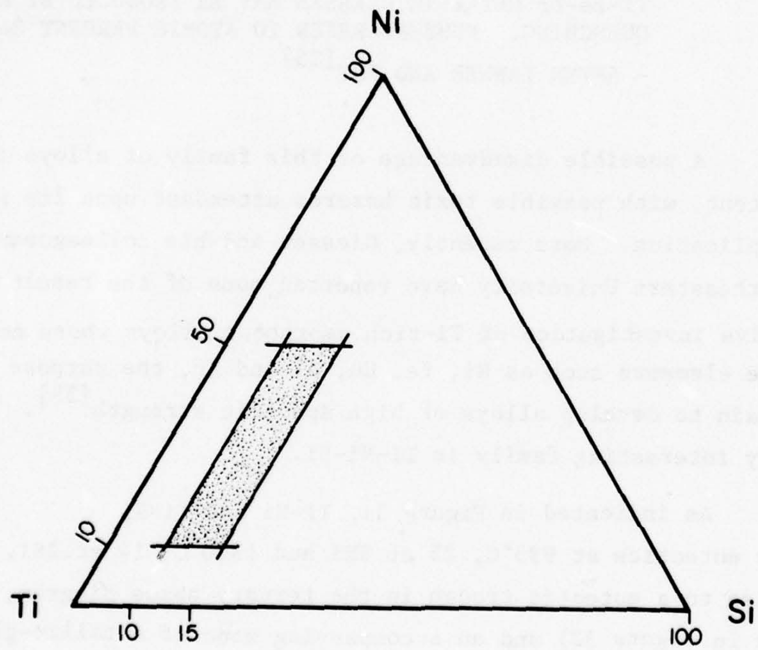

FIGURE 32. SKETCH OF A TERNARY PHASE DIAGRAM FOR Ti-Ni-Si INDICATING ROUGHLY THE REGIME OF EXISTENCE OF AMORPHOUS COMPOSITIONS (ON THE ASSUMPTION THAT SUITABLE QUENCHING PROCEDURES ARE APPLIED)

In fact, Giessen has reported melt-spinning $Ti_{60-55}Ni_{30}Si_{10-15}$ to form metallic-glass ribbons[39]. In the light of these recent results we decided to introduce the following set of alloys into our program:

$$Ti_{60}Ni_{30}Si_{10}$$

$$Ti_{55}Ni_{30}Si_{15}$$

5.2.2 Prospective Metallic Glass Compositions Prepared in This Program By Various Quenching Techniques

Metallic glass alloy samples were prepared in fiber form by pendant-drop melt extraction and melt spinning; in the form of splats by several standard techniques; and by sputtering, either conventionally, or by a high-rate procedure. A list of the materials prepared is given in Table 48.

TABLE 48. COMPOSITIONS OF METALLIC GLASS ALLOYS PREPARED UNDER THIS PROGRAM

Sample Code	Composition	Preparation Technique
S-1	$Fe_{84}B_{16}$	• Sputtering/room temperature
S-1	"	• Splat quenching - gun
1	$Fe_{80}B_{20}$	• Splat - rotating disk
1	"	• Melt extraction - continuous
1	"	• Melt extraction - L/D powder
MS-15	"	• Melt spinning
2	$Fe_{80}Ge_{20}$	• Melt extraction - continuous
2	"	• Splat quenching - disk
6	$Zr_{43}Cu_{57}$	• Melt extraction - continuous, vacuum
6	"	• Melt extraction - continuous, oil-quench
MS-17	"	• Melt spinning
MS-16	$Ni_{50}B_{50}$	• Melt spinning
7	$Ti_{30}Cu_{70}$	• Melt extraction - continuous, oil-quench
S-6	$Ti_{34}B_{66}$	• Sputtering/room temperature
S-5	$Ti_{93}B_{7}$	• Sputtering/room temperature
9	$Ti_{60}Ni_{30}Si_{10}$	• Melt extraction - continuous
10	$Ti_{55}Ni_{30}Si_{15}$	• Melt extraction - continuous
S-7	$Fe_{80}P_{13}C_{7}$	• High-rate sputtering/water quench
S-8	"	• High-rate sputtering/LN quench
MS-7	"	• Melt spinning
S-2	$Fe_{75.2}Cr_{19.6}B_{5.2}$	• Sputtering/room temperature
S-2	"	• Anvil splat quenching

TABLE 48. continued

3	$Fe_{75}B_{10}S_{15}$	• Melt extraction - continuous, vacuum
3	"	• Melt extraction - continuous, oil quench
3	"	• Melt extraction - L/D powder
3	"	• Splat quenching - disk
5	$Fe_{75}Ge_{10}Si_{15}$	• Melt extraction - continuous
5	"	• Melt extraction - continuous, oil quench
4	$(Fe_{22}Ni_{78})_{75}B_{10}Si_{15}$	• Melt extraction - continuous, vacuum
4	"	• Melt extraction - continuous, air
4	"	• Melt extraction - continuous, air, water quench
4	"	• Melt extraction - continuous, vacuum, oil quench
4	"	• Splat quenching - disk
MS-13	$(FeNi)_{80}B_{20}$	• Melt spinning
S-3	$Fe_{73}Cr_{2.5}B_{24.5}$	• Sputtering/room temperature
S-3	"	• splat quenching - gun
S-4	$Fe_{11.2}Cr_{7.5}B_{81.3}$	• Sputtering/room temperature
MS-19/FPCB-2	$Fe_{80}P_{11.7}C_{6.3}B_{2}$	• Melt spinning
MS-20/FPCB-5	$Fe_{80}P_{9.8}C_{5.3}B_{5}$	• Melt spinning
MS-21/FPCB-7	$Fe_{80}P_{8.5}C_{4.5}B_{7}$	• Melt spinning
MS-22/FPCB-10	$Fe_{80}P_{6.5}C_{3.5}B_{10}$	• Melt spinning
MS-23/FPCS-2	$Fe_{80}P_{11.7}C_{6.3}Si_{2}$	• Melt spinning
MS-24/FPCS-5	$Fe_{80}P_{9.8}C_{5.3}Si_{5}$	• Melt spinning
MS-25/FPCS-7	$Fe_{80}P_{8.5}C_{4.5}Si_{7}$	• Melt spinning
MS-26/FPCS-10	$Fe_{80}P_{6.5}C_{3.5}Si_{10}$	• Melt spinning
MS-27/FPCSB-2	$Fe_{80}P_{11.7}C_{6.3}Si_{1}B_{1}$	• Melt spinning
MS-28/FPCSB-5	$Fe_{80}P_{9.8}C_{5.3}Si_{2.5}B_{2.5}$	• Melt spinning
MS-29/FPCSB-7	$Fe_{80}P_{8.5}C_{4.5}Si_{3.5}B_{3.5}$	• Melt spinning
MS-30/FPCSB-10	$Fe_{80}P_{6.5}C_{3.5}Si_{5}B_{5}$	• Melt spinning

SECTION VI

SPUTTERING STUDIES

In support of the metallic-glass melt-quenching segment of this program, investigations of sputtered materials were carried out under subcontract at the University of Rochester; and also through the courtesy of Dr. S. D. Dahlgren, at Battelle's Pacific Northwest Laboratory (BNW), using the high-rate sputtering equipment[1].

Materials prepared by sputtering are listed in Table 49.

TABLE 49. LIST OF SPUTTERED ALLOYS

Sample Code	Composition	Supplier
S-1	$Fe_{84}B_{16}$	Rochester
S-2	$Fe_{75.2}Cr_{19.6}B_{5.2}$	"
S-3	$Fe_{73}Cr_{2.5}B_{24.5}$	"
S-4	$Fe_{11.2}Cr_{7.5}B_{81.3}$	"
S-5	$Ti_{93}B_{7}$	"
S-6	$Ti_{34}B_{66}$	"
S-7	$Fe_{80}P_{13}C_{7}$/Water-Cooled Cu Substrate	BNW
S-8	$Fe_{80}P_{13}C_{7}$/LN-Cooled Cu Substrate	BNW

The work at Rochester was intended partly as a screening program, since if sputtering does not result in the amorphous structure, then certainly liquid quenching will not. However, relatively few alloys were prepared, and none were delivered to Battelle for property evaluation. The work carried out at BNW by Dr. Dahlgren's group turned out to be of greater value to us in that we were able to obtain through sputtering

massive samples (3.8 cm diam. X ~0.25 mm thick) of amorphous ultra-rapidly quenched $Fe_{80}P_{13}C_7$, whose properties we could compare with those of ribbon fiber melt spun from the same starting ingot.

6.1 Electrical Resistivity Studies of Sputtered Films

Electrical resistivity temperature dependences over the temperature range 0 to 650 degrees C, were carried out under an inert atmosphere. Only relative measurements of resistivity were made, the outputs from the potential leads attached to the sample and the furnace thermocouple being connected to the Y and X terminals of a recorder, as indicated in Figure 33.

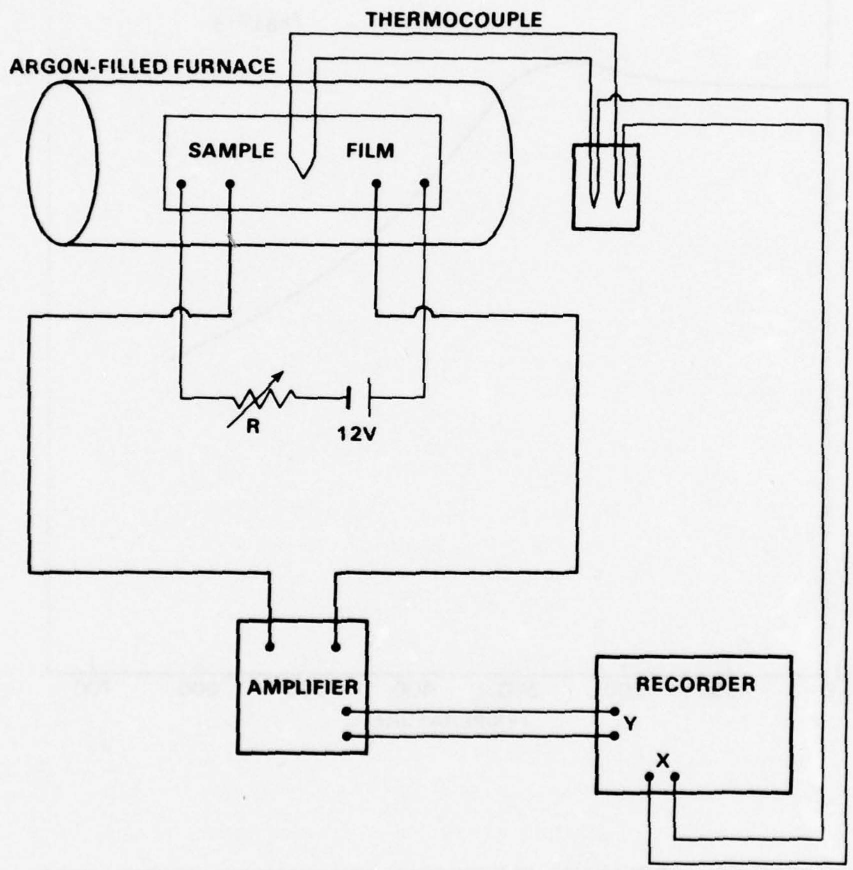

FIGURE 33. APPARATUS USED FOR THE MEASUREMENT OF THE RELATIVE RESISTIVITY TEMPERATURE DEPENDENCES OF SPUTTERED FILMS

The results of electrical resistivity measurements carried out on Samples S-1, S-2 and S-5 (after sputtering on both Al_2O_3 and fused quartz substrates, resp.) are presented in Figures 34, 35, 36, and 37 are discussed below in the context of structure and stability.

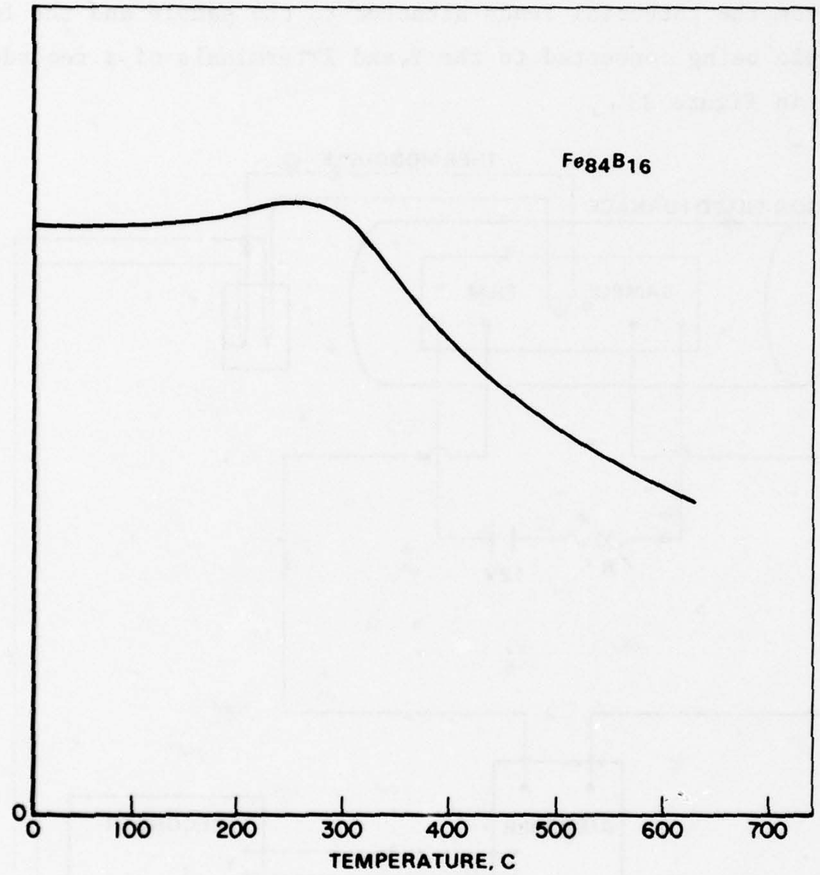

FIGURE 34. RELATIVE ELECTRICAL RESISTIVITY TEMPERATURE DEPENDENCE OF SAMPLE S-1 (SPUTTERED ONTO Al_2O_3 SUBSTRATE)

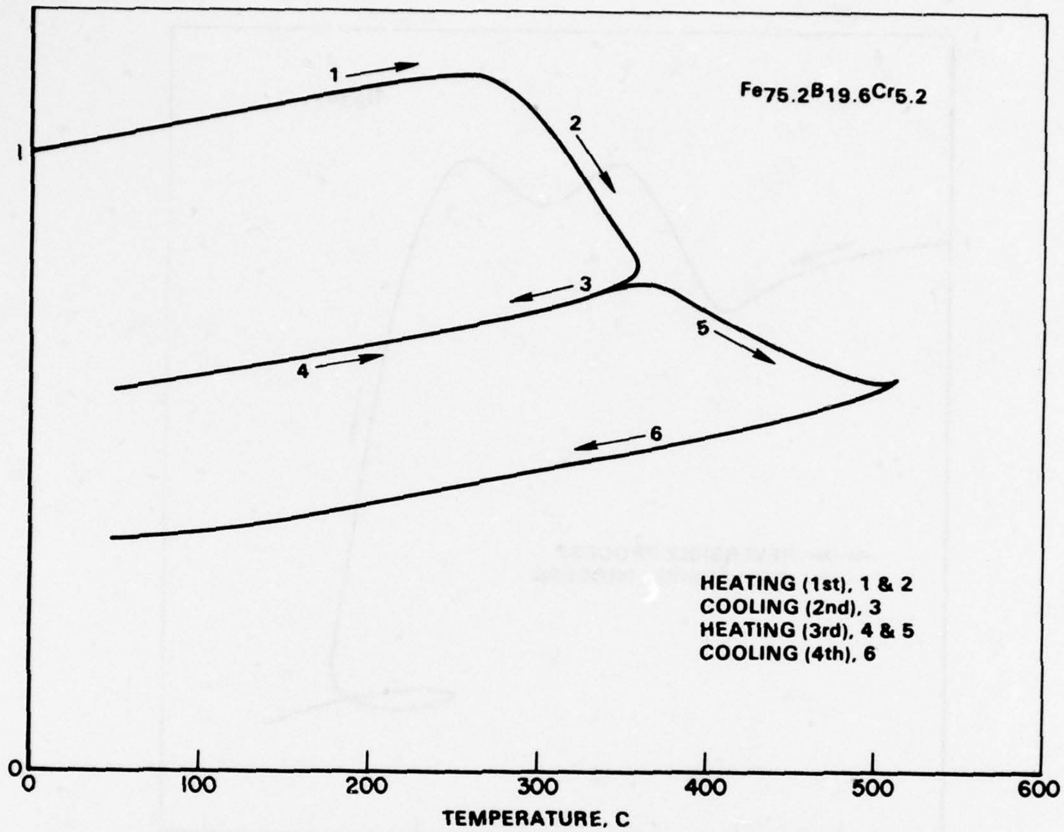

FIGURE 35. RELATIVE ELECTRICAL RESISTIVITY TEMPERATURE DEPENDENCE OF SAMPLE S-2

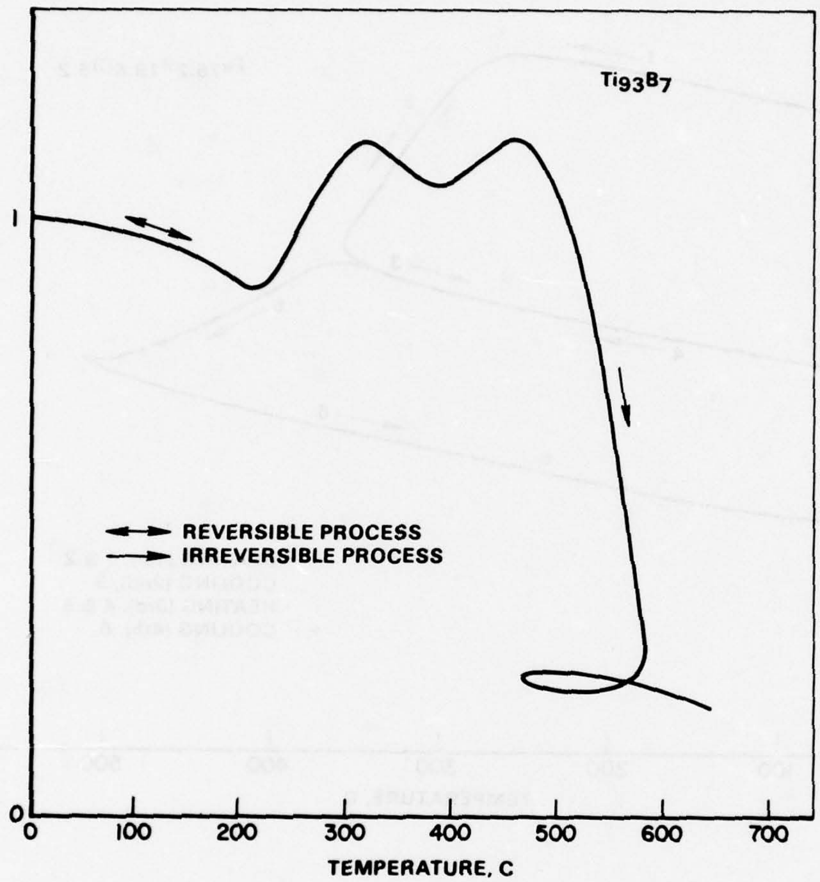

FIGURE 36. RELATIVE ELECTRICAL RESISTIVITY TEMPERATURE DEPENDENCE OF SAMPLE S-5 (SPUTTERED ONTO Al_2O_3 SUBSTRATE)

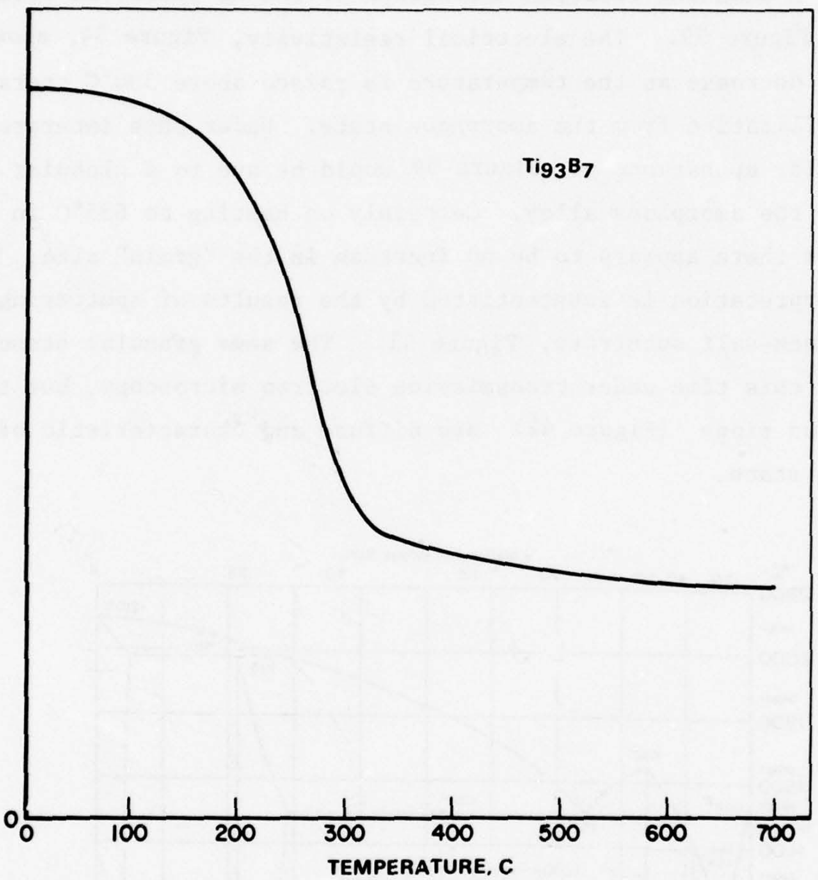

FIGURE 37. RELATIVE ELECTRICAL RESISTIVITY TEMPERATURE DEPENDENCE OF SAMPLE S-5 (SPUTTERED ONTO FUSED QUARTZ SUBSTRATE)

6.2 Electrical Resistivity and Structure of $Fe_{84}B_{16}$ (Sample S-1) Films

The phase diagram of Fe-B, Figure 38 possesses two eutectic points. Because of the lower melting point, it was decided first of all to study the morphology of the iron-rich eutectic alloy $Fe_{84}B_{16}$. Two substrates were selected -- Al_2O_3 and cleaved rock-salt.

A scanning electron micrograph of the as-sputtered film is given in Figure 39. The electrical resistivity, Figure 34, shows an abrupt decrease as the temperature is raised above 300°C characteristic of crystallization from the amorphous state. Under this interpretation, the granular appearance of Figure 39 would be due to a globular condensation of the amorphous alloy. Certainly on heating to 635°C in an argon atmosphere there appears to be no increase in the "grain" size, Figure 40. This interpretation is substantiated by the results of sputtering onto a cleaved rock-salt substrate, Figure 41. The same granular structure is observed, this time under transmission electron microscopy, but the electron diffraction rings (Figure 42) are diffuse and characteristic of the amorphous state.

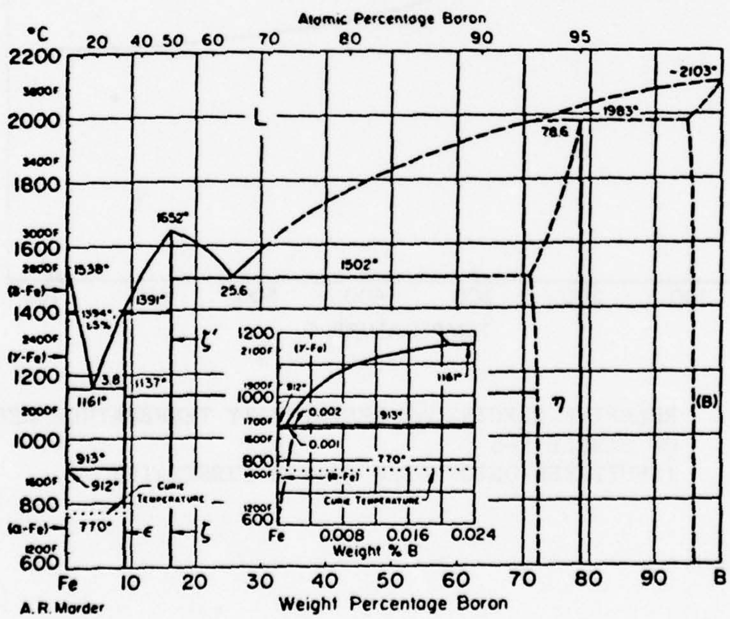

FIGURE 38. EQUILIBRIUM PHASE DIAGRAM OF Fe-B

FIGURE 39. SCANNING ELECTRON MICROGRAPH OF $Fe_{84}B_{16}$ (S-1) SPUTTERED ONTO Al_2O_3 SUBSTRATE X1800

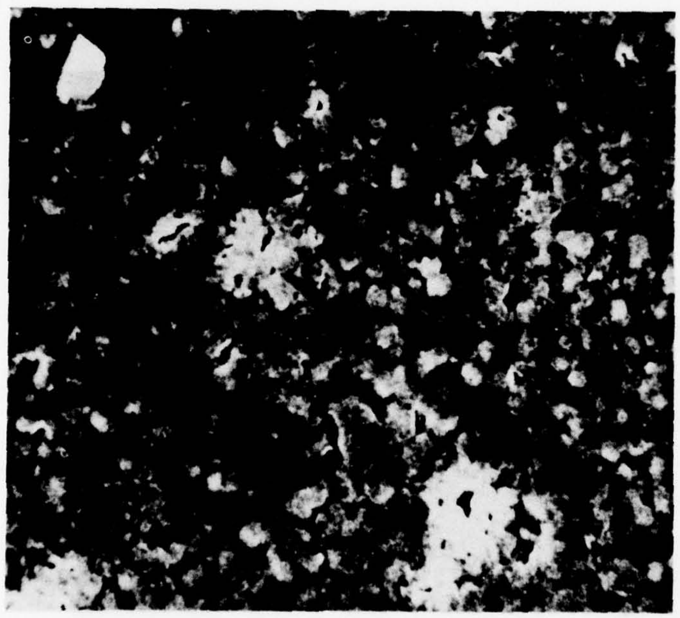

FIGURE 40. SCANNING ELECTRON MICROGRAPH OF $Fe_{84}B_{16}$ (S-1) SPUTTERED ONTO Al_2O_3 SUBSTRATE AND HEATED TO 635°C IN AN ARGON ATMOSPHERE X1800

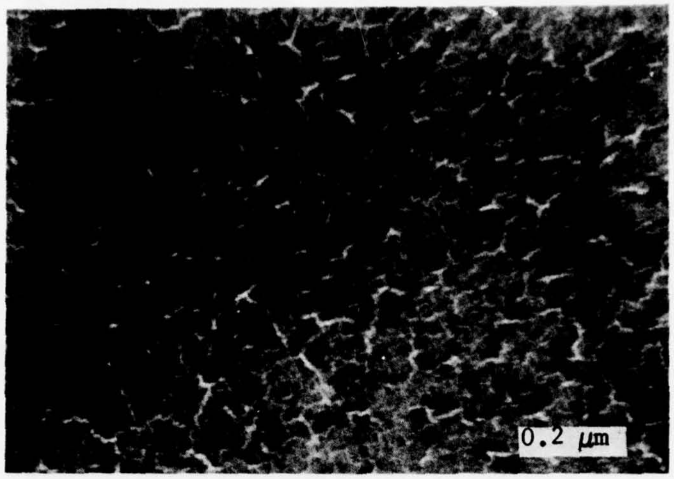

FIGURE 41. TRANSMISSION ELECTRON MICROGRAPH OF $Fe_{84}B_{16}$ (S-1) SPUTTERED ONTO CLEAVED ROCKSALT

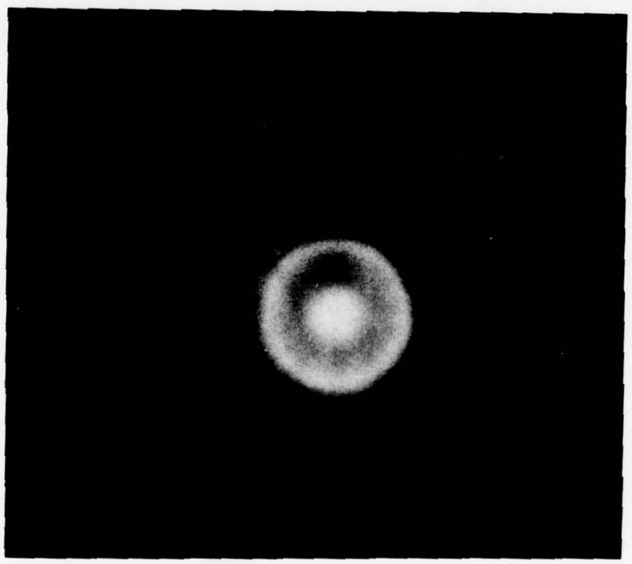

FIGURE 42. ELECTRON DIFFRACTION PATTERN CORRESPONDING TO THE TRANSMISSION MICROGRAPH SHOWN IN FIGURE 41

6.3 Electrical Resistivity Characteristics of Samples S-2, S-3 and S-4

The electrical resistivity-temperature characteristic of S-2 was given in Figure 35. A possible interpretation is that crystallization of the as-deposited amorphous structure sets in above about 275°C, but that the transformation is not complete at least below 500°C. Alternatively, the parallelism of the three lower-temperature branches suggests a Mattheissen's law type of behaviour -- in other words a crystalline solid with three different levels of defect or impurity scattering.

The resistivity temperature dependence of S-3 (not shown), also exhibited hysteresis, with the drop in resistivity occurring at about 350°C.

Sample S-4, on the other hand, gave a negative resistivity temperature dependence (not shown) with very little hysteresis.

The structural states of these films, either in the as-deposited or heat-treated conditions, was not investigated.

6.4 Electrical Resistivities and Structures of $Ti_{93}B_7$ (Sample S-5)

The phase diagram of Ti-B (Figure 43) shows two eutectic compositions, one at the Ti-rich end and the other at the B-rich end. The Ti-rich composition, the deeper eutectic, was chosen for this investigation, and sputtering was carried out onto Al_2O_3, fused quartz and rock-salt substrates.

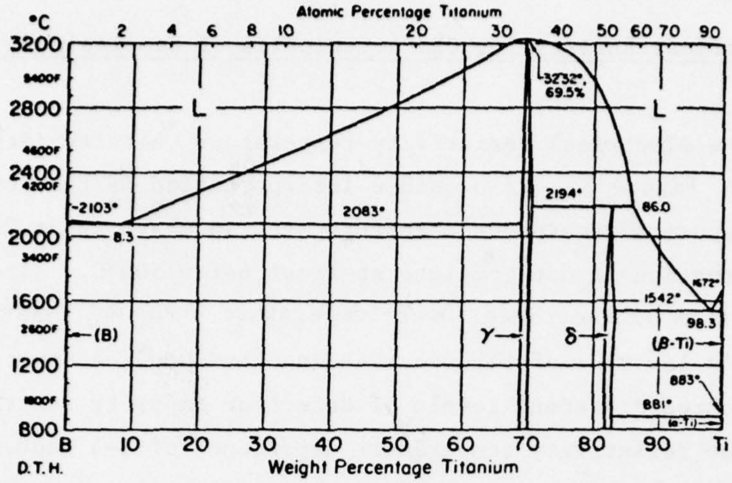

FIGURE 43. EQUILIBRIUM PHASE DIAGRAM OF B-Ti

6.4.1 Deposition of S-5 onto an Al_2O_3 Substrate

Figure 44 is a scanning electron micrograph of the results of sputtering onto an Al_2O_3 substrate, whose surface texture, after gold plating, is shown in Figure 45. The granular or globular structure of the 3 μm thick alloy film seems to replicate that of the plated (~ 100 Å) alumina substrate surface. This result also suggests that the globular structure previously noted in Sample S-1 (Figure 39) may also be nothing more than a replication of the surface texture of the substrate, rather than a demonstration of polycrystallinity.

The results of resistivity temperature dependence measurements Figure 36 indicated the occurrence of a drastic change at about 500°C. Although other structural transformations may explain this behaviour, this effect is most likely due to crystallization of an amorphous alloy, during which some increase in the globule size took place as a result of grain growth, Figure 46.

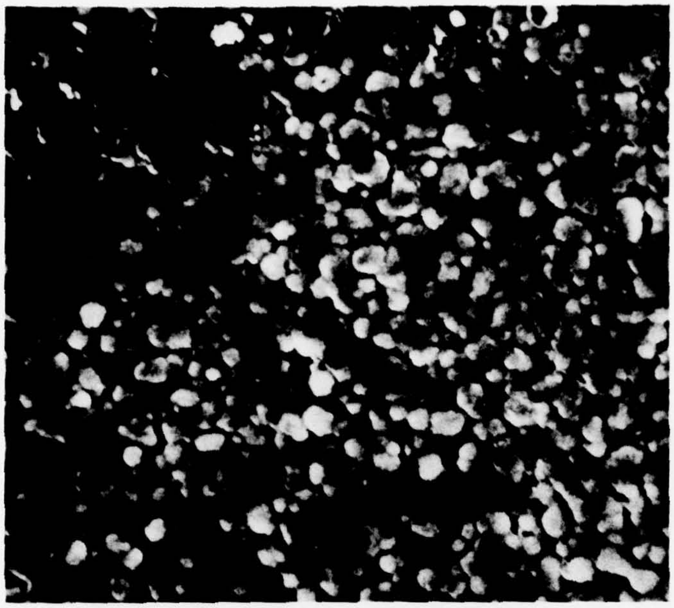

FIGURE 44. SCANNING ELECTRON MICROGRAPH OF $Ti_{93}B_7$ (S-5) SPUTTERED ONTO Al_2O_3 SUBSTRATE X1800

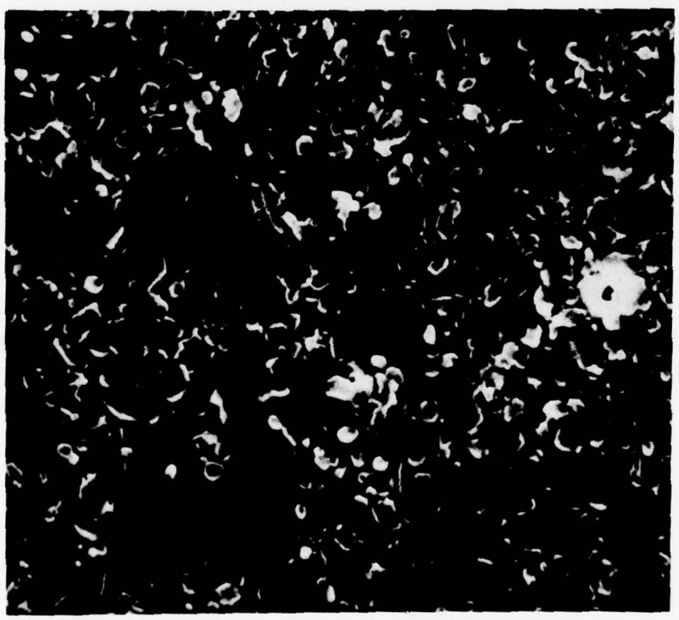

FIGURE 45. SCANNING ELECTRON MICROGRAPH OF GOLD-PLATED Al_2O_3 SUBSTRATE SURFACE X1800

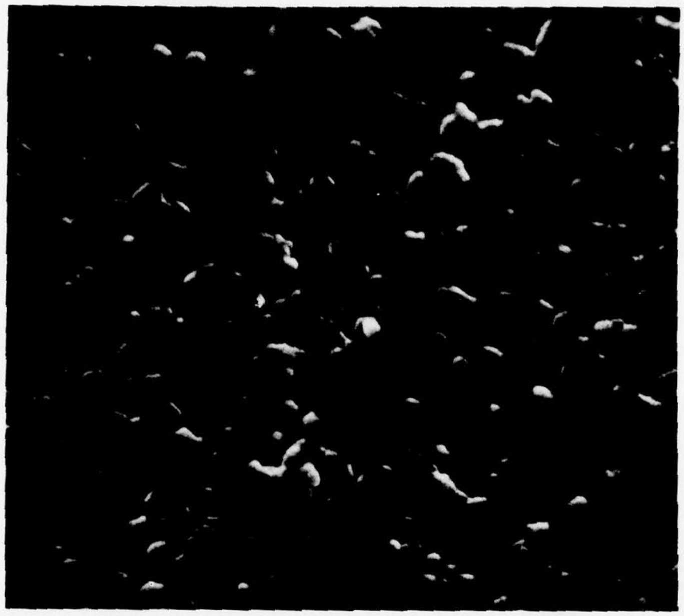

FIGURE 46. SCANNING ELECTRON MICROGRAPH OF $Ti_{93}B_7$ (S-5) SPUTTERED ONTO Al_2O_3 AND HEATED TO 580°C IN AN ARGON ATMOSPHERE X1800

6.4.2 Deposition of S-5 onto a Fused Quartz Substrate

In order, to clarify the situation with regard to the influence of substrate structure on layer morphology, Alloy S-5 was this time sputtered onto a fused quartz substrate. It was predicted that the glassy substrate would not initiate the kind of globularity previously noted with regard to sputtering onto the crystalline saphire substrate (Figure 44), and indeed this turned out to be the case. The films exhibited no surface structure at all. The results of electrical resistivity measurements, Figure 37, showed a transformation taking place as the temperature increased above about 200°C. The behaviour is comparable to that taking place in S-1 (Figure 34) and in the initial part of the R(T) curve for S-5/Al_2O_3 (Figure 36). Presumably S-1, and both of the S-5 samples were amorphous in the as-sputtered condition.

6.4.3 Structures of Sample S-5 By Transmission Electron Microscopy and Electron Diffraction

In order to be suitable for transmission electron microscopy metallic films must be thin (about 1000 Å for 100 kv electrons) and detached from their substrates. In preparation for the electron-transmission experiments, therefore, films were sputtered onto a cleaved rock-salt surface. As a substrate for the purpose, rocksalt has the advantages of being water soluble, of low vapor pressure and of requiring no preparation other than cleavage. It does, however, have certain disadvantages, viz. it has a finite ionic electrical conductivity, which interferes with measurements of film resistivity; its crystalline structure is likely to effect an ordering of the deposited atoms; and it can be chemically reactive.

The results of TEM carried out on Alloy S-5 after removal from a rock salt substrate, Figure 47, show no evidence of grain boundaries. Furthermore, the electron diffraction pattern, Figure 48, consists of the broad diffraction rings characteristic of an amorphous solid. After heating in-situ to 700°C crystallization appeared to take place, Figure 49. Indeed, by doing electron diffraction from one of the dark

patches of the apparent two-phase structure (Figure 50) evidence for crystallinity, in the form of sharp diffraction spots, was noted.

FIGURE 47. TRANSMISSION ELECTRON MICROGRAPH OF $Ti_{93}B_7$ (S-5, 1000 Å THICK) SPUTTERED ONTO CLEAVED ROCK SALT

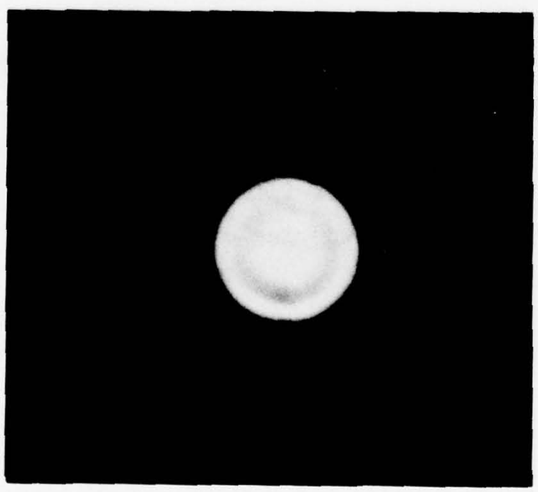

FIGURE 48. ELECTRON DIFFRACTION PATTERN CORRESPONDING TO FIGURE 47

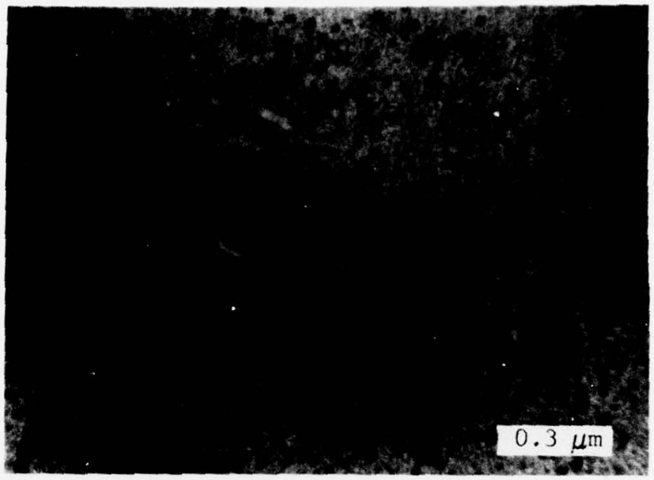

FIGURE 49. TRANSMISSION ELECTRON MICROGRAPH OF $Ti_{93}B_7$ (S-5) SPUTTERED ONTO A CLEAVED ROCK SALT SUBSTRATE AND HEATED TO 700°C

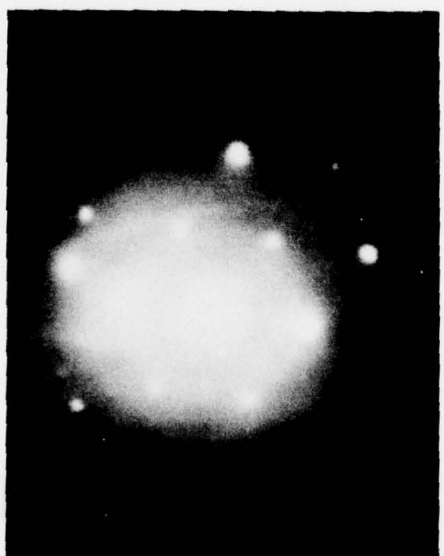

FIGURE 50. ELECTRON DIFFRACTION PATTERN CORRESPONDING TO THE TEM SHOWN IN FIGURE 49

6.5 Structures of a Non-Eutectic Sputtered Alloy (Sample S-6)

After showing that the eutectic alloy $Ti_{93}B_7$ could be produced in the amorphous state it was decided to explore the possibility of preparing a high melting point, non-eutectic, alloy in such a state. The γ-phase intermetallic compound $Ti_{34}B_{66}$ (see Figure 43) was selected for this investigation, and sputtered onto both fused quartz and cleaved rock salt substrates.

The alloy when sputtered onto fused quartz appeared to have no grain structure, Figure 51. However, during heating to 450°C, the nucleation of small grains seems to take place, Figure 52. The appearance of the alloy after sputtering onto a rock salt substrate was suggestive of microcrystallinity, Figure 53.

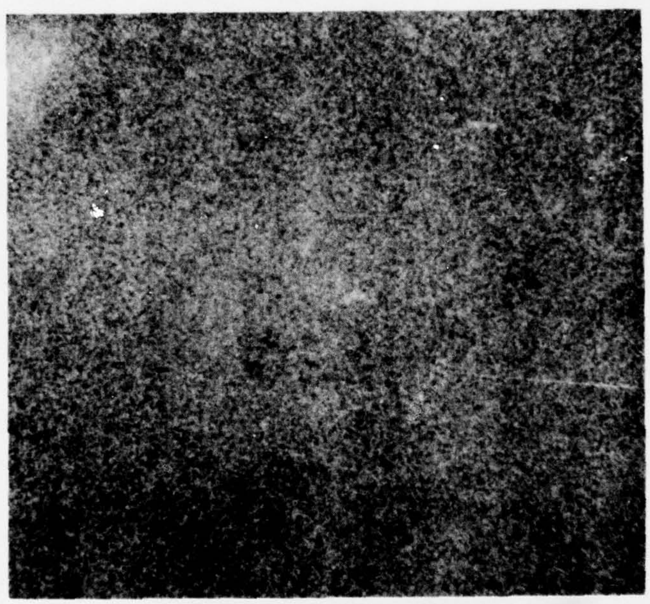

FIGURE 51. SEM OF $Ti_{34}B_{66}$ (S-6) SPUTTERED ONTO FUSED QUARTZ X5400

FIGURE 52. SEM OF $Ti_{34}B_{66}$ (S-6) SPUTTERED ONTO FUSED QUARTZ AND HEATED TO 450°C X5400

FIGURE 53. TEM OF $Ti_{34}B_{66}$ (S-6) SPUTTERED ONTO CLEAVED ROCK SALT

6.6 Preparation and Properties of High-Rate-Sputtered $Fe_{80}P_{13}C_7$

Using high-rate sputtering equipment[1] pre-arc-melted $Fe_{80}P_{13}C_7$ was deposited onto water-cooled (Sample S-7) and liquid-nitrogen-cooled (Sample S-8) copper substrates. Diameter of the disc-shaped samples was 3.8 cm, and the heaviest deposit was ~ 0.3 mm thick. Amorphousness was checked by X-ray diffraction. Figure 54, a typical X=ray diffraction pattern, suggests that Sample S-7 is amorphous.

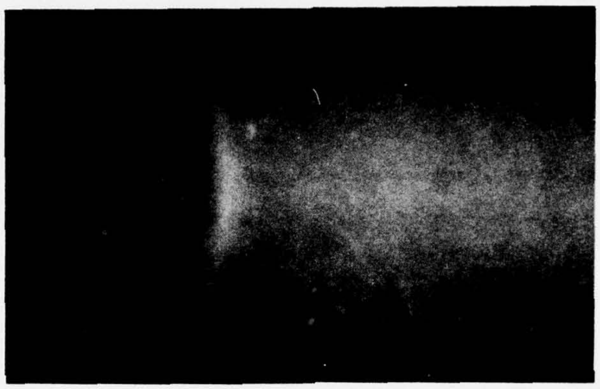

FIGURE 54. X-RAY DIFFRACTION PATTERN OF $Fe_{80}P_{13}C_7$ DEPOSITED ONTO WATER-COOLED-COPPER SUBSTRATE (SAMPLE S-7). THE LAYER IS EVIDENTLY AMORPHOUS

6.6.1 Microhardness of High-Rate Sputtered Layers

Using techniques previously outlined (Section 4.2.2), hardness measurements were performed on Samples S-7 and S-8. The results of this work provided us with standard reference values; that is to say, hardness values appropriate to alloys quenched under ultra-rapid conditions, against which we could compare the results of subsequent hardness experiments on melt-spun ribbon.

The hardness results for the sputtered layers are presented in Tables 50 and 51 and summarized in Table 52, where a comparison is made with some relevant literature data.

TABLE 50. HARDNESS DATA AND VHN'S (25g), FOR SPUTTERED SAMPLE S-7 ($Fe_{80}P_{13}C_7$/WATER-COOLED)

Diagonal Length (μm)			VHN (kg/mm^2)
d1	d2	<d>	
7.0	7.4	7.2	894*
7.6	7.6	7.6	803
7.7	7.5	7.6	803
7.7	7.8	7.75	772
7.8	7.6	7.7	782
8.4	8.0	8.2	689*
7.8	7.9	7.85	752
7.8	7.5	7.65	792
7.6	7.5	7.55	813
7.7	7.5	7.6	803
7.9	7.7	7.8	762
7.7	7.8	7.75	772
7.8	7.7	7.75	772
8.1	7.6	7.85	752
7.9	7.8	7.85	752
8.0	7.8	7.9	743
8.0	7.5	7.75	772
8.0	7.4	7.7	782
8.0	7.5	7.75	772
8.0	7.9	7.95	734
7.9	7.6	7.75	772
7.9	7.7	7.8	762
7.8	7.4	7.6	803
7.9	7.3	7.6	803
7.8	7.8	7.8	762
7.8	7.4	7.6	803
8.0	7.5	7.75	772
7.8	7.7	7.75	772
8.1	7.8	7.95	734
8.0	7.8	7.9	743
8.0	7.8	7.9	743
8.0	7.5	7.75	772
7.8	7.4	7.6	803
7.8	7.4	7.6	803
8.1	8.0	8.05	715*
7.8	7.5	7.65	792
8.2	7.9	8.05	715*
7.8	7.4	7.6	803
Average of 38 values			773 ± 35
Average of 34 (un-starred) values			776 ± 23

TABLE 51. HARDNESS DATA AND VHN'S (25g), FOR SPUTTERED SAMPLE S-8 ($Fe_{80}P_{13}C_7$/LN-COOLED)

Diagonal Length (μm)			VHN (kg/mm^2)
d1	d2	<d>	
7.8	7.3	7.55	813
8.0	7.4	7.7	782
8.1	7.6	7.85	752*
7.5	7.7	7.6	803
7.5	7.9	7.7	782
7.8	7.8	7.8	762
7.8	7.6	7.7	782
7.9	7.5	7.7	782
7.7	7.7	7.7	782
7.9	7.4	7.65	792
7.8	7.2	7.5	824*
7.9	7.2	7.55	813
7.8	7.7	7.75	772
7.8	7.7	7.75	772
7.8	7.5	7.65	792
7.8	7.7	7.75	772
7.7	7.5	7.6	803
7.3	7.5	7.65	792
7.6	7.2	7.4	847*
7.7	7.3	7.5	824*
7.7	7.4	7.55	813
7.8	7.6	7.7	782
7.7	7.5	7.6	803
7.8	7.5	7.65	792
7.6	7.5	7.55	813
8.0	7.8	7.9	743*
7.8	7.6	7.7	782
7.8	7.6	7.7	782
7.7	7.8	7.75	772
7.9	7.7	7.8	762
7.8	7.5	7.65	792
7.7	7.6	7.65	792
7.9	7.6	7.75	772
7.8	7.6	7.7	782
7.7	7.5	7.6	803
7.7	7.7	7.7	782
7.6	7.6	7.6	803
7.6	7.5	7.55	813
7.3	7.5	7.4	847*
7.7	7.6	7.65	792
7.8	7.8	7.8	762
7.3	7.7	7.5	824*
Average of 42 values			792 ± 23
Average of 35 (un-starred) values			788 ± 15

TABLE 52. HARDNESS NUMBERS FOR Fe-P-C SPUTTERED DISCS COMPARED WITH THOSE FOR SEVERAL Fe-BASE AND RELATED LIQUID QUENCHED METALLIC GLASS SAMPLES [21,40]

Alloy Name	Hardness Number (kg/mm^2)
$Fe_{80}P_{13}C_7$ (S-7) water-cooled substrate	776 $\pm$ 23
$Fe_{80}P_{13}C_7$ (S-8) LN-cooled substrate	788 $\pm$ 15
$Fe_{80}P_{20}$	755
$Fe_{80}P_{16}C_3B_1$ (Metglas 2615)	835
$Fe_{40}Ni_{40}P_{14}B_6$ (Metglas 2826)	750
$Fe_{38}Ni_{39}P_{14}B_6Al_3$	750
$Fe_{32}Ni_{36}Cr_{14}P_{12}B_6$ (Metglas 2826A)	880
$Fe_{29}Ni_{49}P_{14}B_6Si_2$ (Metglas 2826B)	792 $\pm$ 30
Average Hardness Number (excluding 2826A)	778 $\pm$ 31

In the absence of information regarding the thermal histories of the melt-quenched alloys listed in Table 52, we will assume that they are in a rapidly-quenched un-aged-amorphous condition, such that an average value is meaningful and represents the hardness to be expected from the amorphous $(Fe,Ni)_{80}Metalloid_{20}$ class of alloy. After excluding 2826A from the averaging process, a hardness of 778 $\pm$ 31 kg/mm^2 was obtained, a value against which we will, in a subsequent section, refer the hardnesses of the family of Fe-P-C-base multicomponent alloys prepared in this program by melt-spinning.

SECTION VII

SPLAT QUENCHING STUDIES

In direct support of the metallic-glass melt spinning and melt extraction segments of this program, investigations of splat-quenched materials were carried out. Table 53 lists the alloys which were splat quenched for us, under subcontract, by the University of Rochester; and also at Harvard University, through the courtesy of Professor D. Turnbull.

TABLE 53. LIST OF SPLAT-QUENCHED ALLOYS

Sample	Composition	Technique and Supplier
S-1	$Fe_{84}B_{16}$	Gun-Quenching (Figure 2) - Rochester
S-3	$Fe_{73}B_{24.5}Cr_{2.5}$	" "
S-2	$Fe_{75.2}B_{19.6}Cr_{5.2}$	Anvil-Quenching - Rochester
1	$Fe_{80}B_{20}$	Rotating Disc [Figure 1f] - Harvard
2	$Fe_{80}Ge_{20}$	" "
3	$Fe_{75}B_{10}Si_{15}$	" "
4	$(Fe_{22}Ni_{78})_{75}B_{10}Si_{15}$	" "

7.1 The Gun-Quenching of $Fe_{84}B_{16}$ and $Fe_{73}B_{24.5}Cr_{2.5}$ Samples S-1 and S-3

Using the equipment of Figure 2, Section 2.2, $Fe_{84}B_{16}$ and $Fe_{73}B_{24.5}Cr_{2.5}$ were gun-quenched into a vacuum of 10^{-3} torr from a nitrogen-pressurized quartz furnace tube, onto a polished curved copper surface. Molten charges weighing typically 0.15 g yielded foils about 1.5 cm^2 in area and about 0.015 cm thick. Morphologies and structures

of the splats were analyzed by transmission electron microscopy and electron diffraction.

7.1.1 Observations on Splat-Quenched $Fe_{84}B_{16}$ (Sample S-1)

The composition of this alloy, corresponding as it does to the eutectic in the binary phase diagram, Figure 38, is favorable for amorphous stability. Indeed the sputtered alloy possessed properties (Subsection 6.2) characteristic of the amorphous structure. An electron diffraction pattern taken from one of the splat-quenched foils, Figure 55, shows the broad ring characteristic of the amorphous structure. Ring broadening was not quantitatively evaluated, and no other measurements were made on this film.

FIGURE 55. ELECTRON DIFFRACTION PATTERN OF GUN-QUENCHED $Fe_{84}B_{16}$

7.1.2 Observations on Splat-Quenched $Fe_{73}B_{24.5}Cr_{2.5}$ (Sample S-3)

Although Sample S-3 had been sputtered, the only prior information to hand regarding its properties is that its resistivity temperature dependence exhibited a drop at about 350°C, followed by hysteresis during cooling back down to room temperature. The splat-quenched material was studied by both electron microscopy and electron diffraction. The transmission micrograph (Figure 56) appears to show an amorphous matrix with a crystalline precipitate (dark patches). A selected area diffraction pattern of the light region contained only broad diffraction rings, while that of the area shown in Figure 56 contains both the broad rings, and diffraction spots from the dark phase (Figure 57).

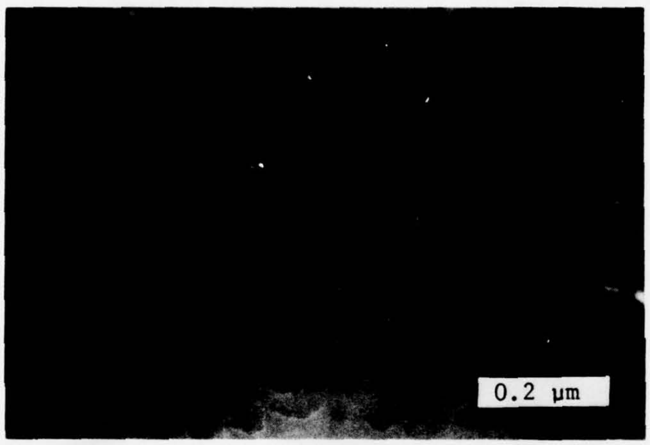

FIGURE 56. TEM (100Kv) OF GUN-QUENCHED $Fe_{73}B_{24.5}Cr_{2.5}$

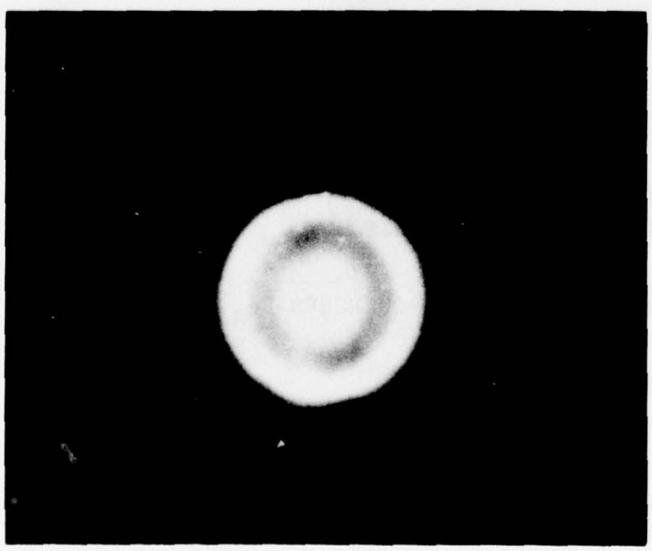

FIGURE 57. ELECTRON DIFFRACTION PATTERN CORRESPONDING TO THE TEM SHOWN IN FIGURE 56

7.2 The Anvil Quenching of $Fe_{75.2}B_{19.6}Cr_{5.2}$ (Sample S-2)

The anvil quenching was carried out within an argon-filled bell-jar arranged for arc melting. Immediately following the arc melting of the alloying ingredients in 0.5 atmosphere of argon, the liquid droplet was side-swiped by a pressure-driven plunger onto a copper block, or anvil, projecting up from the base-plate of the bell-jar.

Sample S-2 was treated in this way, as were other such alloys with additions of Ni to improve ductility. No results were reported for the latter, although electrical resistivity studies were carried out on splat-quenched S-2 itself, a typical result of which is given in Figure 58.

Although the electrical resistivity characteristic of Figure 58 is not inconsistent with the crystallization of an amorphous material with increase in temperature above about 150 K, it is not conclusive evidence for the existence of an as-quenched amorphous state either, since precipitation from a supersaturated solid solution is also generally accompanied by a decrease in resistivity. Determination of a grain size less than about 15 Å through measurement of x-ray diffraction first-peak, half-width, together with the observation of a shoulder on the second line combine to form the only satisfactory evidence for amorphousnous.

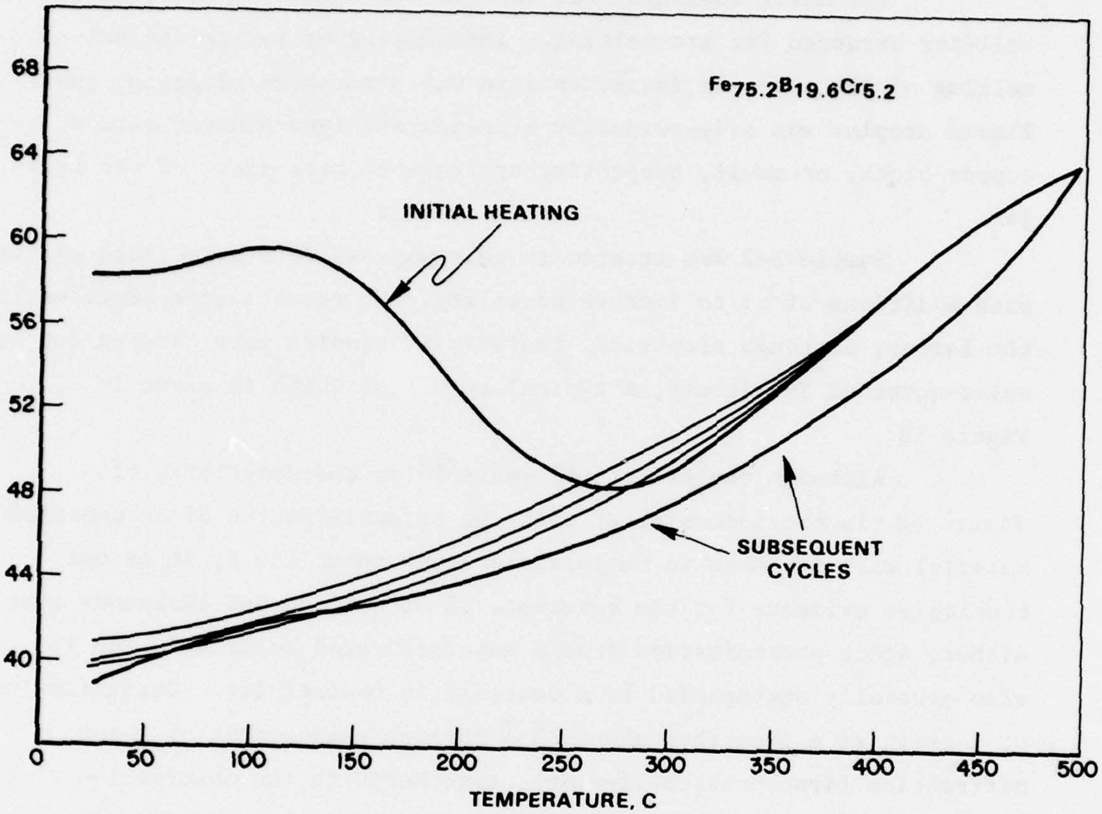

FIGURE 58. RELATIVE ELECTRICAL RESISTIVITY TEMPERATURE DEPENDENCE FOR SAMPLE S-2

7.3 The Rotating Disk Splat Quenching of Samples 1, 2, 3 and 4

Four metallic glass candidate alloys were pre-alloyed by arc melting and submitted to Dr. Turnbull's laboratory at Harvard University for splat quenching. Pieces of alloy were melted by levitation in vacuum and allowed to drop onto a rapidly rotating disk. The cooling rates obtained in this way were estimated by Dr. Turnbull to be in the vicinity of 10^6 K s^{-1}, depending on the thickness of the foil.

The results of optical metallographic studies carried out on splats of various thicknesses are given in Figures 59a through 62b Magnifications were 1000X, which represents a scale of 1 μm to 1 mm on the photograph.

7.3.1 Alloy 1, $Fe_{80}B_{20}$ - Figures 59a and 59b

After splat quenching, thick pieces of sample are crystalline while the thinner parts of a quenched flake, being almost devoid of microstructure, are possibly amorphous. Nucleated regions are visible along both the upper and lower surfaces of a thin quenched foil.

7.3.2 Alloy 2, $Fe_{80}Ge_{20}$ - Figures 60a and 60b

The splat-quenched Fe-Ge exhibits a very fine equiaxed (4 μm) grain structure. Evident in all of the micrographs is a "crust" of what seems to be a more rapidly quenched component, inside of which the alloy is heavily cored, a result no doubt of the existence of a very broad (1340-1125°C) liquid-plus-solid region. $Fe_{80}Ge_{20}$ does not seem to have been a good choice for metallic glass stability although it is a member of the $LTM_{80}Mtld._{20}$ class of alloy. A better composition may possibly be Fe-Ge (60-80 at.%) corresponding to a low-melting-point valley containing two eutectics.

7.3.3 Alloy 3, $Fe_{75}B_{10}Si_{15}$ - Figures 61a and 61b

Alloy 3, based on the $Fe_{80}B_{20}$ formulation but with Si substituted for some of the B seems, after splat quenching, to be amorphous when thin, and microcrystalline (~1μm) in the thicker sections.

7.3.4 Alloy 4, $(Fe_{22}Ni_{78})_{75}B_{10}Si_{15}$ - Figures 62a and 62b

As with Alloy 3, this appears to be amorphous when thin, but possesses a structure characteristic of eutectic solidification when thick.

* * * *

No further examinations were carried out on these alloys; however, the structures obtained were used as references against which the results of pendant drop melt extraction (to be discussed in the next section, Section VIII were compared.

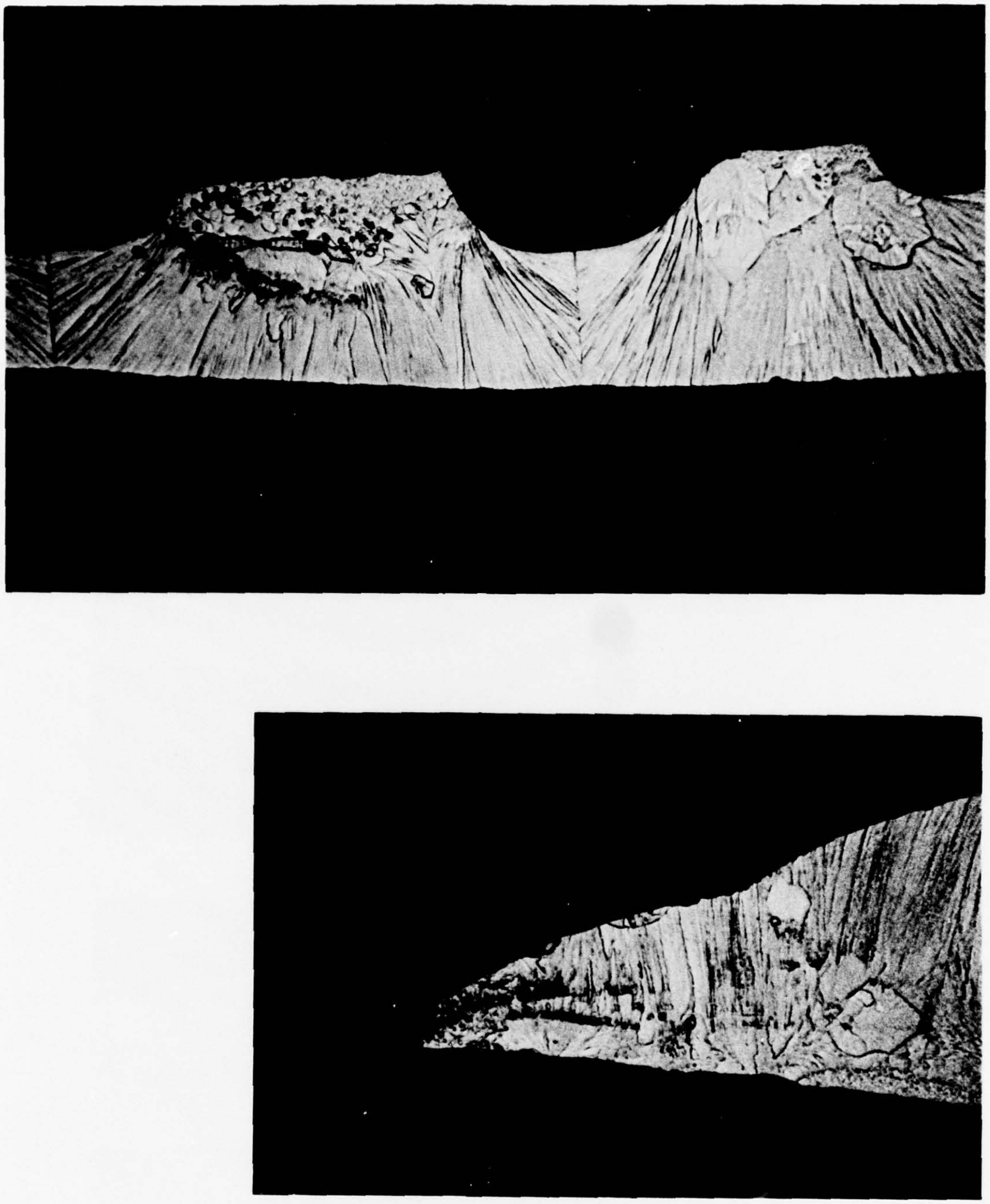

FIGURE 59a. ALLOY 1 SPLAT QUENCHED 1000X

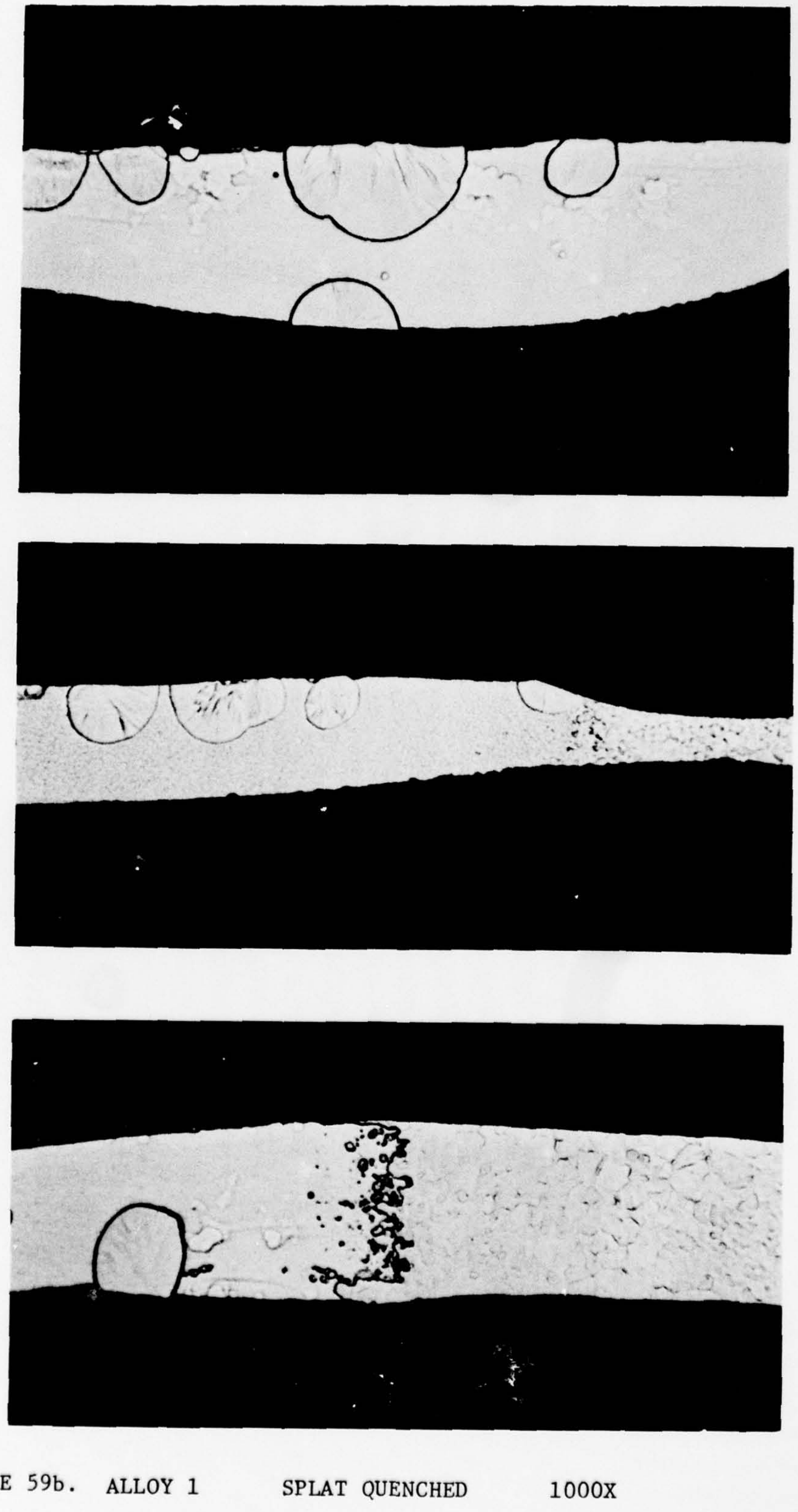

FIGURE 59b. ALLOY 1 SPLAT QUENCHED 1000X

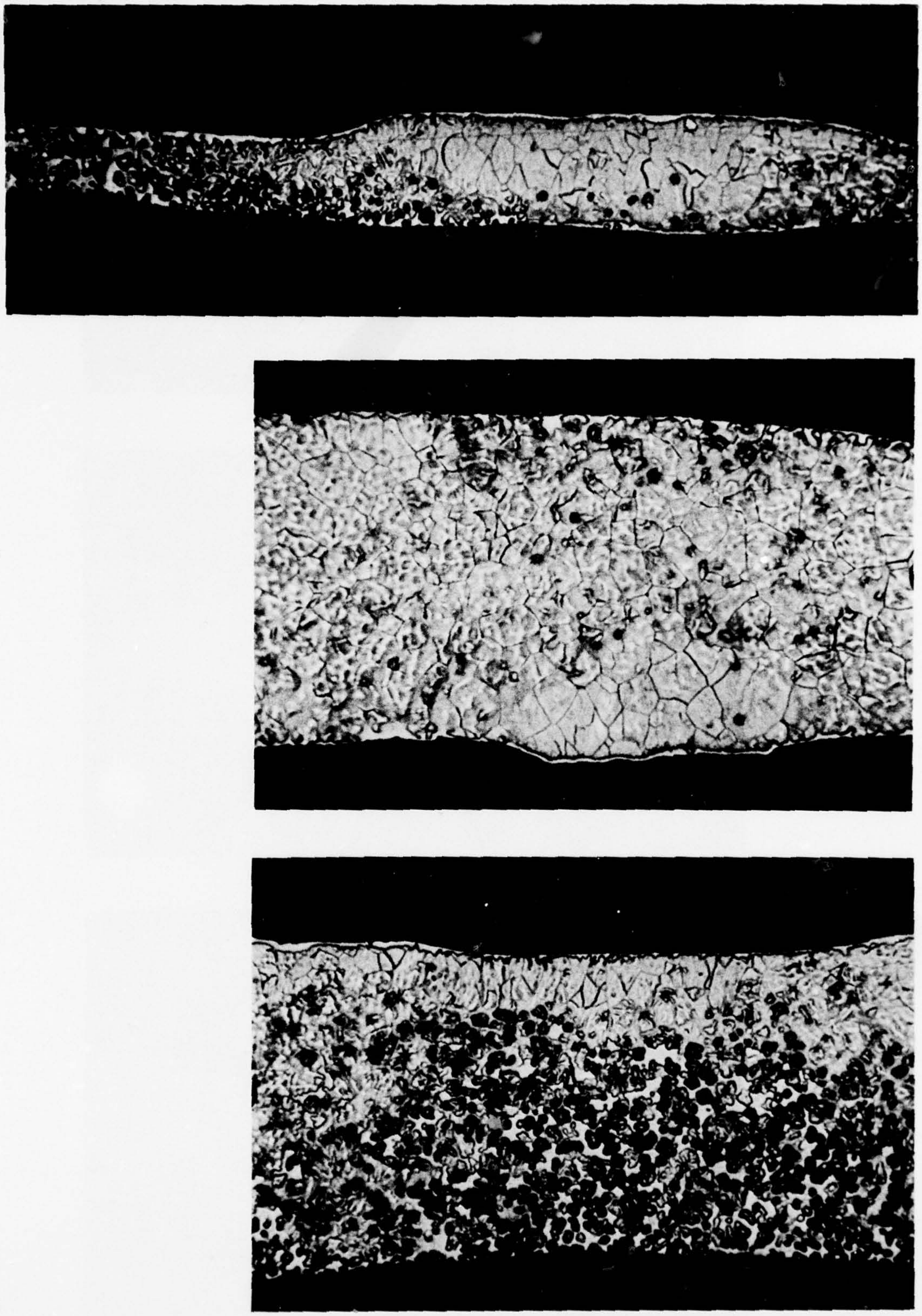

FIGURE 60a. ALLOY 2 SPLAT QUENCHED 1000X

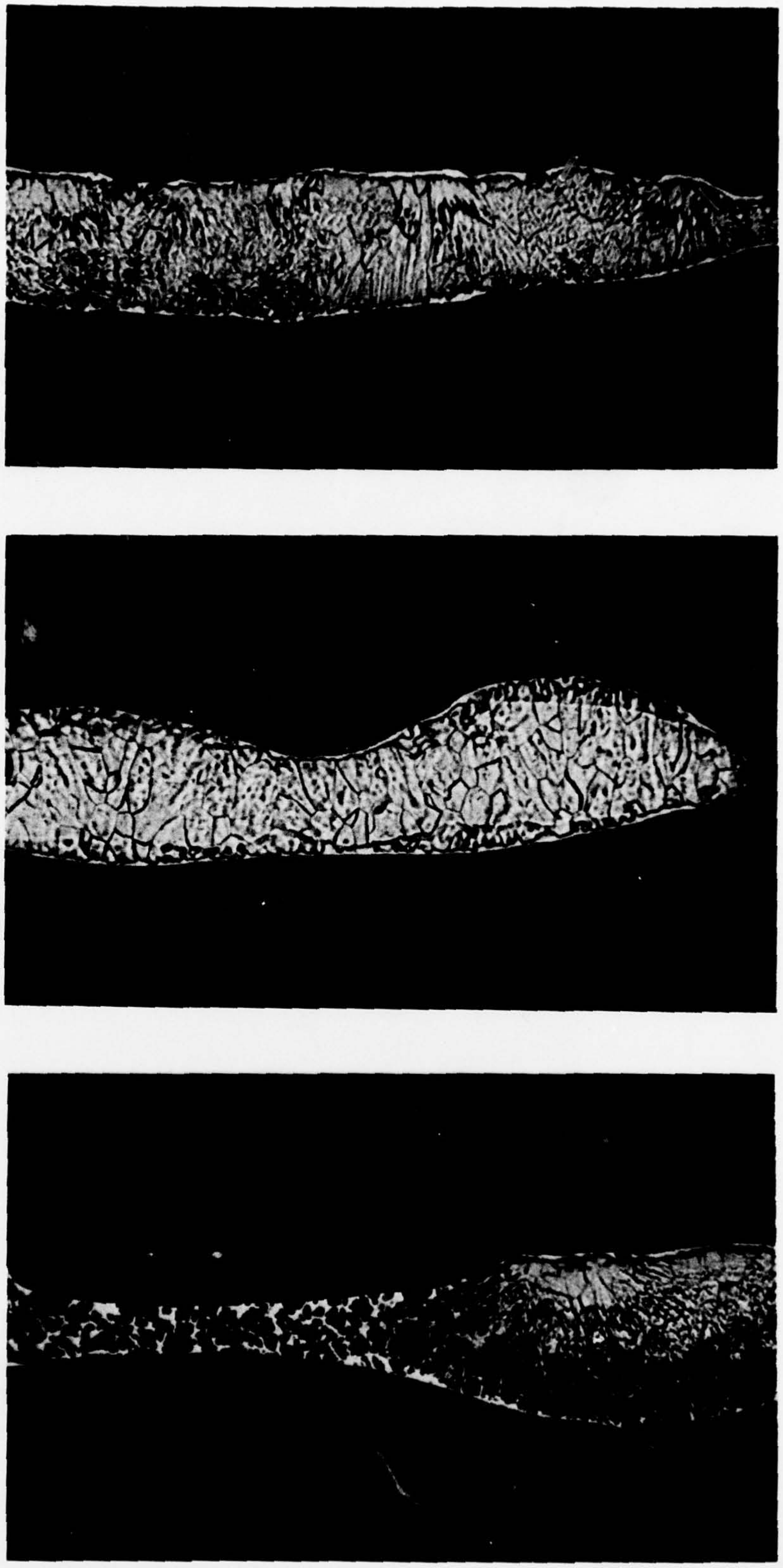

FIGURE 60b.   ALLOY 2   SPLAT QUENCHED   1000X

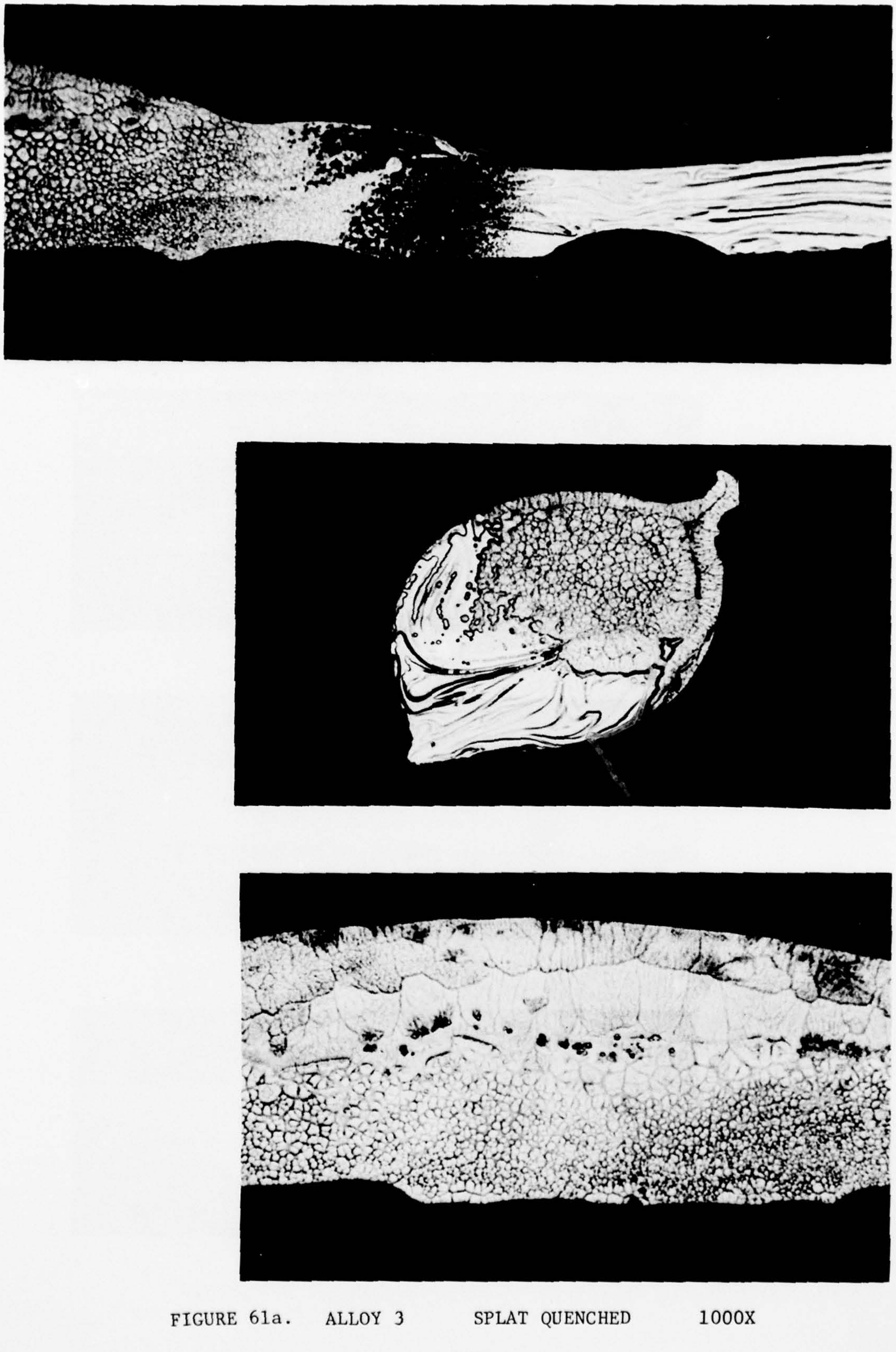

FIGURE 61a.   ALLOY 3   SPLAT QUENCHED   1000X

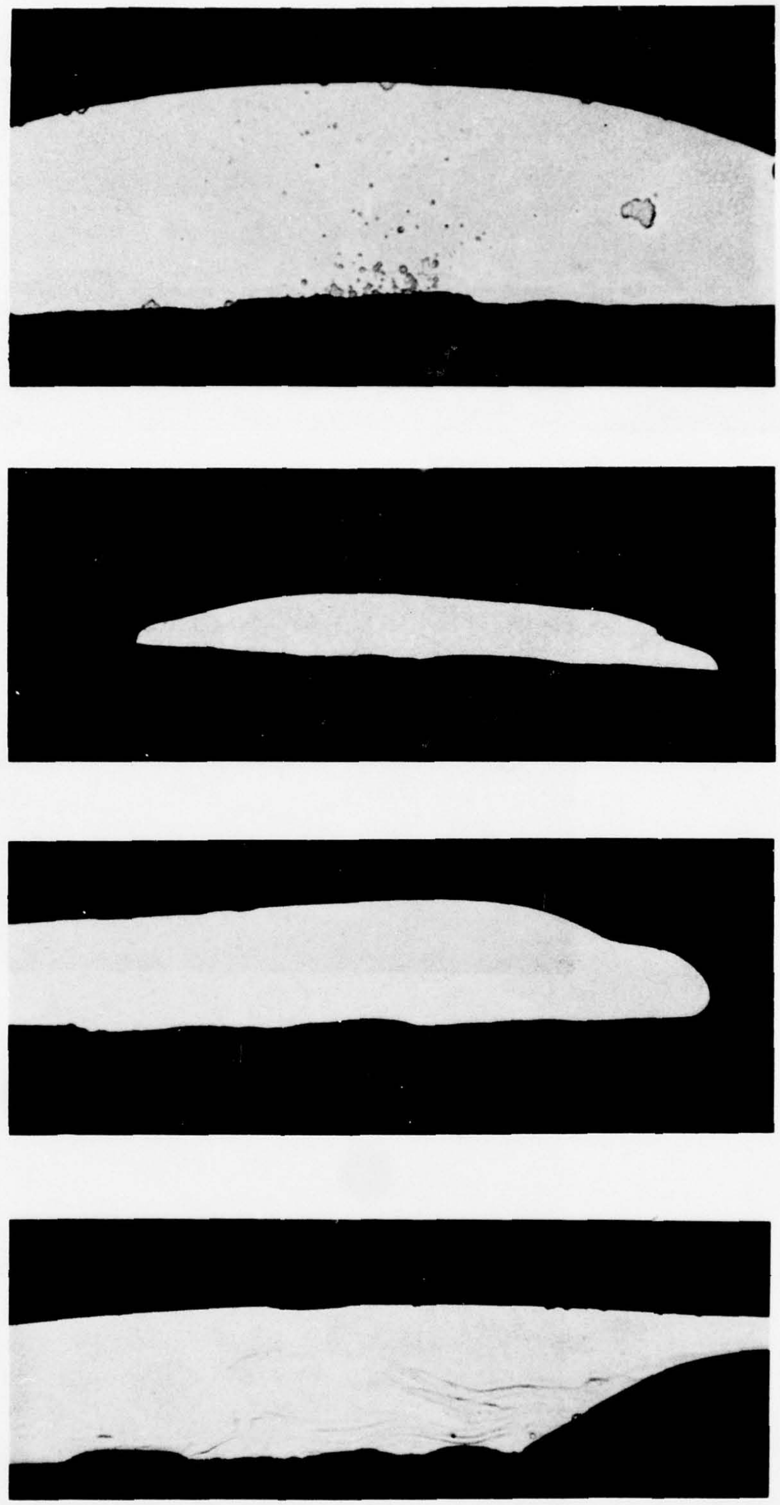

FIGURE 61b. ALLOY 3 SPLAT QUENCHED 1000X

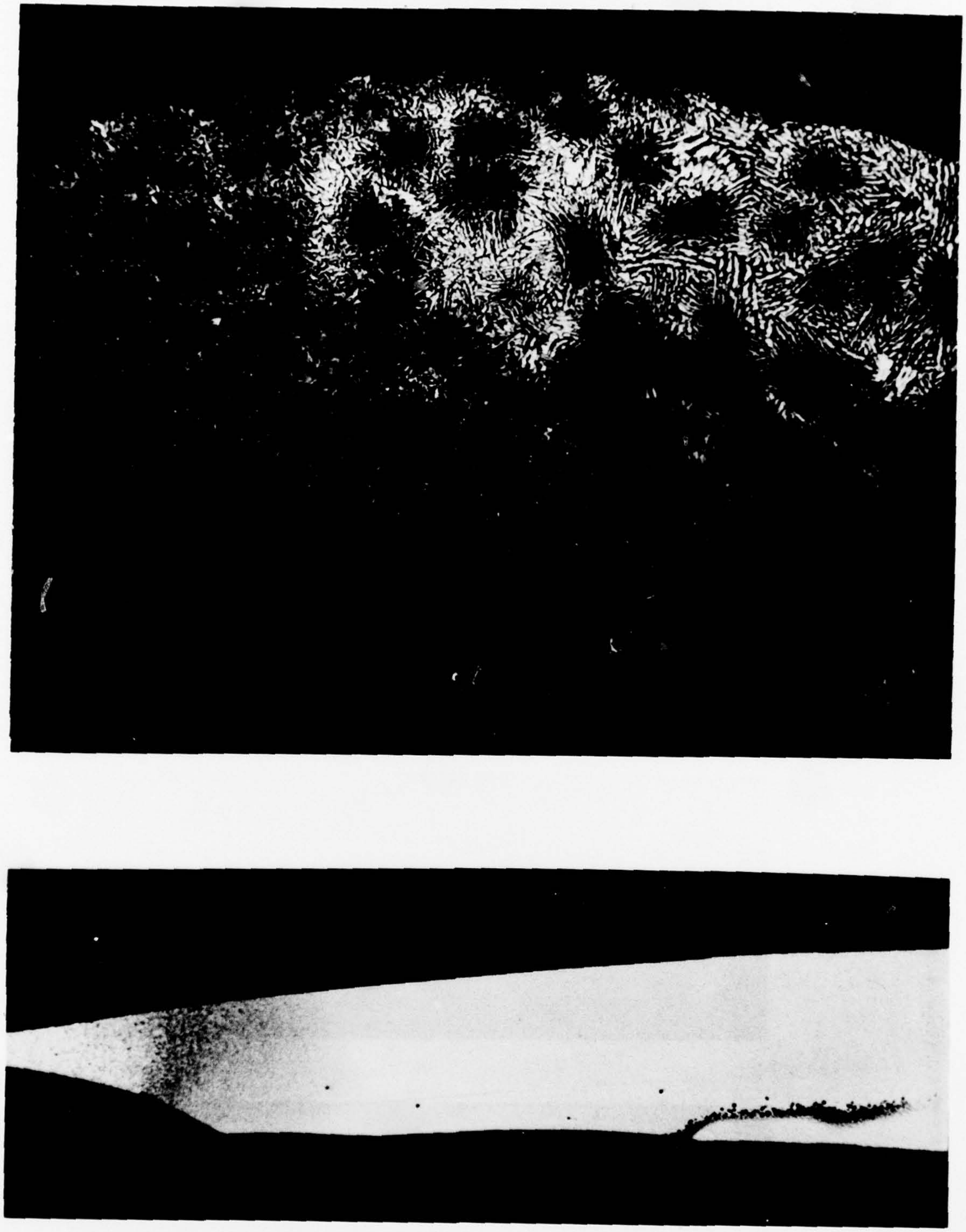

FIGURE 62a. ALLOY 4 SPLAT QUENCHED 1000X

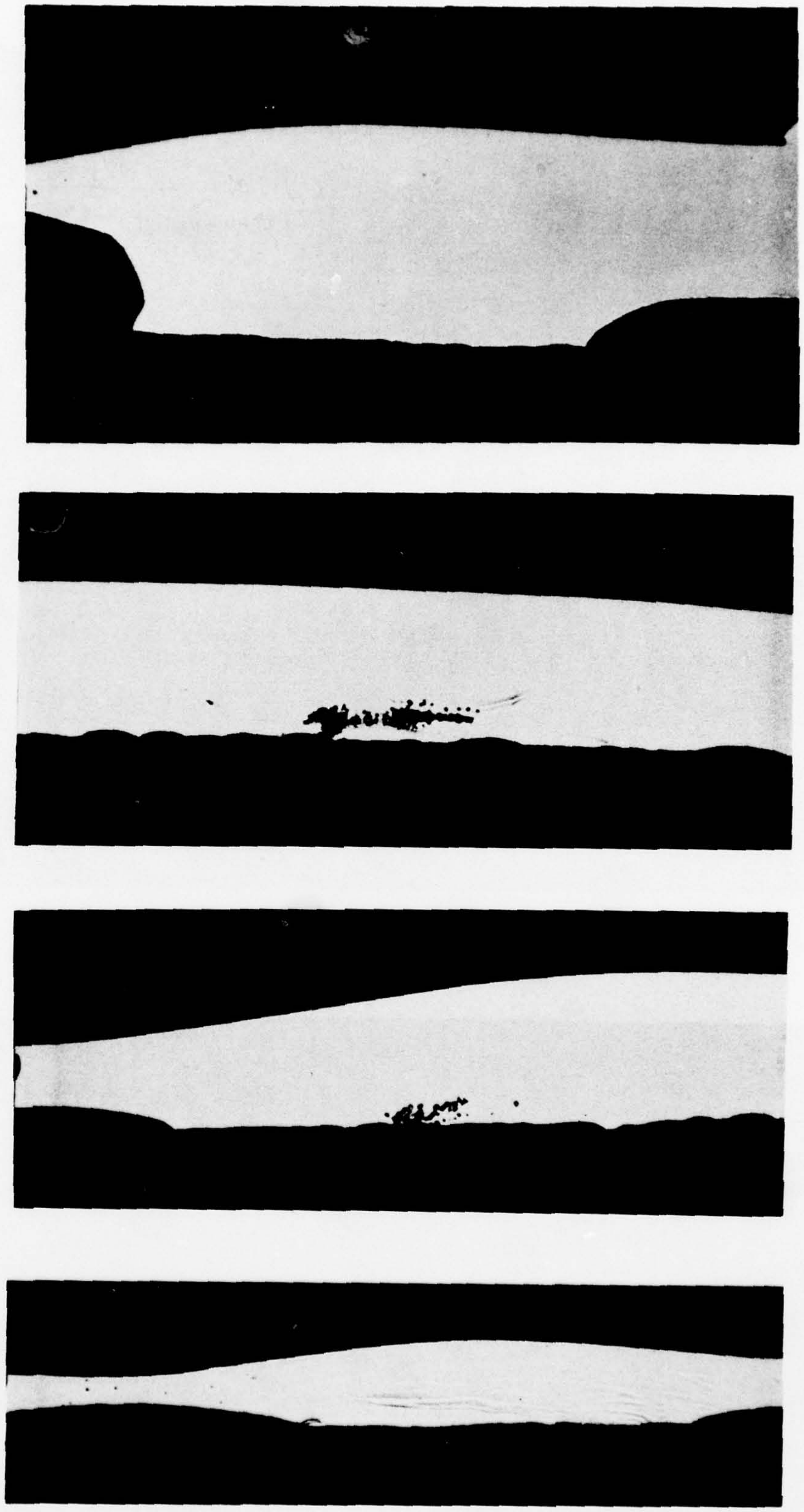

FIGURE 62b.   ALLOY 4   SPLAT QUENCHED   1000X

SECTION VIII

MELT EXTRACTION STUDIES

The rationale underlying composition selection for metallic glass candidate materials to be spun into fiber by pendant drop melt extraction has been considered already in Section V, while the technique itself, together with various applications of it, were discussed in Subsection 2.5. A list of materials prepared by pendant drop melt extraction, and whose structural, and in some cases mechanical, properties are to be considered in this chapter is given in Table 54.

TABLE 54. LIST OF METALLIC GLASS CANDIDATE MATERIALS PREPARED IN FIBER FORM BY PENDANT DROP MELT EXTRACTION

Sample Code	Composition	Process
1	$Fe_{80}B_{20}$	A,E
2	$Fe_{80}Ge_{20}$	A
3	$Fe_{75}B_{10}Si_{15}$	A,D,E
4	$(Ni_{78}Fe_{22})_{75}B_{10}Si_{15}$	A,B,C,D
5	$Fe_{75}Ge_{10}Si_{15}$	A,D
6	$Zr_{43}Cu_{57}$	A,D
7	$Ti_{30}Cu_{70}$	D
8	$Nb_{50}Ni_{50}$	D
9	$Ti_{60}Ni_{30}Si_{10}$	A
10	$Ti_{55}Ni_{30}Si_{15}$	A

where: A = continuous filament (CF) vacuum Melt Extraction (ME)

B = CF, air ME

C = CF, air ME, with water quench

D = CF, vacuum ME, with oil quench

E = low-L/D discontinuous fiber, vacuum ME

Starting materials were prepared by multiple arc melting on a water-cooled copper hearth, and then drop-cast into rod form suitable for mounting in the pendant-drop apparatus, Figure 4. In an initial series of experiments, Alloys 1, 2, 3 and 4 were melt extracted under vacuum into continuous lengths of fiber -- Process A, Table 54. They were examined metallographically, and their microstructures compared with those of a similar series of alloys prepared by a conventional splat cooling process (Section VII).

In order to increase the secondary quench rate (i.e., to achieve further quenching, or to inhibit further heating, after the fiber separated from the extraction disc) the following steps were taken:

- In one or two trial cases the melt extraction process was carried out in air in order to take advantage of ambient-temperature gas quenching. An inert atmosphere would, of course, be generally preferable -- Process B, Table 54.
- The melt-extracted fiber was deposited into a bath of water (apparatus operated in air) -- Process C,
- or oil (vacuum apparatus) -- Process D.
- The casting edge of the wheel was notched (sprocket-like) so as to yield a discontinuous product. The purpose of this modification was to interrupt an otherwise continuous heat path between the pendant droplet and the fiber leaving the wheel -- Process E.

As indicated in Table 54, not all process variants were applied to each candidate composition. Alloys 1 through 8 were examined metallographically, while 9 and 10 were subjected to mechanical property evaluation. The results of these studies are described in the following sections.

8.1 Optical Metallography of Samples 1 through 8

The results of optical metallographic studies carried out on melt-extracted fibers of Samples 1 through 8 are presented in Figures 63

through 70. They represent a comprehensive study of solidification modes. Depending on the quench rate, the microstructures vary from "conventional cast", -- i.e., (a) acicular grains or (b) a rapidly quenched zone merging into a region of columnar or equiaxed grains; to "amorphous" -- i.e., characterized by no visible grain boundaries and a resistance to attack by dilute etchants.

Magnifications are 1000X, which represents a scale of 1 μm to 1 mm on the photograph.

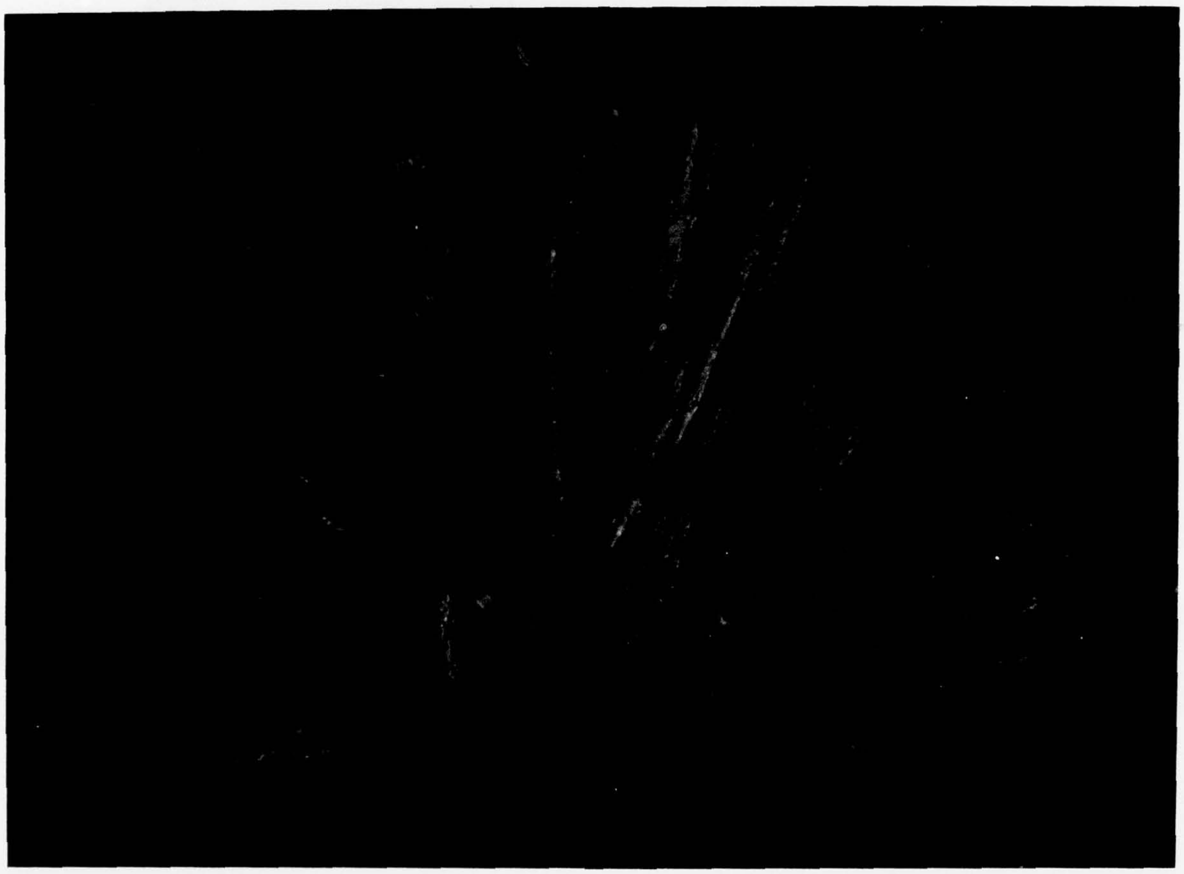

FIGURE 63. ALLOY 1 - PROCESS A, VACUUM MELT EXTRACTED FIBER

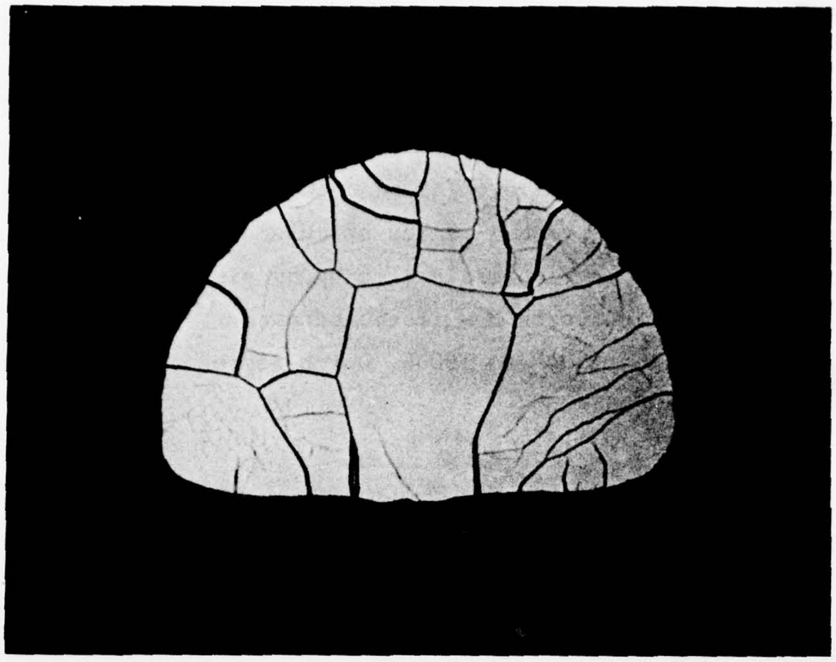

(a) 1000X

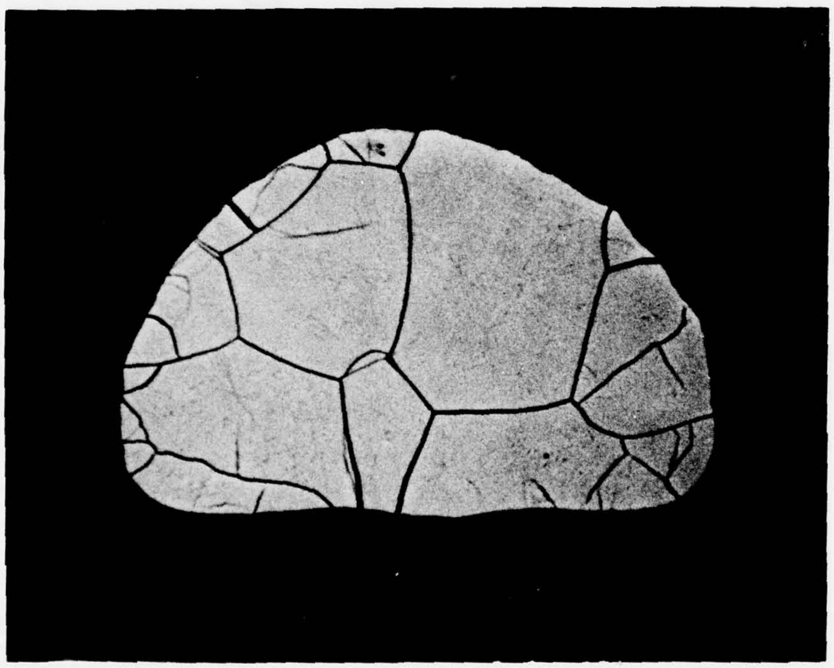

(b) 1000X

FIGURE 64. ALLOY 2 - PROCESS A, VACUUM MELT EXTRACTED FIBER. TWO SECTIONS OF FIBER SHOWN.

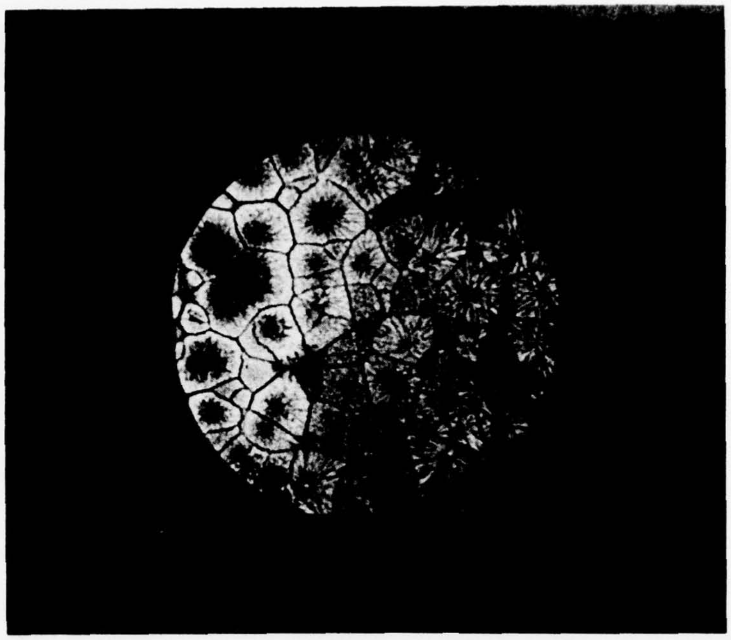

1000X

(a) Alloy 3, melt extracted in vacuum.
Wire diameter about 60 μm (2.5 mil).

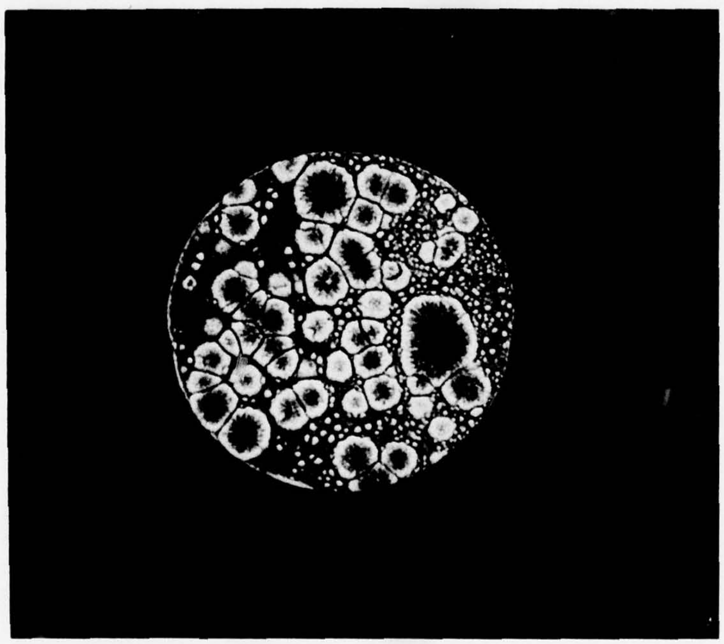

1000X

(b) Another specimen from the vacuum melt extraction experiment. Dendritic growth patterns are visible within each crystalline grain or globule. Wire diameter about 50 μm (2 mil).

FIGURE 65a,b. ALLOY 3 - PROCESS A, VACUUM MELT EXTRACTED FIBER

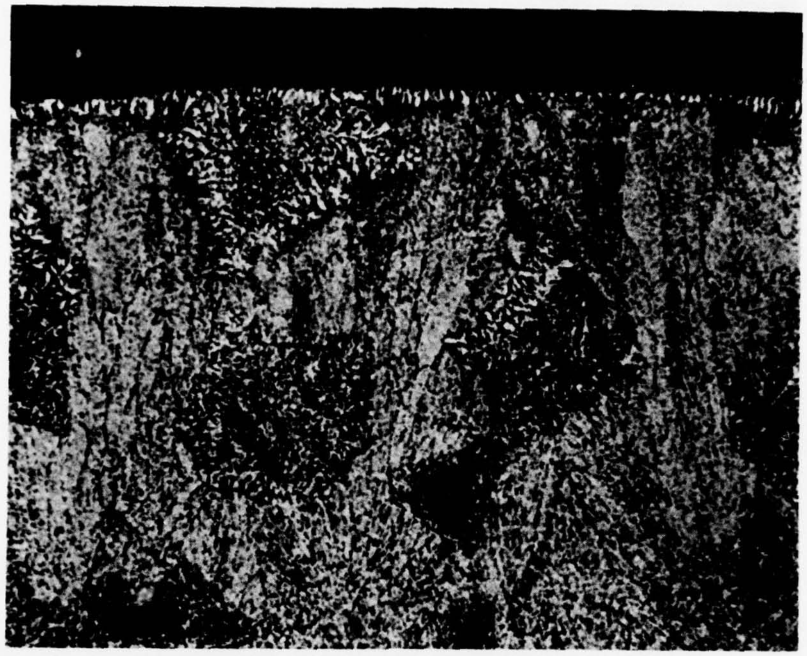

(c) 1000X

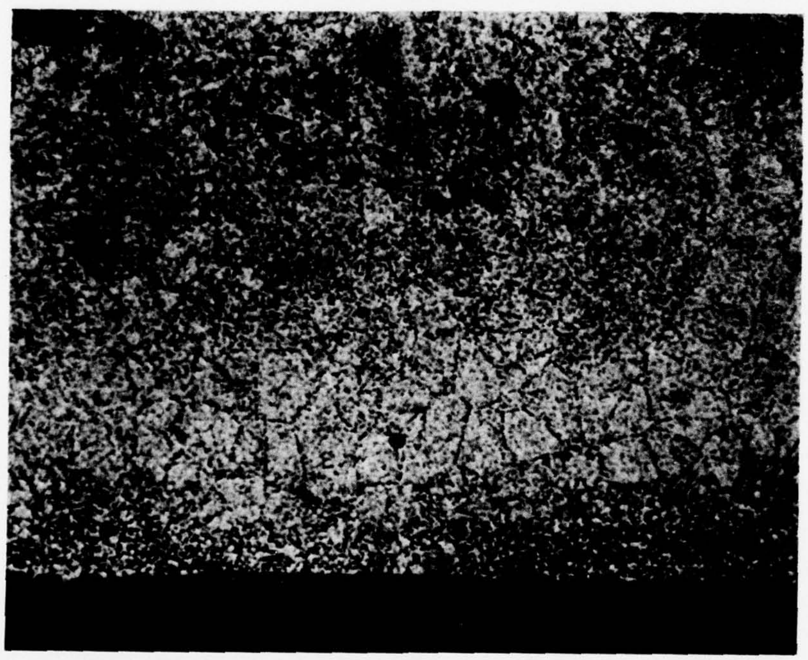

(d) 1000X

FIGURE 65c,d. ALLOY 3 - PROCESS A, VACUUM MELT EXTRACTED. LONGITUDINAL SECTION OF THICK FIBER SHOWING "FREE" (c) AND "WHEEL" (d) SURFACES.

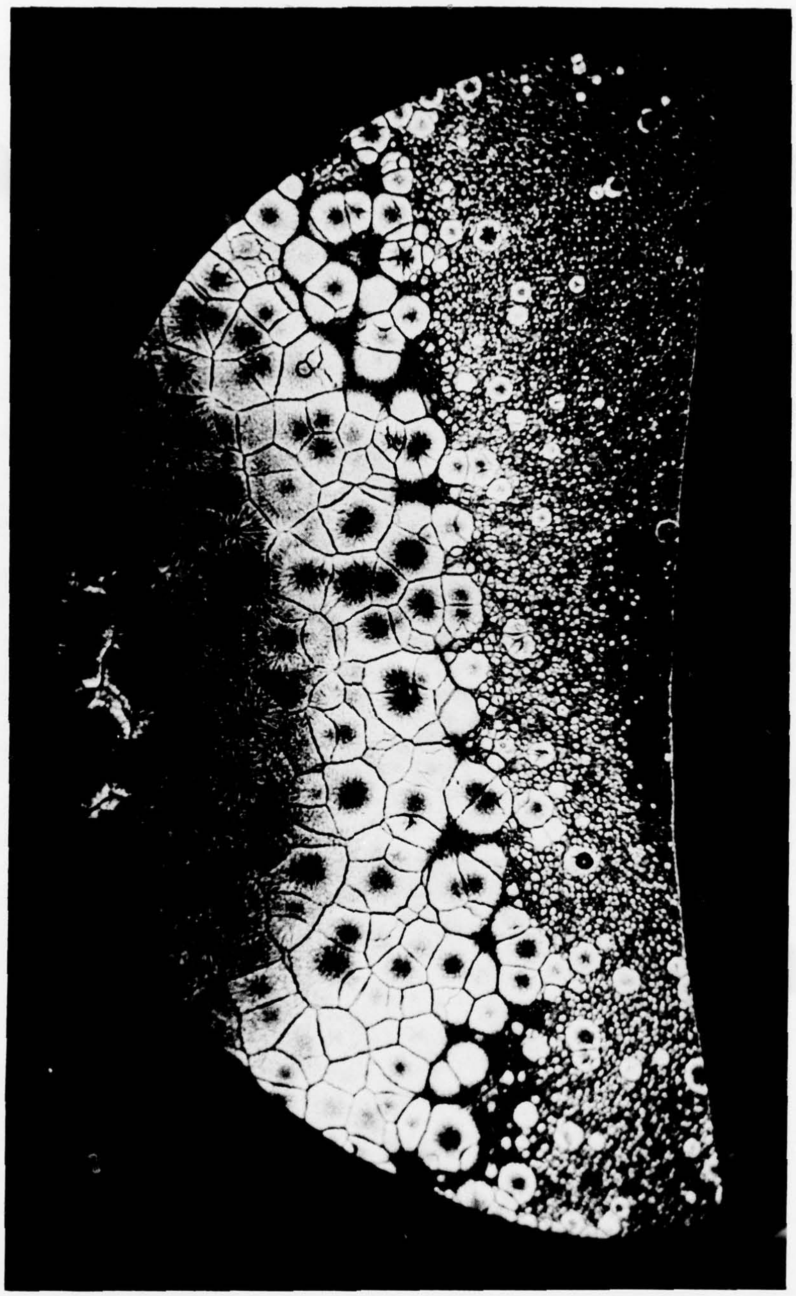

1000X

FIGURE 65e. ALLOY 3 - PROCESS D, vacuum melt extracted and deposited into an oil quench bath. Photomicrograph shows a rapidly chilled zone from contact with the disk, surmounted by an equiaxed grain structure in the slower-cooled outer regions. Dendritic growth patterns are visible radiating from the center of each grain. The dendrites are most pronounced in the slower-cooled outermost grains. Fiber thickness about 106 μm (4.3 mil).

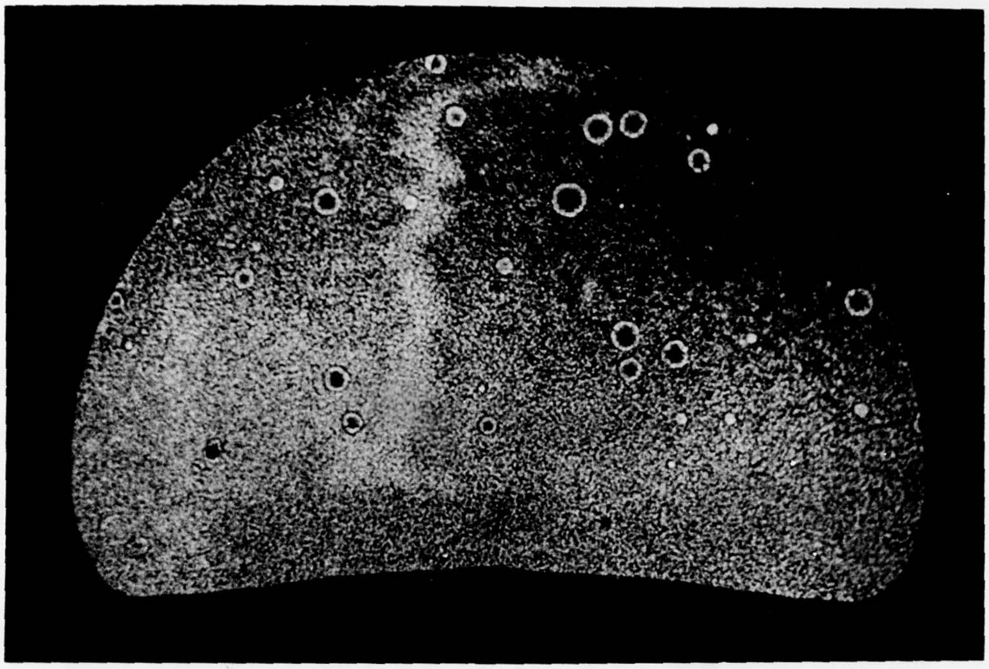

1000X

FIGURE 65f. ALLOY 3 - PROCESS D, vacuum melt extracted and oil quenched. The surface-to-volume ratio of this wire is larger than that for the wire shown in Figure 65e. Accordingly, the quench rate was higher and a very fine grain pattern resulted. The several extra-large dendrite-containing crystalline globules are, presumably, a result of heterogeneous nucleation.

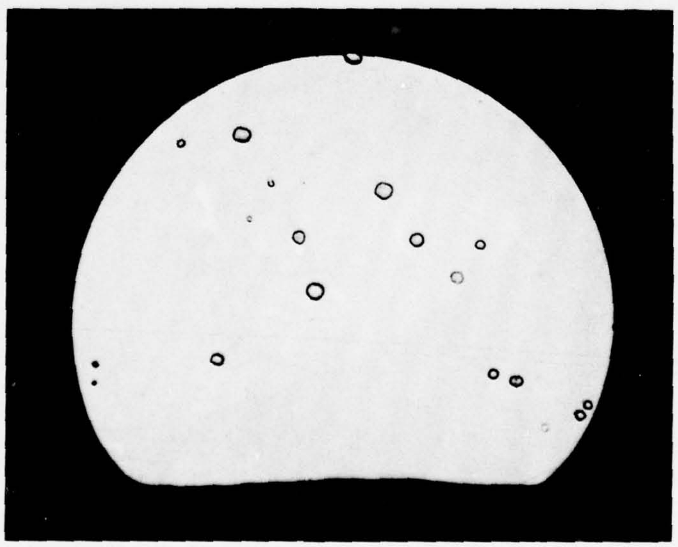

1000X

FIGURE 65g. ALLOY 3 - PROCESS D, vacuum melt extracted and oil quenched. This is the finest wire of this series of three tests, Figures 65e, 65f, and 65g. It possesses no visible grain boundaries but does support a few heterogeneously nucleated crystalline globules. Wire thickness about 65 μm (2.6 mil).

AD-A060 353 BATTELLE COLUMBUS LABS OHIO F/G 11/6
AMORPHOUS GLASSY METAL AND MICROCRYSTALLINE ALLOYS FOR AEROSPAC--ETC(U)
JUN 78 E W COLLINGS, R E MARINGER, C E MOBLEY F33615-74-C-5179
UNCLASSIFIED AFML-TR-78-70 NL

3 OF 3
AD
A060353

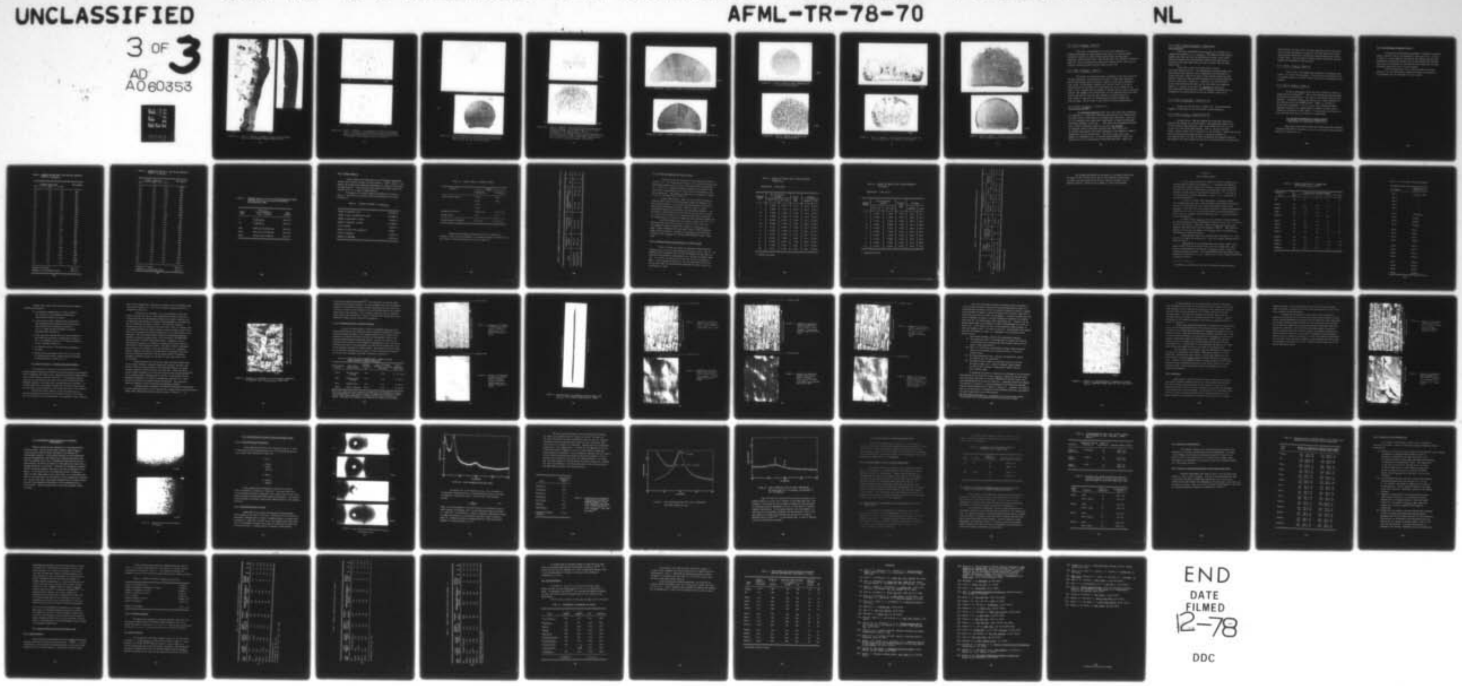

END
DATE
FILMED
12-78
DDC

(h) 1000X

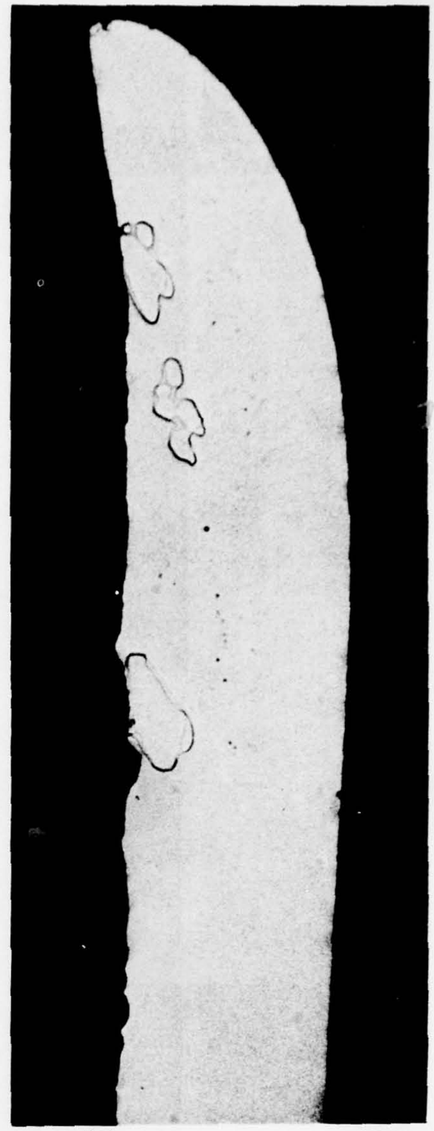

(i) 1000X

FIGURE 65k,i. ALLOY 3 - PROCESS E. FRAGMENT IS PARTLY CRYSTALLINE WHEN THICK (h), AND APPARENTLY AMORPHOUS WHEN THIN (i).

(a) 1000X

(b) 1000X

FIGURE 66a,b. ALLOY 4 - PROCESS A. Two sections of vacuum melt extracted fiber. No visible grain boundaries but with copious heterogeneous nucleation present in the less rapidly chilled region of the fiber. Fiber diameter about 75 μm (3 mil).

(c)

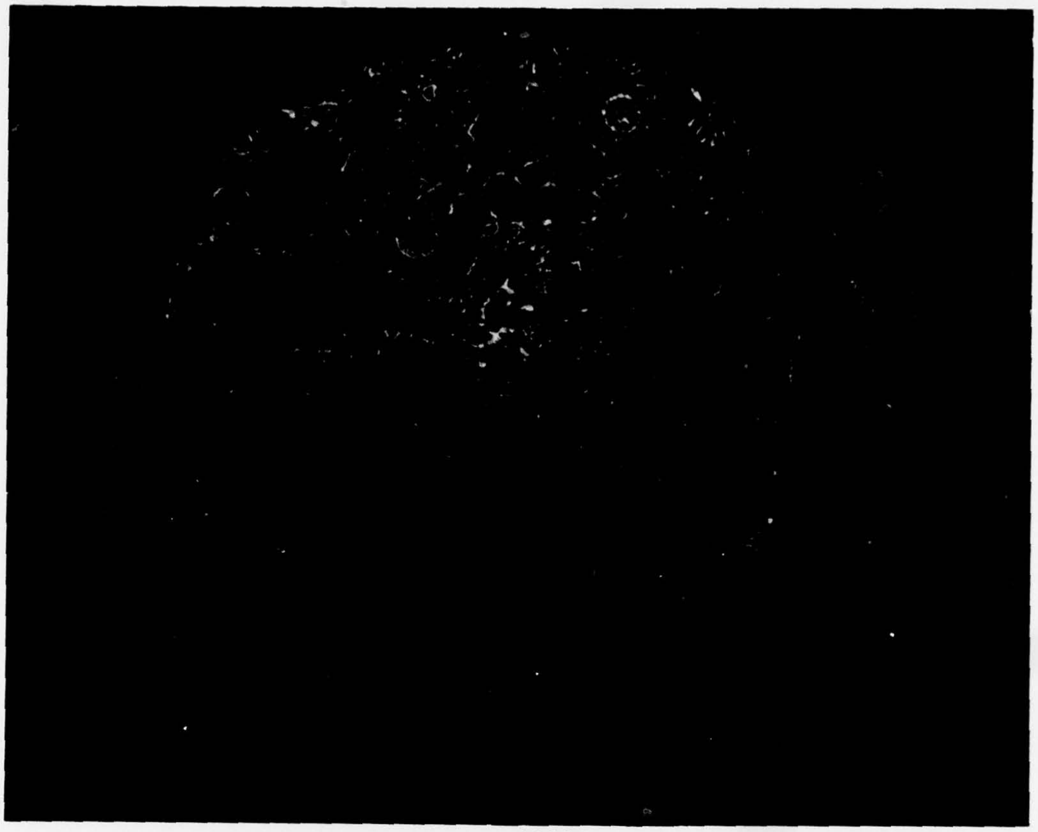

1000X

(d)

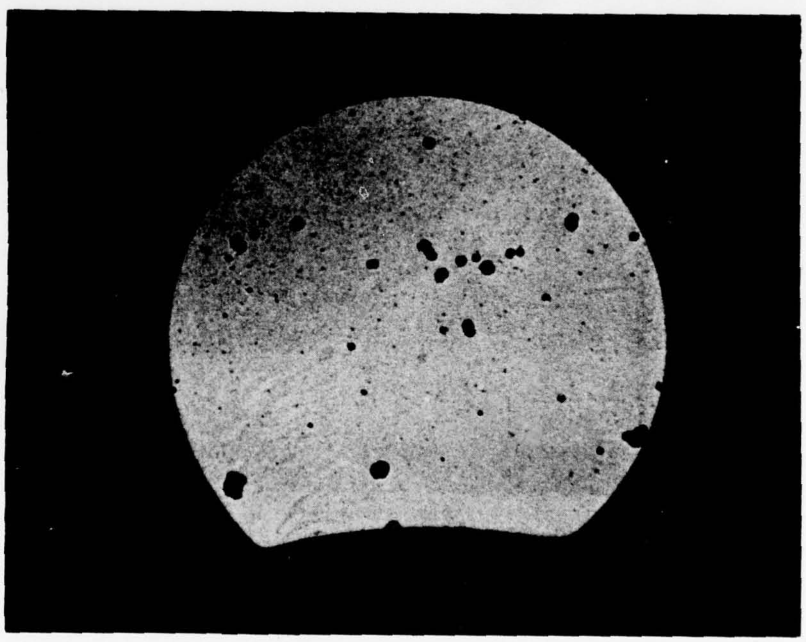

FIGURE 66c,d. ALLOY 4 - PROCESS B, two thicknesses of air-quenched wire. The thick wire (115 μm) shows a dense eutectic structure, while the fine wire (75 μm) seems amorphous.

(e) 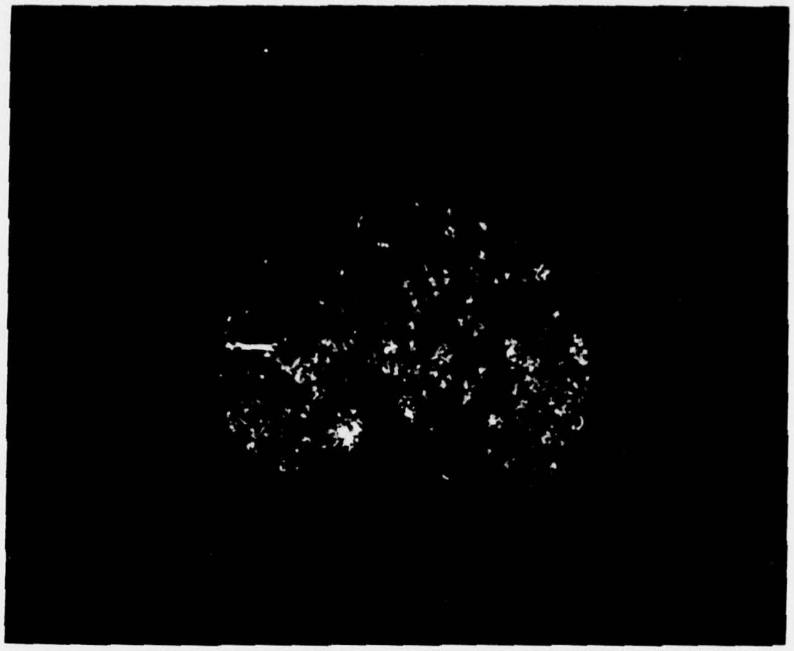 1000X

(f) 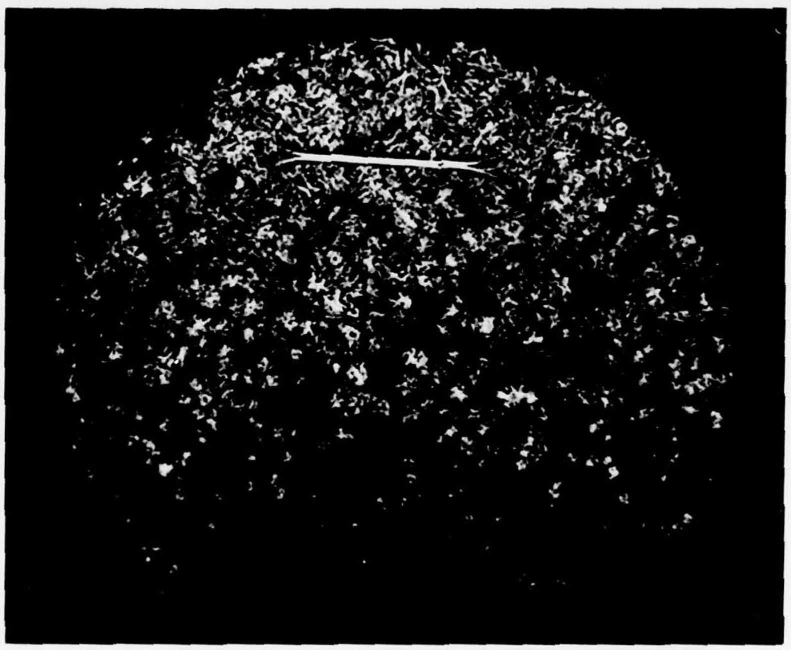 1000X

FIGURE 66e,f. ALLOY 4 - PROCESS D, vacuum melt extraction accompanied by oil-bath quenching. The structure shown in (e) is quite comparable to that shown in Figure 66a, b. Accordingly, it is concluded that any recrystallization of the fiber during its flight from the wheel is complete by the time it reaches the oil bath. Small fiber diameter about 50 μm (2 mil); large fiber diameter, about 100 μm.

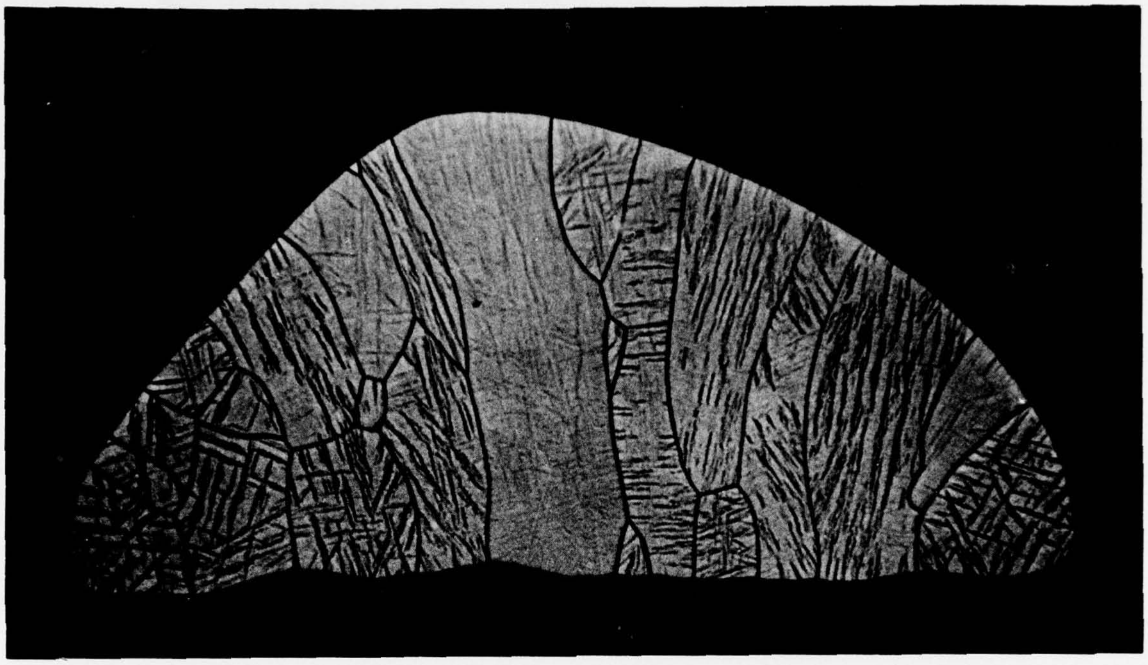

1000X

FIGURE 67a. ALLOY 5 - PROCESS A, VACUUM MELT EXTRACTED FIBER

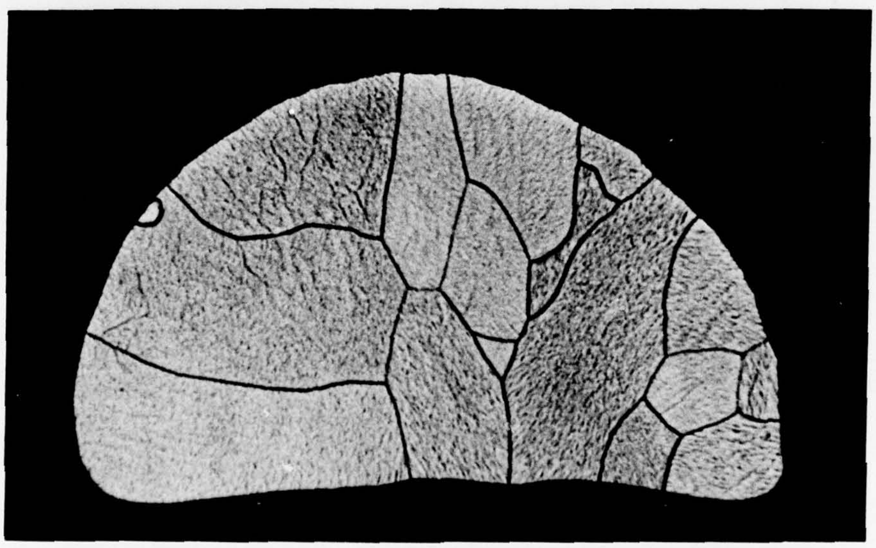

1000X

FIGURE 67b. ALLOY 5 - PROCESS D, VACUUM MELT EXTRACTED FIBER DEPOSITED INTO OIL

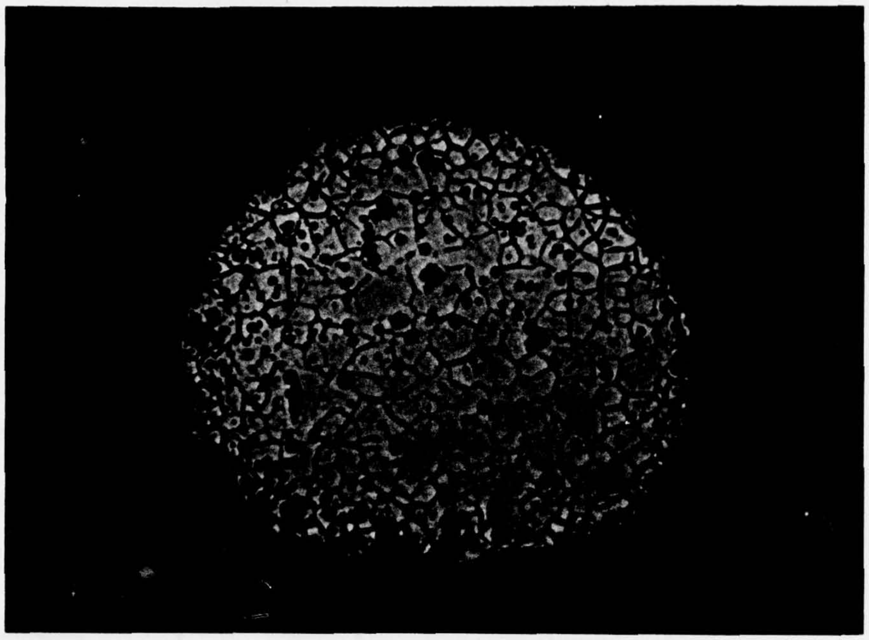

1000X

FIGURE 68a. ALLOY 6 - PROCESS D, SMALL EQUIAXED GRAINS (~ 3-5 μm) WITH PRECIPITATES

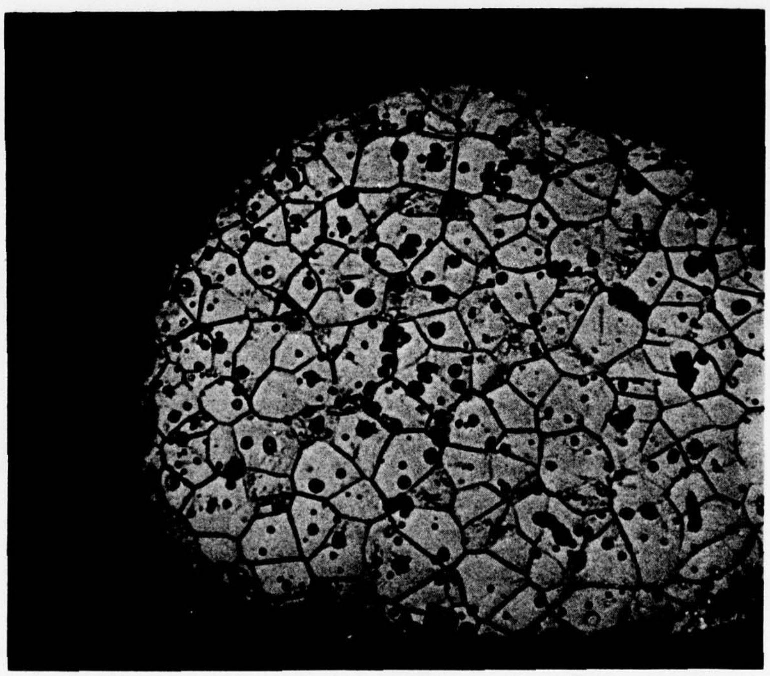

1000X

FIGURE 68b. ALLOY 6 - PROCESS A, EQUIAXED GRAINS (~ 8 μm) WITH PRECIPITATES

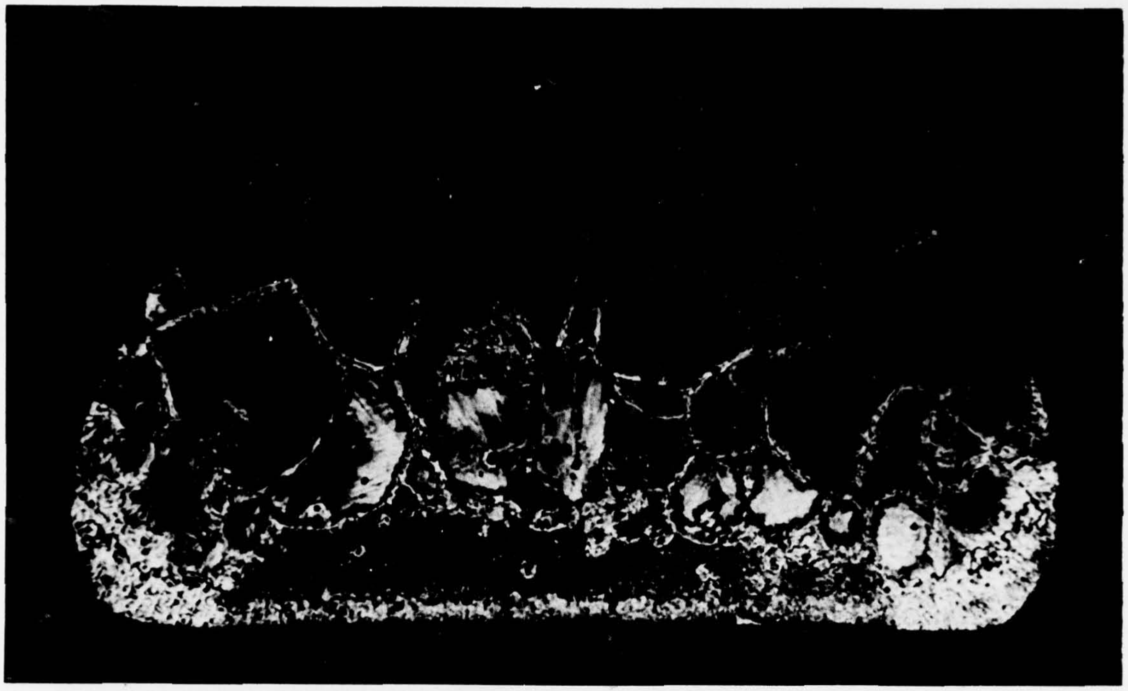

1000X

1000X

FIGURE 69. ALLOY 7 - PROCESS D. The melt extracted and quenched fiber is fully crystalline. Two diameters of wire shown.

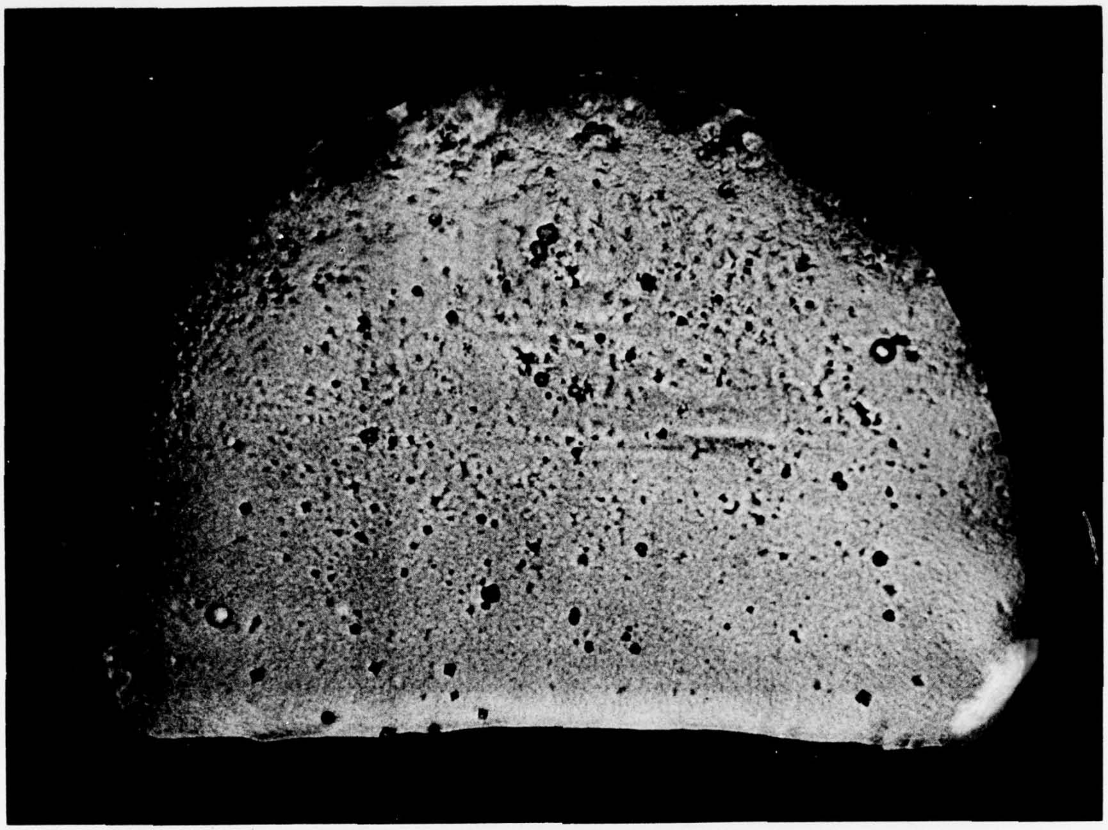

1000X

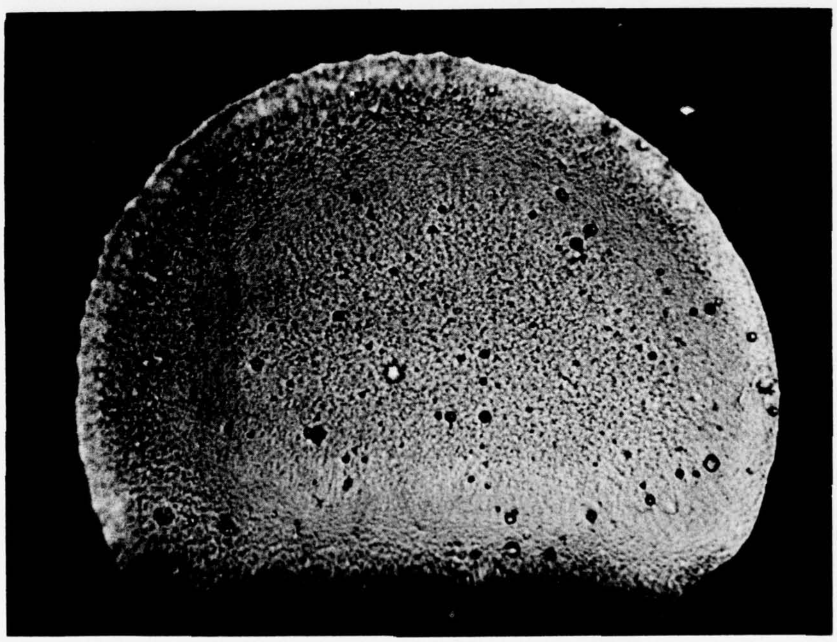

1000X

FIGURE 70. ALLOY 8 - PROCESS D. The melt extracted and quenched fiber possesses no optically detectable grain structure.

8.1.1 Alloy 1, $Fe_{80}B_{20}$ - Figure 63

This alloy, corresponding as it does to the existence of a pronounced (although not exceptionally deep) eutectic in the Fe-B phase diagram was expected to yield a metallic glass after suitably rapid quenching. Melt-extracted fiber, about 84 μm thick, was, however, crystalline. Figure 63 shows a solidification pattern of columnar grains, about 1 μm in diameter, radiating outward from the wheel-contact area.

8.1.2 Alloy 2, $Fe_{80}Ge_{20}$ - Figure 64

This alloy was crystalline after processing by both melt extraction and splat quenching. The melt-extracted fiber (~ 50 μm thick) displays a more-or-less equiaxed grain structure, Figure 64, with grain diameters of about 10 μm. The depression normally cast into the "base" of the melt-extracted fiber by the edge of the extraction disc is not evident in the figure. This, together with the absence of columnar grain structure radiating from the base suggests that solidification was not completed during the dwell period, and that the fiber may have existed in a liquid state for a brief period of time prior to crystallization during its flight away from the wheel. We will refer to this effect as "post-crystallization".

8.1.3 Alloy 3, $Fe_{75}B_{10}Si_{15}$ - Figures 65c,d, 65e, 65f, 65g, and 65k,i

The vacuum-melt-extracted fiber falls just within the crystallization threshold -- a round wire, evidently still molten as it releases from the wheel, either crystallizes to an equiaxed grain structure, Figure 65a, or to an amorphous state supporting a high density of dendrite-containing crystalline globules, Figure 65b. When thick, the vacuum-melt-extracted wire is fully crystalline, Figure 65c,d; and if oil quenched it possesses a fully crystalline structure when thick Figure 65e, but becomes less granular and finally amorphous as the diameter is reduced (Figures 65f and 65g, respectively). The low-L/D staple fiber also appears to be amorphous (i.e., no visible grain boundaries, Figure 65h when thin; but is of course partly crystalline when thick, Figure 65i.

8.1.4 Alloy 4, $(Fe_{22}Ni_{78})_{75}B_{10}Si_{15}$ - Figures 66a,b, 66c,d, and 66e,f

This alloy was derived from $Fe_{75}B_{10}Si_{15}$ by replacing the Fe component by Permalloy A, i.e., $Ni_{78}Fe_{22}$. The absence of wheel imprint suggests that this also left the melt-extraction wheel in the liquid state; and copious post-crystallization seems to have taken place on the side of the fiber remote from the line of contact with the wheel, Figure 66a,b.

Figure 66c,d shows the microstructure of Alloy 4 after melt extraction in air. The significantly increased quench rate, which results when radiation loss is augmented by the equivalent of forced convection, seems to be equal to that achieved during the splat cooling, as seen by comparing the microstructure of the thin fiber with that of a thin splat - Figure 62a. Similarly, the microstructures of the thick melt-extracted fiber and the thick splat are comparable (again c.f., Figures 66c and 62a. Oil quenching in association with vacuum melt extraction does little to increase the quench rate, as evidenced by the microstructure of the wire product, Figure 66e,f.

8.1.5 Alloy 5, $Fe_{75}Ge_{10}Si_{15}$ - Figure 67a, 67b

As was the case for Alloy 2 (Figure 64), the Ge-substituted Fe_{80}Mtld. formulations are not good metallic glass candidates.

8.1.6 Alloy 6, $Zr_{43}Cu_{57}$ - Figures 68a and 68b

As with Alloy 5, this was prepared by vacuum melt extraction, both with and without the oil-bath quench. The composition itself is one of four eutectics which generate a deep trough between about 38 at.% and 73 at.% Zr in the binary phase diagram. Even so, the melt extracted product, which is about 66 to 75 μm thick, is not amorphous. Figures 68a and 68b show an equiaxed microcrystalline fiber, crystallite diameter in the range of about 3 to 8 μm, for both the quenched and unquenched material. The shape of the fiber profile and the form of the microstructure indicate that

solidification took place after the fiber separated from the extraction disc, and that the quench rate could not have been particularly rapid. Copper-colored precipitates, unrelated to grain boundaries are present in both fibers. The wire could be handled without difficulty, was quite springy, but possessed no bend ductility.

8.1.7 Alloy 7, $Ti_{30}Cu_{70}$ - Figure 69

This is one of two compositions situated at a moderately deep eutectic in the Ti-Cu phase diagram. The 25 μm thick melt-extracted and oil quenched product is, however, fully crystalline as confirmed by x-ray analysis.

8.1.8 Alloy 8, $Nb_{50}Ni_{50}$ - Figure 70

The splat quenching of Nb-Ni has been considered in detail by Geissen and his colleagues[41]. Over a wide composition range quenching yielded what was interpreted at the time as a microcrystalline (15-16 Å) structure. Accordingly $Nb_{50}Ni_{50}$ was selected as a likely candidate for melt extraction into the amorphous state. Figure 70 contains no visible grain boundaries -- but, of course, with conventional metallographic techniques and a magnification of 1000X, the lower limit of crystallite resolution is about 5000 Å. X-ray analysis of a 62 μm thick melt-extracted fiber gave no evidence for crystallinity.

8.2 Mechanical Properties of Alloys 9 and 10 ($Ti_{60}Ni_{30}Si_{10}$ and $Ti_{55}Ni_{30}Si_{15}$, Respectively)

These alloys were studied using the hardness measuring techniques previously described in Subsection 4.2.2 and by the tensile testing methods detailed in Subsection 4.4.1.

8.2.1 Microhardness of Samples 9 and 10

The results of measurements performed on vacuum melt extracted fibers of Alloys 9 and 10 are presented in Tables 55 and 56. As shown in Table 57, which summarizes the results and compares them with the hardness values previously obtained for the microcrystalline titanium-base alloys the hardnesses of the Ti-Ni-Si alloys auger well for their possessing impressive values of yield strength.

Yield strengths were in fact directly measured on these materials, and the relationships between the values so obtained and the hardnesses will be discussed in a later section.

TABLE 55. HARDNESS DATA AND VHN'S (25g) FOR MELT EXTRACTED SAMPLE 9, $Ti_{60}Ni_{30}Si_{10}$

Diagonal Length (μm)			VHN (kg/mm^2)
d1	d2	<d>	
7.8	7.4	7.6	803
7.3	7.0	7.15	907
7.6	7.2	7.4	847
7.3	7.0	7.15	907
7.5	7.3	7.4	847
7.6	7.5	7.55	813
7.6	7.6	7.6	803
7.3	6.8	7.05	933*
7.2	7.0	7.1	920*
7.6	7.2	7.4	847
7.3	7.4	7.35	858
7.5	7.4	7.45	835
7.8	7.8	7.8	762*
7.4	7.2	7.3	870
7.3	7.3	7.3	870
7.4	7.3	7.35	858
7.4	7.6	7.5	824
7.5	7.3	7.4	847
7.5	7.3	7.4	847
7.6	7.3	7.45	835
7.0	6.6	6.8	1003*
7.4	7.0	7.2	894
7.7	7.6	7.65	792
7.6	7.0	7.35	858
7.4	7.2	7.3	870
8.1	8.2	8.15	698*
7.7	7.0	7.35	858
7.2	7.0	7.1	920*
7.6	7.5	7.55	813
Average of 29 values			853 ± 57
Average of 23 (un-starred) values			848 ± 31

TABLE 56. HARDNESS DATA AND VHN'S (25g) FOR MELT EXTRACTED SAMPLE 10, $Ti_{55}Ni_{30}Si_{15}$

Diagonal Length (μm)			VHN (kg/mm^2)
d1	d2	<d>	
6.3	6.3	6.3	1168*
6.8	6.5	6.65	1048
6.9	6.8	6.85	988
6.8	6.9	6.85	988
6.9	6.6	6.75	1018
7.0	6.6	6.8	1003
7.0	7.0	7.0	946
6.9	6.4	6.65	1048
7.0	6.6	6.8	1003
7.2	7.0	7.1	920*
6.5	6.4	6.45	1114*
6.6	6.5	6.55	1081*
7.1	6.6	6.85	988
7.0	6.8	6.9	974
7.0	6.7	6.85	988
6.5	6.8	6.65	1048
6.8	6.6	6.7	1033
6.3	6.2	6.25	1187*
7.1	6.9	7.0	946
7.1	6.6	6.85	988
7.1	6.9	7.0	946
7.2	6.7	6.95	960
7.0	6.6	6.8	1003
7.0	6.8	6.9	974
6.9	6.9	6.9	974
7.2	6.8	7.0	946
7.0	6.8	7.0	946
7.0	7.0	7.0	946
6.9	6.7	6.8	1003
6.9	6.9	6.9	974
7.0	6.4	6.7	1033
Average of 31 values			1006 ± 63
Average of 26 (un-starred) values			989 ± 34

TABLE 57. HARDNESS VALUES OF Ti-Ni-Si ALLOYS COMPARED WITH THOSE OBTAINED FOR THE Ti-Al-V-BASE POLYCRYSTALLINE MELT-EXTRACTED FIBERS

Sample Code	Composition (at.% - subscript) (wt.% - prefix)	VHN (kg/mm^2)
9	$Ti_{60}Ni_{30}Si_{10}$	848 ± 31
10	$Ti_{55}Ni_{30}Si_{15}$	989 ± 34
ME-4	80Ti-5.4Al-3.6V-8Fe-3Cu	588 ± 28
ME-6	80Ti-5.4Al-3.6V-6Fe-5Cu	542 ± 30
ME-10	92.5Ti-1.5Al-1V-3Be-2B	673 ± 43

8.2.2 Elastic Modulus

Elastic modulus was determined from the measured longitudinal acoustic wave velocity through the usual formula $v = \sqrt{E/\rho}$; where ρ, the density was obtained from immersion measurements on pieces of the as-cast starting material. Sound velocities were measured at WPAFB through the courtesy of Dr. H. L. Gegel, Program Monitor.

The results of a typical density determination is given in Table 58, and those of the elastic modulus determinations are given in Table 8-6.

TABLE 58. DENSITY OF SAMPLE 9, $Ti_{60}Ni_{30}Si_{10}$

Weight of specimen in air	29.29292 g
Weight of spec.+ suspension in water	24.02688 g
Weight of suspension in water	0.02130 g
Weight of specimen in water	24.00558 g
Loss of weight	5.28734 g
Density of water (20.5 degrees C)	0.9981
Volume of specimen	5.29471 cc
DENSITY OF SPECIMEN	5.530 g/cc

TABLE 59. ELASTIC MODULI OF SAMPLES 9 AND 10

Quantity	Sample	
	$Ti_{60}Ni_{30}Si_{10}$	$Ti_{55}Ni_{30}Si_{15}$
Sound Velocity (km/s)	4.469	4.819
	4.652	4.661
	4.422	
	4.446	
Average Value (km/s)	4.50 $\pm$ 0.11	4.74 $\pm$ 0.11
Density (g/cc)	5.53	5.54
Young's Modulus (10^3kg/mm^2)	11.2 $\pm$ 0.5	12.3 $\pm$ 0.6

Combining the hardness and modulus data, it is possible to estimate a value of yield strength in the manner discussed in Subsection 4.3. The results of these predictions are given in Table 60.

TABLE 60. ESTIMATION OF YIELD STRENGTHS FOR TWO Ti-Ni-Si ALLOYS USING THE METHOD OF SUBSECTION 4.3.2

Alloy	Hardness, H (kg/mm^2)	Young's Modulus, E ($10^3 kg/mm^2$)	Yield Strength, Y		E/Y	H/Y
			(kg/mm^2)	(ksi)		
$Ti_{60}Ni_{30}Si_{10}$(9)	848 ± 31	11.2 ± 0.5	415 ± 29	590 ± 41	27	2.0
$Ti_{55}Ni_{30}Si_{15}$(10)	989 ± 34	12.3 ± 0.6	497 ± 35	707 ± 50	25	2.0

8.2.3 Tensile Properties of Ti-Ni-Si Alloys

Tensile testing was carried out in the manner described in Section 4.4.1. The cross-sectional areas of the fracture surfaces were determined gravimetrically from the optically-obtained shadowgraphs (c.f., Figure 27) enabling ultimate strengths to be computed from the results of measurements on at least ten test specimens for each alloy composition. The results of this work are presented in Tables 61 and 62, and summarized in Table 63.

As mentioned earlier, there is a very large variation in cross-sectional area (some 30-40 percent) along the lengths of the melt-extracted fibers. It was this that necessitated the fracture areas being individually measured. However, there is a good correlation between cross-sectional area and load-to-failure -- the correlation coefficients being 0.84 for Alloy 9; and 0.93 for Alloy 10. Even so, the scatter in the strength values, before rejection of extreme values is 42 percent (Sample 90) and 27 percent (Sample 10).

Specific strengths are also listed in Table Table 63. By comparison with some data listed in Table 42 we see that, while the strength is lower, the specific strength of $Ti_{60}Ni_{30}Si_{10}$ is equal to that of Metglas 2615, and nearly equal to that of Metglas 2826A; while the specific strength of $Ti_{55}Ni_{30}Si_{15}$ approaches that of Metglas 2605 ($Fe_{80}B_{20}$) the strongest known metallic glass ribbon fiber.

8.2.4 Hardness/Strength Relationships in Ti-Ni-Si Alloys

Table 60 shows the results of applying the Marsh Equation (Subsection 4.3.1) to the hardness/modulus data for Alloys 9 and 10. The strength values predicted (viz. 415 and 497 kg/mm^2) are just twice as large as those obtained experimentally (viz. 189 and 253 kg/mm^2, Table 63). As a result the calculated E/Y and H/Y ratios are anomalously small -- H/Y is generally about 3.0, but the calculations yield 2.0. On the other hand, the experimentally obtained H/Y ratios (Table 63) are anomalously high.

TABLE 61. RESULTS OF TENSILE TESTS ON MELT-EXTRACTED $Ti_{60}Ni_{30}Si_{10}$

STRAIN RATE: 0.002 in/min

Specimen Number	Area of Fracture Surface		Fracture Load	Strength	
	(10^{-6} in^2)	(10^{-3} mm^2)	(kg)	(kg/mm^2)	(ksi)
1	4.4286	2.8572	0.611	213.8	304.2
2	2.7088	1.7476	0.335	191.7	272.6
3*	2.2258	1.4360	0.132	91.9	130.7
4*	4.3629	2.8148	0.238	84.6	120.3
5	9.6061	6.1975	0.850	137.2	195.1
6*	6.7828	4.3760	1.010	230.8	328.3
7*	4.1727	2.6921	0.625	232.2	330.2
8	8.8672	5.7208	1.125	196.7	279.7
9	8.1313	5.2460	1.165	222.1	315.9
10	11.4415	7.3816	1.085	147.0	209.1
11	8.9927	5.8017	1.100	189.6	269.7
12	7.5228	4.8534	1.025	211.2	300.4
13*	6.8747	4.4353	1.150	259.3	368.8

* Extrema (strength)

TABLE 62. RESULTS OF TENSILE TESTS ON MELT-EXTRACTED $Ti_{55}Ni_{30}Si_{15}$

STRAIN RATE: 0.002 in/min

Specimen Number	Area of Fracture Surface		Fracture Load (kg)	Strength	
	(10^{-6} in^2)	(10^{-3} mm^2)		(kg/mm^2)	(ksi)
1	1.4938	0.9637	0.215	223.1	317.3
2	2.9159	1.8812	0.444	236.0	335.7
3	1.4121	0.9110	0.281	308.4	438.7
4*	1.5416	0.9946	0.423	425.3	604.9
5*	4.1040	2.6477	0.425	160.5	228.3
6	2.2258	1.4360	0.403	280.6	399.2
7	2.4867	1.6043	0.399	248.7	353.7
8	2.6112	1.6846	0.429	254.6	362.2
9	2.6351	1.7001	0.429	252.3	358.9
10	3.1270	2.0174	0.443	219.6	312.3

* Extrema (strength)

TABLE 63. MEASURED STRENGTHS OF TWO Ti-Ni-Si MELT-EXTRACTED ALLOYS

Alloy	Average Area (10 Values) (10^{-3} mm^2)	Area/Load Correlation Coefficient (8 Pairs)	Validity of Correlation (%)	Average Strength (γ) (10 Values) (kg/mm^2)	Average Strength (γ) (8 Values) (kg/mm^2)	Average Strength (γ) (8 Values) (ksi)	Specific Strength (10^5 cm)	H*/Y
$Ti_{60}Ni_{30}Si_{10}$ (9)	4.3 ± 1.8 (42%)	0.84	99-99.9	170 ± 71	189 ± 31	268 ± 44	34	4.5
$Ti_{55}Ni_{30}Si_{15}$ (10)	1.6 ± 0.5 (31%)	0.93	>99.9	261 ± 70	253 ± 30	360 ± 43	46	3.9

* Hardness, from Table 60.

Two interim conclusions can be drawn: (a) the Marsh formula does not apply to the Ti-Ni-Si alloys, and (b) the measured strength values are lower than anticipated on the basis of hardness readings, due to premature failure. Further work is needed to clarify this problem.

SECTION IX

MELT SPINNING STUDIES

In our initial proposal we claimed it would be necessary in an advanced metallic-glass fiber program to " -- transcend the problem of mere [metallic glass] existence and attempt to predict (and eventually confirm) the particular combination of elements that yield the desired strength, modulus, ductility and density properties. -- ", and that to this end we would consider "additions of the B, C, etc., metalloids as strengthening agents".

In order to satisfy this requirement, we decided to graft our strengthening study onto a well-established rapid-quench fiburization process, melt spinning and a well-established metallic glass alloy, $Fe_{80}P_{13}C_7$. Since the base alloy already contained C, solution strengtheners chosen were Si, B and Si + B, which were added in controlled amounts in such a way as to preserve the Fe-to-metalloid ratio. Alloys were made up in the following way:

A master alloy, $Fe_{80}P_{13}C_7$ was first prepared in massive amounts by induction-melting together appropriate quantities of Fe, Fe-C (4.14 wgt.%), and Fe-P (26.3 wgt.%). Similarly, ingots of $Fe_{80}B_{20}$ and $Fe_{80}Si_{20}$ were prepared from electrolytic iron and elemental B and Si*. When arbitrary amounts of the latter are added to the $Fe_{80}P_{13}C_7$ base, the $Fe_{80}Mtld._{20}$ relationship is always maintained.

Multicomponent alloys were prepared which contained 2, 5, 7 and 10 at.% B, Si and Si+B, respectively. Their full nominal compositions are given in Table 64.

Independently of the strengthening study several other alloys (such as Fe-B, Ni-B and Zr-Cu) were melt spun into ribbon fiber, and a series of experiments was carried out on $Fe_{80}P_{13}C_7$ itself in order to establish process parameters. The experimental details have already been described in Subsection 2.4, and a complete list of melt spinning experiments is given in Table 65.

---

* 99.999% Si, and 99.8% B in the form of 100-mesh crystalline powder.

TABLE 64. NOMINAL COMPOSITIONS OF B-DOPED AND (B+Si)-DOPED $Fe_{80}P_{13}C_7$ ALLOYS

Composition Code	Compositions in Atomic Percent				
	Fe	P	C	B	Si
FPC	80	13	7	0	0
FPCB-2	80	11.7	6.3	2	0
FPCB-5	80	9.8	5.3	5	0
FPCB-7	80	8.5	4.5	7	0
FPCB-10	80	6.5	3.5	10	0
FPCS-2	80	11.7	6.3	0	2
FPCS-5	80	9.8	5.3	0	5
FPCS-7	80	8.5	4.5	0	7
FPCS-10	80	6.5	3.5	0	10
FPCBS-2	80	11.7	6.3	1	1
FPCBS-5	80	9.8	5.3	2.5	2.5
FPCBS-7	80	8.5	4.5	3.5	3.5
FPCBS-10	80	6.5	3.5	5	5

TABLE 65. LIST OF MELT SPINNING EXPERIMENTS

Run Number	Composition or Composition Code
MS- 7	$Fe_{80}P_{13}C_7$ (FPC)
MS- 9	"
MS-10	"
MS-11	"
MS-12	"
MS-13	$(FeNi)_{80}B_{20}$
MS-15	$Fe_{80}B_{20}$
MS-16	$Ni_{50}B_{50}$
MS-17	$Zr_{43}Cu_{57}$
MS-19	FPCB-2
MS-20	FPCB-5
MS-21	FPCB-7
MS-22	FPCB-10
MS-23	FPCS-2
MS-24	FPCS-5
MS-25	FPCS-7
MS-26	FPCS-10
MS-27	FPCSB-2
MS-28	FPCSB-5
MS-29	FPCSB-7
MS-30	FPCSB-10

The melt spun ribbon fibers were subjected to numerous evaluation procedures --

- An extensive investigation of surface features was carried out using Nomarski differential interference-contrast microscopy.
- Structure was studied using electron diffraction, and transmission and scanning electron microscopy. This work was done through the courtesy of Dr. H. L. Gegel and his colleagues at the Air Force Materials Laboratory.
- Other structural studies were by x-ray diffraction, work which was carried out through the courtesy of Dr. S. D. Dahlgren, and by Dr. R. Wang of Battelle's Pacific Northwest Laboratory.
- An extensive series of microhardness measurements was made.
- Tensile tests were made on sets (10 or so to a set) of representative ribbon fibers using the technique described earlier in Subsection 4.4.

9.1 Surface Features of Rapidly-Quenched Filaments

The surface is an important characterizing feature of rapidly-quenched filaments and splats since these products are generally thin (thicknesses less than 50 μm), and possess relatively large surface area to volume ratios, typically 500 cm^2/cc. The product's surface features are influenced by and reflect the fluid flow/solidification phenomena inherent to the particular casting production processes. It is anticipated that the apparent strength and ductility values of the as-cast products are influenced by the surface structure of the samples.

Few data have been reported on the surface features of rapidly-quenched microcrystalline or amorphous products. Even fewer data are available on the interrelation of the sample's surface features

and (i) the filament/splat production variables, such as superheat, heat sink surface finish, etc., and (ii) the products properties, such as strength and ductility.

Typically, the two sides (i.e., the underside or heat sink contact side and the upper or free solidification side) of both the microcrystalline and the amorphous filaments and splats, prepared with a single heat sink system, are readily distinguishable to the naked eye due to differences in surface contour. The product's underside largely replicates the surface of the heat sink. Thus, if the heat sink is finished with 600 grit paper yielding a surface finish of about 15 μm RMS, the cast product will exhibit essentially a 15 μm RMS finish on its underside. The free solidification surface of crystalline materials typically exhibits shrinkage marks, relief dendrites, and mammiforms associated with a starved (decanted) surface. Generally, the free solidification surfaces of crystalline filaments and splats appear as the duller or less reflective surface. The upper surface of amorphous alloy products also exhibits a free solidification (i.e., decanted) surface; however, the extent of surface relief is generally less than with the crystalline materials, and the upper surface of amorphous filaments frequently appears as the shiny or more reflective of the two surfaces.

Several workers [34, 42-44] have noted that while large areas of the as-cast product's underside essentially replicate the heat sink surface, there are numerous areas of the underside which do not appear to have contacted or have lifted off the heat sink. These noncontact areas or holes (referred to as "lift-off" areas by Wood and Honeycombe[43]) in the filament/splat underside may be defects in the product and are generally considered to be areas of reduced heat transfer (i.e., lower quench rate areas) and potential stress intensifiers. The noncontact areas are observed in both crystalline and amorphous products.

A photomicrograph, prepared via Nomarski Differential Interference-Contrast (DIC) Microscopy, of the underside of a commercially-available amorphous ribbon fiber exhibiting noncontact areas is shown in Figure 71. As

(180X)

FIGURE 71. NOMARSKI DIC PHOTOGRAPH OF AS-CAST SURFACE (UNDERSIDE) OF AMORPHOUS ALLOY ($Ni_{40}Fe_{40}P_{14}B_6$) RIBBON FIBER

postulated by Wood and Honeycombe[43], the noncontact or lift-off areas could arise from several causes: (i) gas entrapment under the solidifying material, (ii) thermal contraction during solidification, and (iii) cavitation as a result of the shearing of the solidifying droplet over surface asperities on the substrate. The noncontact areas may also be caused by other liquid flow instabilities, such as capillary wave instability and/or Marangoni (surface tension variation) instability.

9.1.1 Experimental Study of Surface Features

As part of this project, a series of amorphous $Fe_{80}P_{13}C_7$ alloy ribbon filaments was chill block melt spun, using heat sinks with different, controlled surface finishes. The surface features of the filaments were examined to ascertain the effect of the heat sink surface finish on the occurrence/distribution of noncontact areas. In order to correlate the observed surface contour of the filament's underside with that of the free solidification side, a 127 μm diameter hole was drilled through the center of the filament and used as a fiducial mark. The pertinent data for these chill block melt spinning runs are given in Table 66 and photomicrographs of the melt spin filaments are shown in Figures 72 through 80.

TABLE 66. CHILL BLOCK MELT SPINNING RUNS*: EFFECT OF CHILL SURFACE FINISH ON SURFACE MORPHOLOGY

Melt Spinning Run No.	Chill Block Surface Finish	Average Thickness, μm	Ratio of Maximum Thickness to Average Thickness	Photomicrograph Figure No's.
MS-10	400 grit paper (25 RMS)	25.2	1.30	72, 73, and 74
MS-7	600 grit paper (17 RMS)	21.5	1.30	75 and 76
MS-9	Diamond Paste	19.3	1.32	77 and 78
MS-12	Linde A Compound	22.5	1.36	79 and 80

*All of the above runs were conducted in essentially one atmosphere or argon, with 500 μm diameter jets moving at about 5.4 meters per second onto a water-cooled copper disk rotating with a surface velocity about 27 meters per second. The disk was polished in the direction of rotation in all cases.

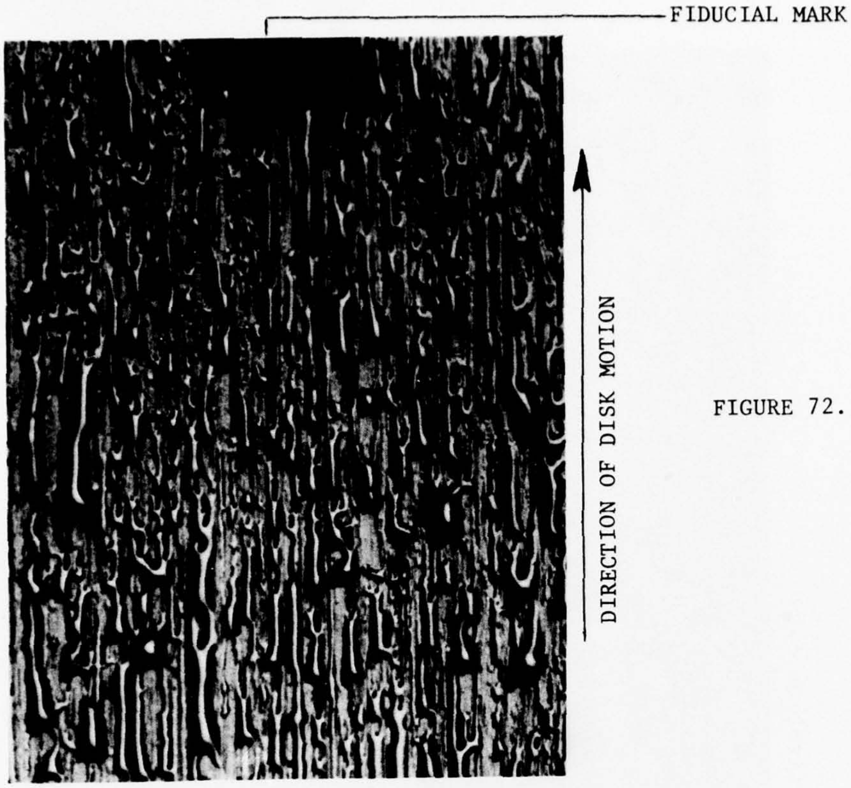

FIGURE 72. NOMARSKI DIC PHOTOGRAPH OF UNDERSIDE OF AS-CAST $Fe_{80}P_{13}C_7$ AMORPHOUS RIBBON FIBER (MS-10) 400 GRIT FINISHED DISK (180X)

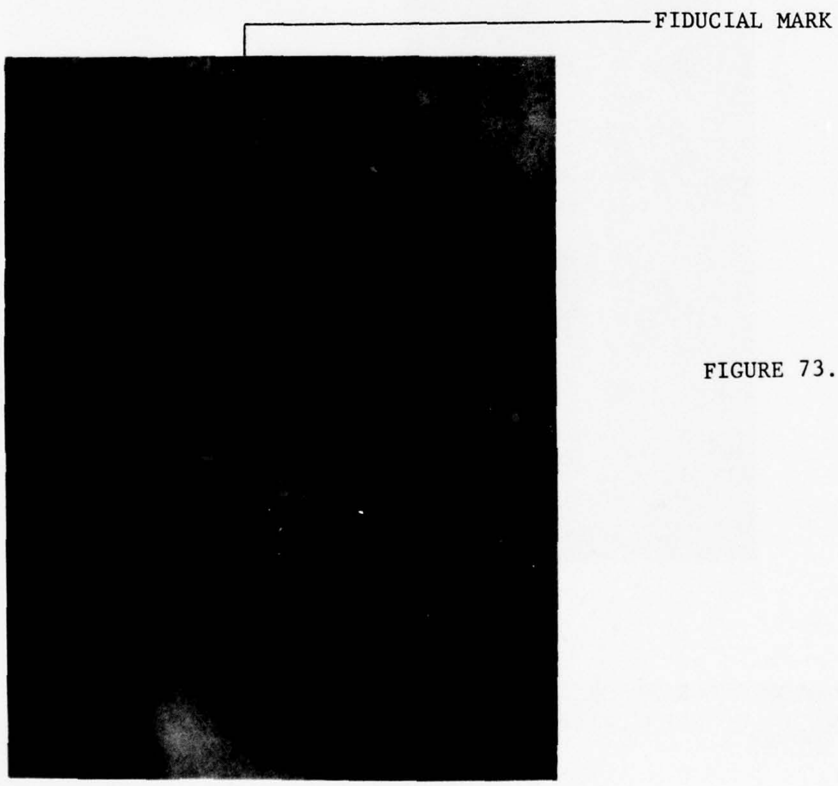

FIGURE 73. NOMARSKI DIC PHOTOGRAPH OF FREE SOLIDIFICATION SURFACE OF AS-CAST $Fe_{80}P_{13}C_7$ AMORPHOUS RIBBON FIBER (MS-10) 400 GRIT FINISHED DISK (180X)

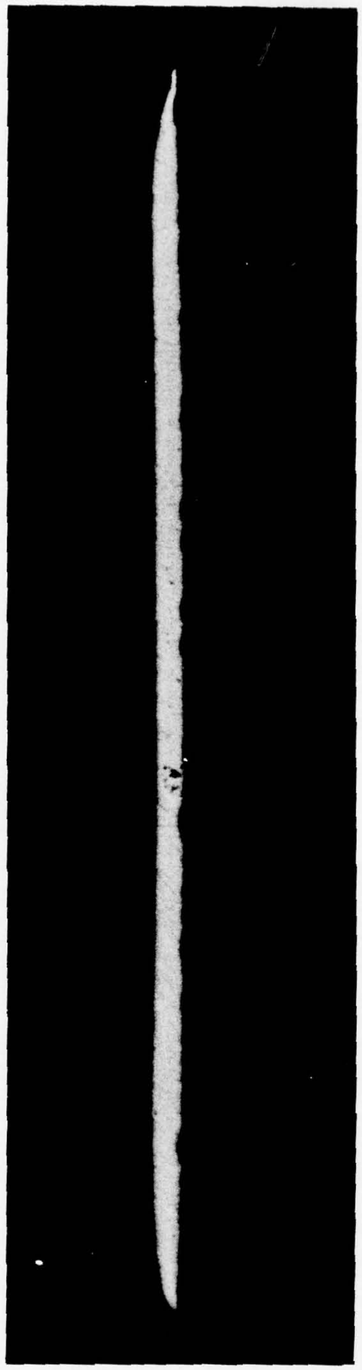

FIGURE 74. PHOTOMICROGRAPH OF TRANSVERSE SECTION OF MELT SPUN $Fe_{80}P_{13}C_7$ ALLOY RIBBON FILAMENT (MS-10) (200X)

FIDUCIAL MARK

DIRECTION OF DISK MOTION

FIGURE 75. NOMARSKI DIC PHOTOMICROGRAPH OF UNDERSIDE OF AS-CAST $Fe_{80}P_{13}C_7$ AMORPHOUS RIBBON FIBER (MS-7) (180X)

FIDUCIAL MARK

FIGURE 76. NOMARSKI DIC PHOTOMICROGRAPH OF FREE SOLIDIFICATION OF AS-CAST $Fe_{80}P_{13}C_7$ ALLOY FILAMENT. 600 GRIT FINISHED DISK (MS-7) (180X)

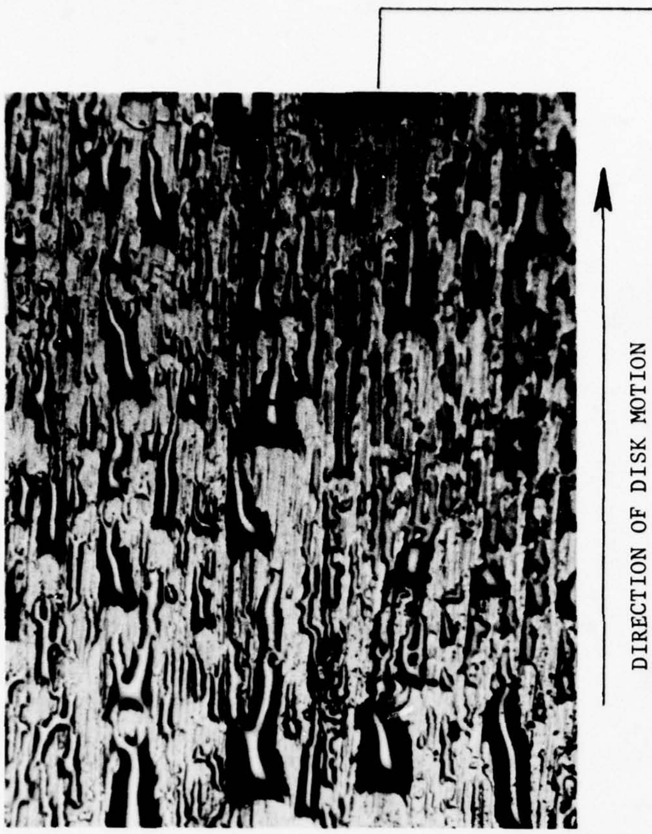

FIGURE 77. NOMARSKI DIC PHOTOMICROGRAPH OF UNDERSIDE OF AS-CAST $Fe_{80}P_{13}C_7$ ALLOY FILAMENT. 6 μm DIAMOND PASTE POLISHED DISK (MS-9) (180X)

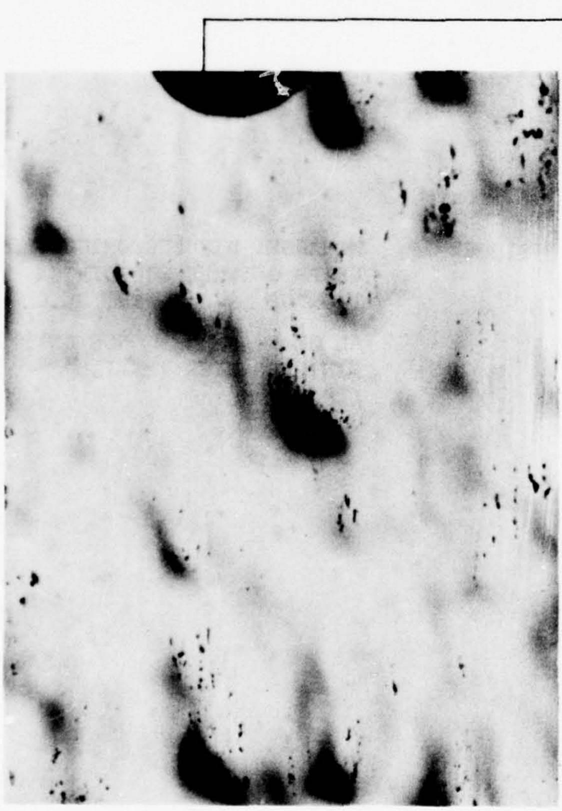

FIGURE 78. NOMARSKI DIC PHOTOMICROGRAPH OF FREE SOLIDIFICATION OF AS-CAST $Fe_{80}P_{13}C_7$ ALLOY FILAMENT 6 μm DIAMOND PASTE POLISHED DISK (MS-9) (180X)

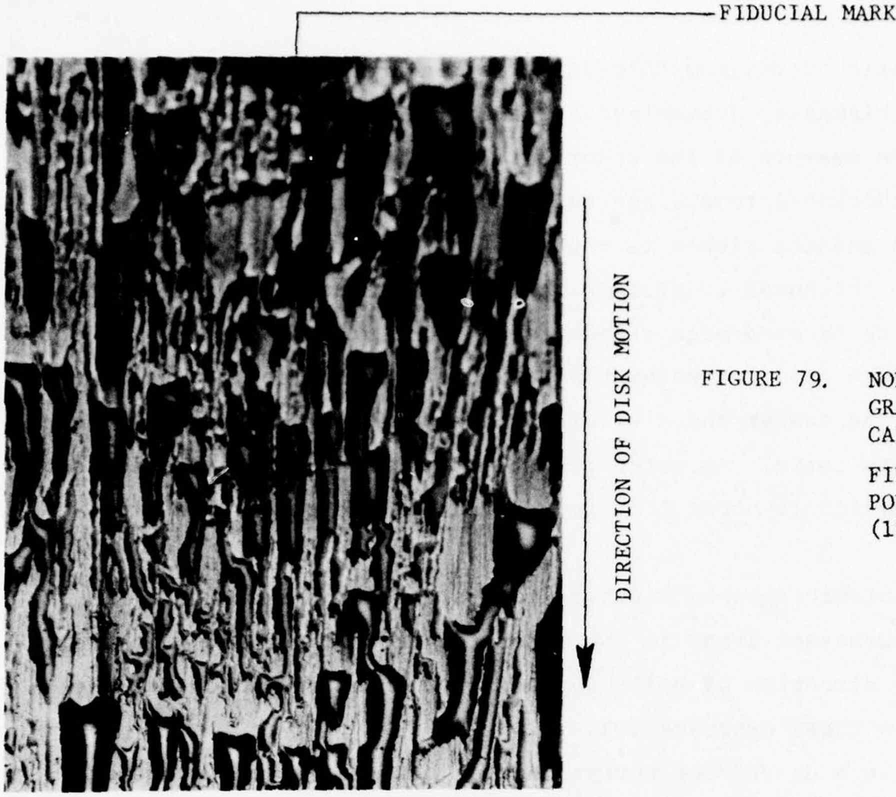

FIGURE 79. NOMARSKI DIC PHOTOMICROGRAPH OF UNDERSIDE OF AS-CAST $Fe_{80}P_{13}C_7$ ALLOY FILAMENT. LINDE A POLISHED DISK (MS-12) (180X)

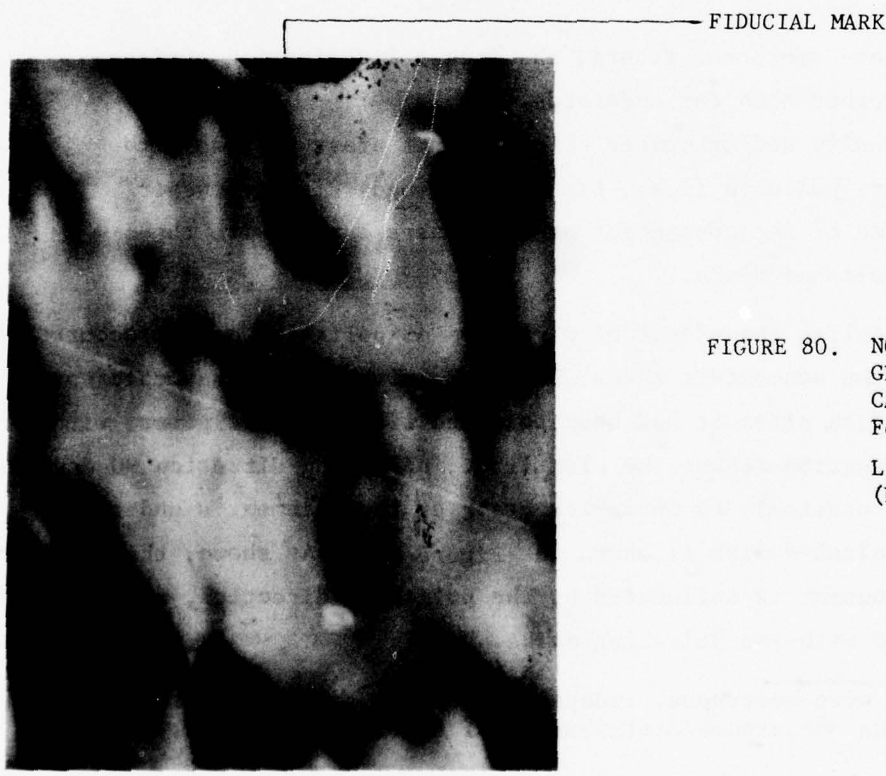

FIGURE 80. NOMARSKI DIC PHOTOMICROGRAPH OF FREE SOLIDIFICATION OF AS-CAST $Fe_{80}P_{13}C_7$ ALLOY FILAMENT LINDE A POLISHED DISK (MS-12) (180X)

The ratio of maximum thickness, as measured with a micrometer, to the average thickness, determined by weight-length-density data, is a semi-quantitative measure of the occurrence of noncontact areas in a sample. If the maximum thickness-to-average thickness ratio is unity, there are no noncontact areas and the ribbon is rectangular. It should be noted that the ratio of maximum thickness to average thickness is expected to be greater than unity for the tapered-edge ribbon (see Figure 74). However, the observed tapered edge only increases the ratio of thicknesses to a value of about 1.05. As the number and size of the noncontact areas increase, so does the thickness ratio. As noted in Table 66, the thickness ratio associated with the samples is about 1.3, independent of the particular disk surface finish.

The photomicrographs indicate four significant features:

(1) The noncontact areas in the underside are aligned and oriented in the direction of polishing and disk rotation (which was the same in these experiments).

(2) There is a one-to-one correspondence between large noncontact areas on the underside and elevations (hills) on the free surface sides.

(3) For these amorphous fibers, the free solidification surface is smoother than the underside.*

(4) The density and/or number of noncontact areas is less with the more polished (i.e., Linde A polished) disks; however, the size of the noncontact areas appears larger with the more polished disks.

To establish the effect of direction of polishing on the occurrence/distribution of the noncontact areas, $Fe_{80}P_{13}C_7$ ribbon fiber was melt spun from the copper disk after it had been polished with 400 grit paper, with the polishing direction across the disk (i.e., polishing direction 90 degrees to direction of rotation). A photomicrograph of the filament's underside from the cross-polished disk is shown in Figure 81. As shown, the orientation of the noncontact is influenced by the polishing direction, with most of the areas aligned with the polishing marks.

---

*All the ribbons were amorphous, independent of the chill block surface finish and/or the occurrence/distribution of the lift-off areas.

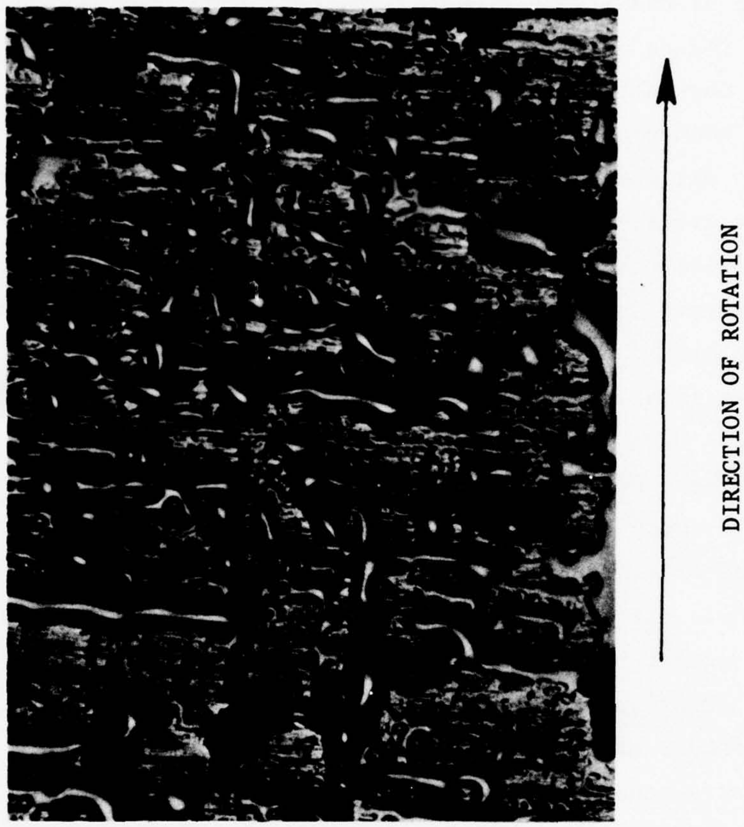

(180X)

FIGURE 81. NOMARSKI DIC PHOTOMICROGRAPH OF UNDERSIDE OF AS-CAST $Fe_{80}P_{13}C_7$ AMORPHOUS RIBBON FIBER 400 GRIT CROSS POLISH

To assess whether or not the noncontact areas were associated with entrapment of gas under the solidifying material, another chill block melt spinning run was conducted with $Fe_{80}P_{13}C_7$ alloy, wherein the casting was done under reduced gas pressure (i.e., about 1500 microns partial pressure argon). The disk was polished with 600 grit paper with the polishing direction parallel to the disk direction of rotation. A photomicrograph of the filament underside, cast under the reduced pressure, is shown in Figure 82.

Casting under reduced gas pressure or vacuum did not significantly alter the occurrence/distribution of the noncontact areas. These observations do not preclude gas entrapment as a mechanism of formation for the noncontact areas, since there may have been a remnant adsorbed layer of gas on the chill-block surface or the particular alloy $Fe_{80}P_{13}C_7$ may have contained a significant quantity of dissolved gas. However, the observed noncontact areas on ribbon cast in vacuum does indicate that bulk gas entrainment (i.e., incorporation of the atomosphere gas between the liquid pool and the heat sink) is not the sole cause of concontact areas.

The occurrence of noncontact areas was observed to be dependent on the alloy composition. For example, under nearly identical casting conditions, significantly fewer noncontact areas were observed on melt spun and melt extracted $Fe_{80}B_{20}$ amorphous fibers than with the $Fe_{80}P_{13}C_7$ alloy. However, this observation does not permti selection of any of the proposed formation mechanisms relative to the others, since each of the proposed causes of noncontact areas would be anticipated to be alloy-composition dependent.

9.1.2 Discussion

Noncontact or lift-off areas are features generally associated with rapidly quenched filaments and splats. Observations have indicated that the occurrence and distribution of the noncontact areas are influenced by the heat sink's surface finish and that the lift-off phenomenon is not solely due to gas entrainment. We believe that the noncontact areas are due to either cavitation induced by disk surface asperities or by a surface tension or solidification instability associated with the rapid-

quenching system. The occurrence/distribution of the noncontact areas would be expected to depend on the heat sink surface finish in each of the above formation mechanisms/models.

Although the occurrence of holes and/or areas of noncontact between the solidified alloy and the heat sink have been reported in ingot and rod casting experiments we believe that the noncontact areas associated with rapidly quenched products differ from the noncontact areas reported in the above two references dealing with materials solidified under lower quench rate conditions. We anticipate that higher quench rates and/or thicker amorphous materials could be obtained, if casting procedures were found in which the noncontact areas could be eliminated or significantly reduced. Further research is required to resolve the formation mechanism of the noncontact areas and their influence on heat transfer and cooling from the remainder of the fiber and, their influences on the properties of the rapidly quenched products.

(180X)

FIGURE 82. NOMARSKI DIC PHOTOMICROGRAPH OF UNDERSIDE OF AS-CAST $Fe_{80}P_{13}C_7$ RIBBON 600 GRIT POLISH, REDUCED GAS PRESSURE CONDITIONS (180X)

(180X)

FIGURE 83. NOMARSKI DIC PHOTOMICROGRAPH OF PENDANT DROP MELT EXTRACTED $Fe_{80}P_{13}C_7$ FIBER UNDERSIDE CAST IN VACUUM (5 X 10^{-3} mm Hg) (180X)

9.2 Transmission Electron Microscopy of Metallic Glass Ribbons

Electron microscopy was performed on a few representative FPC-base alloys. In none of the alloys studied, namely $Fe_{80}P_{13}C_7$ itself as well as FPCB-5, FPCB-7 and FPCS-5, was evidence for crystallinity detected. Of particular interest are the transmission electron micrographs for FPC, Figure 84, in which precipitates some 1000 Å in diameter can be seen. Although the particles are some 30 times smaller, the effect is similar to that seen in melt-spun Alloy 4 (Figures 66a,b, 66c,d, and 66e,f). Selected area diffraction indicated that the particles, whatever they were, were just as amorphous as the matrix. If the particles are a decomposition product forming as a result of some slight aging of the ribbon fiber, it is surprising that they are not crystalline, as the results of such decomposition generally are. On the other hand, some glasses decompose into two glassy phases. It would be interesting to determine if we are observing such an effect in FPC. Clearly further work on this very important subject is needed.

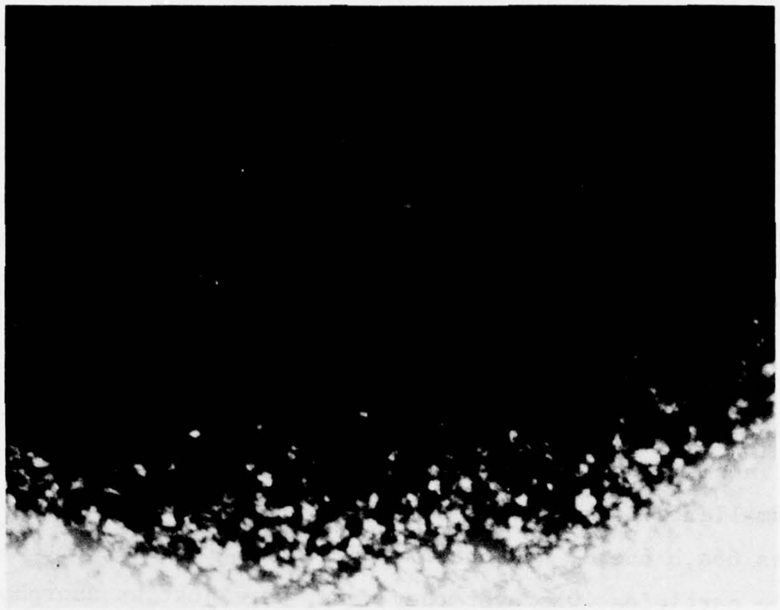

~ 30,000X

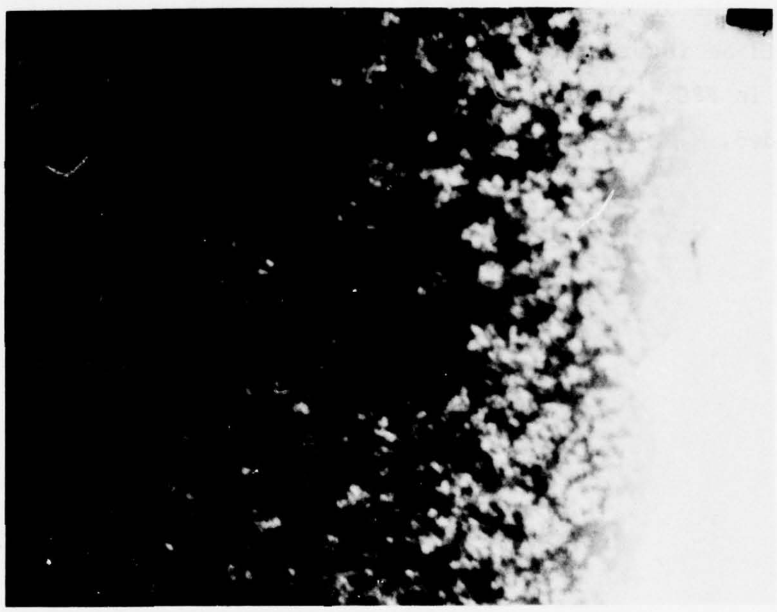

~ 40,000X

FIGURE 84. TRANSMISSION ELECTRON MICROGRAPHS OF $Fe_{80}P_{13}C_7$

9.3 X-Ray Diffraction Studies of Melt-Spun Ribbon Fibers

9.3.1 X-Ray Diffraction Photographs

X-ray diffraction studies were carried out, by Dr. R. Wang of Battelle's Pacific Northwest Laboratory, on the following metallic glass ribbon fiber selected from Table 64:

- FPC
- FPCB-2
  FPCP-7
  FPCP-10
- FPCS-5
- FPCBS-2
  FPCBS-7

Some representative photographs, those for FPC, FPCS-5, FPCB-7 and FPCSB-7, are given in Figure 85. They were taken with a Unicam camera using Fe-K_{α} radiation; two or three layers of the ribbon being necessary to obtain sufficient diffraction intensity. All samples measured showed the diffuse ring patterns characteristic of the amorphous structure.

9.3.2 X-Ray Diffractometer Studies

Sample FPCB-7 was further investigated by diffractometer step-scanning at the rate of 0.03°/min. The results of the diffraction experiment, obtained with two layers of sample mounted on a glass slide, are given in Figure 86; in which we see the rounded first diffraction peak at 44.5 degrees situated on the wing of a peak (partly shown) due to the glass slide. A second peak at 79 degrees is also present.

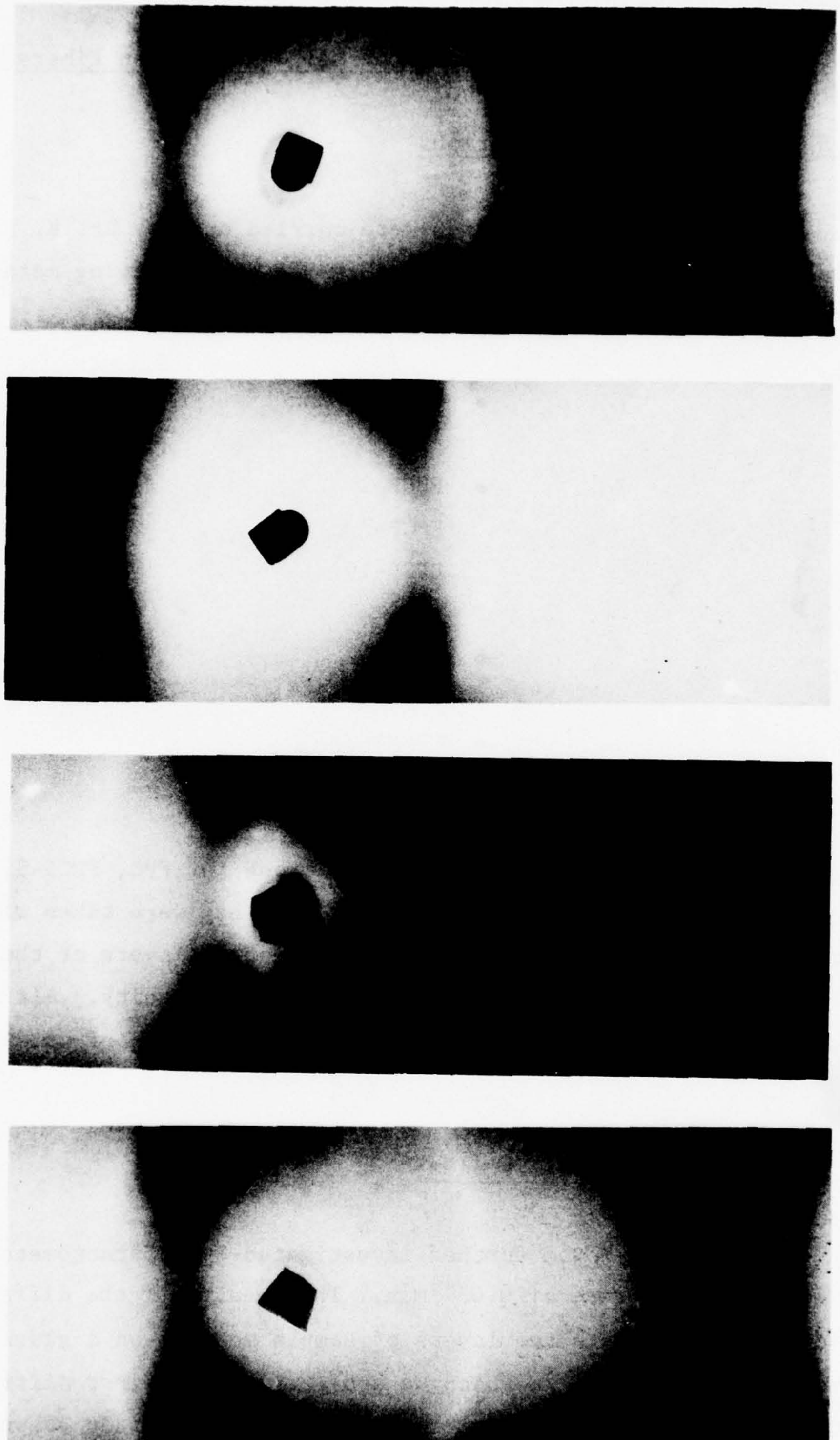

(a) FPC

(b) FPCS-5

(c) FPCB-7

(d) FPCSB-7

FIGURE 85. X-RAY DIFFRACTION PHOTOGRAPHS FOR $Fe_{80}P_{13}C_7$ AND RELATED ALLOYS

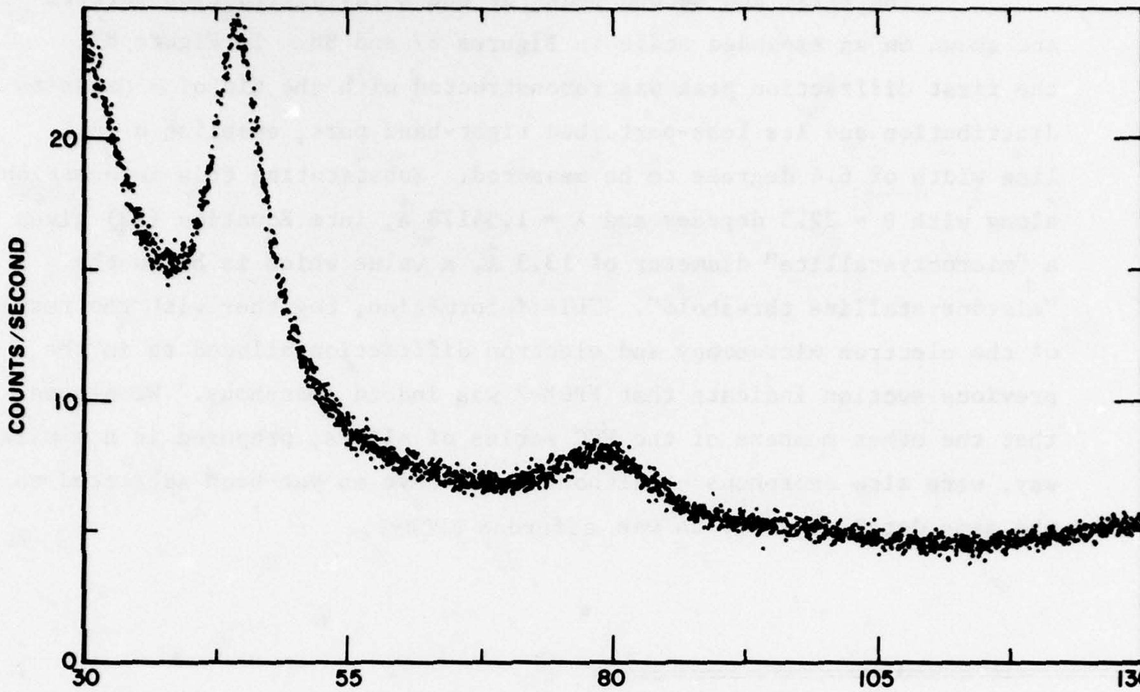

FIGURE 86. X-RAY DIFFRACTION SCAN FOR FPCB-7

As pointed out in the literature [e.g., 10], the width of a diffraction intensity peak for a microcrystalline alloy can be used to calculate a crystallite size, L, with the aid of the Scherrer formula:

$$L = \frac{51\ \lambda}{B\ \cos\theta}\ , \qquad (13)$$

where λ is the wavelength, B the full width of the diffraction line at half intensity (in degrees) and θ is the diffraction angle as defined in Figure 86. The quantity, L, makes an excellent bench-mark by which to judge the existence of an amorphous structure; since as shown in Table 67, amorphous alloys are characterized by a "microcrystallite diameter" of less than about 14 $\pm$ 2 Å.

The first and second peaks of the x-ray diffraction pattern are shown on an expanded scale in Figures 87 and 88. In Figure 87, the first diffraction peak was reconstructed with the aid of a Gaussian distribution and its less-perturbed right-hand part, enabling a full-line width of 6.4 degrees to be measured. Substituting this information, along with $\theta = 22.3$ degrees and $\lambda = 1.54178$ Å, into Equation (13) gives a "microcrystallite" diameter of 13.3 Å, a value which is below the "microcrystalline threshold". This information, together with the results of the electron microscopy and electron diffraction alluded to in the previous section indicate that FPCB-7 was indeed amorphous. We assume that the other members of the FPC series of alloys, prepared in a similar way, were also amorphous -- although none have as yet been subjected to the same detailed study as was afforded FPCB-7.

Alloy	"Crystallite" Diameter, L (A°)
$Fe_{75}P_{15}C_{10}$	15.7
$Fe_{44}Pd_{36}P_{20}$	13.6
$Mn_{75}P_{15}C_{10}$	14.5
$Ni_{53}Pd_{27}P_{20}$	11.7
$Ni_{41}Pd_{41}B_{18}$	12.4
$Pd_{80}Si_{20}$	14.6
$Pd_{80}Si_{10}Ge_{10}$	15.8
Average Crystallite Diameter	14 $\pm$ 2

TABLE 67. MICROCRYSTALLITE DIAMETER", CALCULATED BY APPLYING THE SCHERRER FORMULA, TO THE FIRST INTENSITY PEAK OF THE X-RAY DIFFRACTION PATTERN- AFTER TAKAYAMA[10] AND SINHA AND DUWEZ[47].

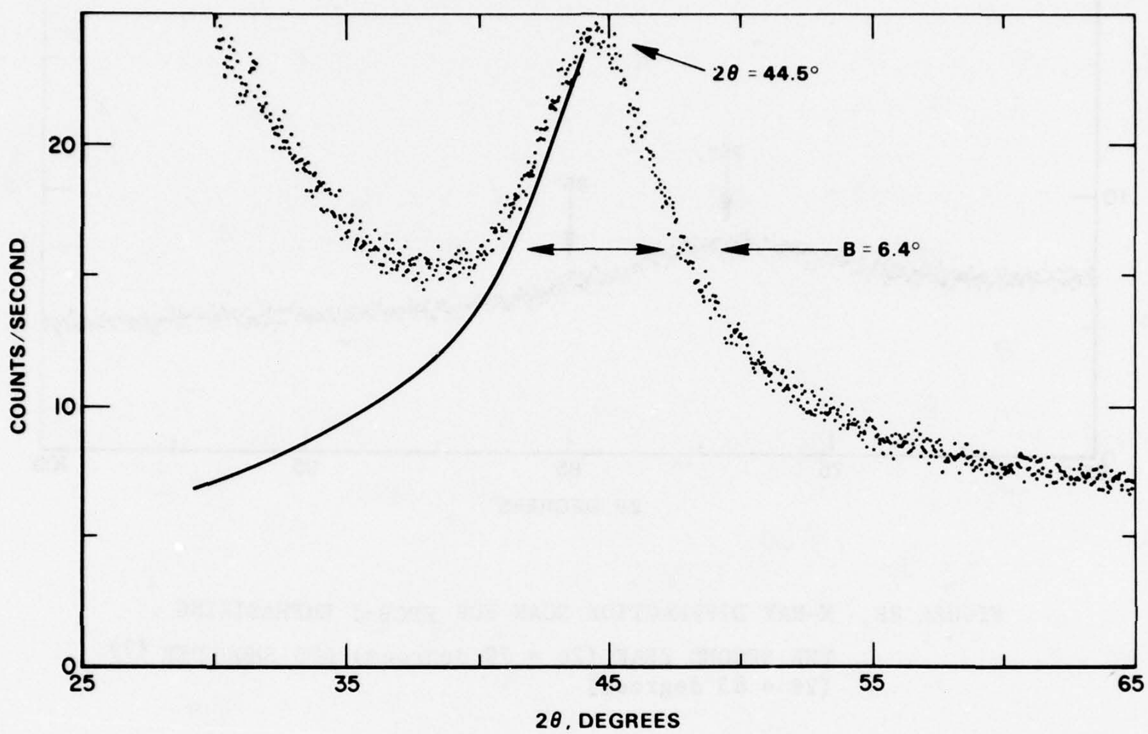

FIGURE 87. X-RAY DIFFRACTION SCAN FOR FPCB-7 EMPHASIZING THE FIRST DIFFRACTION PEAK

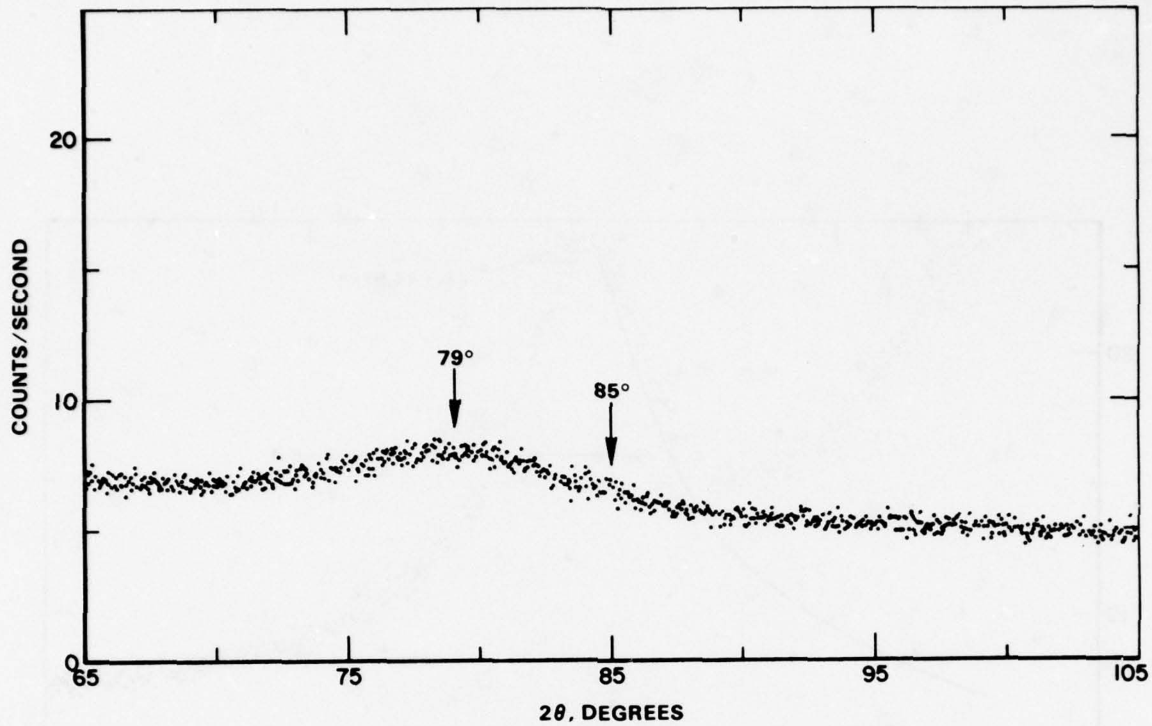

FIGURE 88. X-RAY DIFFRACTION SCAN FOR FPCB-7 EMPHASIZING THE SECOND PEAK (2θ = 79 degrees) AND SHOULDER (?) (2θ = 85 degrees)

Figure 88 shows the second diffraction peak presented on an expanded scale in a search for a shoulder on the high-angle side. The presence of such shoulders can be taken as evidence for the existence of amorphous structure appearing as they do in the results of certain computer calculations. It does seem, however, that the shoulder is a sufficient but not necessary condition for amorphousness, since it has been shown to be absent in the diffraction results for a series of amorphous Ni-Pt-P alloys[47]. In the present case, a trace of shoulder can just be noticed at 85 degrees.

9.4 Hardness Studies of Melt-Spun Ribbon Fibers

Hardness measurements were carried out on a selection of Fe-P-C based metallic glass ribbons using the techniques described in Sub-section 4.2.2. After determining a suitable value of load (25g) and after checking the accuracy of our techniques with the aid of a standard steel hardness block, we explored procedures for conveniently and rapidly mounting the ribbon fibers for measurement.

9.4.1 Mounting Ribbon Fiber for Hardness Measurement

The ribbon fibers were typically 1 mm in width and 0.02 mm thick. The questions to be answered were: how to mount the ribbon, and where to place the impressions. Samples could be mounted in metallographic mounts with the edges or ends exposed to the indentor; or they could be simply attached to a flat surface such as a glass microscope slide, and impressions made into either the "top" or "bottom" ribbon surface, depending on which one was exposed. We finally decided to attach the ribbon with double-stick tape to a glass slide such that the smoother "top" surface of the ribbon was exposed to the indentor. The experiments which indicated that the results so obtained were equivalent to those obtainable *via* any of the other modes indicated above are outlined in the following.

(a) Hardness Differential Between "Top" and "Bottom" Sides of the Ribbon Fiber

As indicated in Sub-section 9.1, and particularly figure-pairs such as Figures 75 and 76 and Figures 77 and 78, etc., the smoother top surface is much the more suitable one from which to obtain hardness impressions. To determine whether possible differences in quench rates or surface conditions resulted in significant differences in hardness value, appropriate experiments were carried out, the results of which are given in Table 68.

The hardness values listed in the last column of Table 68 agree to within one standard deviation of each other, and therefore do not differ significantly.

TABLE 68. HARDNESSES OF TOP AND BOTTOM SURFACES OF METALLIC GLASS RIBBON FIBER.

Alloy	Surface	Number of Impressions	Hardness Number (kg/mm^2)
FPC	Top	25	1093 $\pm$ 107
	-	19	1095 $\pm$ 65
FPC	Bottom	28	1012 $\pm$ 62
	-	22	1012 $\pm$ 44

(b) <u>Hardness Differentials Between Edges, Ends and Surfaces; and Between the Results of Different Mounting Procedures</u>

Using FPCB-10 as test material, samples were mounted edge-up and end-up in metallographic mounts, and smooth-face up on a glass microscope slide with double-stick tape. Table 69 gives an intercomparison of hardness values obtained under these various conditions. The results of Table 69 indicate no significant differences.

As an additional precaution, we also looked specifically for a possible influence on the results of the resilience of the double-stick tape. For several specimens we compared hardness values made on a sample in direct contact with glass, with those made on samples attached with tape to glass along their entire lengths. The null results of these experiments, as presented in Table 70, assured us that the straightforward procedure, in which tape was an intermediate layer between the ribbon and the glass substrate, was quite valid.

TABLE 69. INTERCOMPARISON OF EDGE, FACE, AND END HARDNESS AND TWO METHODS OF SAMPLE MOUNTING. SAMPLE FPCB-10.

Substrate	Impression Directed Parallel to:	Number of Impressions	Hardness Number (kg/mm^2)
Tape on glass slide	Thickness	26 23	1091 ± 66 1081 ± 46
Green bakelite	Length	22 17	1175 ± 51 1178 ± 43
Green bakelite	Width	21 17	1100 ± 66 1096 ± 44

TABLE 70. HARDNESS VALUES UNDER TWO MOUNTING CONDITIONS -- (a) SAMPLE DIRECTLY IN CONTACT WITH GLASS, (b) SAMPLE ATTACHED TO GLASS WITH DOUBLE-STICK TAPE

Sample Name	Substrate	Number of Impressions	Hardness Number (kg/mm^2)
FPCS-2	Glass	19	904 ± 30
	Tape + glass	45	897 ± 26
FPCS-5	Glass	14	883 ± 40
	Tape + glass	46	903 ± 30
FPCS-7	Glass	22	874 ± 41
	Tape + glass	52	922 ± 31
FPCS-10	Glass	18	1003 ± 39
	Tape + glass	53	1103 ± 45

(c) Geometrical Considerations

The diagonal lengths of the square hardness impressions were typically 6.5 μm under the conditions of these experiments. The shape of the indenter then dictated an impression depth of 0.143 x 6.5 μm, which is 1/20 of the thickness of the (~0.02 mm thick) ribbon fiber. The depth of the impression is thus safely within the allowable minimum, viz. 1/10 sample thickness.

9.4.2 Results of Hardness Measurements on Melt-Spun Ribbon Fiber

Hardness measurements were made on each of the thirteen alloys listed in Table 64 and on $Fe_{80}B_{20}$. Some 20 to 60 impressions were made on each alloy in order to obtain good statistics, and in each case a comparison was made between the hardnesses of the melt-spun ribbon fiber and the ingot melt stock. This work, which involved the measurement of more than two thousand impression diagonals is summarized in Table 71.

TABLE 71. HARDNESS VALUES OF FOURTEEN METALLIC GLASS RIBBONS (AND COMPARISONS WITH THE AS-CAST STARTING MATERIALS)

Alloy Name	(Number of Impressions) Crystalline Melt Stock		Hardness Value, kg/mm^2 Metallic Glass Ribbon	
$Fe_{80}B_{20}$	(41)	728 ± 138	(46)	1035 ± 52
	(32)	688 ± 86	(36)	1031 ± 33
FPC	(30)	1100 ± 105	(25)	1093 ± 107
	(21)	1090 ± 53	(19)	1095 ± 65
FPCB-2	(36)	1163 ± 54	(36)	997 ± 60
	(33)	1165 ± 45	(29)	990 ± 43
FPCB-5	(34)	1258 ± 62	(26)	1072 ± 54
	(27)	1252 ± 40	(21)	1070 ± 33
FPCB-7	(31)	1349 ± 113	(28)	1091 ± 51
	(24)	1337 ± 73	(24)	1105 ± 38
FPCB-10	(26)	1262 ± 121	(26)	1091 ± 66
	(18)	1287 ± 67	(23)	1081 ± 46
FPCS-2	(44)	867 ± 54	(53)	899 ± 38
	(30)	862 ± 35	(45)	897 ± 26
FPCS-5	(44)	893 ± 68	(52)	908 ± 46
	(36)	886 ± 42	(46)	903 ± 30
FPCS-7	(60)	826 ± 120	(62)	930 ± 46
	(38)	822 ± 71	(52)	922 ± 31
FPCS-10	(54)	842 ± 47	(67)	1110 ± 61
	(44)	839 ± 32	(53)	1103 ± 45
FPCSB-2	(44)	950 ± 115	(53)	934 ± 37
	(28)	944 ± 66	(44)	936 ± 23
FPCSB-5	(54)	900 ± 62	(58)	972 ± 45
	(42)	884 ± 29	(45)	974 ± 29
FPCSB-7	(51)	896 ± 49	(69)	945 ± 38
	(44)	898 ± 33	(58)	940 ± 23
FPCSB-10	(53)	930 ± 59	(59)	960 ± 24
	(39)	935 ± 31	(50)	959 ± 18

9.4.3 Discussion of the Hardness Data

The results of the hardness study are not in themselves conclusive, but raise a number of interesting comments warranting further investigation.

(a) Hardness of the as-cast as-cast ingot starting material, which contains intermetallic compounds formed between iron and a metalloid, is expected to be high; while that of the corresponding metallic glass which possesses some ductility, is expected to be significantly lower. This expectation is met only in the case of the FPCB series of alloys. In some systems there is little change in going from as-cast to metallic glass, as in FPC and the FPCSB series, while $Fe_{80}B_{20}$ is much less hard in the as-cast condition.

(b) In the metallic glasses, there is a slight trend towards increasing hardness with the addition of B, Si, and B + Si, however, the change is nowhere near as rapid as we had expected. This is probably related to the phenomenon which confers on "unalloyed" glassy FPC its unusual hardness.

(c) Compared to sputtered FPC, and related metallic glass ribbon fibers referred to in the literature, which together have an average hardness of about 780 kg/mm^2 (Table 52), the sample of $Fe_{80}P_{13}C_7$ made under this program with a hardness number of 1090 kg/mm^2 is exceptional.

(d) Taking FPC as an example, the high hardness value compared to that of canonically amorphous sputtered material suggested that the melt-spun ribbon was not fully amorphous. This opinion was reinforced by the observation that the hardness of the ribbon was actually equal to that of the cast starting material. To pursue this problem, we embarked on the electron diffraction and x-ray diffraction

investigations described earlier in this section, in which no evidence for crystallinity was detected in any of the alloys studied. As a result we are lead to the conclusion that the melt-spun ribbon, although amorphous, had been collected in what is equivalent to an aged condition. Either the quench rate was not quite fast enough, to achieve optimal amorphousness, or some post-heating of the ribbon took place after ejection from the wheel surface. Usually the first tangible results of aging in metallic glasses takes the form of crystallite nucleation[48]. As mentioned above, however, we found no evidence for departures from amorphousness, suggesting that some kind of precursor aging reaction can take place even in the amorphous state prior to any crystallization. This is a possibility that warrants further detailed investigation.

As far as the strengthening investigation is concerned, some traces of additional-element hardening are evident for example in the data for the FPCS series, however, the effect we were seeking is possibly masked by the excessive initial hardness of FPC itself, and by additional contributions to the hardnesses of the multicomponent alloys through the postulated aging effect.

9.5 Tensile Properties of Melt-Spun Ribbon Fiber

9.5.1 Elastic Modulus

Elastic modulus was determined from the measured longitudinal acoustic wave velocity through the usual formula $v = \sqrt{E/\rho}$. ρ is here the density of the crystalline starting material, no correction being applied for the 1-3% lower density of the metallic glass structure.

Sound velocities were measured at WPAFB through the courtesy of Dr. M. L. Gegel, Program Monitor. The results of a typical density determination are given in Table 72. The procedure outlined was repeated for each of the fourteen Fe-base metallic glass ribbon materials.

TABLE 72. DENSITY OF FPCBS-7, $Fe_{80}P_{8.5}C_{4.5}B_{3.5}Si_{3.5}$

Weight of specimen in air	7.42600 g
Weight of specimen + suspension in water	6.43500 g
Weight of suspension in water	0.02025 g
Weight of specimen in water	6.41475 g
Loss of weight	1.01125 g
Density of water (20·5°C)	0.9981 g/cc
Volume of specimen	1.01318 cc
DENSITY OF SPECIMEN	7.329 g/cc

9.5.2 Estimated Strengths

Strengths were estimated by combining hardness data (Table 70) and acoustic modulus data in the Marsh Formula (Equation (10) in the manner described in Subsections 4.3.1 and 4.3.2. The results are presented in Table 73, 74, and 75, from which we draw the following conclusions.

(a) E/H Correlation

The correlation coefficient between E and H for all the alloys of Table 73 except $Fe_{80}B_{20}$ is 0.91; for the alloys of Table 74, except FPCS-10, it is 0.89; and for those of Table 75, except FPCBS-10, it is 0.91; indicating that E and H are highly correlated. The correlation coefficient between E and H for all the data except those for $Fe_{80}B_{20}$, FPCS-10, and FPCBS-10, is 0.81; and the mean value of E/H is 13.6 $\pm$ 0.8.

TABLE 73. MODULUS, HARDNESS AND ESTIMATED YIELD STRENGTH - I

Alloy Name	Sound Velocity, v (km/s)	As-Cast Density, ρ (g/cc)	Young's Modulus, E ($10^3 kg/mm^2$)	Hardness, H (kg/mm^2)	Estimated Yield Strength, Y (kg/mm^2)	Estimated Yield Strength, Y (ksi)	Specific Strength ($10^5 cm$)	$\frac{E}{Y}$	$\frac{H}{Y}$	$\frac{E}{H}$
$Fe_{80}B_{20}$	5.46	7.40[1]	22.1	1031	422	600	57	52	2.4	21.4
FPC	4.49	7.312[2]	14.7	1095	531	755	73	28	2.1	13.4
FPCB-2	4.20	7.325	12.9	990	486	691	66	27	2.0	13.0
FPCB-5	4.47	7.326	14.6	1070	515	733	70	28	2.1	13.6
FPCB-7	4.62[3]	7.338	15.7	1105	524	745	71	30	2.1	14.2
FBPC-10	4.38	7.373	14.1	1081	530	754	72	27	2.0	13.0

[1] From Reference [25].

[2] Average of 7.311 and 7.313

[3] Average of 5.114, 4.924, 4.591, 4.443, 4.037.

TABLE 74. MODULUS, HARDNESS AND ESTIMATED YIELD STRENGTH - II

Alloy Name	Sound Velocity, v (km/s)	As-Cast Density, ρ (g/cc)	Young's Modulus, E ($10^3 kg/mm^2$)	Hardness, H (kg/mm^2)	Estimated Yield Strength, Y (kg/mm^2)	Estimated Yield Strength, Y (ksi)	Specific Strength ($10^5 cm$)	$\frac{E}{Y}$	$\frac{H}{Y}$	$\frac{E}{H}$
FPC	(Listed Previously)		14.7	1095	531	755	73	28	2.1	13.4
FPCS-2	4.18	7.236	12.6	897	427	607	59	30	2.1	14.0
FPCS-5	4.27[1]	7.214	13.2	903	423	602	59	31	2.1	14.6
FPCS-7	4.37	7.240	13.8	922	428	609	59	32	2.2	15.0
FPCS-10	5.06	7.265	18.6	1103	490	697	67	38	2.3	16.9

[1] Average of 4.674 and 3.875.

TABLE 75. MODULUS HARDNESS AND ESTIMATED YIELD STRENGTH - III

Alloy Name	Sound Velocity, v (km/s)	As-Cast Density, ρ (g/cc)	Young's Modulus, E (10^3kg/mm^2)	Hardness, H (kg/mm^2)	Estimated Yield Strength, Y (kg/mm^2)	Estimated Yield Strength, Y (ksi)	Specific Strength (10^5cm)	$\frac{E}{Y}$	$\frac{H}{Y}$	$\frac{E}{H}$
FPC	(Listed Previously		14.7	1095	531	755	73	28	2.1	13.4
FPCBS-2	4.19	7.275	12.8	936	450	641	62	28	2.1	13.7
FPCBS-5	4.20	7.292	12.9	974	475	675	65	27	2.1	13.2
FPCBS-7	3.97[1]	7.329	11.6	940	472	672	64	25	2.0	12.3
FPCBS-10	4.50	7.323	14.8	959	440	626	60	34	2.2	15.4

[1] Average of 3.976, 3.799, and 4.128.

It follows that for certain classes of alloy E/H is a fixed ratio in accordance with earlier observations by Davis et al[40]. If then we can rely on the existence of a valid relationship between H and Y only ONE measurement is needed to obtain all three mechanical properties E, H, and Y.

(b) H/Y Relationship

In Tables 73, 74 and 75, the quotient E/Y seems rather small; and H/Y, with an average value of 2.1 ± 0.1 is definitely too small. In agreement with Davis[21], we conclude that metallic glasses, at least the class of glass considered here, do not conform to the Marsh Theory.

The H/Y values in Table 76 have been recorded in the literature:

TABLE 76. EXPERIMENTALLY DETERMINED H/Y VALUES

Alloy	H (kg/mm^2)	Y (kg/mm^2)	H/Y	Reference
$Pd_{77.5}Cu_6Si_{16.5}$	498	157	3.17	[25]
$Pd_{40}Ni_{40}P_{20}$	452	158	2.86	[25]
$Fe_{80}P_{20}$	755	236	3.20	[25]
$Fe_{80}B_{20}$	1100	370	2.97	[25]
$Fe_{80}P_{16}C_3B_1$	835	249	3.35	[25]
$Ni_{36}Fe_{32}Cr_{14}P_{12}B_6$	880	278	3.17	[25]
$Ni_{49}Fe_{29}P_{14}B_6Si_2$	792	243	3.26	[21]
$Fe_{72}P_{16}C_5Si_2Al_5$	770	--	3.67	[21]
$Fe_{76}P_{16}C_4Si_2Al_2$	--	210	3.67	[21]
$Ti_{50}Be_{40}Zr_{10}$	740	231	3.20	[25]
Average H/Y			3.2 ± 0.2	

Accordingly a new table has been constructed (Table 77) in which yield strengths and related quantities are computed from the relationship $Y = H/3.2$. Excluding the starred quantities, specific strengths in the FPCB series are about 45; in the FPCS series, about 39; and in the FPCBS series, about 41.

Again excluding the starred quantities, the ratio E/Y is constant within 6% standard error for the Fe_{80} alloy series, and equal to 43.8 ± 2.6. Thus by measuring only hardness and density the complete set of parameters H, E, and Y can be obtained for this class of alloy.

TABLE 77. YIELD STRENGTH AND RELATED QUANTITIES ESTIMATED FROM THE SEMI-EMPIRICAL RELATIONSHIP Y = H/3.2.

Alloy Name	Young's Modulus, E (10^3 kg/mm^2)	Hardness, H (kg/mm^2)	Estimated Yield Strength, Y = H/3.2 (kg/mm^2)	ksi	Specific Strength (10^5 cm)	$\frac{E}{Y}$
$Fe_{80}B_{20}$	22.1*	1031	322	458	44	69
FPC	14.7	1095	342	487	47	43
FPCB-2	12.9	990	309	440	42	42
FPCB-5	14.6	1070	334	476	46	44
FPCB-7	15.7	1105	345	491	47	46
FPCB-10	14.1	1081	338	480	46	42
FPCS-2	12.6	897	280	399	39	45
FPCS-5	13.2	903	282	401	39	47
FPCS-7	13.8	922	288	410	40	48
FPCS-10	18.6*	1103	345	490	47	54
FPCBS-2	12.8	936	293	416	40	44
FPCBS-5	12.9	974	304	433	42	42
FPCBS-7	11.6	940	294	418	40	39
FPCBS-10	14.8*	959	300	426	41	49

* Anomalously large E values.

REFERENCES

[1] Allen, R. P., Dahlgren, S. D., and Merz, M. D., Rapidly Quenched Metals, edited by Grant, N. J., and Geissen, B. C., M.I.T. Press 1975, 1037.

[2] Duwez, P., and Willens, R. H., Trans. Met. Soc., AIME 227 362 (1963).

[3] Toda, T., and Maddin, R., Trans. Met. Soc., AIME 245 1045 (1969); see also Roberge, R., and Herman, H., Mat. Sci. and Eng., 3 2 (1968).

[4] Beghi, G., Matera, R., and Piatti, G., J. Mater. Sci., 5 820 (1970). See also P. Pietrokowsky, Rev. Sci. Instrum. 34 445 (1963).

[5] Pond, R., and Maddin, R., Trans. Met. Soc., AIME, 245 2475 (1969).

[6] Chen, H. S., and Wang, T. T., J. Appl. Phys., 41 5338 (1970). See also Chen, H. S., and Miller, C. E., Rev. Sci. Instrum. 41 (1970).

[7] Chen, H. S., Leamy, H. J., and Barmatz, M., J. Non-cryst. Solids, 5 444 (1971).

[8] Pampillo, C. A., Scripta, Met., 6 915 (1972).

[9] Chen, H. S., Mat. Sci. and Eng., 25 59 (1976).

[10] Takayama, S., J. Mater. Sci., 11 164 (1976).

[11] Moss, M., Smith, D. L., and Lefever, R. A., Appl. Phys. Letters, 5 120 (1964).

[12] Pond, R. B., Sr., and Winter, J. M., Jr., Rapidly Quenched Metals ed. by Grant, N. J., ans Giessen, B. C., Section II, Mat. Sci. and Eng., 23 83 (1976).

[13] Pond, R. B., U. S. Patent 2,825,108, "Metallic Filaments and Methods of Making Same", March 4, 1958.

[14] Pond, R. B., U. S. Patent 2,976,590, "Method of Producing Metallic Filaments", March 28, 1961.

[15] Mobley, C. E., Clauer, A. H., and Wilcox, B. A., "Microstructures and Tensile Properties of 7075 Aluminum Compacted from Melt-Spin Ribbon", J. Inst. Metals, 100 (1972), 142-145.

[16] Carslaw, H., and Jaeger, J., Conduction of Heat in Solids, Second Edition, 285-288, Oxford Press (1959).

[17] Taylor, C., "Continuous Casting Update:, Met. Trans. B, 63, 355-325 (1975).

[18] Malik, R. K., "Hot Pressing of Titanium Aerospace Components", International J. of Powder, Met., 10 (2), 115-129 (April, 1974); see also Malik, R. K., "Hot Pressing of Titanium Alloy Fittings", paper presented at the Air Force Seminar on Powder Metallurgy, Battelle, Columbus Laborator-es, Columbus, Ohio (June 12-14, 1973); and Malik, R. K., "Diffusion Molding of Titanium", International J. of Powder, Met., 9 (4), 151-160 (October, 1973).

[19] Esslinger, P., Z. Metallkde, 57 109 (1966).

[20] Jones, H., Mater. Sci. Eng., 5 1 (1969).

[21] Davis, L. A., Scripta Met., 9 431 (1975).

[22] Hill, R., The Mathematical Theory of Plasticity, Oxford University Press, London, p. 213 (1967).

[23] Marsh, D. M., Proc. Roy. Soc., A279, 420 (1964).

[24] Marsh, D. M., Proc. Roy. Soc., A282, 33 (1964).

[25] Tanner, L. E., and Ray, R., Scripta Met., 11 783 (1977).

[26] Pampillo, C. A., J. Mater. Sci., 10 1194 (1975).

[27] Nowick, A. S., and Mader, S., IBM J. Res. and Dev., 9 358 (1965).

[28] Bennett, C. H., J. Appl. Phys., 43 2727 (1972).

[29] Frank, F. C., Proc. Roy. Soc., 215A, 43 (1952).

[30] Finney, J. L., Proc. Roy. Soc., 319A, 479 and 495 (1970).

[31] Cargill, G. S., III, J. Appl. Phys., 41 12 and 2248 (1970).

[32] Polk, D. E., Scripta Met., 4 117 (1970); Acta Met., 20 485 (1972).

[33] Marcus, M., and Turnbull, D., Mat. Sci. and Eng., 23 211 (1976).

[34] Jones, H., Rep. Prog. Phys., 36 1425 (1973).

[35] Turnbull, D., J. Phys. (Paris) Colloq., 4 1 (1974).

[36] Collings, E. W., and Gegel, H. L., Physics of Solid Solution Strengthening, Plenum Press, p. 147 (1976).

[37] Giessen, B. C., and Wagner, C.N.J., Liquid Metals, ed. by Beer, S., Dekker, Inc., N.Y., Chapter 15 (1972).

[38] Pearson, W. B., The Crystal Chemistry and Physics of Metals and Alloys, Wiley-Interscience, N.Y. (1972).

[39] Giessen, B. C., et al., 106th AIME Annual Meeting, Atlanta, Georgia, (March 6-10, 1977).

[40] Davis, L. A., Chou, C.P., Tanner, L. E., and Ray, R., Scripta Met. 10 937 (1976).

[41] Ruhl, R. C., Giessen, B. C., Cohen, M., and Grant, N. J., Acta Met., 15 1693 (1967).

[42] Wood, J. V., and Sare, I., Met. Trans., A, 6A 2153 (1975).

[43] Wood, J. V., and Honeycombe, R. K., J. Mat. Sci., 9 1183 (1974).

[44] Jones, H., Rapidly Quenched Metals, Second International Conference, Section I, Ed., by Grant, N., and Giessen, B., 1, Massachusetts Institute of Technology Press (1975).

[45] Pratis, M. and Biloni, H., Met. Trans., 3 1501 (1972).

[46] Efremov, P., and Rutis, V., Steel in the USSR, 12 28 (1974).

[47] Sinha, A. K., and Duwez, P., J. Phys. Chem. Solids, 32 267 (1971).

[48] Chang, H., and Sastri, S., Met. Trans., 8A 1063 (1977).

☆U.S.Government Printing Office: 1978 — 757-080/93